การศึกษาปัจจัยการเจียระไนในการขึ้นรูปทรงกลมโพลียูรีเทนโฟมชนิดพรุน

นาย อิศราวิทย์ เชาว์พานิช

STUDY OF GRINDING FACTORS FOR SPHERICAL FORMING
OF POROUS POLYURETHANE FOAM

Mr. Isarawit Chaopanich
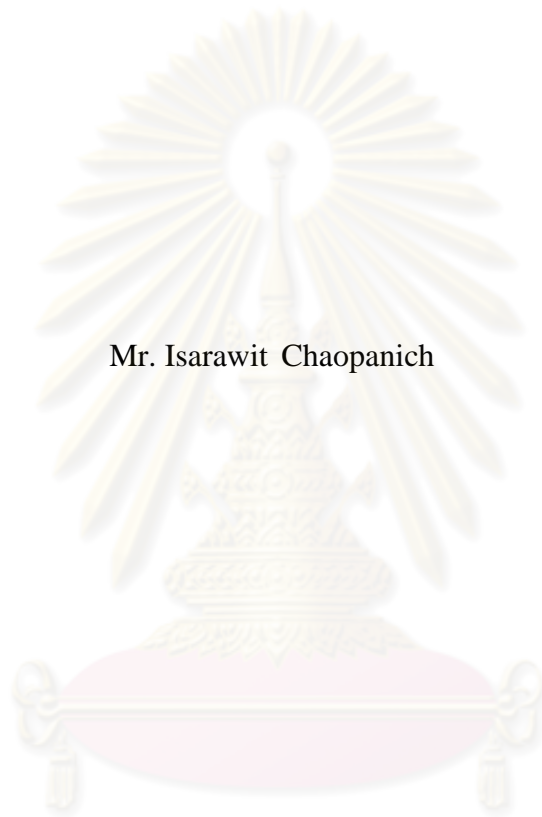
A Dissertation Submitted in Partial Fulfillment of the Requirements

for the Degree of Doctor of Philosophy Program in Industrial Engineering

Department of Industrial Engineering

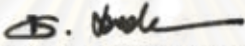Faculty of Engineering

Chulalongkorn University

Academic year 2010
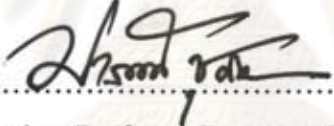
Thesis Title   STUDY OF GRINDING FACTORS FOR SPHERICAL

                      FORMING OF POROUS POLYURETHANE FOAM

By   Mr. Isarawit Chaopanich

Field of Study   Industrial Engineering

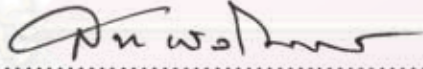Thesis Advisor   Assistant Professor Somchai Puajindanetr, Ph.D.

Accepted by the Faculty of Engineering, Chulalongkorn University in Partial Fulfillment of the Requirements for the Doctoral Degree

.... Dean of the Faculty of Engineering

(Associate Professor Boonsom Lerdhirunwong, Dr.Ing.)
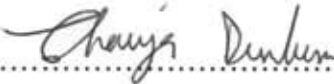
THESIS COMMITTEE

.... Chairman

(Associate Professor Parames Chutima, Ph.D.)

.... Thesis Advisor

(Assistant Professor Somchai Puajindanetr, Ph.D.)

.... Examiner

(Assistant Professor Seeronk Prichanont, Ph.D.)

.... Examiner

(Associate Professor Somchai Puangphuaksook)

.... External Examiner

(Assistant Professor Chaiya Dumkum, Ph.D.)

อิศราวิทย์ เชาว์พานิช : การศึกษาปัจจัยการเจียระไนในการขึ้นรูปทรงกลมโพลียูรีเทนโฟมชนิด
พรุน (STUDY OF GRINDING FACTORS FOR SPHERICAL FORMING OF POROUS
POLYURETHANE FOAM) อ.ที่ปรึกษาวิทยานิพนธ์หลัก : ผศ.ดร. สมชาย พัวจินดาเนตร,
239 หน้า.

     วัตถุประสงค์ของงานวิจัยนี้ เพื่อศึกษาปัจจัยที่มีอิทธิพลต่อการขึ้นรูปทรงกลมวัสดุโพลียูรีเทน
โฟมชนิดพรุน ชิ้นงานลูกบาศก์ขนาด 21 มิลลิเมตรถูกเจียระไนด้วยหินขัดที่มีความละเอียด 20 และ 53
ไมครอน ควบคุมความเร็วตัดระหว่าง 1.41 ถึง 5.18 เมตรต่อวินาที และความเร็วป้อนแนวดิ่งของแผ่น
จานร่องวงกลมที่ 1 3 และ 5 มิลลิเมตรต่อนาที บันทึกค่าสัญญาณแรงเจียระไนด้วยเครื่องวัดไดนาโม
มิเตอร์ ตรวจสอบชิ้นงานเจียระไน ได้แก่ รูปร่าง ขนาดเส้นผ่านศูนย์กลางและค่าผิดพลาดความกลม
ประมวลผล (1) แรงเจียระไนแนวสัมผัสและแรงกดปกติที่สัมพันธ์กับเวลาและความถี่ (2) อัตราการ
ขจัดเนื้อวัสดุออก (3) พลังงานจำเพาะในการเจียระไน และ (4) อิทธิพลของปัจจัยการเจียระไนโดย
วิธีการวิเคราะห์ความแปรปรวน ที่ระดับนัยสำคัญ (α) 0.05

     ผลการศึกษาพบว่า (1) รูปร่างของชิ้นงานหลังเจียระไนจำแนกได้ 4 ประเภท คือ รูปไข่ ทรง
กลม ทรงกลมบางส่วน และทรงสี่เหลี่ยมมน (2) ความเร็วตัดมีอิทธิพลต่อ ค่าผิดพลาดความกลม ขนาด
เส้นผ่านศูนย์กลาง แรงเจียระไนแนวสัมผัส แรงกดปกติ และ อัตราส่วนของแรงเจียระไน ขณะที่
ความเร็วป้อนแนวดิ่งของแผ่นจานร่องวงกลมมีอิทธิพลต่อ อัตราการขจัดเนื้อวัสดุออก และพลังงาน
จำเพาะในการเจียระไน (3) ชิ้นงานทรงกลมขนาดเส้นผ่านศูนย์กลางระหว่าง 19.28 ถึง 19.32 มิลลิเมตร
มีค่าผิดพลาดความกลมระหว่าง 0.57 ถึง 0.61 มิลลิเมตร ที่ช่วงความเชื่อมั่นร้อยละ 95 สามารถขึ้นรูป
ได้โดยใช้ความเร็วตัดระหว่าง 2.83 ถึง 3.77 เมตรต่อวินาที (4) สภาวะการเจียระไนที่ทำให้เกิดชิ้นงาน
ทรงกลมพบว่าสัญญาณแรงเจียระไนแนวสัมผัสและแรงกดปกติเทียบกับเวลา มีแนวโน้มเพิ่มขึ้นด้วย
อัตราเฉลี่ย เท่ากับ 0.64×10^{-4} และ 8.2×10^{-4} นิวตันต่อวินาที ตามลำดับ ความเข้มข้นสูงสุดของสัญญาณ
แรงเจียระไนแนวสัมผัสเกิดขึ้นที่ความถี่ระหว่าง 5.3 ถึง 7.1 เฮริทซ์ และอัตราส่วนของแรงเจียระไน
แนวสัมผัสต่อแรงกดปกติมีค่าเท่ากับ 1.03±0.15 (5) ความเร็วตัด 3.30 เมตรต่อวินาที ความเร็วป้อน
แนวดิ่งของแผ่นจานร่องวงกลม 1 มิลลิเมตรต่อนาที และความละเอียดของหินเจียระไนขนาด 53
ไมครอน สามารถขึ้นรูปชิ้นงานทรงกลมที่มีค่าผิดพลาดความกลมต่ำที่สุดเท่ากับ 0.47 มิลลิเมตร

ภาควิชา ...วิศวกรรมอุตสาหการ...   ลายมือชื่อนิสิต..

สาขาวิชา.. วิศวกรรมอุตสาหการ...   ลายมือชื่อ อ. ที่ปรึกษาวิทยานิพนธ์หลัก..............

ปีการศึกษา ...2553...
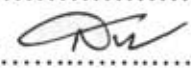
4971841021 : MAJOR INDUSTRIAL ENGINEERING
KEYWORDS: SPHERICAL GRINDING / POROUS POLYURETHANE FOAM/ CIRCULARITY ERROR

ISARAWIT CHAOPANICH: STUDY OF GRINDING FACTORS FOR SPHERICAL FORMING OF POROUS POLYURETHANE FOAM, THESIS ADVISOR: ASST. PROF. SOMCHAI PUAJINDANETR, Ph.D., 239 pp.

The objective of this research was to find the influential factors in the spherical forming porous polyurethane foam (PPUF). The as received cube specimens having dimensions of 21 mm were ground with the abrasive grit sizes of 20 and 53 µm, the grinding speeds varied from 1.41 to 5.18 m/s, and the cross head speeds controlled at 1, 3, and 5 mm/min. The grinding force signals were recorded using dynamometer. The ground specimens were determined which were shapes, finished diameters, and circularity errors. Tangential and normal grinding forces related with time and frequency domain, material removal rate, and specific grinding energy were analyzed. The effects of grinding factors were assessed via Analysis of Variance (ANOVA) with the significance level (α) of 0.05.

The study found that (1) the finished shapes were categorized into four types namely egg, sphere, partial sphere, and squircle (2) the grinding speed significantly influenced on circularity error, finished diameter, tangential force, normal force, and grinding force ratio, while the cross head speed affected on material removal rate and specific grinding energy (3) the finished sphere specimens having diameters between 19.28 and 19.32 mm with circularity errors between 0.57 and 0.61 mm of the 95% confidence interval could be formed at the grinding speed ranged between 2.83 and 3.77 m/s (4) at the grinding conditions where the finished sphere specimens were formed, the tangential and normal forces related with time domain trended to increase with the rates of 0.64×10^{-4} N/s and 8.2×10^{-4} N/s, respectively, the peak frequencies of tangential force signals were between 5.3 and 7.1 Hz, and the grinding force ratio of tangential and normal force was 1.03 ± 0.15 (5) the grinding speed of 3.30 m/s, cross head speed of 1 mm/min, and abrasive grit size of 53 µm was the best condition of the spherical grinding which provided the minimum circularity error of 0.47 mm.

Department....Industrial Engineering...   Student's signature......

Field of study...Industrial Engineering...   Advisor's signature......

Academic year...2010...

ACKNOWLEDGEMENTS

CONTENTS

Page

LIST OF TABLES

TABLE		Page

LIST OF FIGURES

Chapter I

Introduction

1.1 Background

Porous materials come in many types such as metals, polymers, ceramics, woods, and natural sources including calf bone, sea coral and so on. Wide spread usages have been applied in many fields of industry. For example, break pads, oil filters and air filters in automotives are made from porous plastics (Porous Materials Inc., 2008: online). In pharmaceutical applications, porous materials have been used in-situ drug delivery systems. Moreover, the outstanding application of the material seems likely to be in the biomedical fields for artificial organ that can help the patients who suffered from losing their own parts of body (Ponin, 1987). Some kinds of ceramic such as Hydroxyapatite (HA) and Alumina (Al_2O_3) play a significant role in prosthesis implantations for bone filtration and replacement, plasma spray coating on hip joints, and so forth. With open pore structures, porous materials have excellent permeability and a large surface area, as well as excellent biocompatibility (Lee *et al.*, 2007), resulting in promoting fibro vascular and bone tissue in growth.

One of the most invaluable applications of porous materials is spherical orbital implant used in enucleation and evisceration surgery for eye ball replacement. Because of pore matrixes, the orbital implant can be attached directly to tissue via its pores, allowing it to move within the orbit just like the natural eye. Jordan (2004) stated that losing an eye to trauma or end stage ocular disease can be devastating at any ages, and this major impact affects one's self-image, self-confidence, and self-esteem. However, numerous patients have been trying to return to their normal life although there is some loss of depth perception and peripheral vision, but they are not as "handicapped" as many beliefs.

Although having many advantages, porous materials having pore structural matrixes as shown in Figure 1.1 are very sensitive to stress applying on it, and crack propagation can easily be initiated during manufacturing processes. Inherent brittleness is the overriding factor, which limits the ultimate usefulness of porous materials. The cracks, even on micro scale, can hardly be seen by naked eyes, causing tremendous strength degradation. The decrease in mechanical strengths with increased porosity was not surprising and has been described elsewhere by various authors (Huec *et al*., 1995); (Liu, 1997); and (Tian and Tian, 2001).

As a result of high porosity and low strength, forming processes in particular machining are obviously difficult because crack damages, uncontrollable dimensional accuracy and shape variations can occur during operations. This inevitably leads to high manufacturing costs and expensive products.
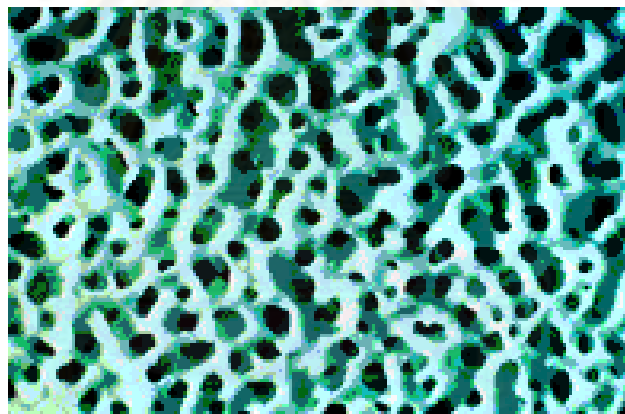
Figure 1.1   Pore structure of a porous ceramic (IOI, 2007: online)

Nowadays, near net shape technology for porous material forming has been developed; however, the shrinkages of porous ceramic material after sintering illustrated in Figure 1.2 cause the shape and dimension variated (Tian and Tian, 2001). Therefore, mechanical operation especially grinding is necessary in forming process to achieve finished shape and dimensional accuracy (Marinescu, 2000).
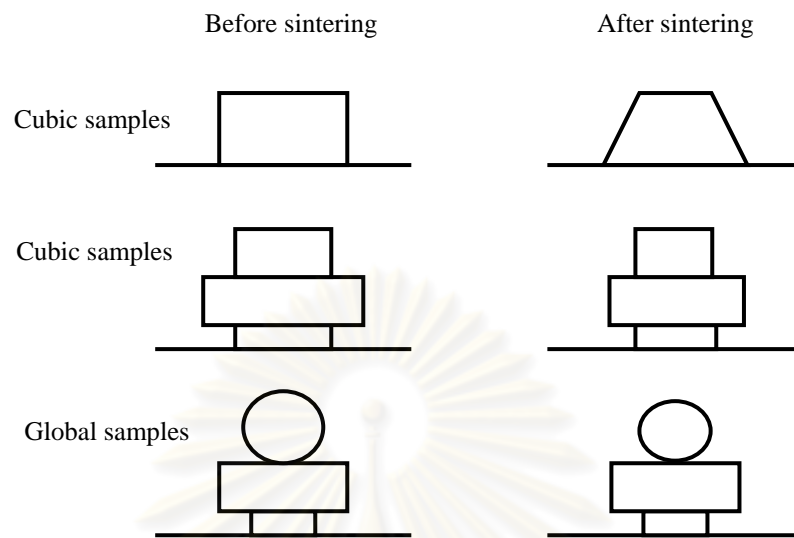
Figure 1.2   Shrinkage of porous materials after sintering

(Tian and Tian, 2001)

In terms of spherical forming partically for orbital implant manufacturing, the traditional hand grinding by highly skilled operators is still required to adjust sizes and shapes fitted to individual requirement. Unfortunately, uncontrollable direction to form sphere shape and over grinding forces may cause in crack damages and high variation in shape and size. As a result, low product quality, time consumption, and high price are not avoided.

Over the past two decades, spherical grinding techniques namely V-groove lapping and magnetic fluid grinding have been introduced for ball bearing production for dense ceramic materials such as silicon nitride. Many researchers have been developing those techniques to achieve low crack damages, high material removal rate, and minimal roundness errors for better performance in high precision work. On the other hand, spherical forming techniques for porous materials have not been widely revealed and studied. Milling and orthogonal cutting operations for porous hydroxyapatite and polyurethane foam were investigated by Chelule *et al.* (2003) and Malak and Anderson (2005).

Therefore, in this research the new spherical grinding process using circular groove pad for forming porous materials in the presence of porous polyurethane foam was introduced. Moreover, the influential factors affecting finished shape, circularity error, finished diameter, grinding forces, grinding force ratio, material removal rate, and specific grinding energy were intensively investigated.

1.2 Objectives of Study

The objectives of this research were as follows,

1. To develop grinding process for spherical forming of polyurethane foam.
2. To study influential grinding factors for spherical forming of polyurethane foam.

1.3 Scopes of Study

The scopes of this research were as follows,

1. Cube porous polyurethane foam having dimensions of 21 mm was used as the specimen to form spherical shapes.
2. Circular groove having radius of 11.30 mm was used in the spherical grinding system.
3. Grinding speeds of grinding wheel were controlled between 1.41 and 5.18 m/s.
4. Cross head speeds of circular groove pad were run at 1.0, 3.0, and 5.0 mm/min.
5. Abrasive grits of silicon carbide sizing 20 and 53 μm were used in this research.

1.4 Expected Results

Expected results of this research were as following,

1. Sphere shape of porous polyurethane foam could be formed using spherical grinding system with circular groove pad.

2. Influential grinding parameters could be revealed.

3. Grinding responses in terms of circularity error, finished diameter, grinding forces, grinding force ratio, material removal rate, and specific grinding energy could be estimated in the spherical grinding system as developed.

4. Proper grinding conditions to receive minimal circularity error and required finished diameter with no damages for the ground specimen could be found.

1.5 Advantages of Study

The expected advantages of this research were as follows,

1. Spherical grinding technique could be applied for spherical parts manufacturing such as orbital implants for enucleation and evisceration surgery.

2. Reproducibility and minimal variation in shape and size could be received from the spherical grinding technique developed.

3. Time consumption in spherical parts forming could be reduced using the developed method instead of hand grinding.

Chapter II

Literature Reviews

In this chapter, literature reviews were surveyed. First of all, overviews of porous materials in terms of meaning, types, properties, and applications were illustrated. Secondly, grinding mechanism, related parameters, and material removal process were described to clearly understand basic concepts in grinding process. Next, machining porous materials and current spherical grinding processes were reviewed. Moreover, spherical measurement and machining force monitoring concepts were concerned.

2.1 Porous Materials

To better understand the machining behavior of porous materials, it is necessary to understand the characteristics of the material before defining proper variables in machining processes. In this section of literature review, types, properties, and applications of porous materials were demonstrated.

2.1.1 Types of Porous Materials

Gibson and Ashby (1988) defined porous materials as a cellular solid that is made up of an interconnected network. Three typical structures were illustrated in Figure 2.1. In addition, they classified types of porous cellular solids into two categories: synthesis and natural porous solids. Porous materials can be synthesized from diverse materials such as metals, polymers, ceramics and glasses as well as can be from natural also.
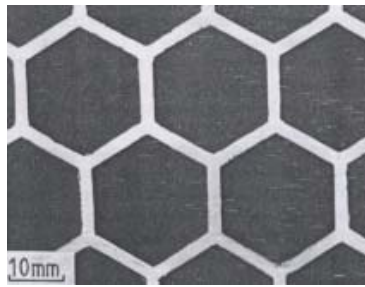
a) A two-dimensional honeycomb   b) A three dimensional cellular with open cells
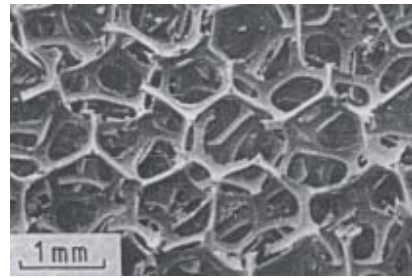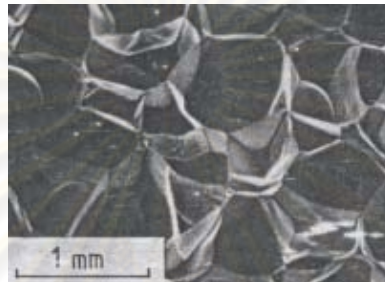
c) A three dimensional cellular with closed-cells

Figure 2.1   Three basic structures of porous materials: a) A two-dimensional
honeycomb, b) A three dimensional cellular with open cells, c) A three
dimensional cellular with closed-cells (Gibson and Ashby, 1988)

1) Synthetic Porous Materials

    a) Polymers

Porous polymers can be produced by foaming gas bubbles into liquid monomer
or hot polymer, allowing the bubbles to grow and stabilize, and then solidifying the
whole thing by cross-linking or cooling. Figure 2.2 showed the structures of open-cell
polyurethane and closed-cell polyethylene that are different each other in that open-cells
are produced by drawing solid materials into struts which form the cell edges, but for
closed-cell solid membranes close off the cell face and is uniformly distributed between
the edges and faces.

a) Open-cell polyurethane   b) Closed-cell polyethylene
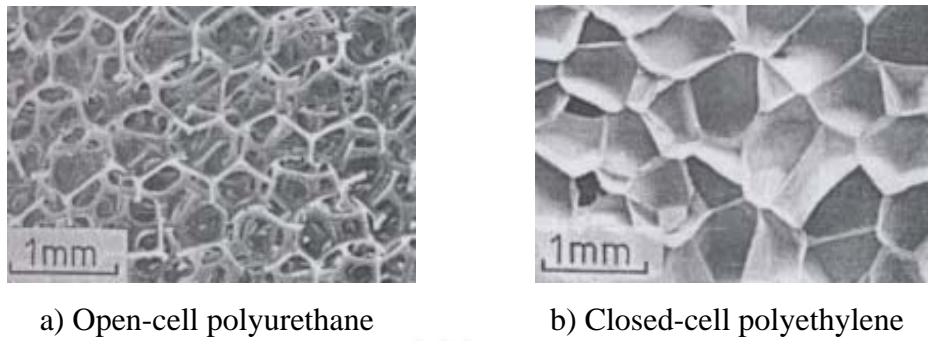
Figure 2.2   Three dimensional porous polymers: a) Open-cell polyurethane,
b) Closed-cell polyethylene (Gibson and Ashby, 1988)

b) Metals

Another type of synthetic porous material is made from metals called metallic porous materials, which are made by mixing organic beads (carbon, for instance) into the metal melt in an inert atmosphere. When the metal is cooled and solidified, the carbon is burnt off, leaving a cellular matrix. Metals can be infiltrated into a low density bed of carbon or ceramic, which is subsequently leached out leaving framework of metal which penetrates the pores. Figure 2.3 showed the structures of metallic porous nickel and copper.
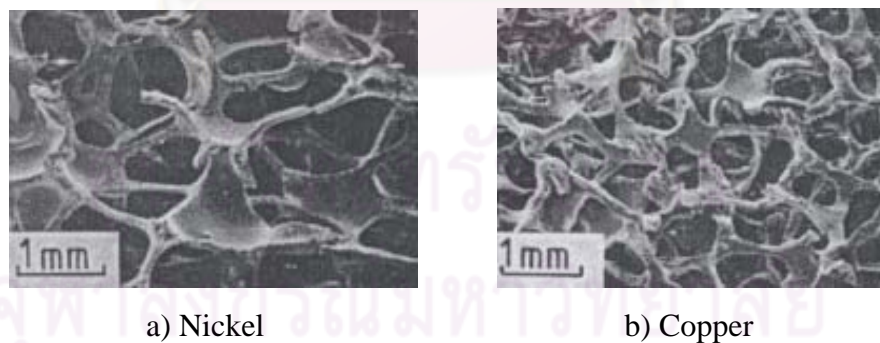
a) Nickel   b) Copper

Figure 2.3   Three dimensional metallic porous materials: a) Nickel, b) Copper
(Gibson and Ashby, 1988)

c) Ceramics

Ceramics can also be fabricated in the form of porous materials by infiltrating polymer foam with a slip (fine slurry of the ceramic in water or some other fluids); when the aggregate is fired, the slip bonds to give pores of the original foam which burns off. Three dimensional structures of Zirconia, Mullite, Hydroxyapatite were depicted in Figure 2.4.

a) Zirconia   b) Mullite

c) Hydroxyapatite (Lee *et al.*, 2007)
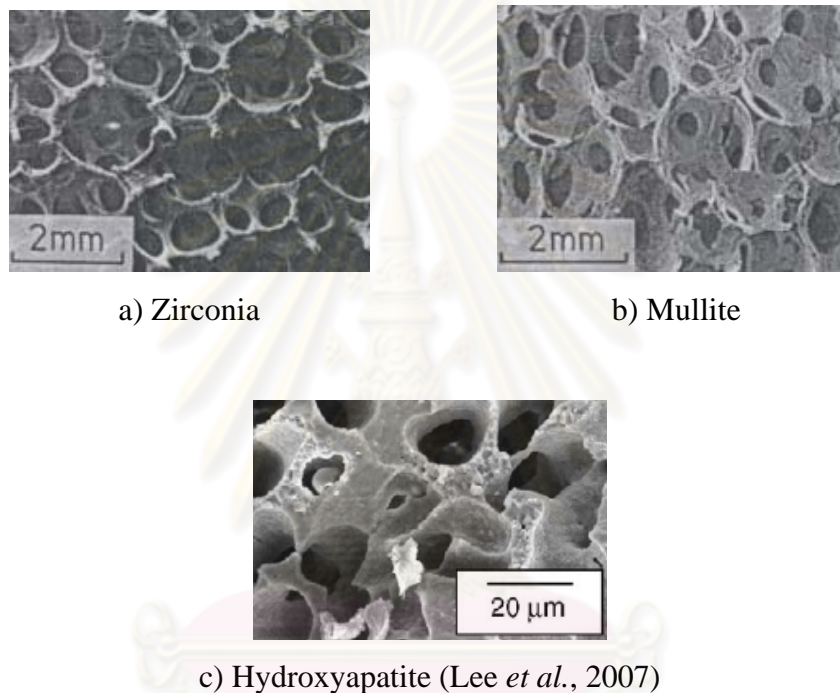
Figure 2.4   Three dimensional porous ceramics: a) Zirconia, b) Mullite,
              c) Hydroxyapatite (Gibson and Ashby, 1988)

2) Natural Porous Materials

Beside from synthetic porous materials, various materials from natural of which structures were shown in Figure 2.5 are defined as natural porous materials. For example, cork and balsa have closed cells which are almost as regular as a honeycomb. On the other hand, sponge and cancellous bone have an open pore with connectivity. Still others, like coral or cuttlefish bone, are obviously anisotropic: the cells are elongated or aligned in particular directions, and this gives them properties which depend on the direction in which they are measured.

| a) Cork | b) Balsa | c) Sponge | d) Cancellous bone |

| e) Coral | f) Cuttlefish bone | g) Iris leaf | h) Stalk of a plant |
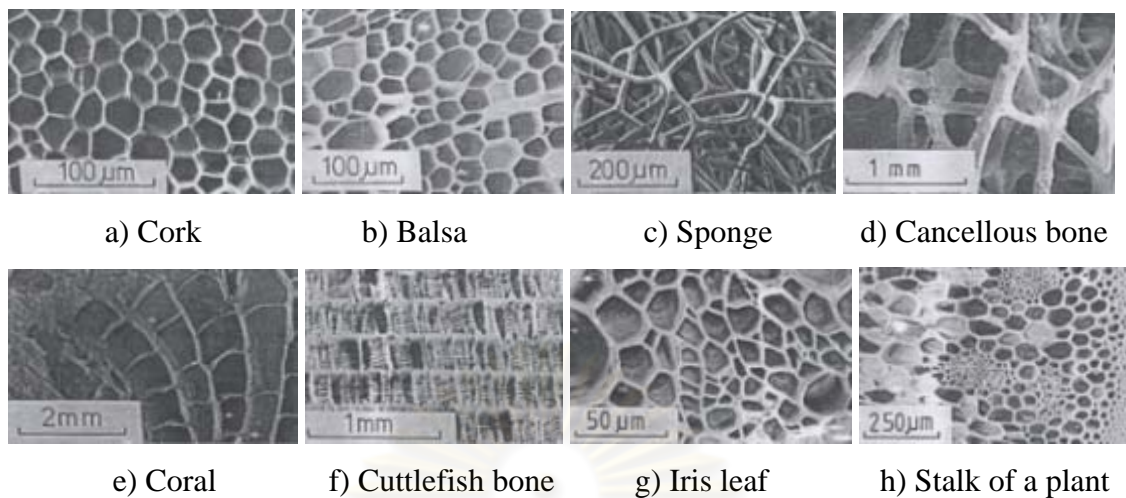
Figure 2.5   Natural cellular materials: a) Cork, b) Balsa, c) Sponge, d) Cancellous bone, e) Coral, f) Cuttlefish bone, g) Iris leaf, h) Stalk of a plant (Gibson and Ashby, 1988)

2.1.2 Porous Material Properties

Due to their pore structures, porous materials have properties different from solid ones of which they are made up. However, the properties of porous materials cannot be exactly indicated because of different fabrication techniques applied. Therefore, properties of solid forms were generally given in Table 2.1, 2.2, and 2.3 in terms of physical, thermal, and mechanical properties and could be relatively compared in Table 2.4. Metal solids having strong metallic bond show greater density, than any other type of material due to the greatest packing density (the face-centered cubic or the close-packed hexagonal structure). In terms of thermal conductivity, metals give the highest value, resulting from rapidly free electron transmission. Ceramics having strong ionic and covalent bonds exhibit higher hardness, yield strength and modulus; on the other hand, because of their brittleness fractural strength and fracture toughness are lower than those of metals. Polymers, naturally containing weak bond and having low density, give low thermal conductivity, high specific heat and thermal expansion. Mechanical properties of polymers are very low when compared to metals and ceramics (Gilbert *et al.*, 1986).

Table 2.1   Properties of Solid Polymers (Gibson and Ashby, 1988)

Material	1. Density ρ_s (g/cm³)	2. Melting point T_g (K)	3. Thermal expansion α_s $\times 10^{-6}$ (K⁻1)	4. Thermal conductivity λ_s (W/m K)	5. Specific heat C_{ps} (J/kg K)	6. Young's modulus at 20°C E_s (GN/m²)	7. Yield strength σ_{ys} (MN/m²)	8. Fracture strength σ_{fs} (MN/m²)	9. Fracture toughness K_{ICS} (MN/m³/²)
Cellulous	1.5	-	-	-	-	25	350	-	-
Epoxies	1.25-1.7	400	55-90	0.2-0.5	1700-2000	5-10	-	40-85	0.6-1.0
Latex rubber	0.9	-	-	-	-	0.0026	-	-	-
Lignin	1.4	-	-	-	-	2.0	-	-	-
Nylon 66	1.15	340	80-90	0.2-0.25	1200-1900	2-3.5	50-110	55-120	3-5
Polybutadiene	1.05	203	-	0.14	-	0.001-0.05	-	-	-
Polychloroprene	0.94	200	-	-	-	0.002-0.1	-	-	-
Polyester	1.25-1.4	340	70-100	0.2-0.24	800-1500	1.3-4.5	-	45-85	0.5
Polyethylene, PE (Low D)	0.91-0.94	270	160-200	0.35	2250	0.15-0.24	-	7-17	1.0
Polyethylene, PE (High D)	0.95-0.97	300	120-160	0.52	2200	0.55-1.0	-	20-37	2.0
Polyisoprene	0.91	220	-	0.14	-	0.002-0.1	-	10	-
Polymethylmethacrylate, PMMA	1.2	378	54-72	0.2	1500	3.3	81	95	0.9-1.7
Polypropylene, PP	0.91	253	70-110	0.2	1900	1.2-1.7	30-70	40-80	3-5.8
Polystyrene, PS	1.05	373	70-110	0.1-0.15	1350	1.4-3.0	30-80	35-90	2.0
Polytetrafluorethylene, PTFE	2.2	-	100	0.25	1050	0.35	-	17-28	-
Polyurethane, PU (rigid)	1.2	-	-	-	-	1.6	127	130	-
Polyurethane, PU (Flexible)	1.2	-	-	-	-	0.045	-	-	-
Polyvinyl chloride, PVC	1.4	-	50-60	0.12-0.18	1400	2.4-3.0	40-59	45-65	2.45
Polyvinylidene fluoride, PVDF	1.78	-	-	-	-	1.8-2.4	20-25	35-40	-
Protein	1.2-1.4	-	-	-	-	-	-	-	-
Suberin	0.9	375	-	-	-	9.0	-	-	-

Table 2.2   Properties of Solid Metals (Gibson and Ashby, 1988)

Material	1.Density ρ_s (g/cm^3)	2.Melting point Tg (K)	3.Thermal expansion α_s $\times 10^{-6}$ (K^{-1})	4.Thermal conductivity λ_s(W/m K)	5.Specific heat C_{ps} (J/kg K)	6.Young's modulus at 20°C E_s (GN/m^2)	7.Yield strength σ_{ys} (MN/m^2)	8.Fracture strength σ_{fs} (MN/m^2)	9.Fracture toughness K_{ICS} (MN/m$^{3/2}$)
Aluminium	2.7	933	24	230	1080	69	40	200	50
Aluminium alloys	2.6-2.9	≤ 933	20-24	88-160	920-960	69-79	100-627	300-700	23-45
Beryllium	1.85	1277	12.4	158	1883	296	34	380	4
Brasses and bronzes	7.2-8.9	≤ 1200	14-20	110-230	380	103-124	70-640	230-890	50-100
Chromium	7.2	2148	6.2	67	936	289	-	-	-
Cobalt and alloys	8.1-9.1	< 1768	12-13	40-69	400-600	200-248	180-2000	500-2500	-
Copper	8.9	1356	16.5	384	493	124	60	400	>100
Copper alloys	7.5-9.0	≤ 1356	14-17	50-230	320-400	120-150	60-960	250-1000	50-100
Gold	19.3	1336	14.2	297	130	82	40	220	>100
Iron	7.9	1809	11.7	75	460	196	50	200	5-100
Lead and alloys	10.7-11.3	≤ 600	28-30	27-35	130-140	14	11-55	14-60	>50
Magnesium alloys	1.74-2.0	≤ 923	26	42-140	1020	41-45	80-300	125-380	15-40
Molybdenum and alloys	10-13.7	≤ 2880	4-5	116-146	250-270	320-365	560-1450	665-1650	-
Nickel	8.9	1726	13.3	92	730	214	70	400	>100
Nickel alloys	7.8-9.2	≤ 1726	12-14	15-65	380-460	130-234	200-1600	400-1200	50-100
Niobium and alloys	7.9-10.0	≤ 2740	7-8	30-58	200-340	80-100	-	-	-
Platinum	21.4	2042	8.9	71	130	172	-	-	>100
Silver	10.5	1234	19.7	420	234	76	55	300	> 100
Steels	7.6-8.1	≤ 1809	11-12	24-66	420-500	190-210	200-1500	500-1200	50-200
Tantalum and alloys	16.6-16.9	≤ 3250	6-7	30-54	100-168	150-186	330-1090	400-1200	-
Titanium and alloys	4.3-5.1	1943	8-9	15-27	500-550	80-130	180-1320	300-1400	55-115
Tungsten and alloys	13.4-19.6	≤ 3680	4-5	160-190	140-145	350-406	1000-1400	1500-1800	-
Urenium	18.9	1405	17	26	126	172	-	-	-
Zinc and alloys	5.2-7.2	≤ 505	20-40	100-112	400-420	43-96	160-421	200-500	10

Table 2.3 Properties of Solid Ceramics and Glasses (Gibson and Ashby, 1988)

Material	1.Density ρ_s (g/cm^3)	2.Melting point Tg (K)	3.Thermal expansion α_s $\times 10^{-6}$ (K^{-1})	4.Thermal conductivity λ_s(W/m K)	5.Specific heat C_{ps} (J/kg K)	6.Young's modulus at 20°C E_s (GN/m^2)	7.Yield strength σ_{ys} (MN/m^2)	8.Fracture strength σ_{fs} (MN/m^2)	9.Fracture toughness K_{ICS} (MN/m$^{3/2}$)
Alumina Al_2O_3	3.9	2323	8.8	25	795	380	5000	150-300	3-5
Beryllia BeO	3.0	2700	9.0	200	1250	380	4000	-	-
Calcite (limestone, coral)	2.7	-	8.0	7.0	-	63	-	30-80	0.9
Cement	2.4-2.5	-	1.2	10-14	-	45-50	-	1-2	0.2
Glass, silica	2.6	1100	0.5-1.0	2.0	750	94	-	-	-
Glass, soda	2.48	720	8.5	1.6	990	74	3600	50	0.7
Glass, borosilicate	2.23	820	4.5	1.2	800	65	-	55	0.8
Graphite	1.82	4000	2.5	120-200	120	27	-	-	-
Ice, H_2O	0.92	273	-	-	-	9.1	-	1.0	0.12
Magnesia, MgO	3.5	3073	13.5	3.0	-	250	3000	-	3.0
Mullite	3.2	-	5.3	-	-	145	-	-	-
Porcelain	2.3-2.5	800	6.0	1.5	-	70	-	45	1.0
Sialon	3.2	-	3.2	20-25	710	300	-	400-800	5.0
Silicon carbide, SiC	3.2	3110	4.3	50-84	1420	410	10000	200-500	3.0
Silicon nitride, Si_3N_4	3.2	2173	3.2	17	-	370	4000	-	4.0
Titanium carbide, TiC	7.2	-	7.4	17	-	370	4000	-	-
Tungsten carbide, WC	14-17	-	-	-	-	450-650	6000	-	-
Zirconia, ZrO_2	5.6	2843	10	2.0	670	200	4000	200-500	-

Table 2.4   Property comparisons of Polymers, Metals, Ceramics and Glasses

Properties	Polymers	Metals	Ceramics and glasses
1.Density ρ_s (g/cm^3)	○	●	◐
2.Melting point T_m (K)	○	◐	●
3.Thermal expansion $\alpha_s \times 10^{-6}$ (K^{-1})	●	◐	○
4.Thermal conductivity λ_s(W/m K)	○	●	◐
5.Specific heat C_{ps}(J/kg K)	●	○	◐
6.Young's modulus at 20°C E_s (GN/m^2)	○	◐	●
7.Yield strength σ_{ys} (MN/m^2)	○	◐	●
8.Fracture strength σ_{fs} (MN/m^2)	○	●	◐
9.Fracture toughness K_{ICS} (MN/m$^{3/2}$)	○	●	○

Low ○   Moderate ◐   High ●

Besides the properties of general solid materials that are processed to porous materials, properties of some interesting synthetic porous bioceramics such as porous hydroxyapatite (HA) used in medical applications are also reviewed in terms of the relationship between physical and mechanical properties.

HA can be derived from natural materials for example cancellous bone (Hing *et al*., 1999) and coral (Xu *et al*., 2001) and also synthesized by various methods such as gel casting (Munoz *et al*., 2001), impregnation a body of porous polyurethane foam with slurry (Tian and Tian, 2001), camphene-based freeze casting (Lee *et al*., 2007). The effect of porosity on mechanical properties plays a crucial role in evaluating the performance of the material in load bearing applications. Wang (1984) proposed that Young's modulus of porous alumina with changing pore structure is a function of porosity that well agreed to the results from much research studied by Hing *et al*. (1999); Pabst *et al*. (2006); Huec, *et al*. (1995), and etc. In the work of Zhang *et al*. (2006), flexural strength, elastic modulus, and fracture toughness of In-situ hardening

hydroxyapatite-based scaffold for bone repair were plotted as functions of pore volume fraction shown in Figure 2.6.
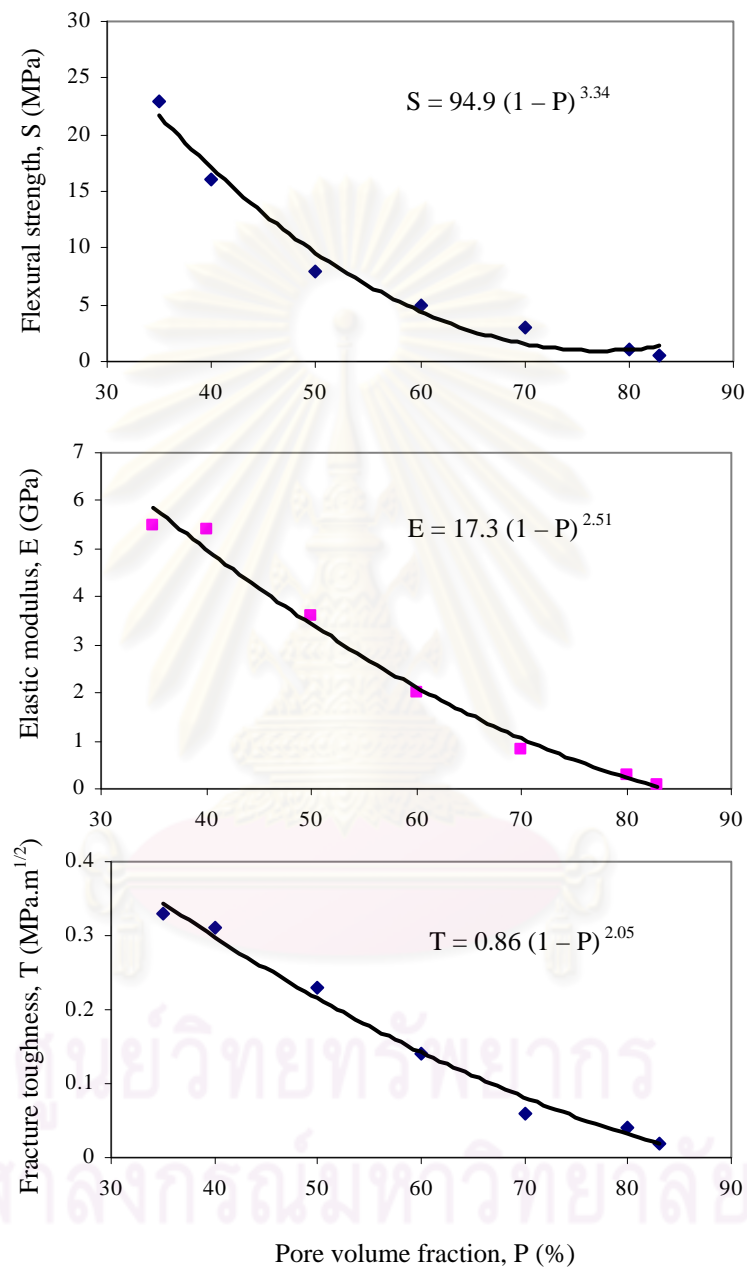
Figure 2.6   Relationship between pore volume fraction and mechanical properties of
In-situ hardening hydroxyapatite-based scaffold for bone repair
(Zhang *et al*., 2006).

2.1.3 Applications of Porous Materials

Porous materials have been expansively used in many fields of industries as well as medical applications. Because of pore network structures and their properties, porous materials give many advantages in terms of low mass and density, low thermal conductivity, and good permeability and biocompatibility. It is almost certainly that porous materials permit the simultaneous optimization of stiffness, strength, and low weight.

1) Thermal Insulation

Porous materials sometimes called porous solids, foams, and cellular materials can be used in fabrication of thermal insulators particularly porous polymers and glasses. Products as humble as disposable coffee cups, and as elaborate as the insulation of the booster rockets for the space shuttle exploit low thermal conductivity. Modern buildings, transport systems (refrigerated trucks and railway cars), and even ships particularly designed for carrying liquid natural gas also take advantage of low thermal conductivity of porous polymers (Gibson and Ashby, 1988). For high operating temperature at 550°C, porous ceramic such as zirconia foam can achieve the application of space shuttle protective thermal tiles (Montanaro *et al*., 1998).

2) Filtration

For production of castings, porous ceramic filters help to improve quality and productivity by removing non metallic inclusions. High temperature resistance is a must for filters, which can contain such reactive elements as aluminium, titanium, hafnium and carbon by a variety of molten metals (Montanaro *et al*., 1998). Applications in automotives including oil filters, air filters, cabin air filters, automotive sintered metal filters, and filter cartridges are determined by their pore structure characteristics. Pore size, pore distribution, gas and liquid permeability, and pore volume are some of the important pore structure characteristics (www.pmiapp.com).

.

3) Packaging (Gibson and Ashby, 1988)

One of the major uses of man-made cellular solids is packing (Kiessling, 1961) cited in Gibson and Ashby (1988). An effective package must absorb the energy of impacts or of forces generated by deceleration without subjecting the contents to damaging stresses. Foams are particularly well suited for this. In addition, foams can undergo large compressive strains (0.7 or more) at almost constant stress, so that large amounts of energy can be absorbed without generating high stresses.

4) Structural (Gibson and Ashby, 1988)

Many natural structural materials are cellular solids: wood, cancellous bone, and coral all support large static and cyclic loads, for long periods of time. The structural use of natural cellular materials by man is as old as history itself. The most obvious example is their use in sandwich panels in modern aircraft by using glass or carbon-fiber composite skins separated by rigid polymer foams giving a panel with enormous specific bending stiffness and strength.

5) Buoyancy (Gibson and Ashby, 1988)

Cellular materials found one of their earliest markets in marine buoyancy. Pliny (AD 77) cited in Gibson and Ashby (1988) described the use of cork for finishing floats. Today, closed-cell porous plastic foams commonly made from porous polystyrene, polyethylene, polyvinyl chloride or silicones are extensively used as supports for floating structures and floatation in boats.

6) Biomedical Applications

The uses of porous materials in biomedical applications are wide spread in replacement of human organs and in pharmaceutical. Porous ceramic materials play a major role to serve the need in biotechnology. Proper pore structure and mechanical properties are required for promoting growth of blood vessels and adequate fluid flow.

a) Scaffolds

Porous ceramics are also utilized as scaffolds in the biomedical field of tissue engineering. The primary purposes of tissue engineering are repair, regeneration and reconstruction of lost, damaged or degenerative tissues. In practice, a degradation rate of the grafting material similar to the rate of tissue formation is desired. Accordingly, one major aspect in the development of bio artificial organs and implants is the fabrication of supporting matrices or scaffolds with an appropriate micro and macroscopic structural morphology. Hydroxyapatite (HA), one of the most important biomaterials in artificial bone applications, can be used as filling material for bone defects (Sopyan *et al*., 2007). Because of their low solubility, high chemical resistance against physiological environment and high biocompatibility, nondegradable aluminum oxide and titanium oxide ceramics are of interest as materials for porous cell barriers and have successfully been utilized for tissue engineering (Eckert *et al*., 1993) and (Wintermantel and Ha, 1996). The cultivation of cardiomyocytes (heart muscle cells) on biocompatible scaffolds made from titanium dioxide ceramics was investigated for in vitro engineering of vital heart tissue (Polonchuk *et al*., 2000).

In orbital implantation, porous HA has been widely used for eye ball prostheses shown in Figure 2.7. It can be derived from coral in Figure 2.8 and synthesized from the technique of impregnating of porous polyurethane foam with slurry containing HA powder in Figure 2.9. The main advantage of HA over other implant materials such silicone, cork, and glass is their inertness or biocompatibility, which is fundamentally due to their low chemical reactivity. HA orbital implant is sutured into a living organism and acts as a passive structure or framework that allows fibrovascular ingrowth, resulting in a wrapped prosthesis with fibrous tissue which provides a natural movement (Munoz *et al*., 2001).
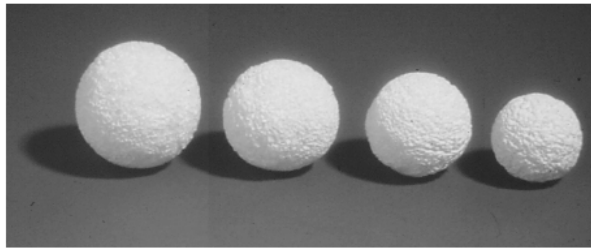
Figure 2.7   Hydroxyapatite implants of various sizes (Moshfeghi *et al*., 2000).
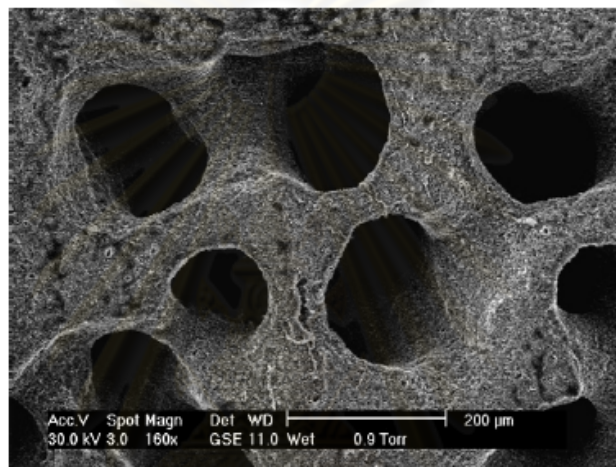
Figure 2.8   Scanning electron microscope image of coralline hydroxyapatite
(Chalasani *et al*., 2007).
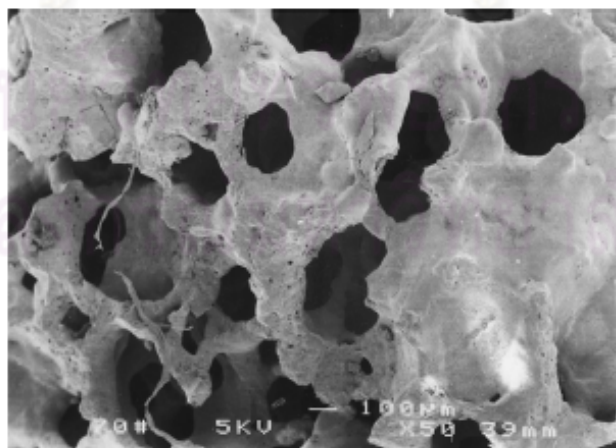
Figure 2.9   Scanning electron microscope image of porous hydroxyapatite from
foam (Tian and Tian, 2001).

b) Drug-Delivery Systems

Porous ceramics may be promising supports or new controlled drug-delivery systems. In case of chronic disease or localized surgical intervention, in which a sustained local drug-delivery becomes important, porous ceramic capsule may be suitable to release pharmacological substances at controlled rate (Ravaglioli and Krajewski, 1997). Recently, Ravaglioli *et al.* (1998) showed the general feasibility of producing a potential ceramic drug-dispensing system with specifically designed morphology and porosity. Furthermore, porous hydroxypatite blocks have been utilized as local drug-delivery systems, allowing slow release of antibiotic substances such as gentamicin (Rogers-foy *et al.*, 1999). The release rate depends partly on the open porosity and the presence of micro and macro pores (Bajpai and Benghuzzi, 1988).

c) Bioactive coating

Synthetic HA is also extensively used as a bioactive coating on porous metal surfaces (for example, prostheses in total hip replacement, orthopaedic, and dental implants) (Lacefield, 1993). The HA layer applied plasma-spraying is able to accelerate the rate of bone growth into the porous layer, resulting in enhanced biological fixation of the implant and improved bonding strength at the bone/implant interface (Hench, 1998).

2.2 Grinding Process

Grinding is one of the oldest manufacturing processes since the Stone age grinding was used to sharpen the tools of the prehistoric man. In the Middle Ages watermill driven grinding stones were used to produce tools, ploughs and weapons. Despite of the drawings of Leonardo Da Vinci around the year 1500, the first actual grinding wheel was manufactured just as late as the 19th century (Malkin, 1989).

Grinding refers to processes for material removal in the form of small chips by mechanical action of irregularly shaped abrasive particles that are used loose in bonded wheels (Dallas, 1976). Even now, the quality and productivity depends still on the experience of the operator. Nevertheless in the sixties of the 20th century, the first model on grinding was proposed based on the two dimensional topography of the grinding wheel.

In the current century, grinding is still involved in the manufacturing of many products because the shaping technology such as sintering is not as accurate as required by the size specifications. The grinding type of machining process is almost chosen for finishing purposes since grinding has a relatively high precision. However, it is well known that the process may induce damage at the machined surface affecting the functional properties of the material being ground. For example, the cracks may reduce the mechanical strength of a component. The residual stress may change the magnetic permeability by magnetostriction (Knowles, 1970), and phase changes can influence the paintability of the material.

2.2.1 Conventional Surface Grinding: A Model of Grinding Process

Schematic of a conventional (down) surface grinding in Figure 2.10 widely used to model grinding process showed various process variables: wheel diameter (D), wheel speed (Vs) , work piece speed (Vw), and depth of cut (d) that can affect a finished work piece in terms of dimensional accuracy, material removal rate, grinding forces, and specific grinding energy. Basic calculations for the conventional surface grinding process were illustrated in Equation 2.1 to 2.6 (Kalpakjian, 1992).
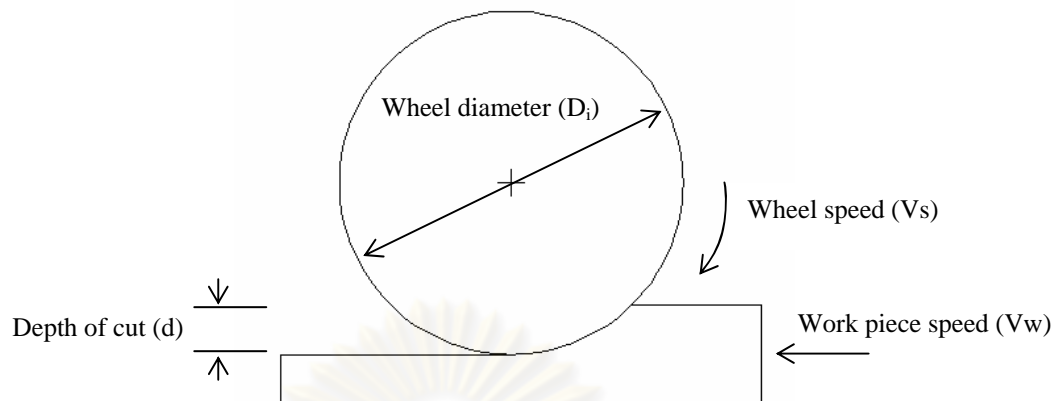
Figure 2.10   Schematic of a conventional (down) surface grinding

$$Vs \quad = \quad \pi \bullet D_i \bullet N \bullet \left(\frac{1}{60}\right) \qquad (2.1)$$

$$MRR \quad = \quad d \bullet b \bullet V_w \qquad (2.2)$$

$$P \quad = \quad MRR \bullet u \qquad (2.3)$$

$$P \quad = \quad T \bullet \omega \qquad (2.4)$$

$$T \quad = \quad F_t \bullet \frac{D_i}{2} \qquad (2.5)$$

$$\omega \quad = \quad 2 \bullet \pi \bullet \frac{N}{60} \qquad (2.6)$$

where

Vs	=	Grinding wheel speed (m/s)
D_i	=	Wheel diameter (m)
N	=	Wheel rotational speed (RPM)
MRR	=	Material removal rate (m^3/s)
d	=	Depth of cut (m)
b	=	Width of cut (m)
Vw	=	Work piece speed or Feed rate (m/s)
P	=	Power (W) or (J/s) or (N.m/s)

u	=	Specific grinding energy per unit volume of material removed (J/m^3)
T	=	Torque (N.m)
ω	=	Rotational angular velocity (rad/s)
Ft	=	Tangential force (N)

2.2.2 Grinding Mechanism

Grinding is typically characterized by the multiple cutting points with large negative rake angles removing chips of small volume at a very high material strain rate. The understanding of mechanism of grinding is important for the prediction of process variables such as grinding forces, surface roughness, etc (Hecker *et al.*, 2004).

The mechanism of the grinding process was investigated in many points of view by many researchers. Chen and Rowe (1996) proposed the study of kinematics relationship between grinding wheel and work piece motion applied to each irregular grain by distinguishing the grinding process into three phases: rubbing, plowing and cutting as shown in Figure 2.11. Rubbing phase occurs when the grain engages with the work piece in up-cut grinding and slides without cutting on the work piece surface due to the elastic deformation of the system. As the stress between the grain and work piece is increased beyond the elastic limit, plastic deformation occurs. This is the plowing phase. When the work piece material piles up to the front and to the sides of the grain to form a groove, a chip is formed and the work piece material can no longer withstand the tearing stress. The chip formation stage is the cutting phase. From the view point of the energy required to remove material, cutting is the most efficient phase. Rubbing and plowing are inefficient, since the energy is wasted in deformation and friction with negligible contribution to material removal.

Kim (2003) demonstrated the relationship between normal grinding force and material removal rate in rubbing, plowing, and cutting stage as shown in Figure 2.12. In the first two stages (rubbing and plowing), although there is a physical contact between the grinding wheel and work piece as previously shown in Figure 2.11, the material removal rate does not happen until the normal grinding force reaches a certain limit value called threshold grinding force where the cutting stage begins.

Furthermore, Chen and Rowe (1996) illustrated the relationships between the inputs and the outputs of grinding process as shown in Figure 2.13. The inputs of the grinding process include the grinding wheel characteristics, the shape of the dressing tool, dressing conditions, grinding conditions, and work piece characteristics, generating the topography of the grinding wheel, chip geometry, and finally single grain load. The single grain load influences the outputs of the grinding process as following; grinding forces, grinding power, grinding temperature, surface integrity, grinding vibration, surface roughness, wheel wear, and size error.
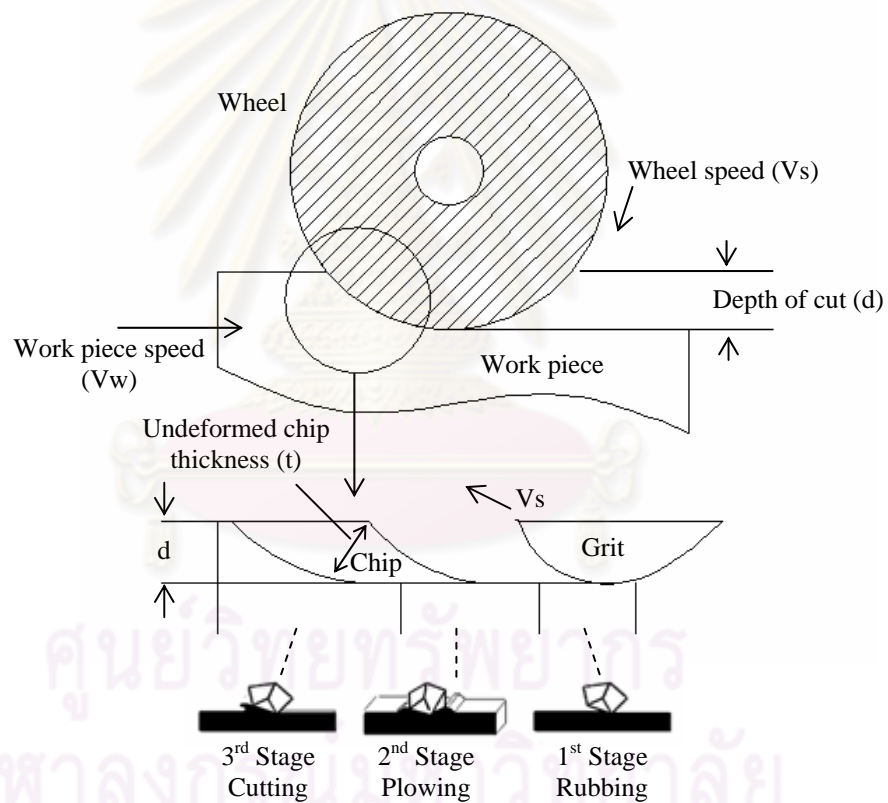
Figure 2.11   Three stages of chip formation for up grinding
              (Chen and Rowe, 1996; Atzeni and Iuliano, 2008)
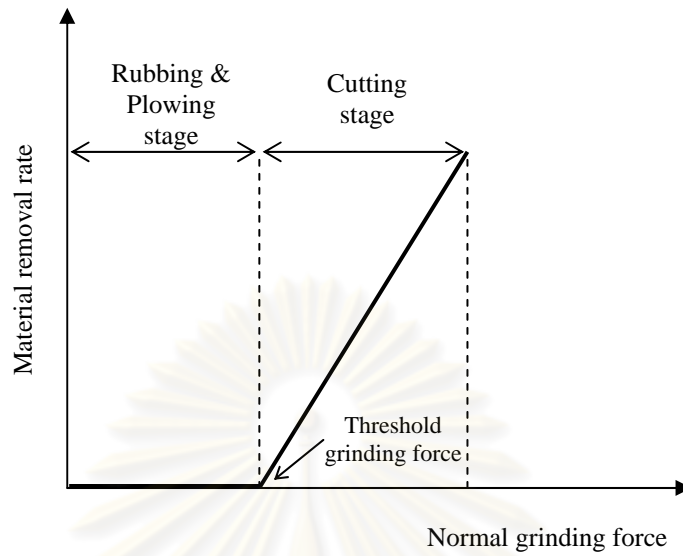
Figure 2.12   Relationship between grinding force and material removal rate (Kim, 2003)
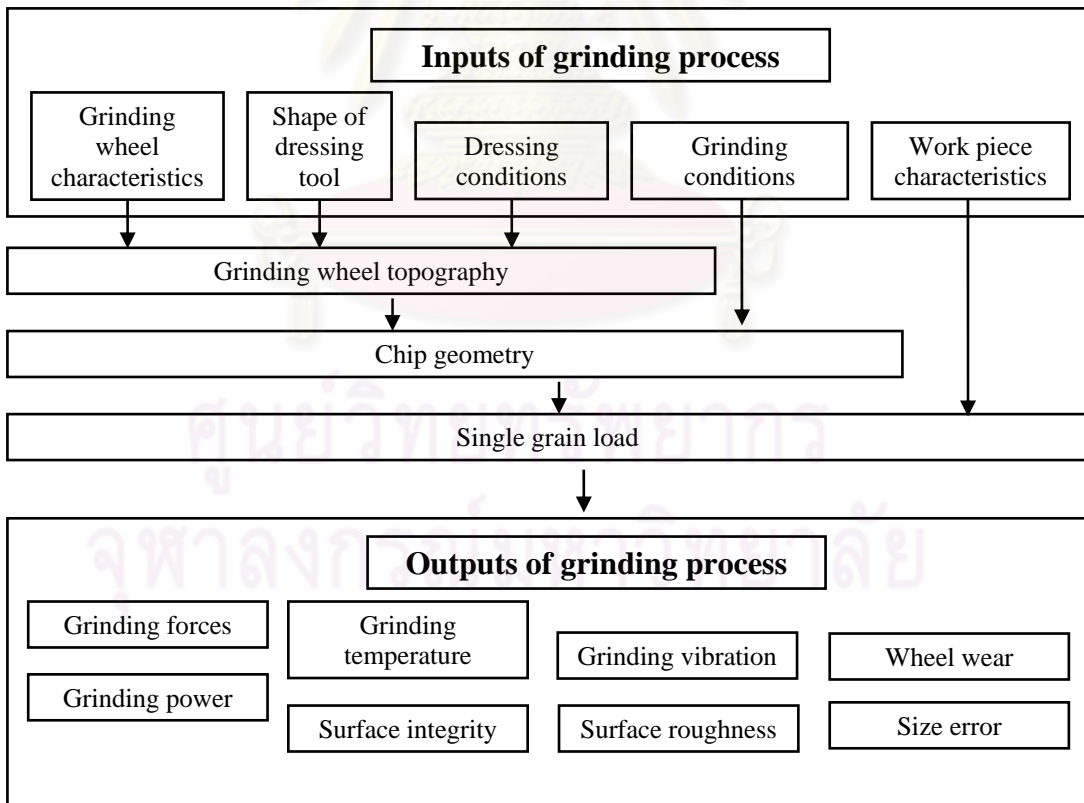
Figure 2.13   Process relationships in grinding process (Chen and Rowe, 1996)

In addition, the important parameters in the mechanics of grinding; the cutting points per unit area, the undeformed chip thickness, the average chip cross-sectional area, and grinding force per grit can be altogether related in the following equations (Malkin, 1989),

$$t \quad = \quad \left[\frac{4}{Cr} \left(\frac{V_w}{V_s} \right) \left(\frac{d}{D} \right)^{\frac{1}{2}} \right]^{\frac{1}{2}} \tag{2.7}$$

$$a_m \quad = \quad L^2 \left(\frac{V_w}{V_s} \right) \left(\frac{d}{D} \right)^{1/2} \tag{2.8}$$

$$L \quad = \quad \frac{2}{Crt} \tag{2.9}$$

Where

t	=	Undeformed chip thickness (m)
C	=	The number of abrasive grains per unit area ($1/m^2$)
r	=	The chip width to thickness ratio
V_w	=	Work piece speed (m/s)
V_s	=	Wheel speed (m/s)
d	=	Depth of cut (m)
D	=	Wheel diameter (m)
a_m	=	Average chip cross-sectional area (m^2)
L	=	The spacing between successive cutting points (m)

To determine grinding force per grit, Japanese Society for Precision Engineering (1987) expressed that the tangential (f_t) and the normal (f_n) forces can be as a power function of a_m :

$$Ft \quad = \quad k_t a_m{}^{x_t} \tag{2.10}$$

$$Fn \quad = \quad k_n a_m{}^{x_n} \tag{2.11}$$

Where

k_t =   Tangential force per unit cross-sectional area (N/m^2)

k_n =   Normal force per unit cross-sectional area (N/m^2)

x_t =   The power number of cross-sectional area (a_m) for tangential force (Ft)

x_n =   The power number of cross-sectional area (a_m) for normal force (Fn)

x_t and x_n depend on the work material and the cutting conditions. The normal force per grit f_n is related to f_t by a constant ratio λ :

$$f_t \quad = \quad \lambda f_n \tag{2.12}$$

Chen *et al.* (2009) used the ratio of normal force to tangential force to describe the machining ability of grinding alumina and found that material removal rate lowered with increasing grinding force ratio. Also, Zhang *et al.* (2008) applied the grinding force ratio in monitoring grinding burn on the surface of a high temperature alloy and illustrated that burns occurred when the grinding force ratio was increased.

In general, grinding processes can be considered as a series of localized small-scale indentation events, and the indentation fracture-mechanics relationships can be used to account for the mechanism of material removal in ceramic grinding (Malkin and Ritter, 1989). Evant and Marshall (1981) distinguished grinding process into two classes: brittle fracture and ductile mode regime by approximating the critical indenting load of crack initiation as Equation 2.13.

$$P^* \approx 2 \times 10^5 \frac{K_c^{\,4}}{H^3} \tag{2.13}$$

Where

P^* = Critical indentation load (N)

K_c = Fracture toughness (MPa m$^{1/2}$)

H = Hardness (N/m^2)

However, some researchers presented two modes in terms of coarse and fine grinding. Shaw (1996) classified the grinding process into two categories, namely, form and finish grinding (FFG) and stock removal grinding (SRG). The main objective in FFG was to obtain required form, finish, and accuracy while the primary objective in SRG was to obtain high removal rate. In FFG, fine grain size (< 140 µm) abrasives such as alumina and silicon carbide in a vitrified bonded grinding wheel are generally used. In SRG, coarse grain size (351 – 715 µm) abrasives such as alumina and alumina – zirconia were used in a resin bonded grinding wheel.

2.2.3 Effects of Grinding Conditions on Grinding Forces and Specific Energy Consumption

This section described the effects of grinding conditions such as wheel speed, work piece speed, and depth of cut on grinding forces and specific grinding energy investigated by many researchers in the field of ceramic grinding.

One of the most important parameters is grinding force playing a significant role in process monitoring. The two components including tangential force and normal force were prevalently presented in most previous research. Malkin and Kannappan (1972) described the effects of grain size and operating parameters on the mechanics of grinding. Liu *et al*. (2001) investigated the relationships between normal grinding force and grinding variables namely table speed, depth of cut, and removal rate and found that grinding force was increased by increasing the three variables.

Kalpakjian and Schmid (2001) stated that in the grinding process if cutting force on the grain was proportional to the cross sectional area of the undeformed chip

thickness, the grain force (tangential force on the wheel) was also proportional to process variables as follows:

$$Grain\ force\ \alpha \left(\frac{V_w}{V_s}\sqrt{\frac{d}{D}} \right)(Strength\ of\ Material) \qquad (2.14)$$

From Equation 2.14, it was obvious that grinding force was affected by wheel speed (V_s), work piece speed (V_w), depth of cut (d), wheel diameter (D), and strength of material. This equation has been proved in much research. For example, the investigation of the machining behavior of green gelcast ceramics in the work of Kamboj *et al.* (2003) indicated that the increase in tangential and normal force in surface grinding were much more rapid for higher depth of cut and for binder-containing samples that have high vicker hardness number implying high strength of the material. The results from Huang *et al.* (2003) for surface grinding of silicon nitride (Si_3N_4) were graphically illustrated in Figure 2.14 and 2.15 and showed that normal forces (Fn) decreased as wheel speed (V_s) increased, well agreed with the relationship in Equation 2.14.

In addition to wheel speed effect, work piece speed markedly influenced on normal forces. Figure 2.16 and 2.17 illustrated that in surface grinding of silicon carbide and 12 mol% cerium oxide (CeO_2) stabilized tetragonal zirconia polycrystal (12Ce-TZPs) having different grain sizes, when increasing work piece speed and depth of cut, normal forces dramatically increased (Liu *et al.*, 2001).

According to the vertical grinding on silicon nitride (Si_3N_4) and glass investigated by Shen *et al.* (2002), tangential force was affected by the two important factors; pressure and rotational wheel speed. The tangential forces increased with grinding pressure increased at a constant rotational wheel speed of 1,000 rpm for various abrasive grit sizes of diamond as shown in Figure 2.18 and inversely decreased with rotational wheel speed increased at a constant pressure of 3 Pa as shown in Figure 2.19.
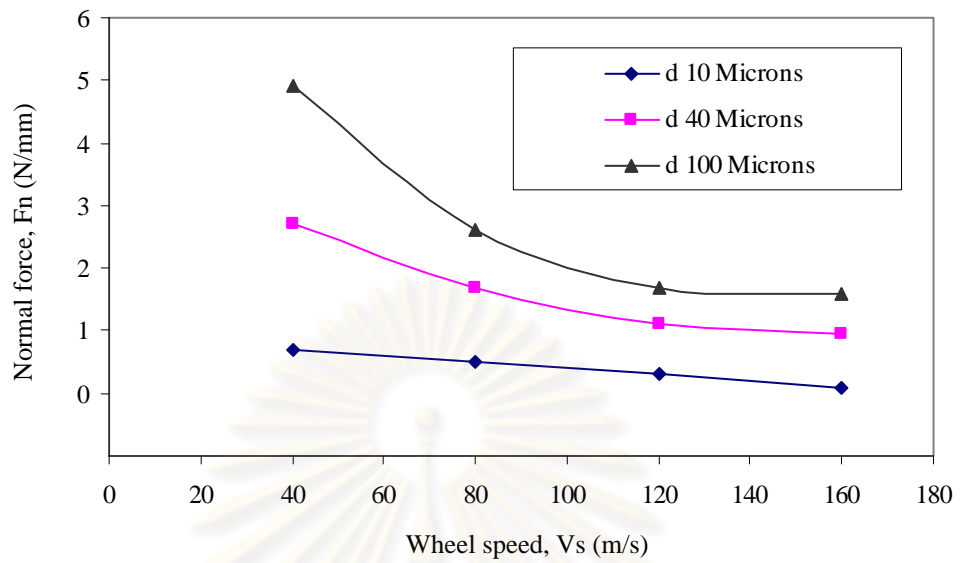
Figure 2.14   Normal force (Fn) versus wheel speed (Vs) for various depth
of cuts (d) at work piece speed (Vw) 500 mm/min (Huang *et al.*, 2001)
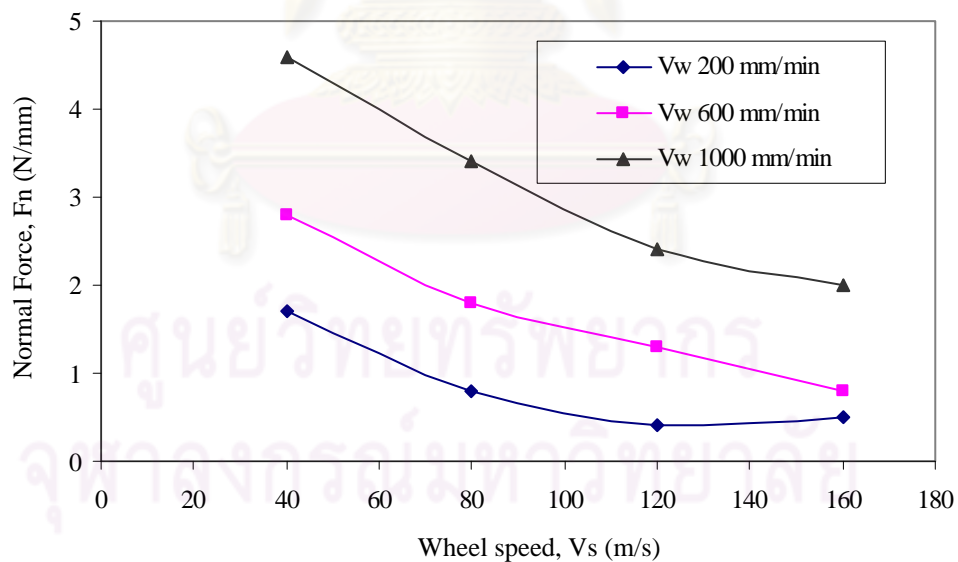
Figure 2.15   Normal force (Fn) versus wheel speed (Vs) for various work piece
speeds (Vw) at depth of cut (d) 40 μm (Huang *et al.*, 2001)
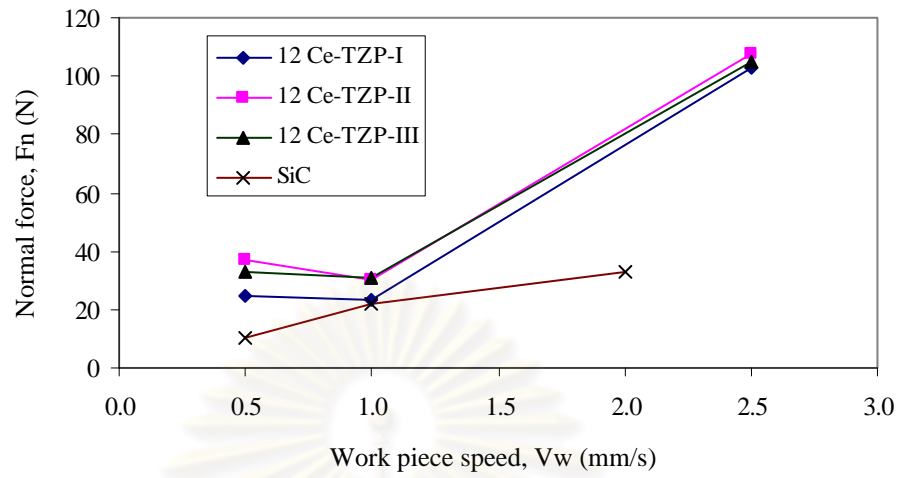
Figure 2.16   Effect of work piece speed (Vw) on normal force (Fn)
(Liu *et al*., 2001)
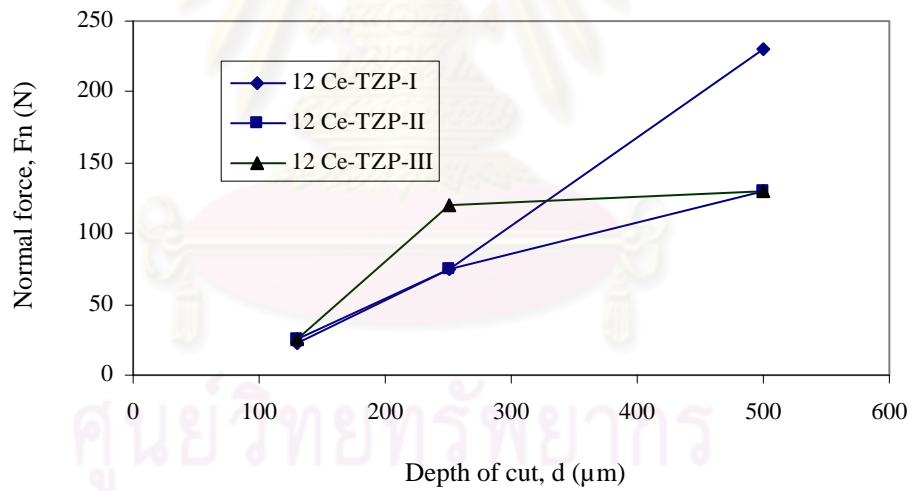
Figure 2.17   Effect of depth of cut (d) on normal force (Fn)
(Liu *et al*., 2001)
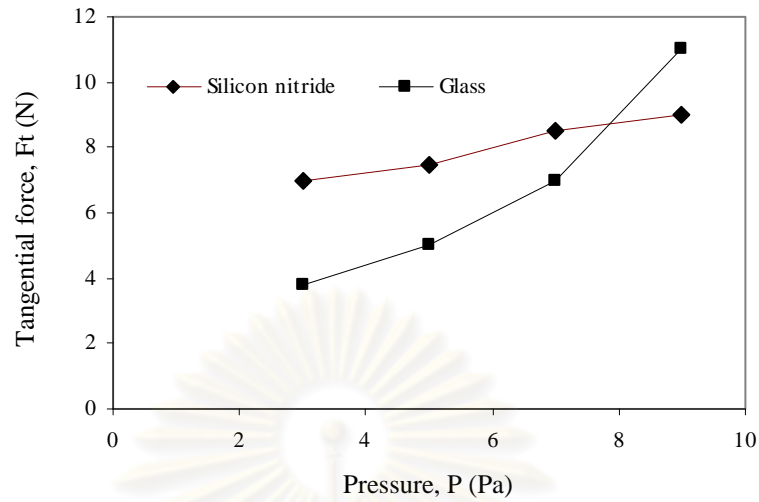
Figure 2.18   Tangential forces (Ft) versus pressures (P) at constant rotational wheel
speed of 1000 rpm for silicon nitride and glass with abrasive grit size
of 37 µm (Shen *et al.*, 2002)
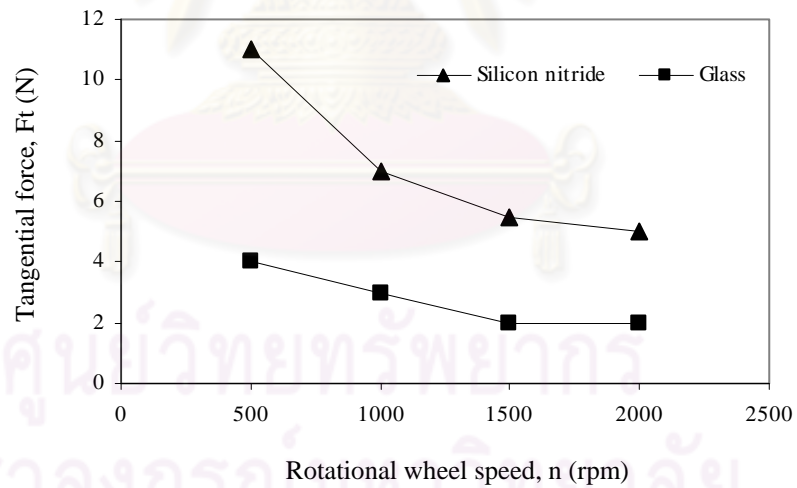
Figure 2.19   Tangential forces (Ft) versus rotational wheel speed (n) at constant
pressure of 3 Pa for silicon nitride and glass ground with abrasive grit
size of 37 µm (Shen *et al.*, 2002)

Besides the effects of grinding conditions on grinding forces, influences of wheel speed and depth of cut on specific grinding energy were also investigated. The specific grinding energy was defined as the ratio of the energy needed to remove an elementary volume of material (Barge *et al*., 2008). Figure 2.20 and 2.21 performed the relationship of specific energy and grain depth of cut (Yui and Lee, 1996) and rotational wheel speed (Shen *et al*., 2002). It can be seen that specific grinding energy decreased with high depth of cut and increased as rotational wheel speed increased corresponded to the work developed from Agarwal and Rao (2008) and Chen *et al*. (2009) for silicon nitride and alumina grinding.
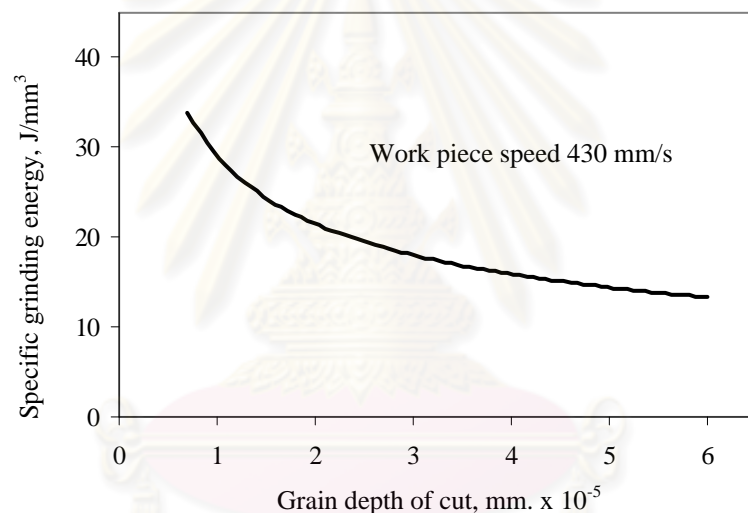
Figure 2.20   Relationship between specific grinding energy and grain depth of cut with work piece speed of 430 mm/s (Yui and Lee, 1996)
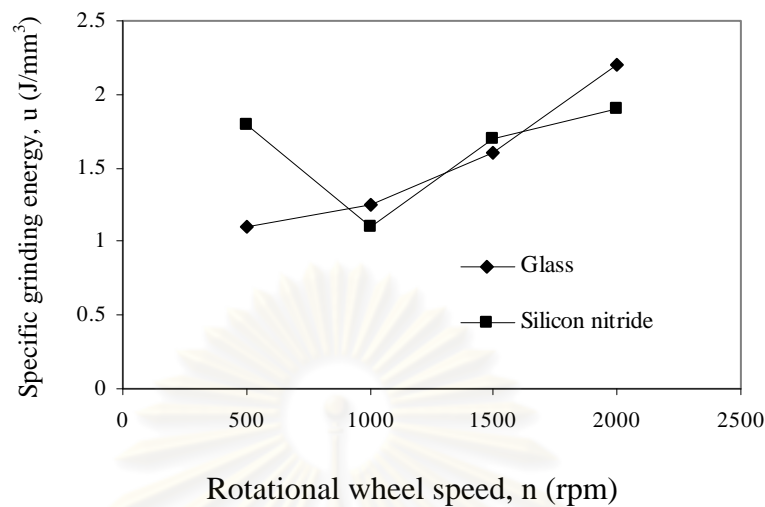
Figure 2.21   Relationship between specific grinding energy (u) and
                rotational wheel speed (n) for vertical grinding of silicon nitride
                and glass (Shen *et al*., 2002)

2.2.4   Effects of Grinding Conditions on Material Removal

In the abrasive process, material removal mechanism of the ground surface can be investigated via the two obvious equations namely Archard's wear equation and Preston's coefficient equation, which are prevalently used to explain the effect of parameters on the wear rate of material removed in particular grinding conditions.

Archard set his formula in 1957 based on the previous work of Holm made in 1946. The Archard's equation (Rodil, 2006) in Equation 2.15 is used for the analysis of wear when the deformation of the specimen is plastic. This equation gives a relation between the volume of wear, the normal load, the sliding speed, and the hardness of the material.

$$\frac{dV}{dt} = \frac{K \bullet Fn \bullet Vs}{Hv} \tag{2.15}$$

Where

$\dfrac{dV}{dt}$ = Material removal rate (m^3/s)

K = Friction coefficient

Fn = Normal force (N)

Vs = Sliding speed (m/s)

Hv = Vicker hardness of soft material (N/m^2)

According to K (friction coefficient), Archard said " K may be described as the coefficient of wear and in a series of experiments with the same combination of materials, changes in K denote changes in surface conditions". In general, to determine the K value, pin on disk experiment in Figure 2.22 is applied by pressing a stationary pin using a preload into the surface of a rotating disk. The preload is known, and the sliding distance can be determined from the rotational speed of the disk and time spent. The amount of wear on the pin is determined by change in mass (weight) and also volume of the pin and the constant K calculated (Thompson, 2006).
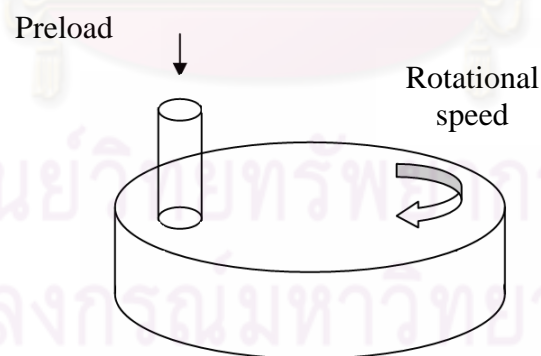
Figure 2.22   Pin on Disk configuration for measuring wear coefficient
(Thompson, J., 2006)

Apart from Archard's wear equation, Preston's coefficient equation is another important expression explaining material removal rate in abrasive process mainly dependent on parameters such as material properties, tool conditions and removal

mechanism. Li, *et al*., (2004) measured Preston coefficient of fine bronze tools for different process parameter combinations. Hwang, *et al*. (1999) mentioned that the Preston coefficient decreased exponentially as the grit depth of cut was reduced, which was often referred to as the "size effect". The Preston's coefficient is defined as Equation 2.16 (Preston, 1927).

$$\frac{dV}{dt} = Cp \bullet Vs \bullet Fn \qquad (2.16)$$

Where

$\frac{dV}{dt}$ = Material removal rate (m^3/s)

Cp = Preston coefficient (1/Pa)

Vs = Surface speed between the tool and work piece (m/s)

Fn = Normal grinding force (N)

For grinding, Preston coefficient (Cp) is more commonly expressed in terms of the specific grinding energy (u), which is defined as the energy consumed per unit volume of material removed and friction coefficient (K). The relation can be written in Equation 2.17.

$$Cp = \left(\frac{1}{u}\right) \bullet (K) \qquad (2.17)$$

Where

u = Specific grinding energy per unit volume of material removed (N.m/m^3) or (J/m^3) or (W.s/m^3)

K = Friction coefficient

Therefore, Equation 2.16 can be rewritten as Equation 2.18 (Tong *et al.*, 2006),

$$\frac{dV}{dt} = \left(\frac{1}{u}\right) \bullet \left(K \bullet F_n\right) \bullet V_s \qquad (2.18)$$

2.3 Machining of Porous Materials

An increase in the use of porous materials for restorative implants has been evidenced in the recent past. However, there was a little research dealing with machining porous materials. Despite the fact that the material possesses the capability to be manufactured economically to near net shape by pressing and sintering, a problem arises because machining processes has been still a basic requirement to ensure dimensional and geometrical accuracy (Chelule *et al.*, 2003). In machining porous materials, microstructure plays a significant role as stated by Rice and Speronello (1976) that the weaker materials would reduce the machining forces in proportion to its lower bulk strength and hardness resulting from higher porosity and grain size. On the other hand, as a result of fine grain size would experience greater machining forces proportional to its greater strength. Therefore, to machine higher strength materials, it is necessary to consume higher material removal force. The relation of porosity and strength of porous materials was depicted in Figure 2.23. It was a good agreement from much previous work that the strength of materials is strongly affected by porosity (Lee *et al.*, 2007). Pores can be occasionally defined as flaws or cracks that influence the fracture strength of the materials as demonstrated by Griffith (1920) in Equation 2.19.

$$\sigma_f \quad = \quad A\left(\frac{E\gamma}{C}\right)^{1/2} \tag{2.19}$$

Where

σ_f = Fracture stress

A = A constant that depends on the specimen and flaw geometries

E = Elastic modulus

γ = Fracture energy

C = Flaw size
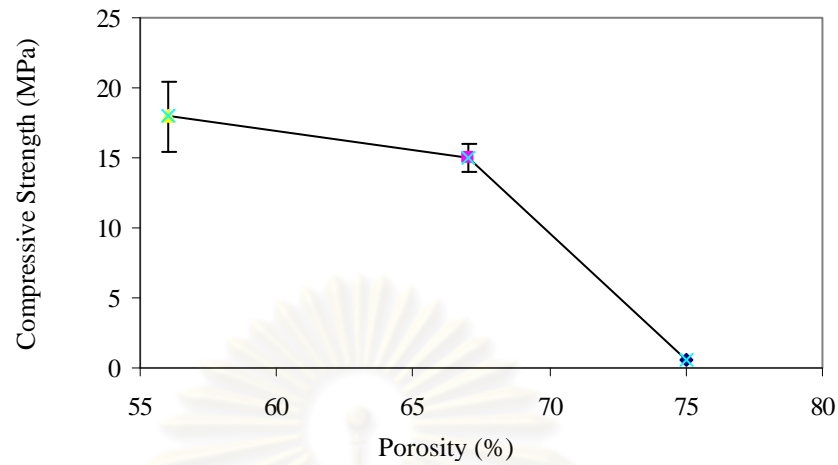
Figure 2.23   Compressive strengths of the porous HA bioceramics as a function of the porosity (Lee *et al.*, 2007)

As mentioned in the previous section, the specific energy consumed to remove material is the effect of grinding conditions on grinding parameters. For machining porous material, Malak and Anderson (2005) investigated the interrelation between specific cutting energy and depth of cut for orthogonal cutting of cellular polyurethane foams. From the experimental results in Figure 2.24, specific cutting energies decreased as the depth of cut was increased. In contrary, increasing the foam density increased the magnitude of specific cutting energy. The results from this study were agreed to that from the metal surface grinding experiment of Yui and Lee (1996). Another example of machining porous materials was an orthogonal bone cutting operation for orthopaedic surgery investigated by Plaskos *et al.* (2003). It was found that cutting forces also increased with a rise of depth of cut, and specific cutting energy was decreased as increasing depth of cut

In addition, Chelule *et al.* (2003) investigated the effects of machining variables on surface roughness of porous HA and found that feed rate, depth of cut, and cutting speed did not play a significant role in surface roughness of porous HA because its pore structures provided easy paths for crack propagation. These accelerated chip formation and generated surface falling above or below the depth of cut line as shown in Figure 2.25.
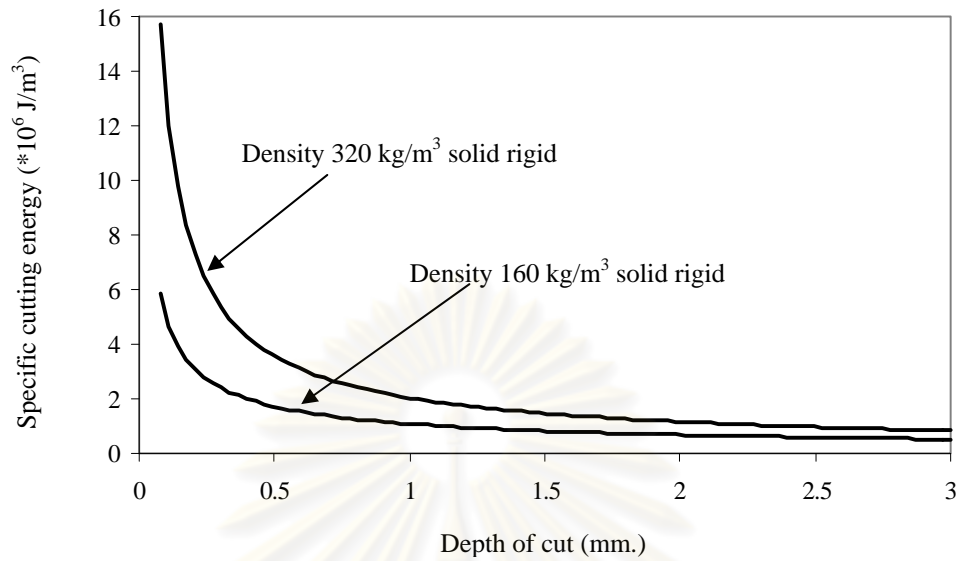
Figure 2.24 Specific cutting energy of polyurethane foam orthogonal cutting with various densities (Malak and Anderson, 2005)
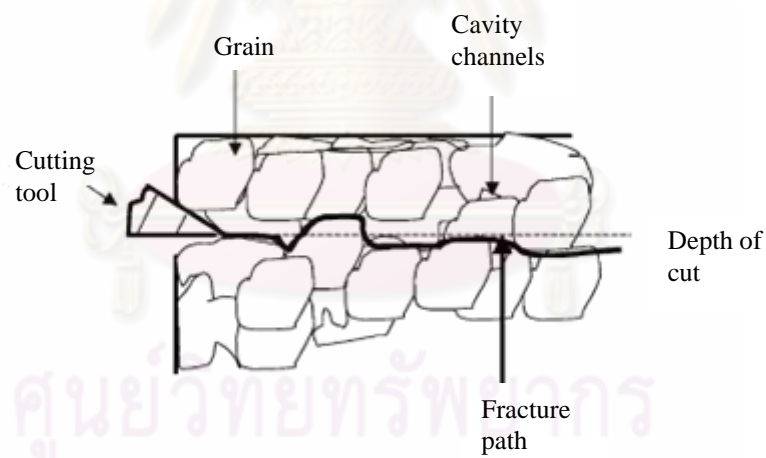
Figure 2.25 Fracture path following the inter-grain boundaries in a granular structure of porous hydroxyapatite (Chelule *et al*., 2003)

2.4   Spherical Surface Generation

In general, spherical surface generation has been applied for ball bearing manufacturing in precision applications. Nowadays, there have been a few techniques namely magnetic fluid grinding and lapping used for grinding ceramic balls such as silicon carbide (SiC), silicon nitride (Si_3N_4), and alumina (Al_2O_3) to meet specifications in terms of low sphericity error, low surface roughness, and minimal surface damages. Due to its brittleness and low toughness, difficulty in grinding leading to considerable manufacturing cost hinders their widespread applications (Kang and Hadfield, 2005). Cracks inevitably occur resulting from some loads applied to the work piece material that can decrease material performance in withstanding for applications.

2.4.1   Magnetic Fluid Grinding

Magnetic fluid grinding, originally developed in the end of 1980s in Japan by Umehara and Kato, in the UK by Childs, and in the US by Komanduri, was based on the magneto-hydrodynamic behavior of a magnetic fluid. The schematic of magnetic fluid grinding was shown in Figure 2.26. Material removal process occurred when the driving shaft rotated and drove the balls around the guide ring. A magnetic field in the fluid levitated non-magnetic materials (the balls and abrasives) to float and contacted the shaft (Childs *et al*., 1995). Meanwhile, the float placed beneath the balls was buoyant and intensified the load between a ball and the shaft. The magnetic fluid grinding has been the most "gentle" technique with high speeds ranging from 1,000-10,000 rpm and low levels of controlled forces approximately 0.5-2 N per ball. Komanduri *et al*. (1999) proposed the advantages of this technique as follows,

- High accuracy finished surface can be obtained
- Very little or no surface damage resulting from low controlled force, high speed, fine abrasives, and flexible support
- Shorter processing time
- Small lot can be processed
- Fewer grinding steps are required
- Low capital and running cost
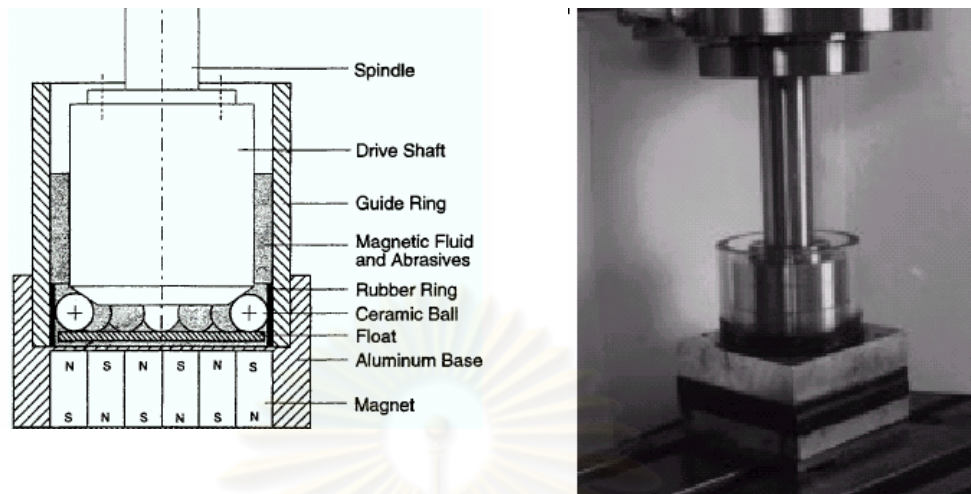
Figure 2.26   Schematic of magnetic fluid grinding (Raghunandan *et al*., 1997)

Figure 2.27 showed the relationship between the volumetric removal rate (V) and the product of the load (Ws) and skidding velocity (Vs) (Umehara and Kato, 1996). It was shown that the material removal rate was proportional to the skidding velocity and load applied between the ball and the driving shaft.
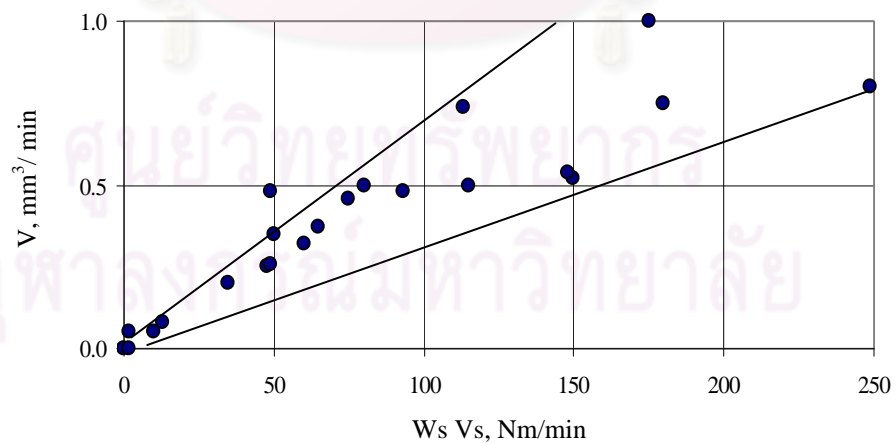
Figure 2.27   Removal rate (V) dependence on the product of load and skidding
velocity (WsVs) (Childs *et al*., 1994)

1) Magnetic Fluid Grinding Mechanics

Modeling mechanics of magnetic fluid grinding has been first developed by Child *et al.* (1994) to predict the onset of skidding motions. It considered the force and moment equilibrium of the balls acted on by the forces and moments at the balls' contacts with the driving shaft. From the theoretical analysis of kinematics of magnetic fluid grinding in Figure 2.28, Childs *et al.* (1995) defined a relationship among skidding velocity (Vs), ball circulation rate (Ωb), shaft angular speed (Ωs), float angular speed (Ωf), radius of the float (Rf), and radius of the shaft (Rs) in Equation 2.20. While, the relationships among radius of the float (Rf), radius of the container (Rc), radius of the ball (Rb), and radius of the shaft (Rs) were illustrated in Equation 2.21 and 2.22.
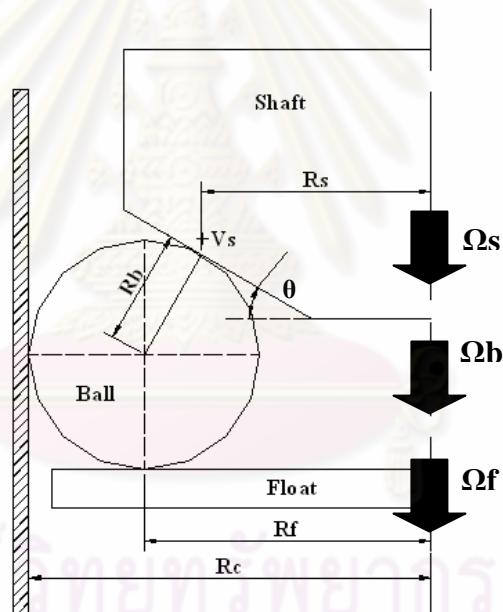
Figure 2.28   Detail of motions in magnetic fluid grinding
(Childs *et al.*, 1995)

$$(1+\cos\theta+\sin\theta)(\frac{\Omega b}{\Omega s}) \quad = \quad \frac{Rs}{Rf} - \frac{Vs}{Rf\Omega s} + \cos\theta(\frac{\Omega f}{\Omega s}) \qquad (2.20)$$

$$Rf \quad = \quad Rc - Rb \qquad\qquad\qquad\qquad\qquad (2.21)$$

$$Rs \quad = \quad Rf - Rb\sin\theta \qquad\qquad\qquad\qquad (2.22)$$

2) Float Stiffness

Hydrodynamic force (Buoyant force) of magnets can levitate non-magnetic objects: balls and float to be abraded with the abrasives at the contact between the driving shaft and the balls through magnetic fluid. Umehara and Kato (1996) indicated the effect of float stiffness on sphericity and material removal rate of Si_3N_4 balls and found that greater stiffness gave a higher removal rate and a quickly decreasing rate of sphericity error. On the other hand, lower float stiffness provided smaller sphericity error.

3) Fluids Used in Magnetic Fluid Grinding

Magnetic fluids used in the magnetic fluid grinding plays a major role in generating skidding velocities in which the material removal rate of the Si_3N_4 balls can be achieved. Childs *et al*. (1995) investigated the effect of type and viscosity of magnetic fluid associated with driving shaft speed (Ωs) on skidding velocity (Vs). It was found that high viscosity fluids could give higher skidding velocities when driving shaft speed was raised. From their experiment, the viscosity of magnetic fluids was an important variable causing in different skidding motions.

4) Abrasives

Many types and sizes of abrasive grits can be used in the magnetic fluid grinding to grind ceramic balls from the as received condition to meet its final dimension. They are generally added to magnetic fluids, working as loose abrasives and also fixed one. Abrasives used can affect surface roughness, surface damages in terms of cracks, and material removal rate. It is important to select the appropriate abrasive in different purposes. Jiang and Komanduri (1998) used a soft abrasive such as cerium oxide (CeO_2) in Chemo-mechanical polishing of Si_3N_4 balls that yielded an extremely smooth and damage-free surface with a surface finish Ra of 4 nm and Rt of 40 nm and a sphericity error of 0.15 - 0.25 μm.

Table 2.5 showed the abrasives used in magnetic fluid grinding proposed by several researchers. It can be seen that silicon carbide (SiC) with grit size of 38 μm provided a large material removal rate 12.4 μm/min. On the other hand, using smaller abrasive sizes of SiC 1.6 μm and Diamond (D) 20 - 40 μm could achieve small

sphericity error. While, chromium oxide (Cr_2O_3) abrasive was suitable for fine finishing.

In addition, Umehara and Kato (1996) indicated that the removal rate with free abrasive was smaller than with a fixed one because free abrasive possibly escaped from the contact surface between the balls and the driving shaft by the high centrifugal force of abrasives during finishing at high driving shaft speeds. However, using fixed abrasive could lead to damaged balls.

Table 2.5 Si_3N_4 ball properties achieved in magnetic fluid grinding for various

abrasive grits (Umehara and Kato, 1996)

Researchers	Abrasive type and size	Removal rate (μm/min)	Sphericity error (μm)	Surface roughness (μm)
Umehara and Kato (1988)	SiC, 38 μm	12.4	2	0.50 Rmax
Umehara and Kato (1990)	SiC, 1.6 μm	-	0.14	0.12 Rmax
Childs *et al* ., (1994)	D, 2-4 μm	7.5	0.7	0.05 Ra
Raghunandan *et al* ., (1996)	Cr_2O_3, 1-5 μm	0.13	-	<0.01 Ra

2.4.2 Lapping for Ceramic Balls

Lapping is one of the oldest manufacturing processes for high precision work of advanced ceramic ball bearings. Lapping process occurs by the sliding frictions between particles and a surface. The lap travels across a work surface against which particles of slurry are forced to the point of contact.

1) Aspect of Processes with Loose Abrasives

There are fixed and loose abrasives for lapping using abrasives. Processing with the loose abrasives includes buffing and abrasive shot machining in addition to lapping and polishing. Lapping and polishing are considered as two of the most outstanding processing methods because of their capability to secure high accuracy. The processing method is achieved by causing sliding frictional forces between the work surface and the tool. Slurry is constantly fed into the tool during this process.

Depended on the type of work piece materials, the choice of abrasives and tools is not severely fixed, and the finishing appearance of surface may be varied. As a matter of fact, the definition of lapping and polishing is not used with severe distinguish. The following are the characteristics of lapping and polishing techniques (Marinescu *et al.*, 2000):

1. Processing is easily performed, through the relative motions of the sliding work piece against the tool, using slurries.

2. Almost all solid materials, such as metal and non-metal materials, can be processed.

3. Operating with micro-actions of abrasives, processing efficiency is generally low.

4. Since the processing efficiency is so low, it is possible to approximate the desired level of precision; this is a great advantage for high precision processing.

5. A very sophisticated processing machine is not required.

6. Control of slurries is complicated due to some problems such as slurry splashing and accumulation of chips in slurries.

Figure 2.29 presented various types of V-groove lapping for ceramic balls. Upper lapping plate is usually rotated, but in some applications lower lapping plate can be either rotated or fixed. Lapping can be considered as a three-body wear, with abrasive particles acting like indenters sliding and rolling between the lapping plate and the work piece (Kang and Hadfield, 2005).
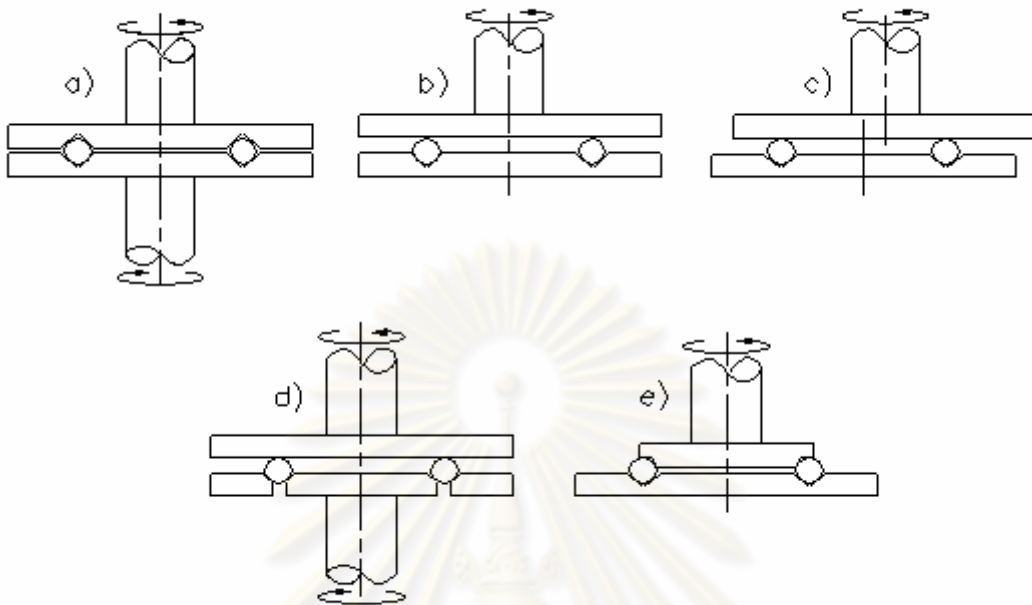
Figure 2.29   Various types of V-Groove lapping

2) Parameters in Lapping Process for Advanced Ceramic Balls

Over the past decade, there has been much research dealing with improvement of surface integrity and material removal rate in lapping process for ceramic ball bearings particularly Si_3N_4. Due to having high hardness and brittleness, ceramic balls should be carefully processed. Therefore, it is necessary to understand process parameters such as lapping speed, lapping load, as well as slurry containing lapping fluid and abrasive particles affecting surface quality, geometry, and material removal.

a) Lapping Speed

Kang and Hadfield (2005) presented the relationship between material removal rate in terms of ball diameter reduced per hour and different lapping speed with fixed diamond abrasive size of 45 μm in water-based lubricant at a ratio 1g : 60ml and average lapping load of 12.75 N/ball. The small-scale eccentric lapping machine was used in this investigation. The upper plate was stationary and had a flat lapping surface, and the lower plate which had a circular V-groove on it was driven by a micro-inverter controlled AC motor through a belt and pulley system. The

experimental results in Figure 2.30 showed that material removal rates in terms of ball diameter reduced of Si_3N_4 from two manufacturers were strongly dependent on lapping speed. However, for high speed lapping, cracks were found on the lapped balls.
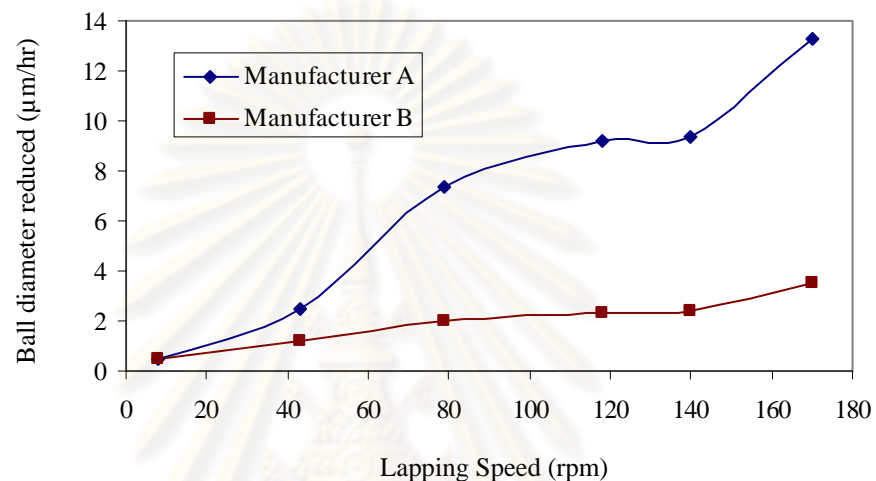
Figure 2.30   Relationship between ball diameter reduced and lapping speed (Kang and Hadfield, 2005)

In the experimental schematic investigated by Stolarski (1999) in Figure 2.31, cone and cup made of stainless steel grade 304 working as upper and lower lapping plate were demonstrated to study the effect of cone and cup rotational speed on material removal rate. The results in Figure 2.32 indicated that the cup rotation speed of 40 rpm with different applied loads with 15 μm oil-based slurry at 3000 rpm cone speed for test duration of 1 hour resulted in a measurable increase in the material removal rate when compared with stationary cup.
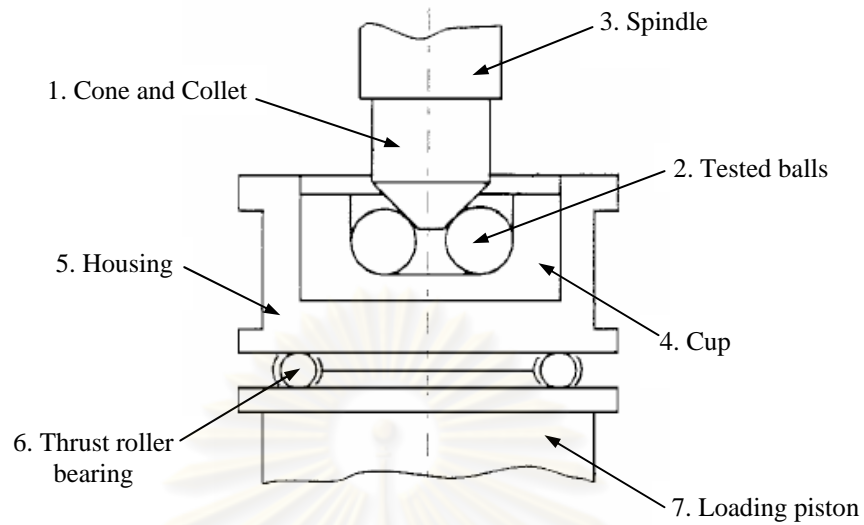
Figure 2.31   Schematic of contact configuration with additional cup rotation
                (Stolarski, 1999)
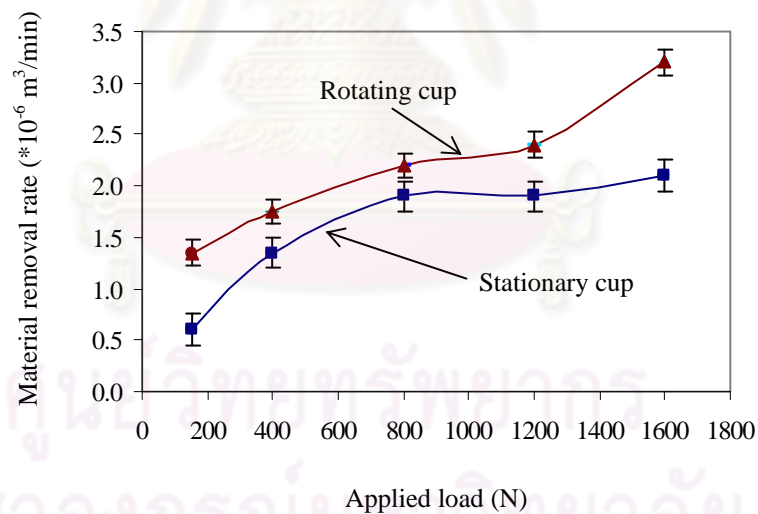
Figure 2.32   Effect of cup rotation on the material removal rate
                (Stolarski, 1999)

b) Lapping Load

Kang and Hadfield (2001) used Taguchi methods to optimize the lapping parameter and found that lapping load was the most influential factor on material removal rate. Also, the investigation of lapping load for Si_3N_4 ball bearing was further

studied by Kang and Hadfield (2005). It was revealed in Figure 2.33 that the maximum removal rate in terms of ball diameter reduced was achieved at the lapping load of 43 N/ball. While, at high lapping loads of 78 and 107 N/ball, the material removal rate slightly decreased. Furthermore, high roundness error and surface damages were found on the lapped balls. In contrary, material removal rate in terms of ball diameter reduced for cup and cone lapping in Figure 2.34 developed by Stolarski and Tobe (1997) slightly increased as increasing lapping loads as presented in Figure 2.35. Abrasive particle of 15 μm with 3 ml oil-based diamond slurry and cone speed of 3,000 rpm was applied in this experiment for test duration of 1 hour.
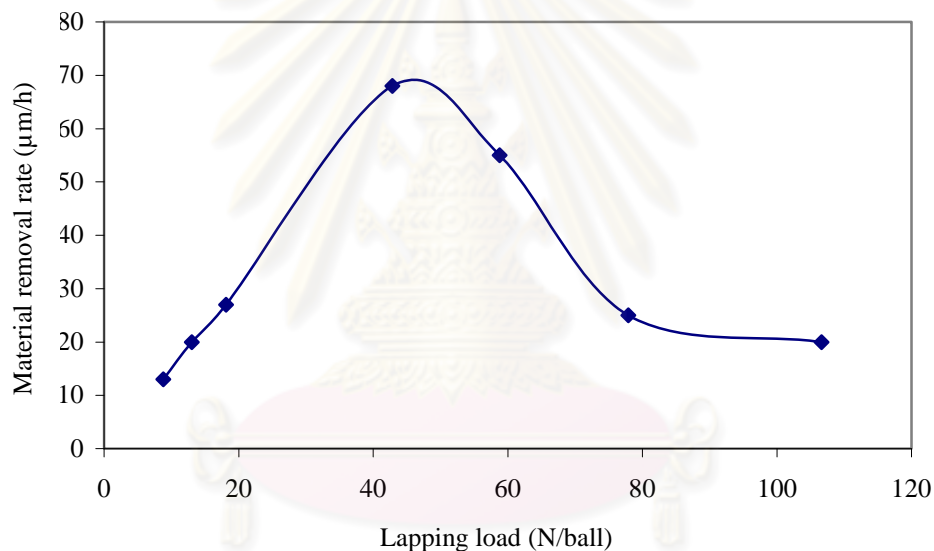
Figure 2.33   Effect of lapping load on material removal rate for Si_3N_4 ball
(Kang and Hadfield, 2001)
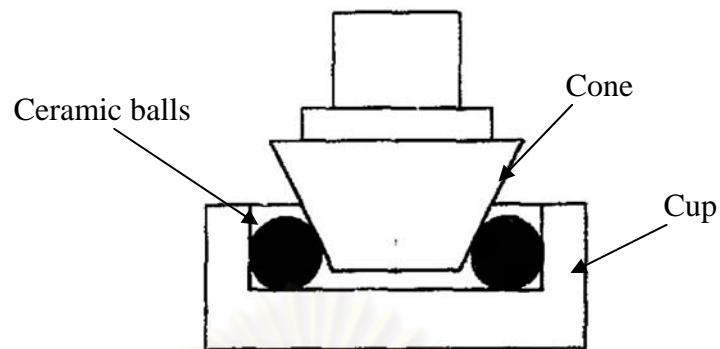
Figure 2.34   Schematic representation of the contact configuration
              for grinding experiment (Stolarski and Tobe, 1997)
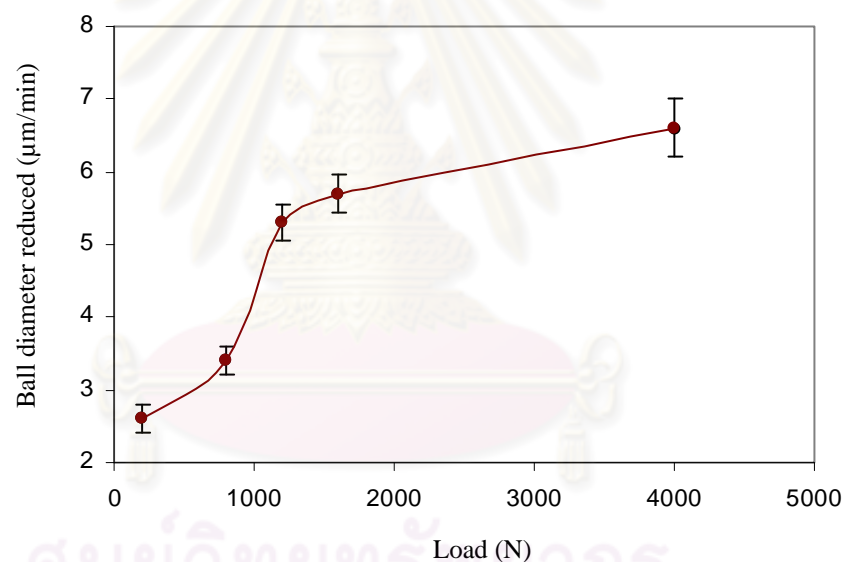
Figure 2.35   Ball diameter reduced as a function of load
              (Stolarski and Tobe, 1997)

Beside material removal rate, roundness of ceramic balls can be affected by load applied as well. Stolarski and Tobe (1997) indicated in Figure 2.36 that higher loads resulting in high material removal rates caused large roundness errors. On the other hand, the minimum roundness error could be obtained for the light load.
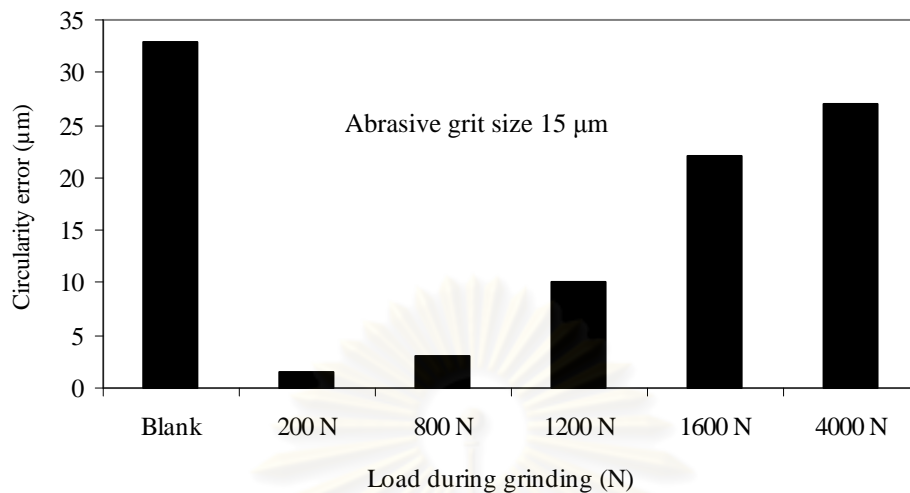
Figure 2.36   Change in roundness errors under controlled loads for abrasive grit
size of 15 μm (Stolarski and Tobe, 1997)

c) Lapping Fluids and Abrasives

Slurries used in lapping process play an important role in generating material removal process and are lubricants of the contact between ceramic balls and lapping plates to reduce friction causing surface damages. In general, slurry mixtures contain abrasive particles and lapping fluid made from oil or water-based liquid. In the work of Kang and Hadfield (2005), different lapping fluids affected the material removal rate of Si_3N_4 balls.

However, lapping fluids are usually filled with some chemicals, organic and inorganic additives to improve material removal rate by means of chemical effects accompanied with mechanical action. Stolarski (1999) stated that phosphoric acid and potassium hydroxide used as inorganic additives mixed in oil-water based fluid were identified as very effective abrasives. Moreover, abrasive particle size markedly influenced on roundness of Si_3N_4 ceramic balls as shown in Figure 2.37 (Stolarski and Tobe, 1997). The best result was obtained for small sizes of abrasive particle.
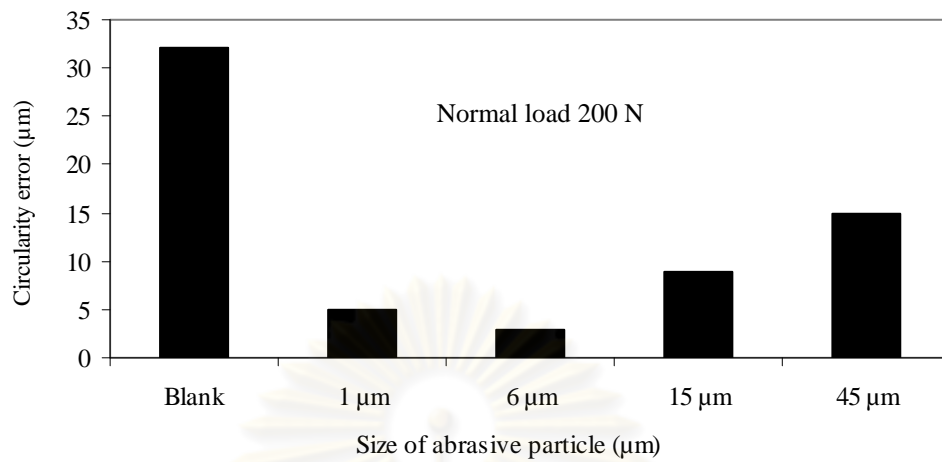
Figure 2.37   Changes in roundness errors under controlled abrasive particle sizes for constant load of 200 N (Stolarski and Tobe, 1997)

2.5 Spherical Measurement

2.5.1 Circularity Error and Sphericity Error

The International Standard ISO 1101 for rolling bearings defined circularity error as the radial distance between two concentric circles separated by minimum possible distance and containing all the measurement points on the given profile as shown in Figure 2.38 a) (Samuael and Shunmugam, 2003). However, sphericity evaluation is to be done with reference to two concentric spheres containing all points of the data set and having the minimum separation, as shown in Figure 2.38 b). Once such assessment feature is established, the circularity or sphericity error is evaluated with reference to these assessment features as:

Circularity error / Sphericity error $\quad = \quad e_{max} - e_{min}$ (2.23)

Where, e_{max} and e_{min} are the maximum and minimum deviations of the data points from the assessment feature, respectively.

In evaluating the circularity error using coordinate data, the assessment circle is established with (x'_0, y'_0) as center and radius r_0 as shown in Figure 2.39 a). The normal deviation of a point (x_i, y_i) on the profile from the assessment circle is determined as given below:

$$e_i \quad = \quad [(x_i - x'_0)^2 + (y_i - y'_0)^2]^{1/2} - r_0$$ (2.24)

Also, the normal deviation formula in Equation 2.25 of a point from the assessment sphere with center (x'_0, y'_0, z'_0) and radius r_0 as shown in Figure 2.39 b) is used to evaluate sphericity error.

$$e_i \quad = \quad [(x_i - x'_0)^2 + (y_i - y'_0)^2 + (z_i - z'_0)^2]^{1/2} - r_0$$ (2.25)
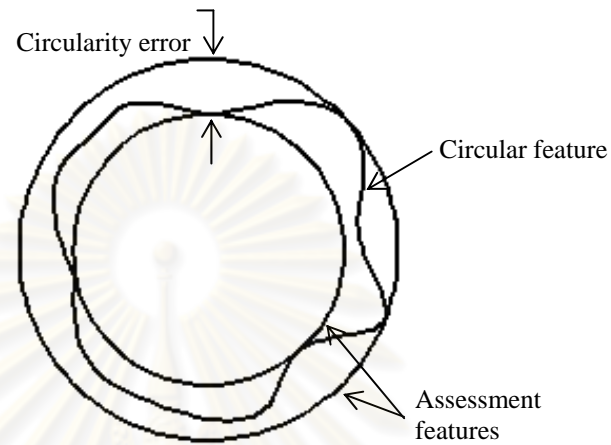
a) Circularity error
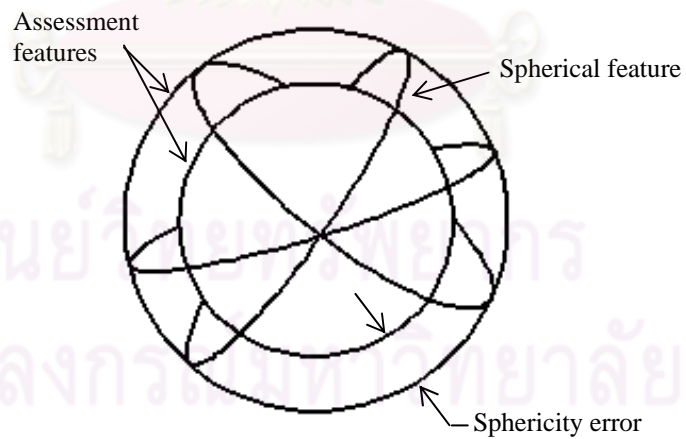
b) Sphericity error

Figure 2.38   Minimum zone evaluation for a) Circularity error and

b) Sphericity error (Samuael and Shunmugam, 2003)
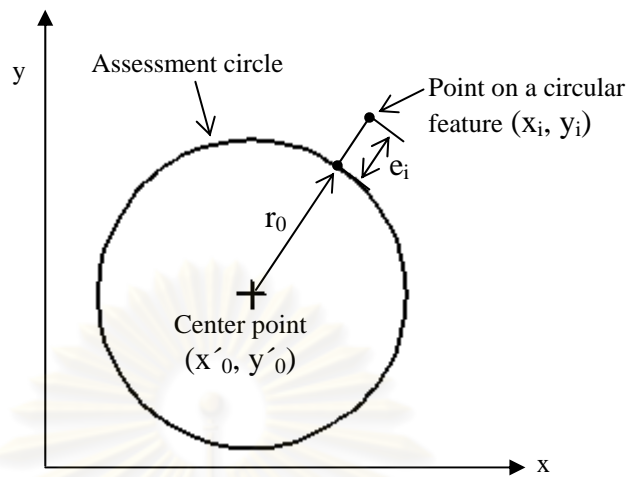
a) Circularity error
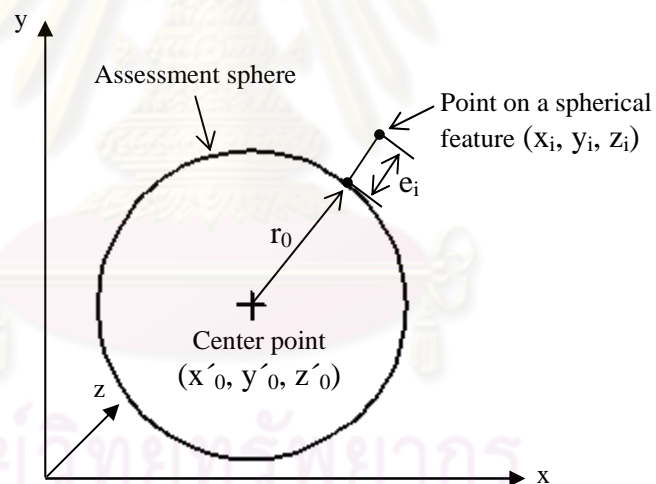
b) Sphericity error

Figure 2.39   Assessment circle and sphere using coordinate data: a) Circularity error
and b) Sphericity error (Samuael and Shunmugam, 2003)

2.5.2 Assessment Circles

Assessment circle and sphere have to be first determined for circularity error
and sphericity error calculation in the coordinate system. Dhanish and Mathew (2006)
concluded the four different criteria illustrated in Figure 2.40. The minimum zone

criterion has been adopted for definition of form error by most standards including the ISO. According to this criterion, two concentric circles enclose all the measured points, and the distance between the two circles is a minimum. This is equivalent to determining a circle called the minimum zone circle (MZC). However, determination of the MZC is not easy: therefore, the least squares criterion was generally used in stead, called the least squares circle (LSC). The sum of the squares of the distances of the individual points from this circle is minimized. Another assessment circle is the minimum circumscribed circle (MCC) having minimum radius such that all the points are included within the circle. While, the maximum inscribed circle (MIC) is the circle with maximum radius such that all the points are outside the circle.
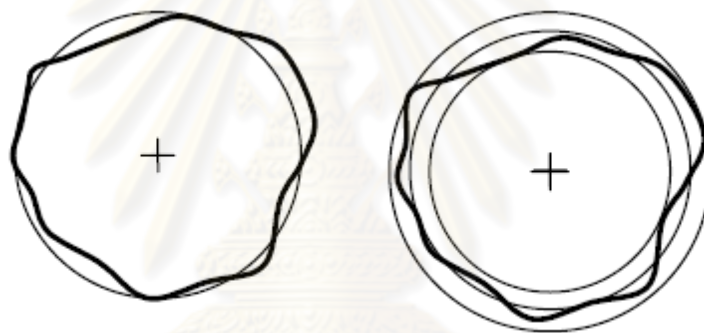
a) Least square circle   b) Minimum zone circle
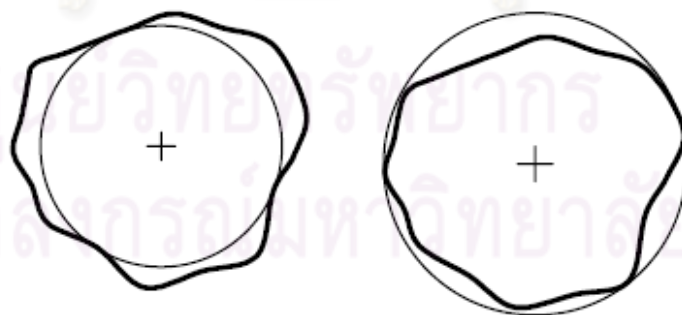
c) Maximum inscribed circle   d) Minimum circumscribing circle

Figure 2.40   Different criteria for circular substitute features: a) Least square circle,
b) Minimum zone circle, c) Maximum inscribed circle,
d) Minimum circumscribing circle (Dhanish and Mathew, 2006)

2.5.3 Spherical Measurement Techniques

There have been many techniques in measuring roundness, circularity error, and sphericity error of machined parts for 2D and 3D. For 2D measurement, radial method schematically shown in Figure 2.41 was introduced in the traditional manner as presented by Kanada (1997) for ball bearings. A cross-sectional profile on an equatorial plane, which is a plane with the maximum diameter, is measured using a roundness measuring system in which a radial method is used to measure a rotating specimen. The cross-sectional profile is determined using a stylus placed in contact with the specimen with a contact force of 70 mN. The stylus tip diameter is 1.6 mm. In the IS0 standard, the deviation from spherical form (sphericity) is measured in two or three equatorial planes at 90° to each other.
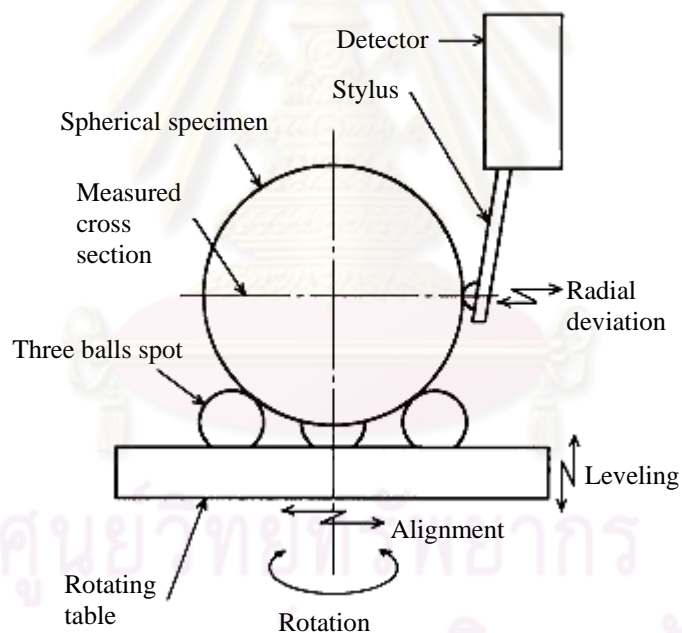
Figure 2.41   Specimen and measuring schematic of radial method (Kanada, 1997)

The above sphericity evaluation method is based on 2D measurement data, but sphericity evaluation based on 3D measurement, which is currently in great demand. Song and Wang (2007) presented the novel non-contact optical 3D measurement method - Shape From Shading (SFS). SFS is a visual inspection method dealing with the recovery of shape from a gradual variation of shading image formation. This

technique differs from other vision techniques because it can visualize the 3D-data of an object by measuring only one image. Figure 2.42 illustrated spherical featue captured by CCD camera. All the coordinate data can also be used to evaluate sphericity error via the common analysis of assessment sphere including least square sphere, minimum circumscribed sphere, maximum inscribed sphere, and minimum zone solution.
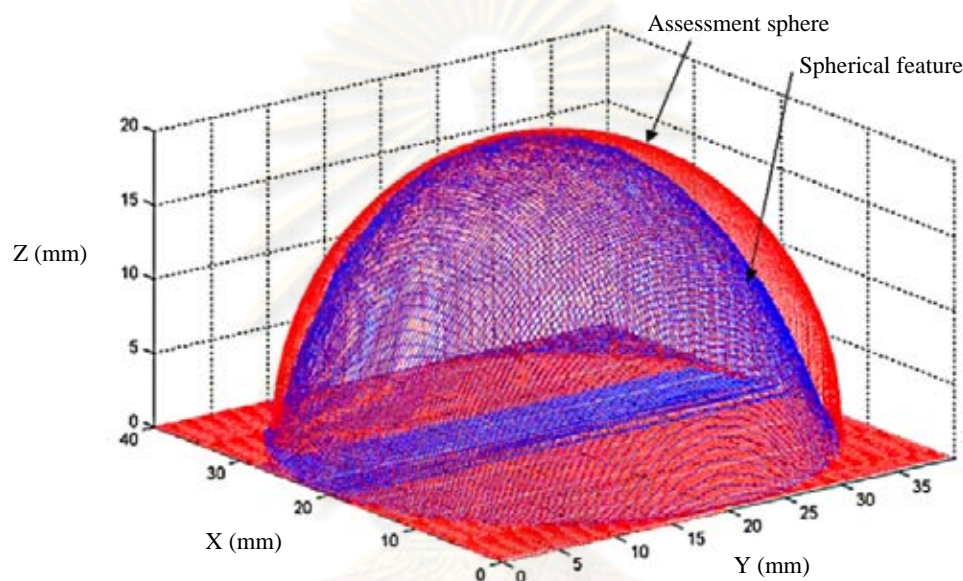
Figure 2.42   Spherical feature and assessment sphere characterized by Shape From Shading (SFS) (Song and Wang, 2007)

However, in the new technology development, coordinate measuring machine (CMM) has been recently used in automated inspection for both the on-line and off-line inspection of manufactured components. It can be used to measure roundness errors by collecting a large number of sampling points from the profile of the rounded parts for 2D and 3D (Gadelmawla, 2010). The CMM has been proven to be reliable and flexible. Laser scan, probe, and optical camera can be used to examine dimensional accuracy of the parts. Also, coordinate points and images of a specimen are captured and then analyzed by image processing tools. High precision parts such as ball bearings are widely measured for sphericity error via CMM as demonstrated by Samuael and Shunmugam (2003); Dhanish and Mathew (2006).

2.6 Machining Force Monitoring

The monitoring of machining tool conditions such as chatter, tool wear and fracture, and built up edge has been increasingly applied for a few decades. There has been a dramatic rise in demand for more sophisticated and precise parts resulting in a need for more intelligent machine tools. Therefore, monitoring the machining process is considered to be the most imperative (Cho *et al.*, 1999). Many indicators representing the machining states included cutting forces, torque, vibration, acoustic emission, temperature variation of the cutting tool, and power or current consumption of spindle (Sarhan *et al.*, 2001). Time and frequency domain was used to pinpoint the exact nature of changes on the signals due to alteration of the machining conditions.

For machining force monitoring, force signal data (F_1, F_2,...,F_N) in a time series recorded from various kinds of force sensors could be quantified in terms of Root Mean Square (RMS) as expressed in Equation 2.26 which was used in some research developed by Kwak and Song (2001); Sun *et al.* (2004); Salgado and Alonso (2006)

$$F_{RMS} \qquad = \qquad \sqrt{\frac{1}{N}\sum_{i=1}^{N}F_i^2} \qquad\qquad (2.26)$$

Where N is the number of sample

In frequency domain, to demonstrate an intensity of the machining force at a specified frequency, spectral density was carried out. Discrete Fourier Transform (DFT) algorithm generally used to transform time series data to frequency domain is primarily concerned with the identification of the different frequency components of a given signal (Hearn and Metcalfe, 1995). The coefficients (a_t and b_t) of least squares estimates expressed in Equation 2.27 and 2.28 were used in periodogram (I_t) estimation in Equation 2.29 at a fourier frequency (f_t) illustrated in Equation 2.30. The periodogram was smoothed and scaled by $1/(4\pi)$ to form the spectral density, and the specified frequency (f_z) in Hertz (Hz) was calculated from Equation 2.31 according to the sampling theorem early developed by Shannon (1949).

$$a_t \quad = \quad \frac{2}{N} \sum_{i=1}^{N} F_i \cos(f_t i) \tag{2.27}$$

$$b_t \quad = \quad \frac{2}{N} \sum_{i=1}^{N} F_i \sin(f_t i) \tag{2.28}$$

$$I_t \quad = \quad \left(a_t^2 + b_t^2\right) \tag{2.29}$$

$$f_t \quad = \quad \frac{2\pi t}{N} \tag{2.30}$$

$$f_z \quad = \quad f_t \times f_s \tag{2.31}$$

For $i = 1,2,...,N$, and $t = 1,2,\ldots,N/2$

Where i is the sample number in the time domain, N is the number of samples, and t is the number of cycles within the sequence of length N.

In the previous research, time domain analysis was also incorporated with the information from frequency domain revealing the characteristics of the machining process effectively. Choi *et al.* (2008) illustrated thrust force in drilling steel AISI1045 with a 10 mm diameter of high speed steel (HSS) tool in time domain and found that high thrust force dispersed from 1,200 up to 7,600 N came out in drill failure as shown Figure 2.43 a) remarkably different from that stable around 1,400 N in a normal tool stage as shown in Figure 2.43 b). Sarhan *et al.* (2001) studied the relationship between tool wear and cutting force variation in end milling process in frequency domain. It could be observed from spectral density that the cutting force (FRR) of about 250 N at the peak frequency (Freq.) of 46.875 Hz for the high flank wear width (VB) of 0.22 mm of defect tool in Figure 2.44 a) was higher than that of about 150 N for no flank wear width (VB) of 0.0 mm of normal tool in Figure 2.44 b). Correspondingly, Kalvoda and Hwang (2010) indicated that the higher amplitude of

the acceleration signal could result in high tool wear as demonstrated in their investigation of a cutter tool monitoring in turning.

However, the materials being cut could affect the signal patterns in frequency domain as well. Sze *et al.* (2006) indicated that distinctive patterns of frequency distribution were observed in power spectral density plots of the main cutting forces of polycrystalline aluminum, copper, and copper nickel with different textures in the single point diamond turning as shown in Figure 2.45, 2.46, and 2.47, respectively. For straight rolled textures, the peak frequency at 50 Hz was illustrated for turning aluminium and copper and was shifted to 25 Hz for turning copper nickel. For cross rolled texture, the peaks for turning aluminium, copper, and copper nickel were 200 Hz, 50 Hz, and 225 Hz, respectively. From their study, it could be concluded that different rolling textures for various materials resulted in a variation of signal patterns despite turning with the same depth of cut, cutting speed, feed rate, and tool rake angle.
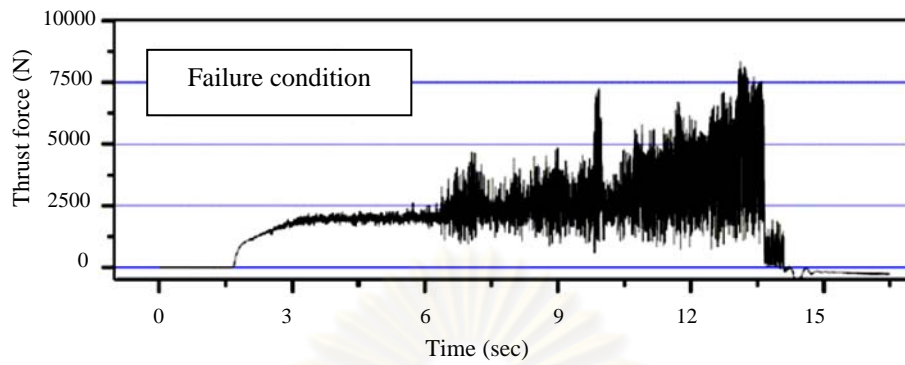
a) Defect drill
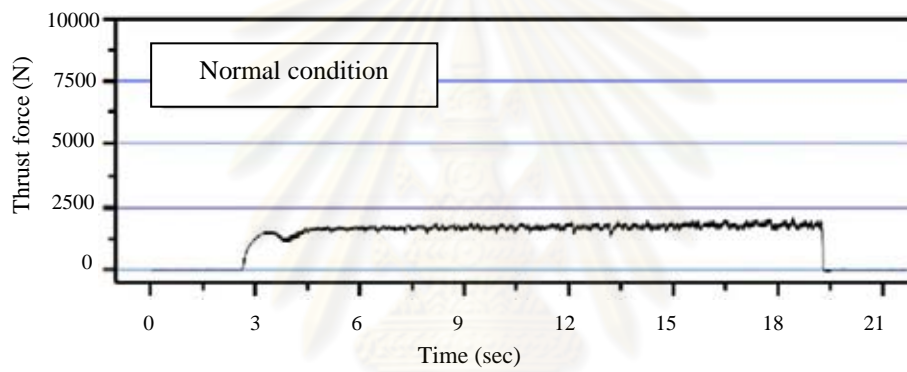
b) Normal drill

Figure 2.43   Thrust force comparison in drilling steel AISI1045 with rotational speed
of 800 rpm and feed rate of 144 mm/min between a) Defect drill and
b) Normal drill (Choi *et al.*, 2008)
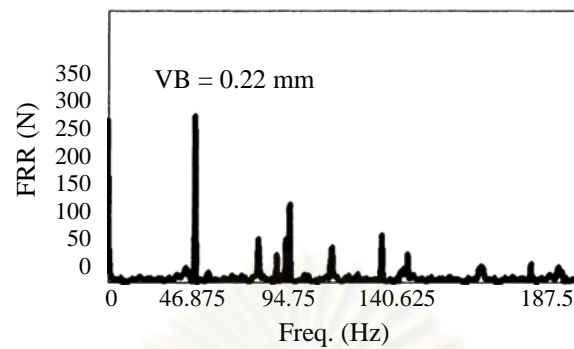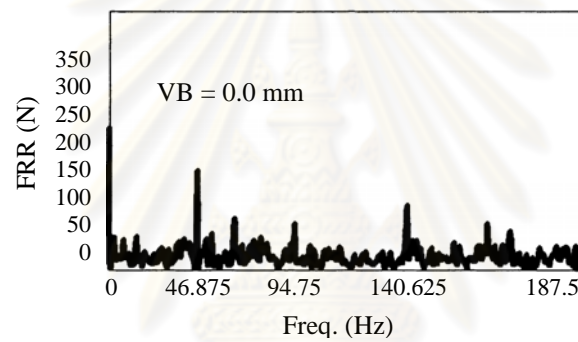
a) Defect tool

b) Normal tool

Figure 2.44   Spectral density of cutting force (FRR) for different flank wear width
            (VB) of a) Normal tool and b) Defect tool at cutting speed of 580 rpm,
            feed rate of 28 mm/min, and depth of cut of 1 mm (Sarhan *et al.,* 2001)
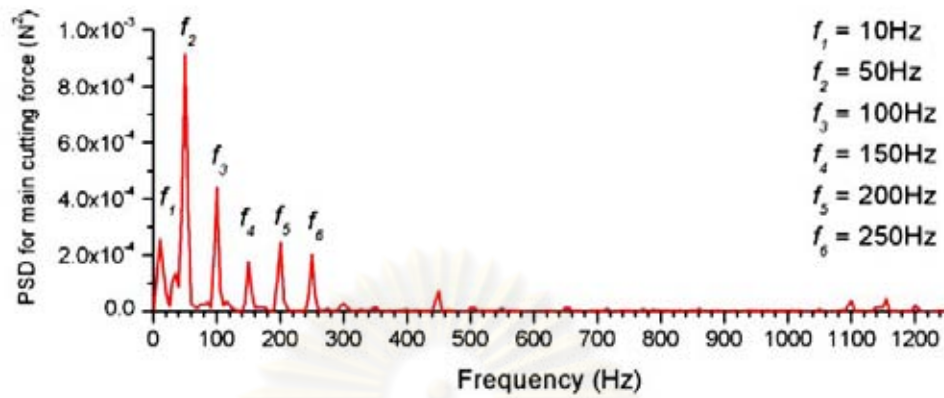
a) Straight rolled textures
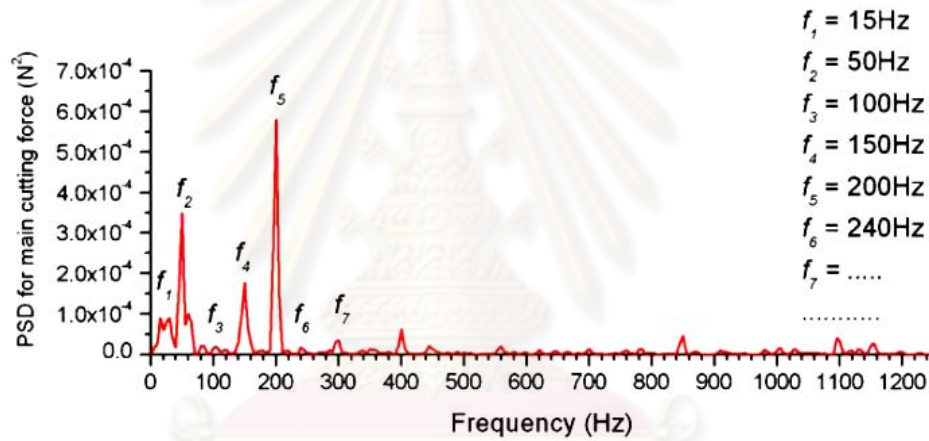
b) Cross rolled textures

Figure 2.45   Power spectral density (PSD) plots of main cutting force of Aluminum
for a) Straight rolled textures and b) Cross rolled textures
(Sze *et al.,* 2006)
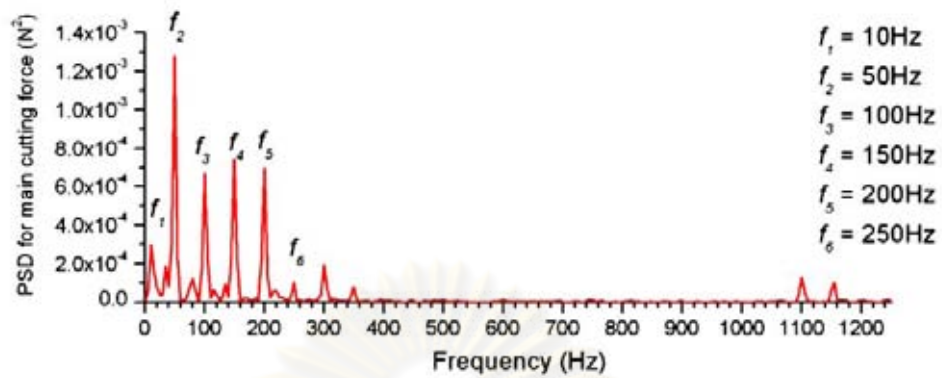
a) Straight rolled textures
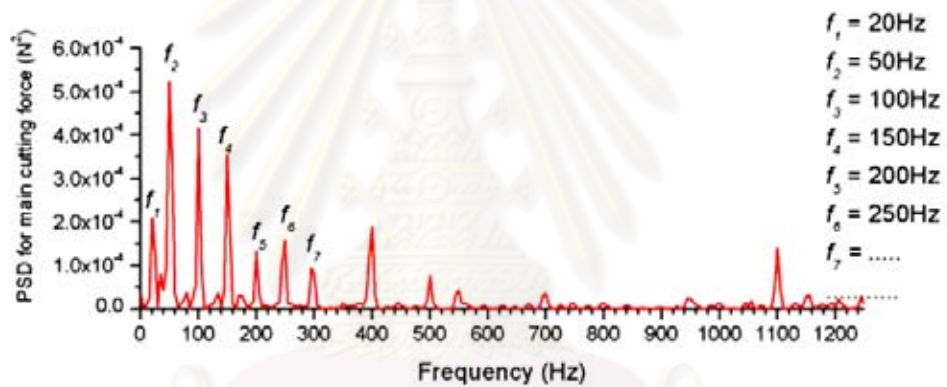
b) Cross rolled textures

Figure 2.46   Power spectral density (PSD) plots of main cutting force of Copper
for a) Straight rolled textures and b) Cross rolled textures
(Sze *et al.*, 2006)
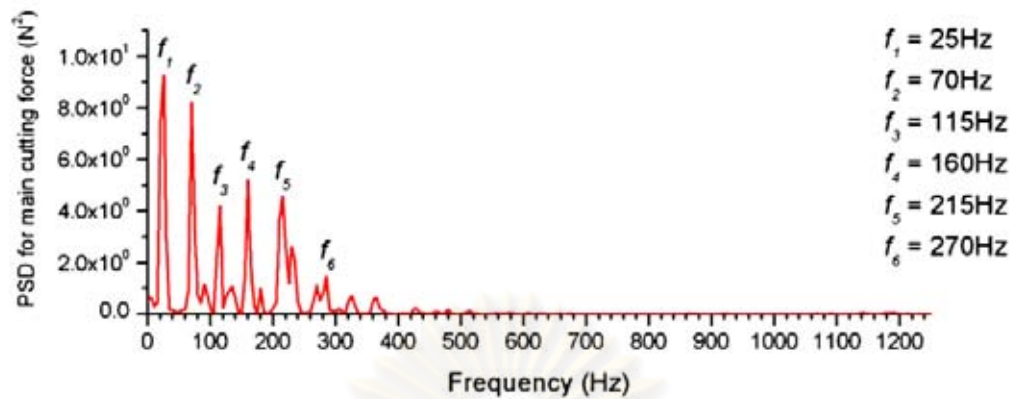
a) Straight rolled textures
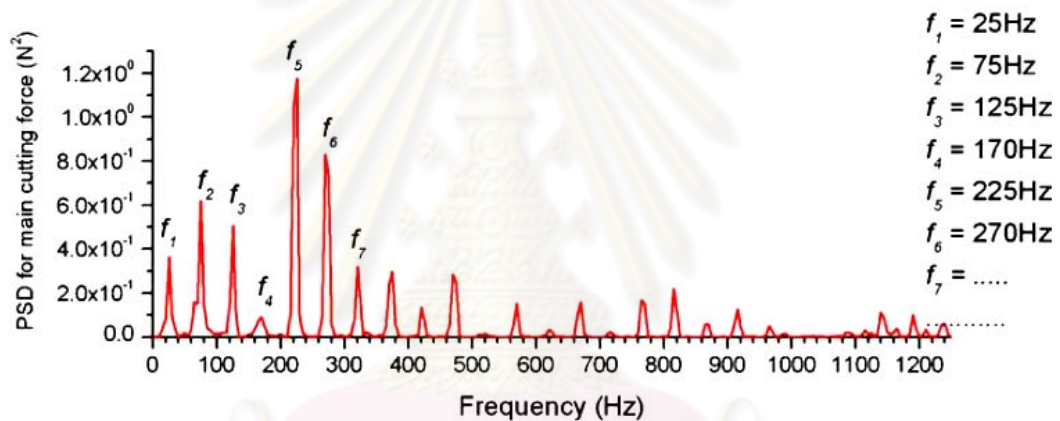
b) Cross rolled textures

Figure 2.47　Power spectral density (PSD) plots of main cutting force of Copper
Nickel for a) Straight rolled textures and b) Cross rolled textures
(Sze *et al.,* 2006)

2.7 Summary

The literature reviews in this chapter summarized the backgrounds of porous materials and the concepts and features of various machining processes including the conventional grinding process, machining porous materials, spherical grinding techniques along with the previous research studying the effects of various grinding or cutting parameters on cutting forces, material removal rate, specific grinding energy, surface roughness, and sphericity error. The techniques and methodologies in spherical measurement were also revealed, which was used for finished specimen inspection to examine dimensional accuracy. In addition, the research in the field of monitoring machining processes was reviewed to demonstrate in-process controlling for tool wear, breakages, and failures directly affecting the machined part quality through the vibration and cutting force signals.

The concepts of vertical spherical grinding technique with a grinding groove for dense materials namely lapping and magnetic fluid grinding were applied to integrate the spherical grinding system for porous polyurethane foam as developed in this research. The V-groove for a conventional lapping of steel and ceramic balls was redesigned to be a circular groove pad in order to increase the ground surface area to form a spherical specimen. Because of restricted grinding area in the V-groove, a specimen will not be promoted to change its own previous position to encounter the grinding wheel around it during grinding path. This may resulted in a cone finished shape after grinding. On the other hand, the circular groove pad used having larger grinding area as compared with the V-groove pad caused the specimen changes its previous orientation and hence spherical part formation.

However, proper grinding conditions such as grinding speed, cross head speed, and also abrasive grit size used in the spherical grinding porous polyurethane foam should be examined to form the spherical finished specimen with a minimal circularity error and required finished size diameter.

Chapter III

Materials and Methods

In this chapter, materials, equipment, and methods to be used in the spherical grinding experiment for porous polyurethane foam via circular groove pad were represented. Material characterizations in terms of physical and mechanical properties were illustrated. Besides, experimental equipment set up, experimental procedures, and experimental plan to form spherical shape were described.

3.1 Materials

3.1.1 Porous Polyurethane Foam

Porous polyurethane foam in Figure 3.1 was introduced as the material in the spherical grinding experiment. Its pore sizes were seemingly closed to those of about 200-700 µm (Jordan, 1999) used for commercial orbital implants although mechanical strengths were quite different. However, the price of porous polyurethane foam was reasonable for the first attempt in the spherical forming consuming several specimens for all grinding conditions in order to find influential grinding factors affecting grinding responses.
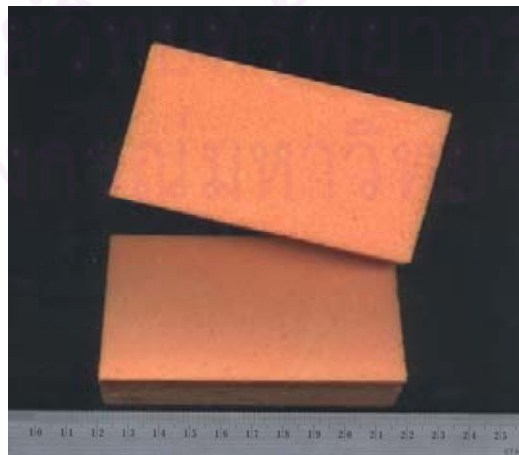
Figure 3.1   Porous polyurethane foam

3.1.2 Abrasive

Silicon carbide (SiC) sand paper in Figure 3.2 having diameter of 125 mm was the abrasive in the spherical grinding system. Two abrasive grit sizes of 20 and 53 µm were used to grind porous polyurethane foam from as received cube specimen to be spherical finish shape.

Figure 3.2   Silicon carbide sand paper

3.2 Material Characterizations

Porous polyurethane foam which was used as the material in this research was characterized in terms of physical and mechanical properties.

3.2.1 Pore Size

Pore size of porous polyurethane foam specimen was approximated by microstructure analysis via scanning electron microscopy (SEM) with magnification of 50 and 100.

3.2.2 Bulk Density and Porosity

Dimensional measurements for width, thickness, and length of as received specimens before grinding were performed by digital vernier caliper having accuracy of 0.01 mm. Volume of the specimen could be calculated from its dimensions, and mass was measured by digital balance with accuracy of 0.001 g. The volume and mass of the specimen were then used to calculate bulk density following ASTM D 1622-03 Standard Test Method for Apparent Density of Rigid Cellular Plastics in Equation 3.1. Additionally, porosity of porous polyurethane foam was determined from Equation 3.2. The theoretical density of polyurethane foam is 1.2 Mg/m^3 (Gibson and Ashby, 1988)

$$BD = \frac{M}{V} \qquad (3.1)$$

$$PO = [1 - \frac{BD}{D_T}] \times 100\% \qquad (3.2)$$

Where

BD = Bulk density (Mg/m^3)

PO = Porosity (%)

M = Mass (Mg)

V = Volume (m^3)

D_T = Theoretical density (Mg/m^3)

3.2.3 Mechanical Property Characterizations

According to mechanical properties of porous polyurethane foam, flexural and compressive strength were investigated. Three point bending was carried out to examine flexural strength following ASTM D 790-03 Standard Test Methods for Flexural Properties of Unreinforced and Reinforced Plastics and Electrical Insulating Materials. The specimen was prepared by saw blade cutting for various sizes having thickness from 4 to 8 mm, width from 8 to 13 mm, and length of about 55 mm. Each specimen was tested on multi-purposes testing machine, SHIMADZU SERVOPULSER, MODEL: SFL 50kN as shown in Figure 3.3. The radius of loading nose and supports were set to be 0.25 mm, and supporting span was 40 mm. Cross

head speed used in testing could be calculated by Equation 3.3. The three point bending schematic was shown in Figure 3.4. Maximum forces applied on the specimen and deflection data were collected for calculating flexural strength as expressed in Equation 3.4.

$$R \quad = \quad \frac{ZL^2}{6d} \qquad (3.3)$$

Where

R =   rate of crosshead motion, mm/min.

L =   supporting span, mm.

d =   thickness of specimen, mm.

Z =   rate of straining of the outer fiber, mm/mm/min. (Z shall be equal to 0.01)

$$\sigma_{fM} \quad = \quad \frac{3PL}{2bd^2} \qquad (3.4)$$

Where

σ_{fM} =   Flexural strength, MPa

P =   Maximum load at the mid span, N

L =   Supporting span, mm.

b =   Width of specimen, mm.

d =   Thickness of specimen, mm.

Figure 3.3   Testing machine

R2.5 (3)

40 mm
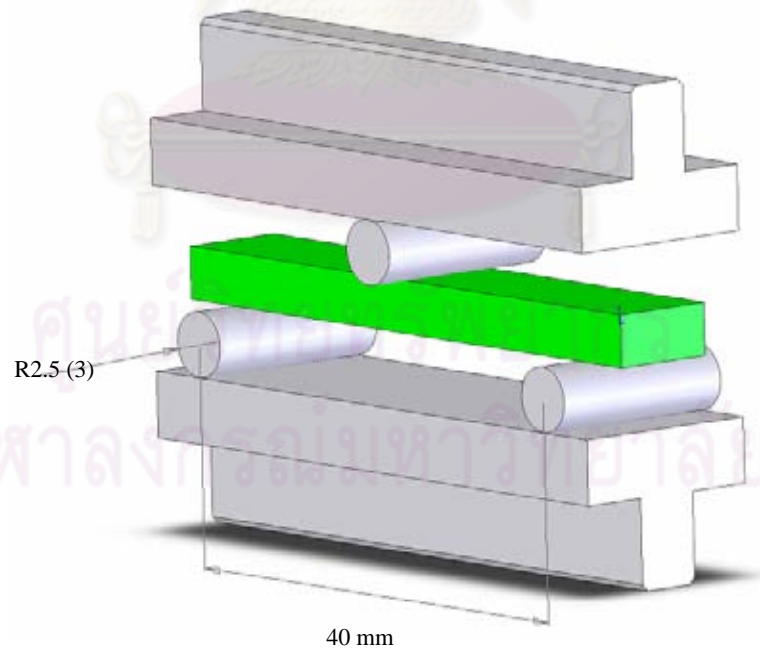
Figure 3.4   Three point bending schematic

In compression, the testing procedures following ASTM D 1621-04a Standard Test Method for Compressive Properties of Rigid Cellular Plastics was carried out to examine compressive strength of porous polyurethane foam specimen. The specimen for compression test was prepared by saw blade cutting to have dimensions of 20 mm. in width and length with 15 mm. thickness. Each specimen was placed on the testing apparatus as schematically shown in Figure 3.5 and was tested with constant cross head speed of 2.5 mm/min on the same testing machine as flexural strength testing. Forces applied on the specimen were collected and used to calculate compressive strength as expressed in Equation 3.5.
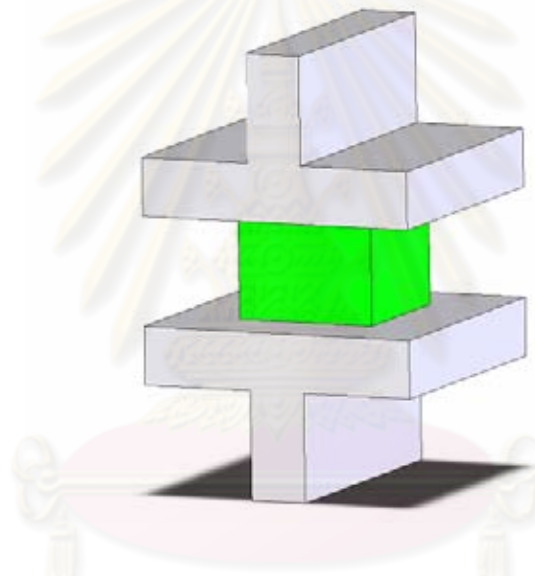
Figure 3.5   Compressive testing schematic

$$CS = \frac{P_y}{A_0}$$ (3.5)

Where

CS = Compressive strength, MPa

P_y = Load at yield point, N

A_0 = Initial cross-sectional area of the specimen, mm^2

Additionally, weibull distribution function shown in Equation 3.6 widely used to evaluate variation of strength for porous materials was conducted to examine characteristic flexural strength and spread of flexural strength and compressive strength for porous polyurethane foam specimen.

$$F(x) \quad = \quad 1 - e^{-\left(\frac{x}{\alpha}\right)^{\beta}}$$ (3.6)

Where

$F(x)$	=	Weibull cumulative distribution (Probability of failure)
x	=	Flexural strength at a given F(x)
β	=	Beta (Weibull shape parameter or Weibull modulus)
α	=	Alpha (Weibull characteristic strength)

3.3 Experimental Equipment Set Up

Equipment used in the spherical grinding system installed and integrated with multi-purposes testing machine, SHIMADZU SERVOPULSER, MODEL: SFL 50kN shown in Figure 3.6 was composed of four main units as following, circular groove pad, cross head speed control unit, grinding speed control unit, grinding force measurement unit.
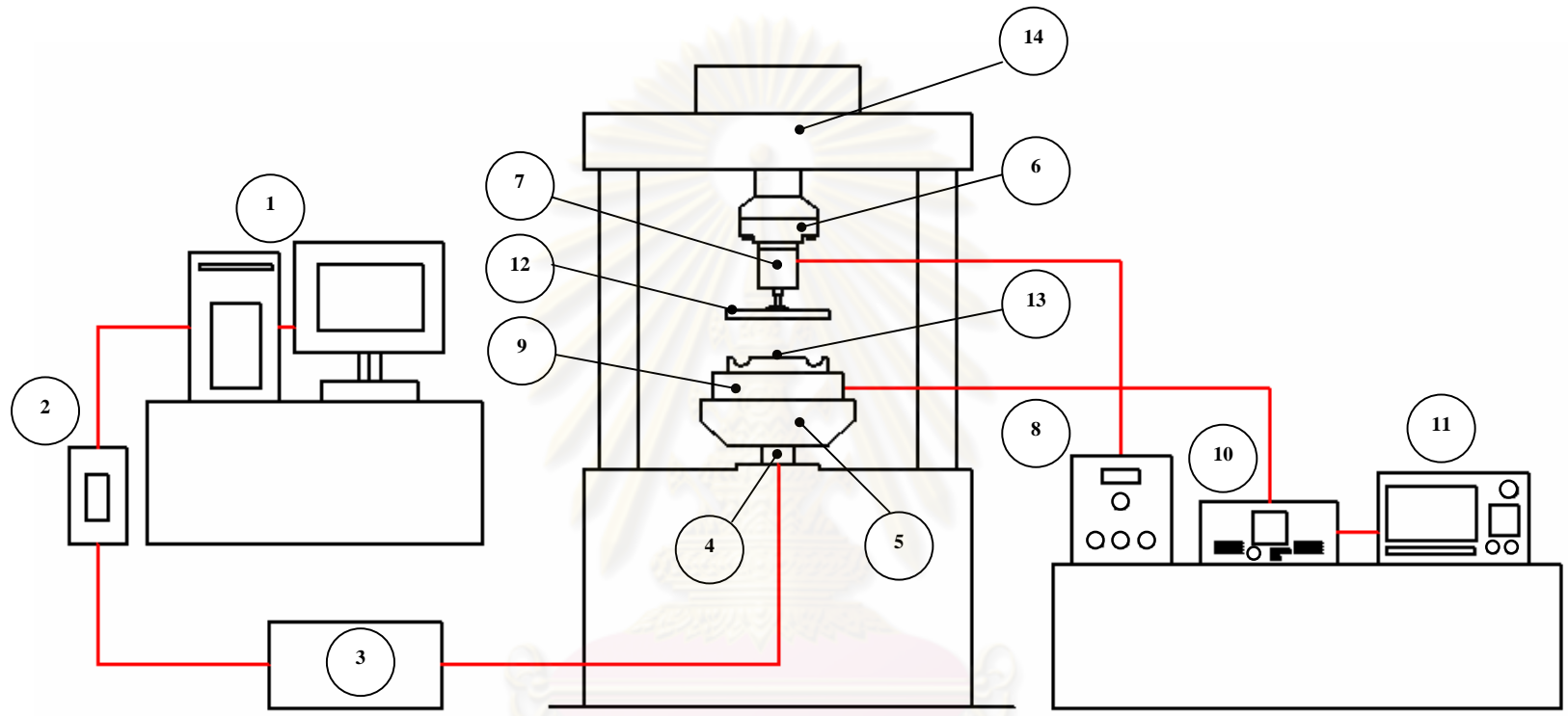
Figure 3.6   Experimental equipment components: 1.Personel computer, 2.Controller, 3.Hydraulic pump, 4.Drive shaft,

5.Lower flange, 6.Upper flange, 7.AC motor, 8.Inverter with user interface, 9.Dynamometer, 10.Charge amplifier,

11.Oscilloscope, 12.Grinding wheel, 13.Circular groove pad, 14.Testing machine

3.3.1 Circular Groove Pad

A circular groove pad made from stainless steel grade 304 was designed to be used as a mold to form spherical parts. It was attached on dynamometer in the spherical grinding system as shown in Figure 3.7. Dimensions of the groove were illustrated in Figure 3.8. The V-groove for a conventional lapping of steel and ceramic balls was modified to be the circular groove in order to increase the ground surface area to form a spherical specimen in this research. From the preliminary V-groove grinding test of porous polyurethane foam, it was found that a specimen could not be moved to change its own previous position to encounter the grinding wheel around the groove because of its restricted grinding area of the V-groove. As a result, as received cube specimen was obviously transformed to be a finished cone shape. Therefore, the circular groove pad having larger grinding area was applied to promote the changes in specimen's orientation during grinding and spherical part formation.
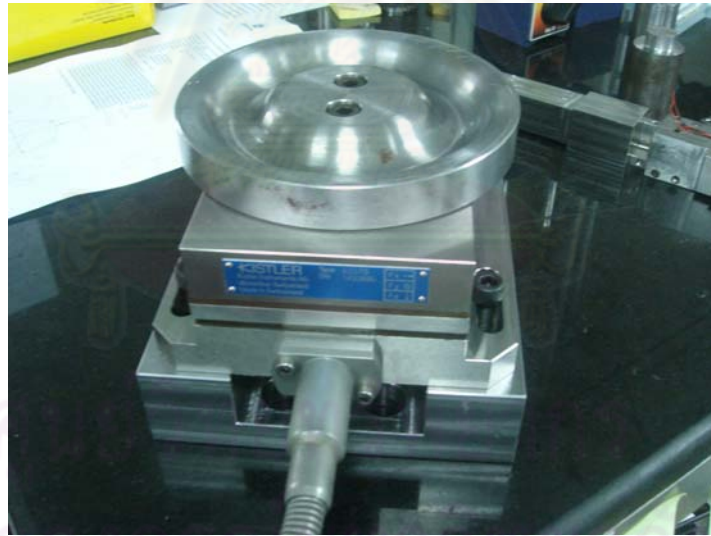
Figure 3.7   Circular groove pad attached on dynamometer
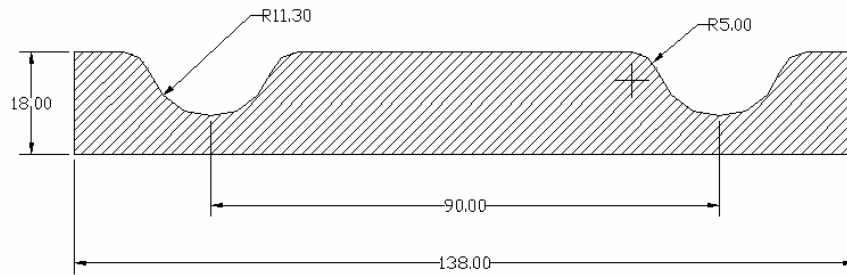
Unit: mm

Figure 3.8   Dimensions of circular groove pad

3.3.2 Cross Head Speed Control Unit

To generate specified an upward motion of the circular groove pad for material removal, cross head speed control unit components were illustrated in Figure 3.9. Personal computer in Figure 3.9 a) working with Gluon software and controller in Figure 3.9 b) of the testing machine was used to operate hydraulic pump in Figure 3.9 c) with rated power of 5.5 KW, rated voltage of 380 V and rated speed of 1440 rpm to generate cross head speed of the lower flange, which was connected to the drive shaft of the testing machine as shown in Figure 3.9 d).

a) Personal computer

b) Controller

c) Hydraulic pump

d) Lower flange and drive shaft

Figure 3.9   Cross head speed control unit: a) Personal computer, b) Controller,
c) Hydraulic pump, d) Lower flange and drive shaft

3.3.3 Grinding Speed Control Unit

Grinding speed control unit was comprised of upper flange, AC motor 240 Watt with rated torque of 0.81 N-m and rated speed of 2790 rpm, grinding wheel having diameter of 125 mm., and inverter with user interface. The AC motor was coupled with the upper flange of the testing machine, and its spindle was connected to the grinding wheel as shown in Figure 3.10. The inverter with user interface in Figure 3.11 was connected to the AC motor to adjust specified grinding speeds in the spherical grinding experiment.
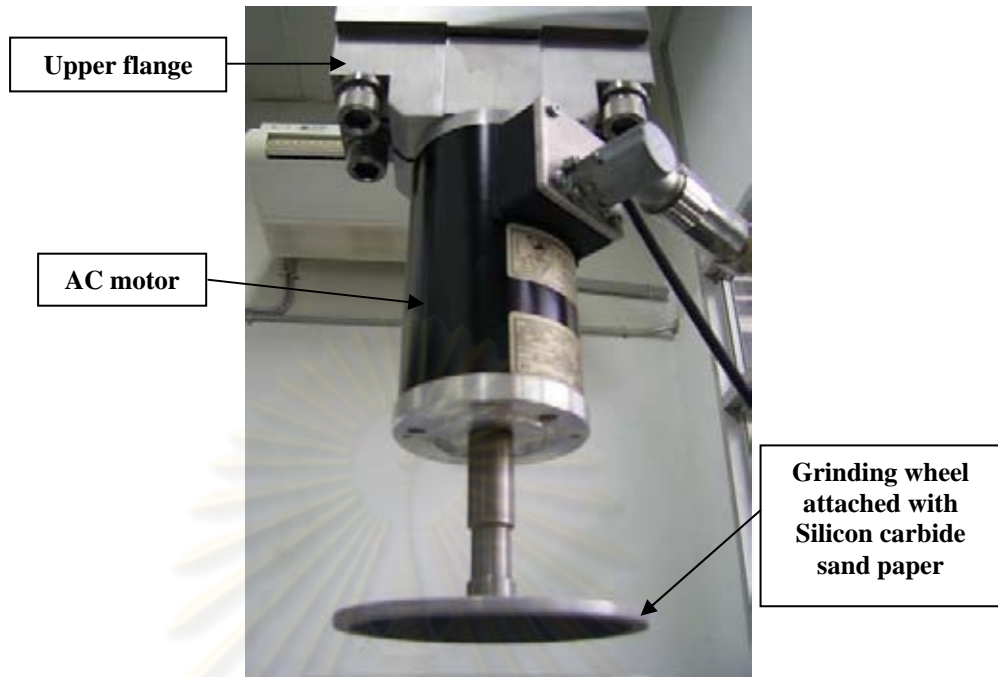
Figure 3.10   Upper flange, AC motor, and grinding wheel

Figure 3.11   Inverter with user interface

3.3.4 Grinding Force Measurement Unit

Grinding force measurement unit including Kistler dynamometer type 9257B, Kistler charge amplifier type 5070A, and Yokogawa oscilloscope type DL750 were illustrated in Figure 3.12. During grinding, piezoelectric sensors in Kistler dynamometer in Figure 3.12 a) produced a charge varied linearly with the load acting on the sensor and was sent to charge amplifier in Figure 3.12 b) via connecting cable. The charge was then converted to a voltage signal, and outputs were illustrated and recorded on oscilloscope in Figure 3.12 c). Sensitivity of the charge amplifier as shown in Table 3.1 for the three force components was set as regarded to calibration certification. In addition, a sampling rate for data collection in oscilloscope was set to be 20 samples per second.

a) Dynamometer   b) Charge amplifier

c) Oscilloscope

Figure 3.12   Force measurement unit: a) Dynamometer, b) Charge amplifier,
c) Oscilloscope

Table 3.1 Sensitivity for three force components

Force component	Calibrated range (N)	Sensitivity (pC/N)
Fx	0-500	-7.950
Fy	0-500	-7.951
Fz	0-100	-3.701

3.4 Experimental Procedures

Experimental methods of spherical grinding porous polyurethane foam were as follows,

1. Prepare cube specimen of porous polyurethane foam with the dimensions of 21 x 21 x 21 mm shown in Figure 3.13 using saw blade cutting.

2. Examine volume, mass, and bulk density of as received specimen.

3. Attach SiC sandpaper on the grinding wheel.

4. Put an as received cube specimen into the circular groove pad as shown in Figure 3.14.

5. Set initial head distance (Hi) of 31.30 mm and expected final head distance (Hf) between circular groove pad and grinding wheel as shown in Figure 3.15 from Gluon software installed in the personal computer of the testing machine.

6. Set grinding speed (Vs) from the user interface of the inverter motor and upward cross head speed (f) from the Gluon software installed in the personal computer of the testing machine.

7. Operate grinding system including cross head speed control unit, grinding speed control unit, and grinding force measurement unit after setting all grinding conditions correctly.

8. Stop grinding system and record voltage values of grinding forces in card recorder of the oscilloscope.

9. Characterize finished specimens in terms of shape, circularity error, and diameter after each grinding experiment finished.

10. Examine material removal rate, grinding forces, grinding force ratio, and specific grinding energy.

Figure 3.13   A cube specimen prepared
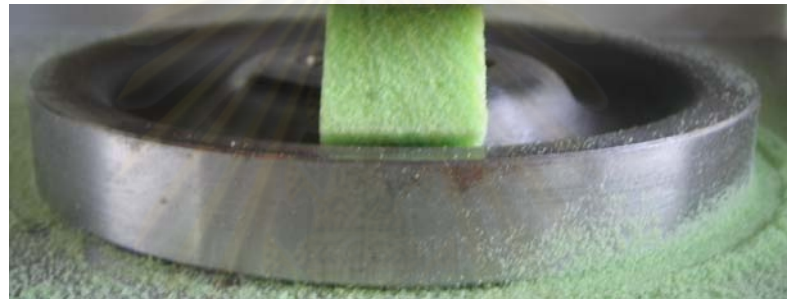
Figure 3.14   A cube specimen was placed in circular groove pad
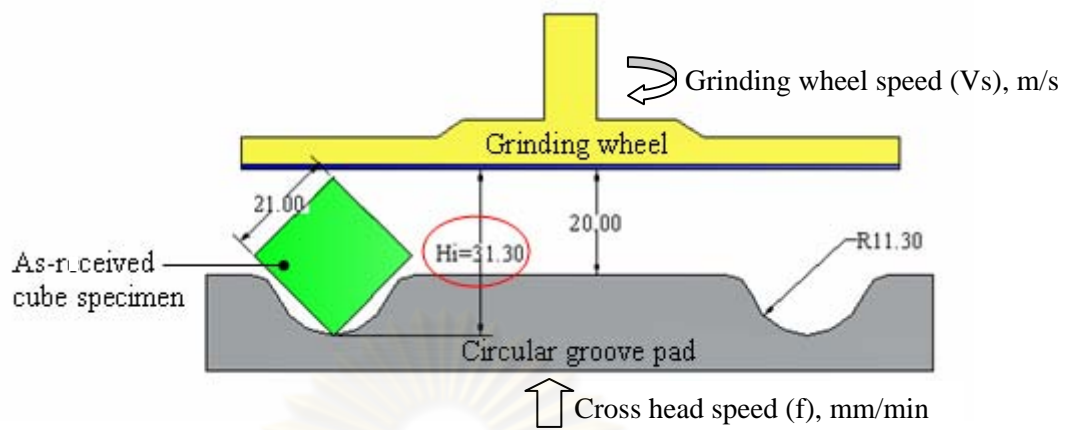
a) Initial head distance (Hi)
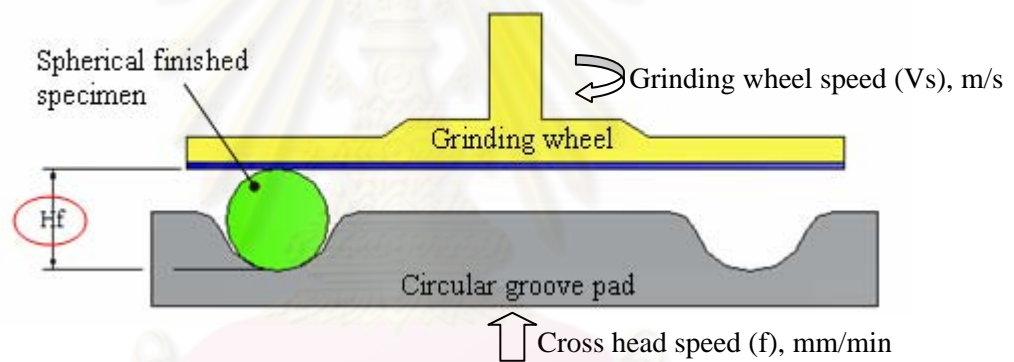
b) Final head distance (Hf)

Unit: mm.

Figure 3.15   Spherical grinding schematic at: a) Initial head distance (Hi) and
b) Final head distance (Hf)

3.5 Finished Specimen Characterizations

Finished specimens after grinding were characterized for their shape, circularity error, and finished diameter. Shape of each finished specimen was initially examined by visual inspection and categorized into four types namely egg, sphere, partial sphere, and squircle shape. For more precise measurement of the finished specimen, Mitutoyo Vision Measuring Machine (VMM) with magnification of 0.5X and resolution of 0.0001 mm illustrated in Figure 3.16 was carried out to measure circularity error and finished diameter. Outer profile of the specimen as shown in Figure 3.17 was automatically focused and plotted into X, Y, and Z coordination system which were then transferred to image processing software to calculate circularity error and diameter. Four planes for each finished specimen were measured as shown in Figure 3.18.

Figure 3.16   Vision measuring machine
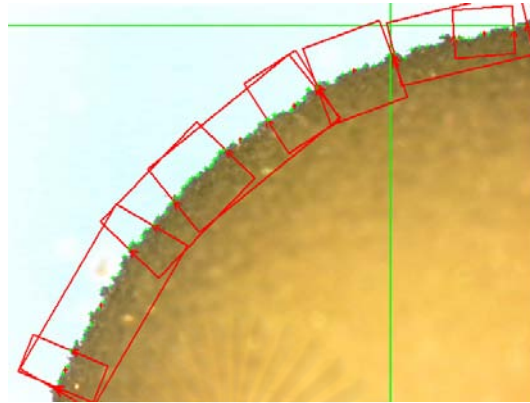
Figure 3.17   Outer profile plots of finished specimen
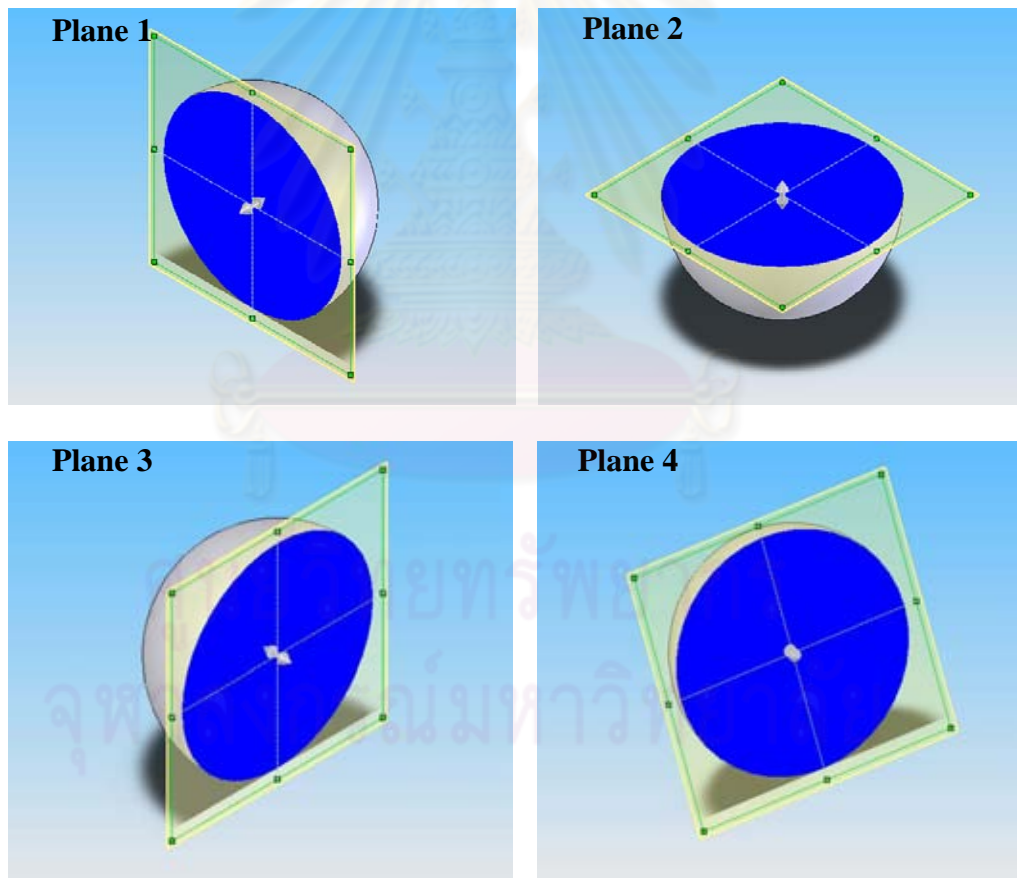
Figure 3.18   Four planes for circularity error and finished diameter measurement

3.6 Grinding Response Examination

After grinding, responses in terms of material removal rate, grinding forces, grinding force ratio, and specific grinding energy were examined.

3.6.1 Material Removal Rate

Material removal rate in the spherical grinding system was estimated by means of the volume of material removed per unit time and could be expressed in Equation 3.7. In addition, as received cube specimen volume and finished specimen volume were expressed in Equation 3.8 and 3.9, respectively.

$$MRR = \frac{V_A - V_F}{T} \qquad (3.7)$$

$$V_A = W \times L \times H \qquad (3.8)$$

$$V_F = \frac{4}{3} \times \pi \times \left(\frac{D}{2}\right)^3 \qquad (3.9)$$

Where

MRR	=	Material removal rate, mm^3/s
V_A	=	As received cube specimen volume, mm^3
V_F	=	Finished specimen volume, mm^3
T	=	Grinding time, s
W	=	Width of as received cube specimen, mm
L	=	Length of as received cube specimen, mm
H	=	Height of as received cube specimen, mm
D	=	Finished diameter measured from vision measuring machine, mm

3.6.2 Grinding Forces

Voltage signal values of F_x, F_y, and F_z caused by loads acting on piezoelectric sensors in the dynamometer on X, Y, Z axis were collected in the card recorder of the oscilloscope in CSV (Comma-separated valued) file. These voltage values could be converted to grinding forces by multiplying Force Generator Scale Factor (FGSF) having value of 10 N/V as expressed in Equation 3.10 to 3.12. Force components in the spherical grinding system were shown in Figure 3.19. Tangential force (Ft) acting in the direction of cutting was the resultant of F_x and F_y force component and could be calculated from Equation 3.13. Normal force (Fn) normal to cutting direction was presented as F_z force component as shown in Equation 3.14. Subsequently, all data of the tangential and normal force were calculated in terms of Root Mean Square (RMS) as expressed in Equation 3.15 for each experiment run.

$$F_x \quad = \quad V_x \times FGSF \qquad (3.10)$$

$$F_y \quad = \quad V_y \times FGSF \qquad (3.11)$$

$$F_z \quad = \quad V_z \times FGSF \qquad (3.12)$$

Where

Fx, Fy, Fz	=	Grinding force component in X, Y, Z axis, N
Vx, Vy, Vz	=	Voltage value in X, Y, Z axis, V
FGSF	=	Force Generator Scale Factor, 10 N/V
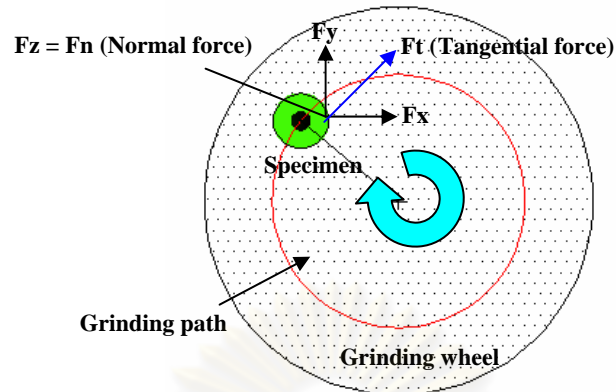
Figure 3.19   Grinding force components

$$Ft \quad = \quad \sqrt{F_x^2 + F_y^2} \qquad (3.13)$$

$$Fn \quad = \quad F_z \qquad (3.14)$$

Where

Ft	=	Tangential force, N
Fn	=	Normal force, N
F_x , F_y , F_z	=	Grinding force in axis X, Y, Z, N

$$F_{(RMS)} \quad = \quad \sqrt{\frac{1}{n}\sum_{i}^{n} F_i^2} \qquad (3.15)$$

Where

$F_{(RMS)}$	=	Grinding force root mean square, N
i	=	Sequence of data from 1 to n
F_i	=	Grinding force at i
n	=	Number of all data

3.6.3 Grinding Force Ratio

The ratio of tangential force and normal force was expressed in Equation 3.16 generally used as the indicator to evaluate machining difficulty of materials meaning to the cutting ability of grinding wheels.

$$R = \frac{Ft_{RMS}}{Fn_{RMS}} \qquad 3.16)$$

Where

R = Grinding force ratio

Ft_{RMS} = Tangential force root mean square, N

Fn_{RMS} = Normal force root mean square, N

3.6.4 Specific Grinding Energy

Specific grinding energy, one of the most important characteristics in material removal processes, defined as the energy expended per unit volume of material removal (Malkin and Hwang, 1996) can be calculated by Equation 3.17.

$$u = \frac{Ft_{RMS} \times Vs}{MRR} \qquad 3.17)$$

Where

u = Specific grinding energy, J/m^3

Ft_{RMS} = Tangential force root mean square, N

Vs = Grinding wheel speed, m/s

MRR = Material removal rate, m^3/s

3.7 Experimental Design

To study the effects of three grinding factors including grinding speed, cross head speed, and abrasive size on circularity error, finished diameter, material removal rate, tangential and normal force, grinding force ratio, and specific grinding energy, grinding conditions were set up as illustrated in Table 3.2 based on the initial study of spherical grinding for porous polyurethane foam via circular groove pad presented by Chaopanich *et al.* (2007). The grinding factors were set at 7 levels (a) for grinding speeds (Vs) from 1.41 to 5.18 m/s, 3 levels (b) for cross head speeds (f) of 1.0, 3.0, and 5.0 mm/min, and 2 levels (c) for abrasive grit sizes (A) of 20 and 53μm. Meanwhile, the initial head distance (Hi) and final head distance (Hf) were fixed at 31.30 and 19.50 mm, respectively. The linear grinding speeds indicated were examined from Equation 2.1 in Chapter II with rotational speeds from 300 to 1,100 RPM and the diameter of circular groove of 90 mm.

Experimental plan for fixed effect general full factorial design was shown in Table 3.3 and randomly run. The two experimental replications (n) for each grinding condition were conducted because of time consumption in collecting grinding force data and in examining circularity error and finished diameter measured from the Vision Measuring Machine (VMM).

Table 3.2   Grinding conditions for spherical grinding porous polyurethane foam

Grinding condition	Value
1.Grinding speed (Vs)	1.41, 2.36, 2.83, 3.30, 3.77, 4.24, 5.18 m/s
2.Cross head speed (f)	1, 3, 5 mm/min
3.Abrasive grit size (A)	20, 53 μm
4.Initial head distance (Hi)	31.30 mm.
5.Final head distance (Hf)	19.50 mm.

Table 3.3   Experimental plan

Cross head speed (f)		Abrasive grit size (A)										
		20 µm						53 µm				
		1.0 mm/min		3.0 mm/min		5.0 mm/min		1.0 mm/min		3.0 mm/min		5.0 mm/min	
		R1	R2	R1	R2	R1	R2	R1	R2	R1	R2	R1	R2
Grinding speed (Vs)	1.41 m/s	58	39	63	27	79	23	57	21	81	3	69	36
	2.36 m/s	78	28	65	1	71	7	73	2	80	33	50	19
	2.83 m/s	64	6	53	13	54	22	43	20	51	31	49	37
	3.30 m/s	46	34	52	29	77	41	84	4	68	40	76	9
	3.77 m/s	82	25	70	17	60	30	66	38	55	26	44	12
	4.24 m/s	75	18	48	15	59	35	83	10	62	11	74	14
	5.18 m/s	56	8	45	24	47	16	67	5	61	42	72	32

Remark:

1, 2, 3,…., 84	=	Experiment run number
R1, R2	=	Experiment replication 1, 2

3.8 Statistical Analysis

3.8.1 Effects of Grinding Factors on Grinding Responses

Analysis of variance (ANOVA) in Table 3.4 was carried out to investigate the effects of grinding factors in terms of grinding speed, cross head speed, abrasive grit size, and their interactions on the following responses.

1. Circularity error (CE)
2. Finished diameter (D)
3. Tangential force (Ft $_{RMS}$)
4. Normal force (Fn $_{RMS}$)
5. Grinding force ratio (R = Ft $_{RMS}$/Fn $_{RMS}$)
6. Material removal rate (MRR)
7. Specific grinding energy (u)

Significance level (α) was set to be 0.05 because it is a feasible level at which to do research work having a fair chance of picking up those effects which are large enough to be of scientific interest (Bross, 1971). In addition, many researchers in the field of steel and ceramic machining used the significance level mentioned in their work to see which parameters have a significant effect on the surface roughness

(Bagci and Aykut, 2006). Experimental results for all responses above were analyzed by Minitab R14 statistical software to investigate their effects.

Table 3.4　Analysis of variance table for the three factors fixed effect general full factorial design

Source	Degree of Freedom (DF)	Sum of Square (SS)	Mean Square (MS)	F Ratio	% Contribution
Vs	a - 1	SS_{Vs}	MS_{Vs}	MS_{Vs}/MS_E	MS_{Vs}/MS_{Total}
f	b - 1	SS_f	MS_f	MS_f/MS_E	MS_f/MS_{Total}
A	c - 1	SS_A	MS_A	MS_A/MS_E	MS_A/MS_{Total}
Vs*f	(a - 1)(b - 1)	SS_{Vs*f}	MS_{Vs*f}	MS_{Vs*f}/MS_E	MS_{Vs*f}/MS_{Total}
Vs*A	(a - 1)(c - 1)	SS_{Vs*A}	MS_{Vs*A}	MS_{Vs*A}/MS_E	MS_{Vs*A}/MS_{Total}
f*A	(b - 1)(c - 1)	SS_{f*A}	MS_{f*A}	MS_{f*A}/MS_E	MS_{f*A}/MS_{Total}
Vs*f*A	(a - 1)(b - 1)(c - 1)	SS_{Vs*f*A}	MS_{Vs*f*A}	MS_{Vs*f*A}/MS_E	MS_{Vs*f*A}/MS_{Total}
Error	abc(n - 1)	SS_E	MS_E		
Total	abcn - 1				

Remark:　a = the number of grinding speed level　　b = the number of cross head speed level

　　　　　c = the number of abrasive grit size level　n = the number of experimental replications

　　　　　MS = SS/DF　　　　　　　　　　　　　MS_{Total} = Sum of MS

3.8.2 Regression Analysis

Experimental results from the general full factorial design as planned in Table 3.3 were also used to generate regression model (Second order model) to predict grinding responses in terms of grinding factors in the form of full quadratic equations. Analysis of variance (ANOVA) was carried out to investigate the significance of the model, and R-Square was also indicated. Furthermore, model reduction was conducted through stepwise regression technique to remove insignificant terms from the regression models by using significance level (α) of 0.05.

3.8.3 Confirmation Experiment

Grinding conditions of a new experimental plan were set up for model validation as shown in Table 3.5 and Table 3.6. Single replicate experiment with random order was run. The actual results of all grinding responses were paired wise compared with the estimated results from the regression models. The two results were tested for difference with significance level (α) of 0.05.

Table 3.5   Grinding conditions for confirmation

Grinding conditions	Values
1.Grinding speed (Vs)	2.83, 3.30, 3.77 m/s
2.Cross head speed (f)	1, 3, 5 mm/min
3.Abrasive grit size (A)	20, 53 μm
4.Initial head distance (Hi)	31.30 mm.
5.Final head distance (Hf)	19.50 mm.

Table 3.6   Experimental plan for confirmation

		Abrasive grit size (A)					
		20 μm			53 μm		
Cross head speed (f)		1.0 mm/min	3.0 mm/min	5.0 mm/min	1.0 mm/min	3.0 mm/min	5.0 mm/min
Grinding speed (Vs)	2.83 m/s	1	3	2	9	8	5
	3.30 m/s	10	18	12	14	11	13
	3.77 m/s	6	7	4	17	15	16

Remark: 1, 2, 3,….,18   =   Experiment run number

Chapter IV

Experimental Data Analysis

Experimental data including circularity error, finished diameter, grinding forces, material removal rate, and specific grinding energy from various grinding conditions were analyzed by means of descriptive statistics. Moreover, grinding force characteristics of the spherical grinding process developed were in depth demonstrated for tangential and normal force in time and frequency domain.

4.1 Circularity Error and Finished Diameter Data Analysis

Finished specimens after grinding run were measured in terms of circularity error (CE) and finished diameter (D) via Vision Measuring Machine (VMM). Measured data were reported in Appendix D, and averaged values were shown in Table 4.1 and 4.2 for each grinding condition. It was seen that the minimum circularity error of 0.46 mm was ground with the grinding speed of 3.30 m/s, cross head speed of 1.0 mm/min, and abrasive grit size of 53 µm for Replication 2.

In addition, descriptive statistics of circularity error and finished diameter for all grinding conditions were summarized in Table 4.3. Circularity error was reported in average of 0.83 ± 0.41 mm with 95% confidence interval between 0.74 and 0.92 mm, while the mean value of finished diameter was 19.25 ± 0.58 mm with 95% confidence ranged from 19.12 to 19.37 mm. Distribution of the data were illustrated in histograms as shown in Figure 4.1 and 4.2.

Table 4.1   Circularity error (CE, mm) for various grinding conditions

Cross head speed (f)		Abrasive grit size (A)										
		20 µm						53 µm				
		1.0 mm/min		3.0 mm/min		5.0 mm/min		1.0 mm/min		3.0 mm/min		5.0 mm/min	
		R1	R2	R1	R2	R1	R2	R1	R2	R1	R2	R1	R2
Grinding speed (Vs)	1.41 m/s	1.69	1.36	1.77	1.98	1.87	1.75	1.20	1.11	1.49	1.49	1.93	1.71
	2.36 m/s	0.60	0.51	0.67	0.65	1.30	1.26	0.47	0.57	0.68	0.60	0.89	1.43
	2.83 m/s	0.53	0.51	0.62	0.64	0.67	0.75	0.55	0.53	0.63	0.62	0.76	0.58
	3.30 m/s	0.55	0.50	0.48	0.61	0.54	0.62	0.47	0.46	0.61	0.62	0.73	0.57
	3.77 m/s	0.47	0.64	0.59	0.59	0.54	0.60	0.49	0.52	0.56	0.63	0.60	0.62
	4.24 m/s	0.60	0.59	0.64	0.49	0.57	0.61	0.64	0.88	0.62	0.68	0.63	0.65
	5.18 m/s	1.35	0.68	0.77	0.70	1.21	1.05	0.77	0.78	1.81	1.70	0.83	1.01

Remark: R1, R2   =   Experimental replication 1, 2

Table 4.2   Finished diameter (D, mm) for various grinding conditions

Cross head speed (f)		Abrasive grit size (A)										
		20 µm						53 µm				
		1.0 mm/min		3.0 mm/min		5.0 mm/min		1.0 mm/min		3.0 mm/min		5.0 mm/min	
		R1	R2	R1	R2	R1	R2	R1	R2	R1	R2	R1	R2
Grinding speed (Vs)	1.41 m/s	19.93	19.86	20.03	19.61	19.34	19.94	19.85	19.64	19.57	19.67	19.84	19.71
	2.36 m/s	19.49	19.46	19.38	19.31	19.72	19.64	19.44	19.40	19.23	19.27	19.51	19.76
	2.83 m/s	19.48	19.42	19.37	19.27	19.36	19.18	19.35	19.38	19.20	19.26	19.24	19.22
	3.30 m/s	19.37	19.40	19.31	19.28	19.34	19.30	19.36	19.40	19.18	19.26	19.21	19.23
	3.77 m/s	19.38	19.35	19.38	19.25	19.26	19.18	19.33	19.33	19.18	19.24	19.24	19.15
	4.24 m/s	19.37	19.35	19.29	19.31	19.23	19.29	19.30	18.52	19.21	19.20	19.21	19.13
	5.18 m/s	18.21	19.19	19.09	19.36	18.94	19.06	15.74	16.49	18.17	18.68	19.02	18.97

Remark: R1, R2   =   Experimental replication 1, 2

Table 4.3   Descriptive statistics summary for circularity error (CE) and finished
diameter (D) for all grinding conditions

	Min.	Mean	Max.	SD	CV	95% C.I.	N
CE (mm.)	0.46	0.83	1.98	0.41	49.4%	[0.74, 0.92]	84
D (mm.)	15.74	19.25	20.03	0.58	3.0%	[19.12, 19.37]	84

Remark: Min. and Max.   =   Minimum and Maximum value

SD   =   Standard deviation

CV   =   Coefficient of variation

C.I.   =   Confidence interval

N   =   Number of specimen
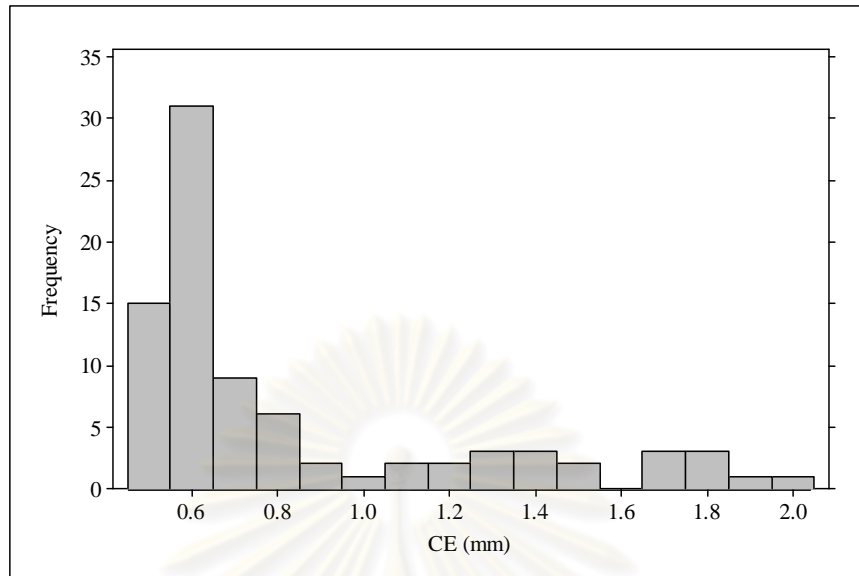
Figure 4.1   Histogram of circularity error (CE) for all data
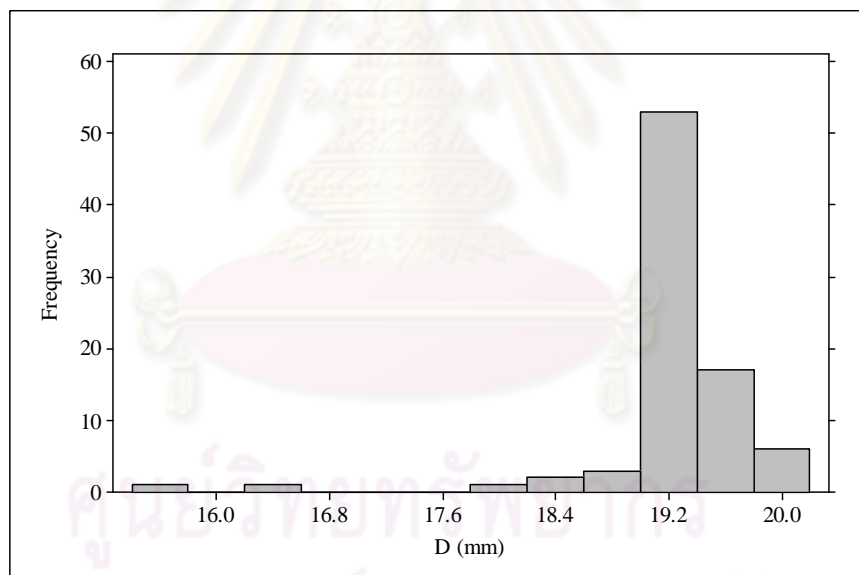
Figure 4.2   Histogram of finished diameter (D) for all data

4.2 Grinding Force Data Analysis

4.2.1 Root Mean Square of Tangential and Normal Force and Grinding Force Ratio

Root mean squares of tangential (Ft $_{RMS}$) and normal (Fn $_{RMS}$) force were calculated from all data collected by recorder in the grinding system and reported for each grinding conditions in Table 4.4 and 4.5. The ratio of tangential and normal force expressed as a grinding force ratio was also summarized in Table 4.6. To analyze data of root mean square of tangential and normal force as well as grinding force ratio, statistical results in Table 4.7 and also histograms in Figure 4.3, 4.4, and 4.5 were demonstrated. Tangential force was reported in average of 0.18 ± 0.08 N with 95% confidence interval between 0.17 and 0.20 N, and the mean value of normal force was 0.17 ± 0.09 N with 95% confidence ranged from 0.15 to 0.19 N. Additionally, grinding force ratio was illustrated to be 1.14 in average, having 95% confidence interval between 1.08 and 1.20.

Table 4.4   Root mean square tangential force (Ft $_{RMS}$, N) for various grinding conditions

		Abrasive grit size (A)										
		20 µm						53 µm				
Cross head speed (f)		1.0 mm/min		3.0 mm/min		5.0 mm/min		1.0 mm/min		3.0 mm/min		5.0 mm/min
		R1	R2	R1	R2	R1	R2	R1	R2	R1	R2	R1	R2
Grinding speed (Vs)	1.41 m/s	0.32	0.29	0.28	0.35	0.31	0.43	0.19	0.22	0.36	0.36	0.44	0.22
	2.36 m/s	0.17	0.26	0.27	0.29	0.24	0.28	0.15	0.15	0.15	0.19	0.28	0.21
	2.83 m/s	0.12	0.20	0.16	0.20	0.16	0.24	0.12	0.14	0.18	0.20	0.24	0.20
	3.30 m/s	0.12	0.22	0.18	0.20	0.15	0.17	0.11	0.11	0.11	0.15	0.26	0.13
	3.77 m/s	0.11	0.18	0.22	0.16	0.11	0.16	0.10	0.11	0.10	0.10	0.19	0.11
	4.24 m/s	0.09	0.18	0.15	0.17	0.14	0.21	0.11	0.11	0.14	0.12	0.19	0.19
	5.18 m/s	0.11	0.15	0.10	0.14	0.09	0.16	0.10	0.14	0.09	0.10	0.11	0.09

Table 4.5   Root mean square normal force (Fn $_{RMS}$, N) for various grinding
conditions

Cross head speed (f)		Abrasive grit size (A)										
		20 µm						53 µm					
		1.0 mm/min		3.0 mm/min		5.0 mm/min		1.0 mm/min		3.0 mm/min		5.0 mm/min	
		R1	R2	R1	R2	R1	R2	R1	R2	R1	R2	R1	R2
Grinding speed (Vs)	1.41 m/s	0.30	0.33	0.27	0.32	0.38	0.45	0.20	0.28	0.39	0.37	0.46	0.22
	2.36 m/s	0.20	0.28	0.27	0.28	0.24	0.26	0.15	0.16	0.16	0.20	0.27	0.18
	2.83 m/s	0.14	0.23	0.16	0.18	0.18	0.23	0.12	0.12	0.21	0.21	0.20	0.19
	3.30 m/s	0.10	0.22	0.21	0.20	0.17	0.20	0.12	0.11	0.12	0.12	0.22	0.13
	3.77 m/s	0.11	0.16	0.23	0.13	0.14	0.18	0.07	0.08	0.09	0.09	0.20	0.10
	4.24 m/s	0.07	0.16	0.11	0.13	0.12	0.18	0.08	0.05	0.10	0.08	0.18	0.13
	5.18 m/s	0.07	0.09	0.08	0.11	0.06	0.08	0.06	0.09	0.05	0.09	0.07	0.06

Table 4.6   Grinding force ratio (R) for various grinding conditions

Cross head speed (f)		Abrasive grit size (A)										
		20 µm						53 µm					
		1.0 mm/min		3.0 mm/min		5.0 mm/min		1.0 mm/min		3.0 mm/min		5.0 mm/min	
		R1	R2	R1	R2	R1	R2	R1	R2	R1	R2	R1	R2
Grinding speed (Vs)	1.41 m/s	1.07	0.88	1.01	1.07	0.83	0.96	0.93	0.80	0.94	0.97	0.96	0.97
	2.36 m/s	0.86	0.94	1.03	1.04	0.99	1.08	1.03	0.98	0.93	0.94	1.02	1.18
	2.83 m/s	0.89	0.88	1.01	1.09	0.93	1.04	1.02	1.15	0.88	0.92	1.23	1.07
	3.30 m/s	1.12	0.99	0.86	0.96	0.86	0.83	0.87	0.99	0.91	1.26	1.16	1.05
	3.77 m/s	1.02	1.10	0.93	1.20	0.80	0.92	1.45	1.30	1.22	1.13	0.91	1.02
	4.24 m/s	1.19	1.15	1.39	1.31	1.17	1.19	1.45	2.15	1.41	1.52	1.09	1.48
	5.18 m/s	1.67	1.66	1.23	1.25	1.49	1.99	1.59	1.50	2.02	1.14	1.56	1.53

Table 4.7   Descriptive statistics summary for root mean square tangential force (N)
and normal force (N) and grinding force ratio for all grinding conditions

	Min.	Mean	Max.	SD	CV	95% C.I.	N
Ft $_{RMS}$ (N)	0.09	0.18	0.44	0.08	43.2%	[0.17, 0.20]	84
Fn $_{RMS}$ (N)	0.05	0.17	0.46	0.09	52.8%	[0.15, 0.19]	84
R	0.80	1.14	2.15	0.28	24.5%	[1.08, 1.20]	84

Remark: Min. and Max.   =   Minimum and Maximum value

SD   =   Standard deviation

CV   =   Coefficient of variation

C.I.   =   Confidence interval

N   =   Number of specimen

Figure 4.3   Histogram of root mean square tangential force (Ft $_{RMS}$) for all data
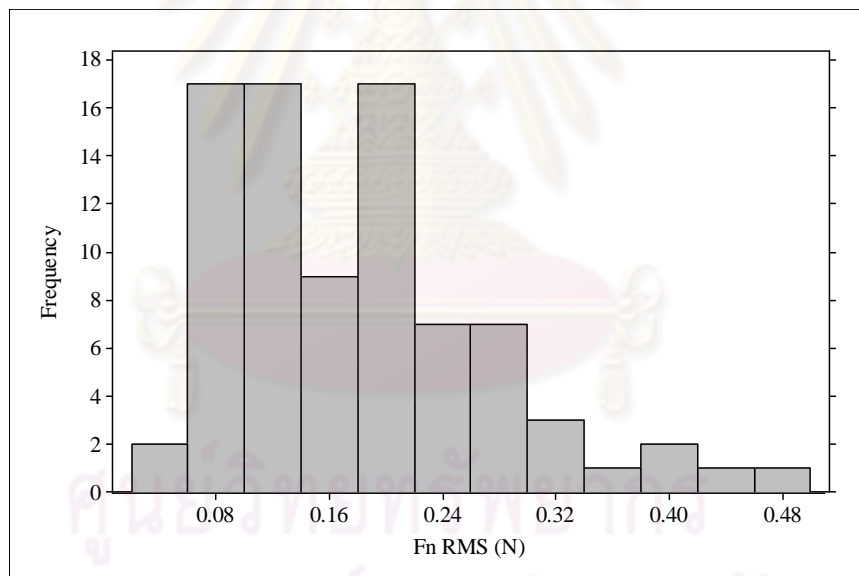
Figure 4.4   Histogram of root mean square normal force (Fn $_{RMS}$) for all data
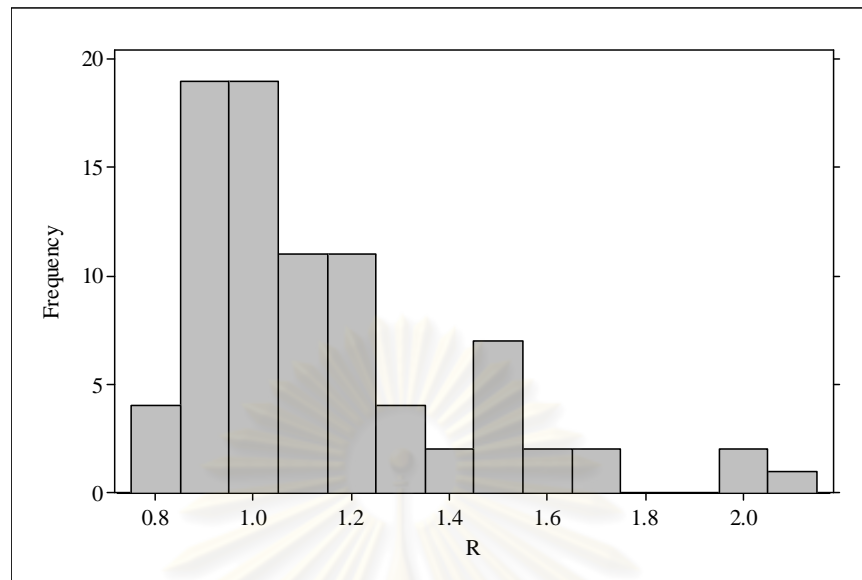
Figure 4.5   Histogram of grinding force ratio (R) for all data

4.2.2 Time and Frequency Domain Analysis for Grinding Force Signals

In this section, tangential and normal force signals were investigated to examine their characteristics for the selected various grinding conditions in Table 4.8 in time domain and frequency domain. In time domain, location of the grinding force signals was analyzed via the slope of linear estimation. In frequency domain, spectral density of the grinding force signals was illustrated.

Table 4.8   Selected grinding conditions for grinding force signal analysis

		Abrasive grit size (A)										
		20 µm						53 µm				
Cross head speed (f)		1.0 mm/min		3.0 mm/min		5.0 mm/min		1.0 mm/min		3.0 mm/min		5.0 mm/min	
		R1	R2	R1	R2	R1	R2	R1	R2	R1	R2	R1	R2
	1.41 m/s	58	39	63	27	79	23	57	21	81	3	69	36
Grinding speed (Vs)	2.83 m/s	64	6	53	13	54	22	43	20	51	31	49	37
	3.30 m/s	46	34	52	29	77	41	84	4	68	40	76	9
	3.77 m/s	82	25	70	17	60	30	66	38	55	26	44	12
	5.18 m/s	56	8	45	24	47	16	67	5	61	42	72	32

Remark: 58, 64, 82, 56, 39,…,12, 32   =   Experiment run number

R1, R2   =   Experimental replication 1, 2

4.2.4.1 Time Domain Analysis

One way to quantify a change in location over time is to fit a straight line to the data set. If there is no significant drift in the location, the slope parameter should be zero (National Institute of Standards and Technology, 2010: online). Therefore, tangential (Ft) and normal (Fn) force signals for the selected various grinding conditions were plotted versus grinding time (t) in second as illustrated in Appendix E from Figure E-1 to E-12. As can be observed from those graphs, slightly upward trends for Ft performed at the lowest grinding speed of 1.41 m/s for all cross head speeds and abrasive grit sizes. In contrast, the trends of Ft were more stable for grinding speeds between 2.83 and 3.77 m/s and had a downward trend at the highest grinding speed of 5.18 m/s. For Fn, the trends were also increased at the lowest grinding speed of 1.41 m/s but slightly decreased as increasing grinding speeds from 2.83 to 5.18 m/s.

The results of slope for tangential (Ft) and normal (Fn) force versus grinding factors including grinding speed (Vs), cross head speed (f), and abrasive grit size (A) were concluded in Table 4.9 and graphically illustrated by means of main effect plots of data mean in Figure 4.6 and 4.7, respectively. The slopes for Ft was 5.21×10^{-4} N/s at the lowest grinding speed of 1.41 m/s and stable around 0.28×10^{-4} to 0.89×10^{-4} N/s at grinding speeds between 2.83 and 3.77 m/s, then dropping to -2.36×10^{-4} N/s at the highest grinding speed of 5.18 m/s. Increasing cross head speed resulted in a slight increase in the slope of Ft. While, the large abrasive grit size of 53 µm contributed to a low level of slope than the small one of 20 µm. For Fn, slopes were also decreased from 12.49×10^{-4} to 0.42×10^{-4} N/s as increasing grinding speeds from 1.41 to 5.18 m/s. At the grinding between 2.83 and 3.77 m/s, slopes gradually decreased from 9.08×10^{-4} to 7.41×10^{-4} N/s. On the other hand, a substantial increase in slope performed with increasing cross head speeds from 1.0 to 5.0 mm/min.

Table 4.9   Slope of tangential (Ft) and normal (Fn) force signal data from selected
grinding conditions

Grinding conditions			Slope (x 10^{-4}N/s) for R1		Slope (x 10^{-4}N/s) for R2	
Vs (m/s)	f (mm/min)	A (µm)	Ft	Fn	Ft	Fn
1.41	1	20	4.11	5.09	2.80	5.37
		53	1.30	3.93	2.15	5.46
	3	20	3.03	8.83	5.58	7.86
		53	5.67	15.04	6.24	11.73
	5	20	9.85	22.40	11.73	24.19
		53	6.18	28.15	3.85	11.89
2.83	1	20	0.57	2.97	0.42	4.21
		53	0.30	2.30	-0.15	2.18
	3	20	-0.43	8.28	2.77	7.53
		53	-0.81	10.28	-0.68	12.40
	5	20	2.34	13.73	3.11	15.72
		53	2.46	15.58	0.82	13.74
3.30	1	20	0.54	0.21	1.19	4.36
		53	-0.19	1.89	0.38	1.87
	3	20	0.84	10.70	2.92	7.81
		53	-0.14	6.28	-1.30	5.67
	5	20	1.18	14.69	-1.30	14.01
		53	-0.65	18.45	-0.10	9.58
3.77	1	20	0.40	2.13	0.97	3.06
		53	-0.13	0.55	0.16	1.60
	3	20	3.21	13.28	2.77	6.99
		53	-0.44	4.65	-0.41	5.28
	5	20	0.63	11.68	-0.22	13.84
		53	2.86	18.03	-0.82	7.82
5.18	1	20	-1.29	-0.66	-0.77	0.28
		53	-2.04	-0.74	-2.13	-1.13
	3	20	-2.98	0.21	-0.13	4.32
		53	-3.48	-1.15	-1.80	1.29
	5	20	-3.71	0.05	-0.50	2.54
		53	-6.78	-1.35	-2.74	1.36
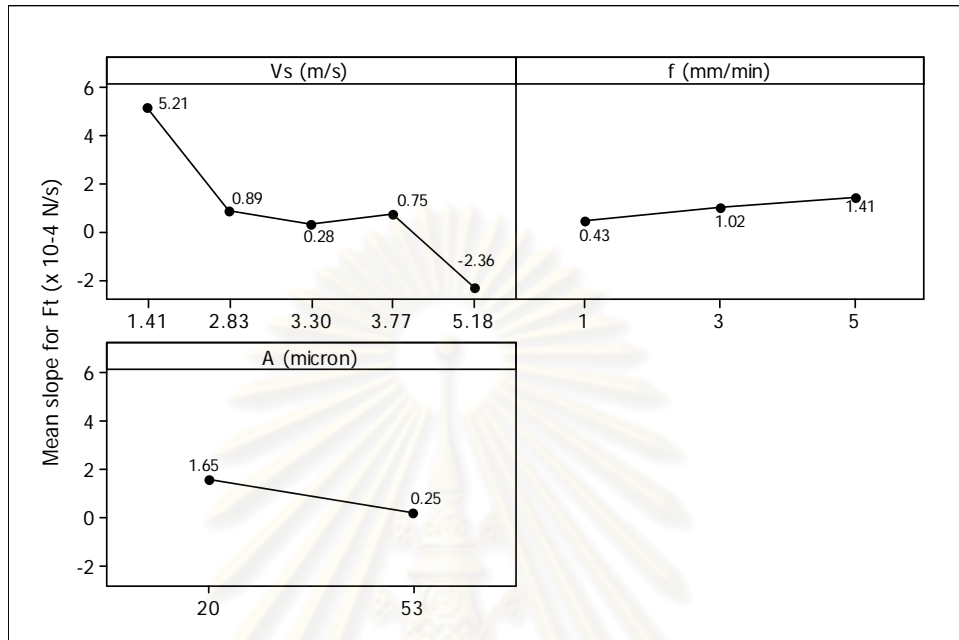
Figure 4.6   Main effect plots of data mean for slope of tangential force (Ft)
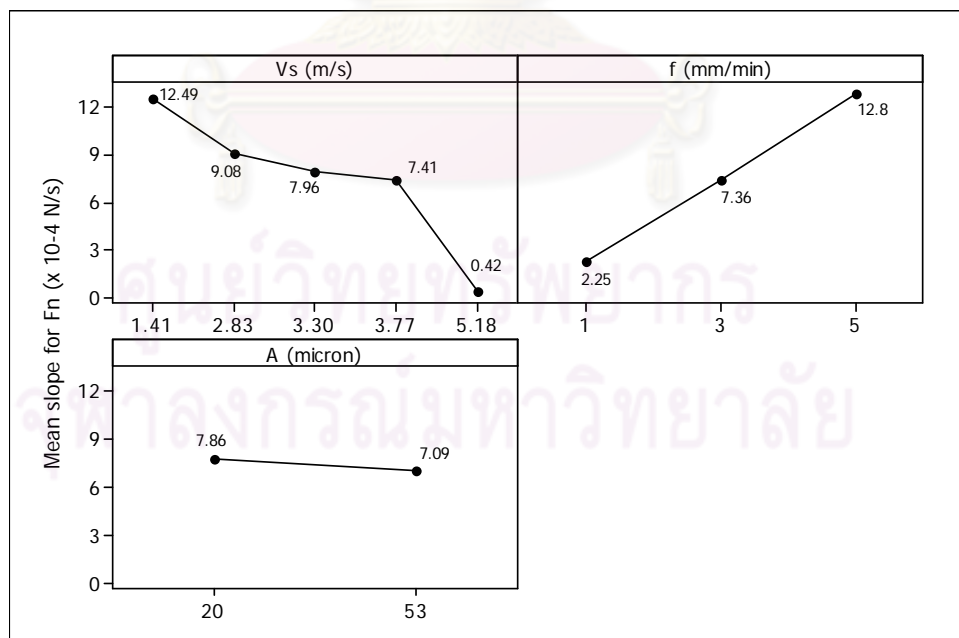
Figure 4.7   Main effect plots of data mean for slope of normal force (Fn)

4.2.4.2 Frequency Domain Analysis

In frequency domain, spectral density of the grinding force signal was applied to show how the intensity of grinding force was at a specified frequency and also to distinguish the characteristics of the spherical grinding process for various conditions. Time domain data can generally be changed to frequency domain using Discrete Fourier Transform (DFT). The spectral densities of tangential (Ft) and normal (Fn) forces versus frequency (fz) were shown in Appendix E from Figure E-13 to E-24. Table 4.10 summarized peak frequencies in the spectral densities for the selected grinding conditions. It was seen that at the lowest grinding speed of 1.41 m/s peak frequencies were at about 2.6 Hz and 2.4 Hz in average for tangential (Ft) and normal force (Fn), respectively. For the grinding speed of 2.83 m/s, peak frequencies were located at about 5.3 Hz for Ft and at 5.3 and 9.4 Hz for Fn. At the grinding speed of 3.30 m/s, the peaks were around 6.2 Hz for Ft and 6.2 and 7.5 for Fn. Moreover, peak frequencies performed at approximately 7.1 Hz for Ft and 5.8 and 7.1 Hz for Fn at the grinding speed of 3.77 m/s. At the highest grinding speed of 5.18 m/s, distinctive peak frequencies did not occur in the spectral densities for all conditions. However, it was also observed from the tangential force spectrum that increasing grinding speeds (Vs) from 1.41 to 3.77 m/s resulted in a shift of peak frequency from 2.6 to 7.1 Hz for all cross head speeds (f) and abrasive grit sizes (A).

Table 4.10 Peak frequency of tangential (Ft) and normal (Fn) force signal data from selected grinding conditions

Grinding conditions			Peak Freq. (Hz) for R1		Peak Freq. (Hz) for R2	
Vs (m/s)	f (mm/min)	A (µm)	Ft	Fn	Ft	Fn
1.41	1	20	2.5	2.5	2.6	2.5
		53	2.6	2.6	2.6	2.6
	3	20	2.6	2.3	2.5	2.3
		53	2.5	2.3	2.5	2.5
	5	20	2.6	-	2.6	2.2
		53	2.6	-	-	-
2.83	1	20	5.3	5.3, 9.5	5.2	5.2, 9.5
		53	5.4	5.4, 9.3	5.4	5.3, 9.3
	3	20	5.3	5.3	5.4	5.4, 9.3
		53	5.3	-	5.3	9.5
	5	20	-	5.2	-	5.1
		53	5.4	5.4, 9.3	-	-
3.30	1	20	6.3	6.3, 7.6	6.2	6.2, 7.5
		53	6.2	6.2, 7.5	6.2	6.3, 7.5
	3	20	6.2	6.2	6.2	6.2, 7.5
		53	6.2	6.2, 7.5	6.2	6.3, 7.5
	5	20	-	-	6.2	5.9, 7.6
		53	-	-	-	-
3.77	1	20	7.1	5.8, 7.1	7.1	5.8, 7.1
		53	7.1	5.9	7.1	5.8, 7.1
	3	20	7.1	5.8, 7.1	7.1	5.8
		53	7.0	5.9	7.1	5.8, 7.1
	5	20	7.1	5.8	7.0	6.9
		53	7.1	5.9	7.1	5.8
5.18	1	20	-	-	-	-
		53	-	-	-	-
	3	20	-	-	-	-
		53	-	-	-	-
	5	20	-	-	-	-
		53	-	-	-	-

4.3 Material Removal Rate Data Analysis

Material removal rate (MRR) data for all grinding conditions calculated from Equation 3.7 to 3.9 were illustrated in Table 4.11. Descriptive statistics and distribution of the data were concluded in Table 4.12 and illustrated in histogram as shown in Figure 4.8, respectively. The average value of material removal rate in the spherical grinding system was reported 25.71 ± 14.10 mm^3/s with 95% confidence interval between 22.65 and 28.77 mm^3/s.

Table 4.11   Material removal rate (MRR, mm^3/s) for various grinding conditions

Cross head speed (f)		Abrasive grit size (A)											
		20 µm						53 µm					
		1.0 mm/min		3.0 mm/min		5.0 mm/min		1.0 mm/min		3.0 mm/min		5.0 mm/min	
		R1	R2	R1	R2	R1	R2	R1	R2	R1	R2	R1	R2
Grinding speed (Vs)	1.41 m/s	7.58	8.03	22.78	22.06	38.08	36.39	8.05	8.77	23.94	24.44	42.02	40.86
	2.36 m/s	8.02	8.32	22.52	24.74	41.02	39.31	9.05	8.99	24.95	25.13	45.35	38.42
	2.83 m/s	7.95	8.95	25.42	25.28	44.16	40.59	8.44	8.26	26.23	26.84	46.36	42.96
	3.30 m/s	8.04	8.75	24.85	25.50	42.02	41.69	9.27	8.54	26.33	25.86	44.50	44.90
	3.77 m/s	8.20	8.58	25.57	25.67	41.62	42.83	8.51	9.06	25.91	27.60	45.02	43.14
	4.24 m/s	8.15	8.74	24.50	24.35	44.13	41.07	8.89	9.92	27.79	25.62	43.38	45.96
	5.18 m/s	9.22	9.02	25.93	26.20	47.91	43.82	12.30	10.72	30.33	28.93	47.07	43.56

Table 4.12   Descriptive statistics summary for material removal rate (MRR) for all grinding conditions

	Min.	Mean	Max.	SD	CV	95% C.I.	N
MRR (mm^3/s)	7.58	25.71	47.91	14.10	54.8%	[22.65, 28.77]	84
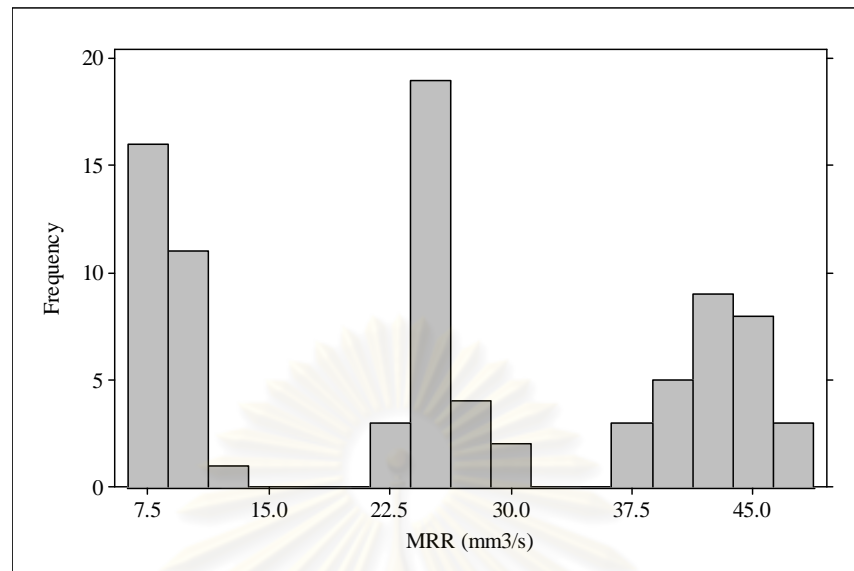
Figure 4.8   Histogram of material removal rate (MRR) for all data

4.4 Specific Grinding Energy Data Analysis

Specific grinding energy (u) data, the product of tangential force (Ft), grinding speed (Vs), and material removal rate (MRR), calculated from Equation 3.17 was shown in Table 4.13 for all grinding conditions and expressed in descriptive statistics in Table 4.14. Moreover, distribution of the data was demonstrated in histogram as shown in Figure 4.9. The specific grinding energy for the spherical grinding system was 29.57 ± 19.73 MJ/m^3 in average with 95% confidence interval between 25.29 and 33.86 MJ/m^3.

Table 4.13   Specific grinding energy (u, MJ/m^3) for various grinding conditions

		Abrasive grit size (A)										
		20 µm						53 µm				
Cross head speed (f)		1.0 mm/min		3.0 mm/min		5.0 mm/min		1.0 mm/min		3.0 mm/min		5.0 mm/min	
		R1	R2	R1	R2	R1	R2	R1	R2	R1	R2	R1	R2
Grinding speed (Vs)	1.41 m/s	59.7	51.7	17.2	22.3	11.7	16.7	32.6	36.1	21.5	20.9	14.8	7.5
	2.36 m/s	51.1	73.7	28.7	28.1	13.7	16.8	39.1	40.5	14.2	17.5	14.6	12.7
	2.83 m/s	43.7	64.3	18.3	22.1	10.5	16.4	39.9	47.2	19.6	20.7	14.6	13.1
	3.30 m/s	47.7	81.2	23.7	25.4	11.5	13.3	37.5	41.7	14.1	18.5	19.0	9.9
	3.77 m/s	49.6	77.6	31.7	22.8	9.9	14.2	45.8	44.5	15.2	14.1	15.5	9.2
	4.24 m/s	45.2	88.0	25.8	30.2	13.9	21.8	52.0	48.8	21.2	19.9	19.0	17.7
	5.18 m/s	61.8	85.8	20.6	28.5	10.1	18.6	43.3	66.5	16.0	18.8	12.3	10.9

Table 4.14   Descriptive statistics summary for specific grinding energy (u) for all grinding conditions

	Min.	Mean	Max.	SD	CV	95% C.I.	N
u (MJ/m^3)	7.50	29.57	88.00	19.73	66.7%	[25.29, 33.86]	84
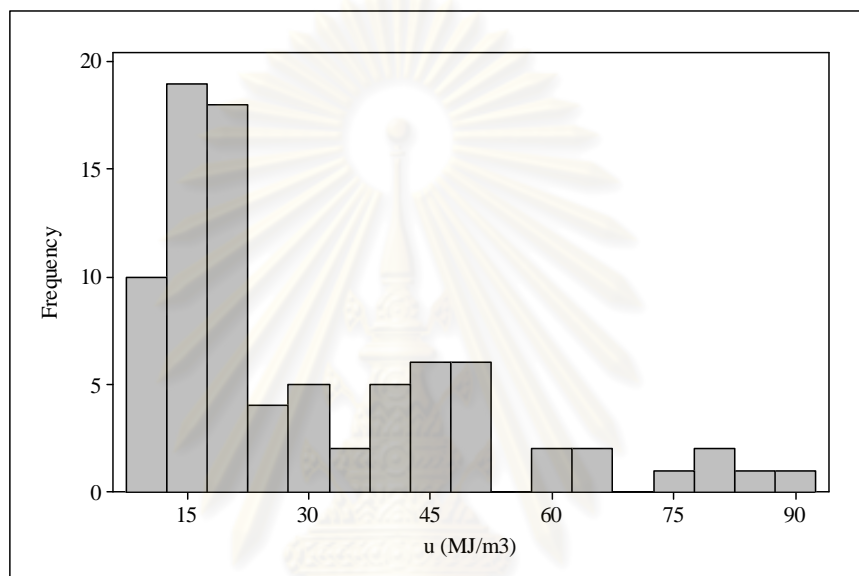
Figure 4.9   Histogram of specific grinding energy (u) for all data

Chapter V

Experimental Results

This chapter illustrated the research results in terms of material characterizations of porous polyurethane foam, experimental results, and statistical analysis from the spherical grinding system. Firstly, physical and mechanical properties of the material were reported. In addition, experimental results as follows, finished shape, circularity error, finished diameter, grinding forces, material removal rate, and specific grinding energy were demonstrated. For further investigation, the effects of grinding factors on grinding responses were performed via analysis of variance. Regression analysis was also conducted to construct effective models for grinding response estimation. Finally, confirmation results were represented.

5.1 Material Characterizations

5.1.1 Pore Size

From Scanning Electron Microscope (SEM) results, pore structures for magnification of 50X and 100X were depicted in Figure 5.1 a) and b), respectively. Pore diameter of porous polyurethane foam specimen was approximated to be 200 - 400 µm.

5.1.2 Bulk Density and Porosity

Results of bulk density and porosity of as received specimens were detailed in Appendix A. Table 5.1 summarized average, standard deviation, and coefficient of variation of bulk density and porosity for 84 specimens.

| a) 50X | b) 100X |
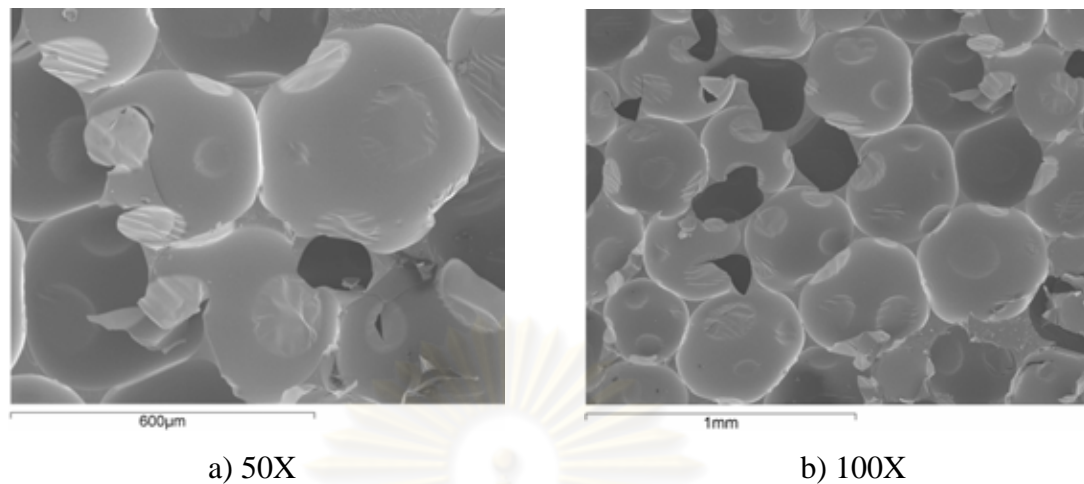
Figure 5.1   Pore structures of polyurethane foam: a) Magnification 50X and

b) Magnification 100X

Table 5.1   Summarized data for bulk density and porosity of porous polyurethane foam

	Bulk density (g/cm^3)	Porosity (%)
Average	0.125	89.6%
Standard deviation	0.014	1.2%
Coefficient of variation	11%	1.3%
Number of specimen	84	84

5.1.3 Mechanical Property Characterizations

Experimental tested results for flexural and compressive strength in Appendix B and Appendix C analyzed by Weibull statistics were concluded in Table 5.2 to represent characteristic strength (Alpha, α) and Weibull modulus (Beta, β) indicating variation of the material strength. Furthermore, linear regression plots between ln(ln(1/1-F(x)))) and ln (Strength) for flexural and compressive strength having R-square of 0.90 and 0.91 respectively were demonstrated in Figure 5.2. From the plots, the slope was the Weibull modulus of the material. Also, failure probability plots for flexural and compressive strength were shown in Figure 5.3.

Table 5.2   Mechanical properties: Flexural and Compressive Strength

Properties	Characteristic strength, α (MPa)	Weibull modulus, β
Flexural strength	2.14	4.52
Compressive strength	1.05	7.88
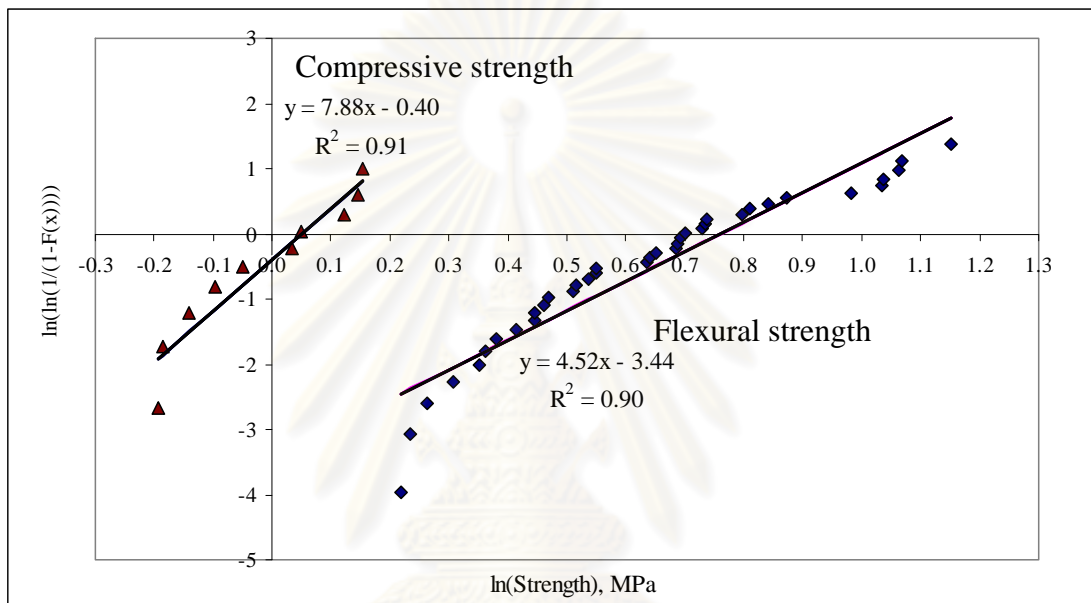
Figure 5.2   Linear regression plots between ln(ln(1/1-F(x)))) and ln (Strength)
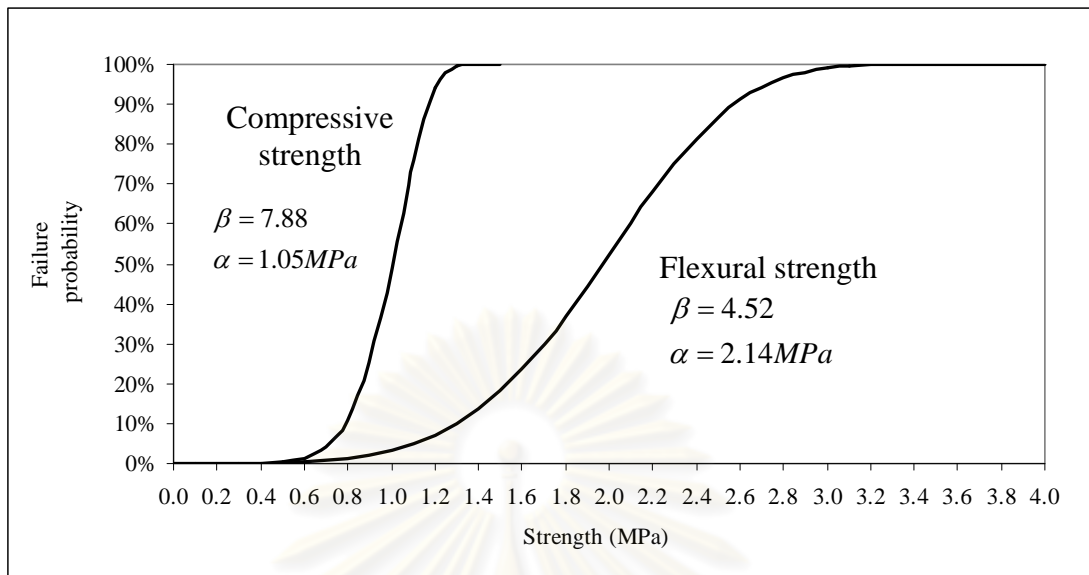
Figure 5.3   Failure probability plot for flexural and compressive strength

5.2 Finished Specimen Characterization Results

5.2.1 Finished Shape and Circularity Error (CE)

After grinding run, finished shapes of the ground specimen were visually inspected and could be categorized into four types: egg, sphere, partial sphere, and squircle as shown in Figure 5.4. Table 5.3 summarized various finished shapes from all grinding conditions and found that egg shapes were formed at the lowest grinding speed of 1.41 m/s. Meanwhile, grinding speeds from 2.83 to 3.77 m/s contributed to sphere shapes for all cross head speeds and abrasive grit sizes. At the highest level grinding speed of 5.18 m/s, partial sphere and squircle shapes were formed. In addition, for grinding speeds of 2.36 and 4.24 m/s, egg, sphere, and partial sphere shapes emerged at some levels of cross head speeds and abrasive grit sizes.

Aside from finished shape consideration, averages and standard deviations of the circularity error from the two replications for all grinding conditions as previously shown in Table 4.1 in Chapter IV were plotted versus grinding speeds with various cross head speeds for abrasive grit sizes of 20 and 53 µm in Figure 5.5 and 5.6. It could be seen from the graphs that large circularity errors greater than 0.8 up to 1.8 mm performed at grinding speeds of 1.41 and 5.18 m/s. Minimal circularity errors approximately 0.50 mm could be achieved for grinding speed run between 2.83 to

3.77 m/s with cross head speed of 1.0 mm/min for both abrasive grit sizes. Faster cross head speeds contributed to high levels of circularity errors. While, the minimum circularity error of 0.47 mm in average was reported at the grinding speed of 3.30 m/s, cross head speed of 1.0 mm/min, and abrasive grit size of 53 µm.

Furthermore, to categorize various shapes by circularity error, dot plot in Figure 5.7 was depicted and found that circularity errors below 0.625 mm contributed to all sphere shapes formed, discriminating sphere shape from the others. Sphere, partial sphere, and squircle shapes could be formed for circularity errors approximately above 0.625 to 0.75 mm. In addition, partial sphere, squircle, and egg shapes could occur with circularity errors above 0.75 to 2.0 mm.

Descriptive statistics in terms of minimum, mean, maximum, standard deviation, coefficient of variation, and confidence interval of circularity error for various shapes were demonstrated in Table 5.4. The ground sphere shape of 54 specimens (64% of all 84 specimens) provided the lowest average circularity error of 0.59 ± 0.07 mm, and also the 95% confidence interval with the range of 0.57 and 0.61 mm.
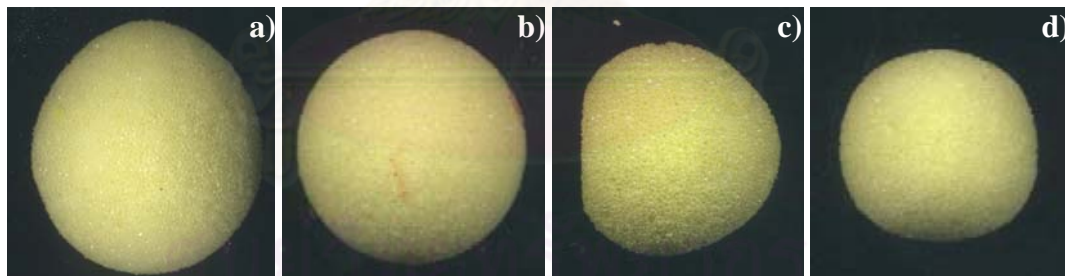
Figure 5.4   Various finished shapes: a) Egg, b) Sphere, c) Partial sphere, and d) Squircle

Table 5.3   Results of finished shapes after grinding

Cross head speed (f)		Abrasive grit size (A)											
		20 µm						53 µm					
		1.0 mm/min		3.0 mm/min		5.0 mm/min		1.0 mm/min		3.0 mm/min		5.0 mm/min	
		R1	R2	R1	R2	R1	R2	R1	R2	R1	R2	R1	R2
Grinding speed (Vs)	1.41 m/s	E	E	E	E	E	E	E	E	E	E	E	E
	2.36 m/s	S	S	S	S	E	E	S	S	S	S	E	E
	2.83 m/s	S	S	S	S	S	S	S	S	S	S	S	S
	3.30 m/s	S	S	S	S	S	S	S	S	S	S	S	S
	3.77 m/s	S	S	S	S	S	S	S	S	S	S	S	S
	4.24 m/s	S	S	S	S	S	S	P	P	S	S	S	S
	5.18 m/s	P	P	SQ	P	P	P	SQ	SQ	P	P	P	P

Remark: R1, R2 =   Experimental replication 1, 2

E   =   Egg   S   =   Sphere

P   =   Partial sphere   SQ   =   Squircle
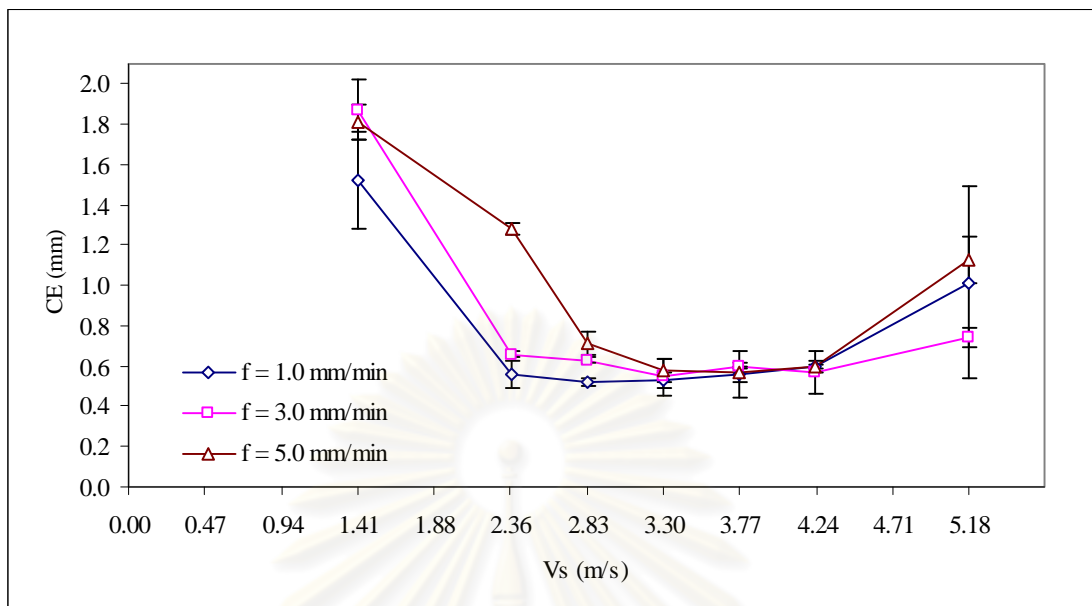
Figure 5.5   Relationship between circularity error (CE) and grinding speed (Vs)
with various cross head speeds (f) for abrasive size (A) of 20 µm
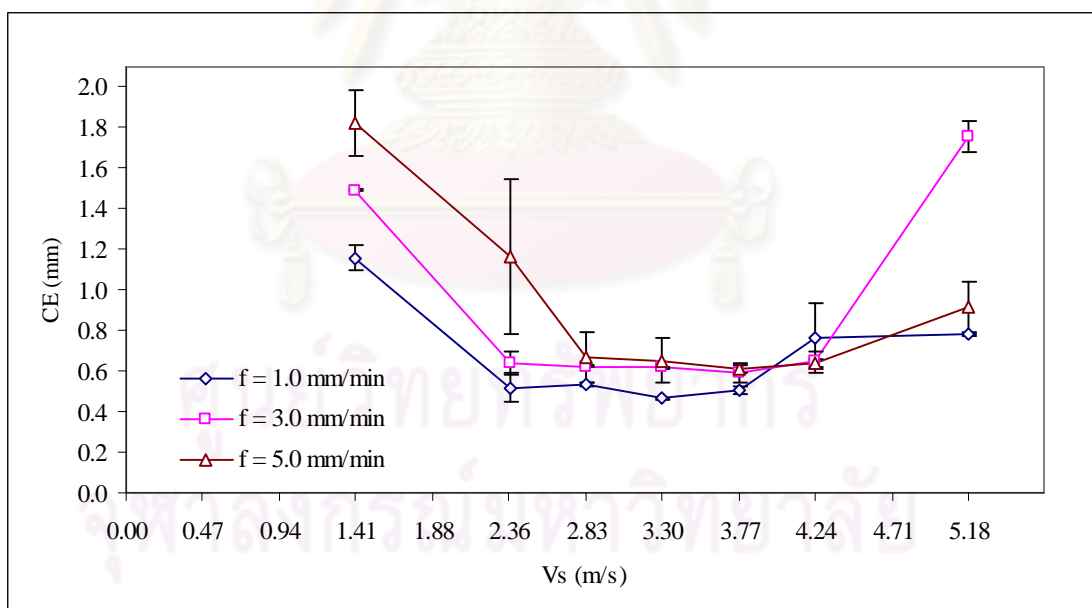
Figure 5.6   Relationship between circularity error (CE) and grinding speed (Vs)
with various cross head speeds (f) for abrasive size (A) of 53 µm
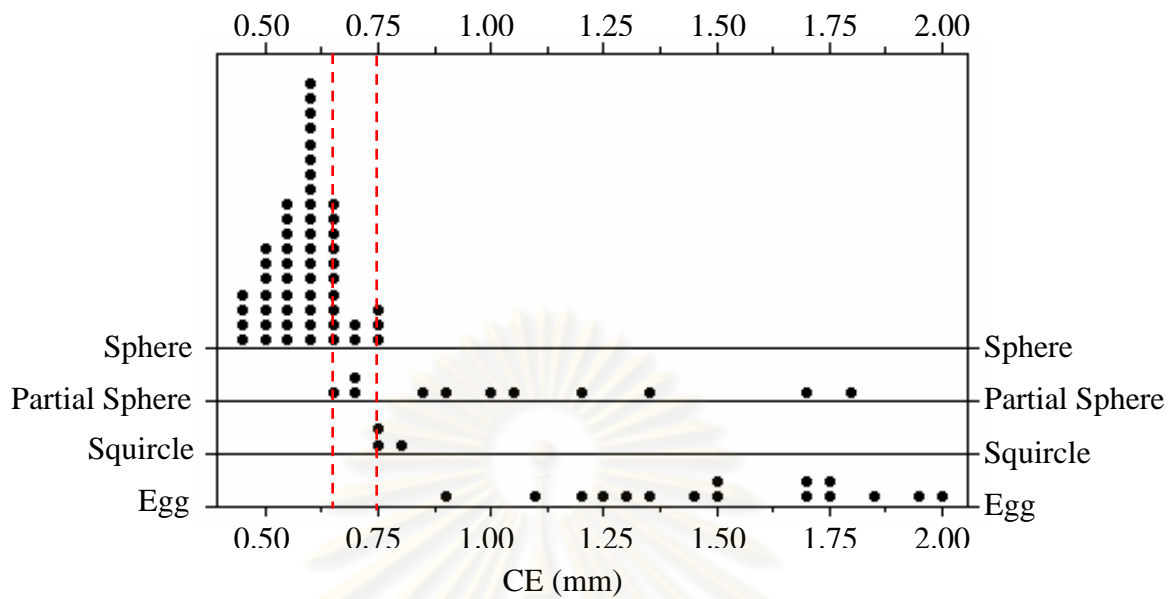
Figure 5.7   Dot plot of circularity error for various shapes

Table 5.4   Descriptive statistics summary for circularity error (mm) for
various shapes

Shape	Min.	Mean	Max.	SD	CV	95% C.I.	N (%)
Egg	0.89	1.51	1.98	0.32	20.8%	[1.35, 1.68]	16 (19%)
Sphere	0.46	0.59	0.76	0.07	12.0%	[0.57, 0.61]	54 (64%)
Partial sphere	0.64	1.08	1.81	0.40	37.2%	[0.81, 1.35]	11 (13%)
Squircle	0.77	0.78	0.78	0.01	0.9%	[0.76, 0.79]	3 (4%)
							84 (100%)

Remark	Min. and Max.	=	Minimum and Maximum value
	SD	=	Standard deviation
	CV	=	Coefficient of variation
	C.I.	=	Confidence interval
	N	=	Number of specimen

5.2.2 Finished Diameter (D)

Averages and standard deviations of the finished diameter from the two replications for all grinding conditions shown in Table 4.2 in Chapter IV were graphically illustrated versus grinding speeds with various cross head speeds for abrasive grit sizes of 20 and 53 µm in Figure 5.8 and 5.9. From the graphs, finished diameters decreased from around 20 to 16 mm as increasing grinding speed from 1.41 to 5.18 m/s. Rapid changes in finished diameter for grinding speed ranges of 1.41 to 2.83 m/s and 4.24 to 5.18 m/s were demonstrated. High variation of finished diameters performed at the lowest and highest grinding speeds of 1.41 and 5.18 m/s, respectively. On the other hand, a gradual decrease in finished diameter from around 19.40 to 19.20 mm occurred when grinding speeds were between 2.83 and 4.24 m/s for both abrasive grit sizes. Grinding with faster cross head speeds did not show any obvious indications on finished diameters, while increasing abrasive grit size seemed to give smaller sizes of finished specimens.

Furthermore, dot plot in Figure 5.10 indicated that the finished diameter of sphere shape had a small range than those of egg, partial sphere, and squircle shape. Descriptive statistics in terms of minimum, mean, maximum, standard deviation, coefficient of variation, and confidence interval of finished diameter for various shapes were illustrated in Table 5.5. It was found that the finished diameter of sphere shape specimens was in average of 19.30 ± 0.09 mm, and the 95% confidence interval with the range of 19.28 and 19.32 mm.
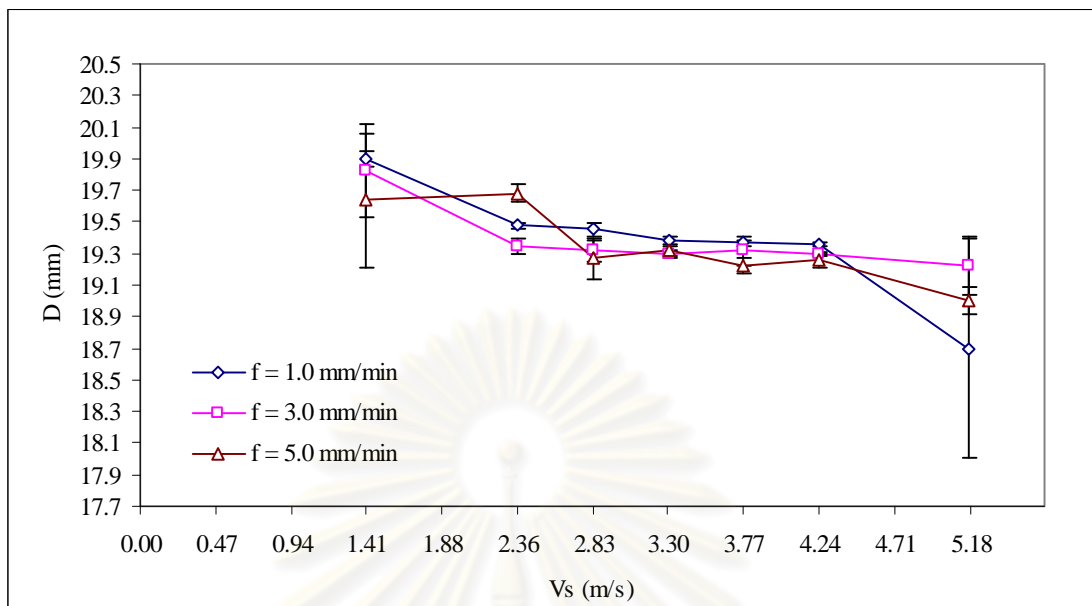
Figure 5.8   Relationship between finished diameter (D) and grinding speed (Vs)
with various cross head speeds (f) for abrasive size (A) of 20 µm
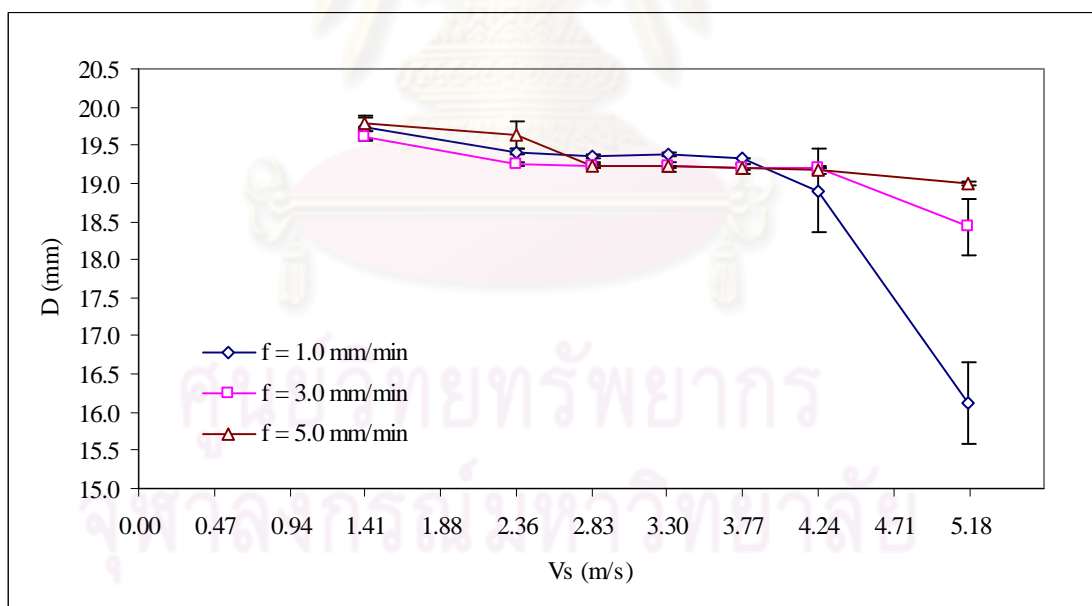
Figure 5.9   Relationship between finish size diameter (D) and grinding speed (Vs)
with various cross head speeds (f) for abrasive size (A) of 53 µm
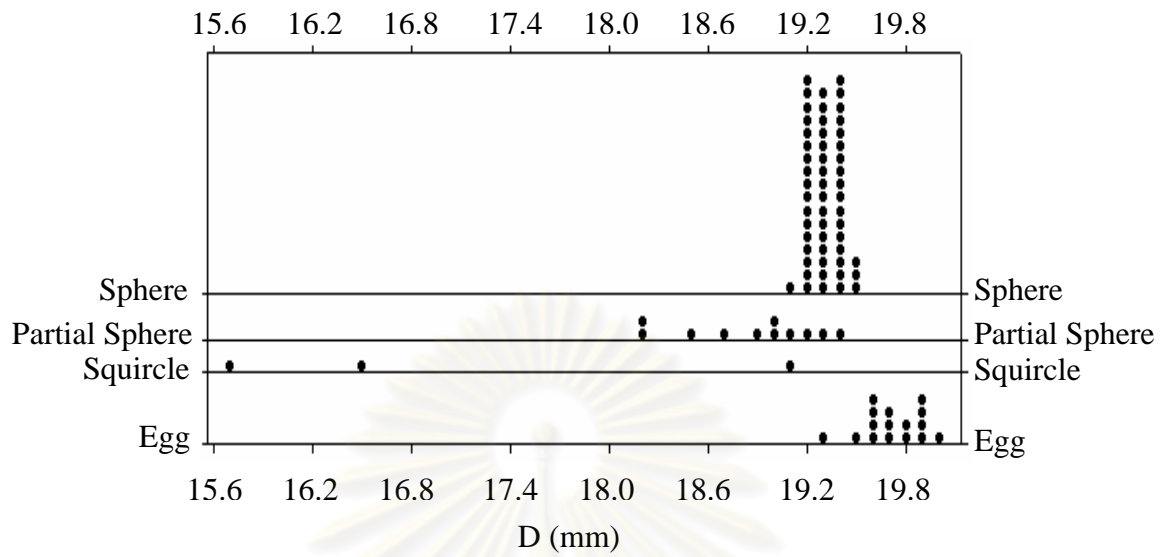
Figure 5.10   Dot plot of finished diameter for various shapes

Table 5.5   Descriptive statistics summary for finished diameter (mm) for
various shapes

Shape	Min.	Mean	Max.	SD	CV	95% C.I.	N (%)
Egg	19.34	19.73	20.03	0.18	0.9%	[19.63, 19.82]	16 (19%)
Sphere	19.13	19.30	19.49	0.09	0.5%	[19.28, 19.32]	54 (64%)
Partial sphere	18.17	18.86	19.36	0.41	2.2%	[18.58, 19.20]	11 (13%)
Squircle	15.74	17.11	19.09	1.76	10.3%	[12.74, 21.47]	3 (4%)
							84 (100%)

Remark	Min. and Max.	=	Minimum and Maximum value
	SD	=	Standard deviation
	CV	=	Coefficient of variation
	C.I.	=	Confidence interval
	N	=	Number of specimen

5.3 Grinding Force Results

5.3.1 Tangential Force (Ft)

Tangential force data in Table 4.4 from Chapter IV for all grinding conditions were averaged and plotted against grinding speeds with various cross head speeds for two abrasive grit sizes of 20 and 53 µm in Figure 5.11 and 5.12. From the graphs, tangential forces were ranged between 0.10 and 0.37 N and slightly decreased as increasing grinding speed from 1.41 to 5.18 m/s. In addition, grinding with a low cross head speed tended to give low tangential forces for all grinding conditions.

5.3.2 Normal Force (Fn)

Normal force data in Table 4.5 from Chapter IV for all grinding conditions were depicted for average and standard deviation versus various grinding speeds and cross head speeds for abrasive grit sizes of 20 and 53 µm as shown in Figure 5.13 and 5.14. It was found that the normal force performed downward trends (around 0.40 to 0.07 N) as the same pattern as tangential force when increasing grinding speed from 1.41 to 5.18 m/s. In contrary, increasing cross head speed seemingly contributed to higher normal forces.

5.3.3 Grinding Force Ratio (R)

Grinding force ratio results for all grinding conditions from Table 4.6 in Chapter IV were drawn in terms of average and standard deviation in Figure 5.15 and 5.16. As found from the graphs, grinding force ratios were quite stable around 1.0 when grinding speeds ranged from 1.41 to 3.30 m/s and then substantially increased to reach approximately 1.6 in average at grinding speed of 5.18 m/s for all cross head speeds and abrasive grit sizes.
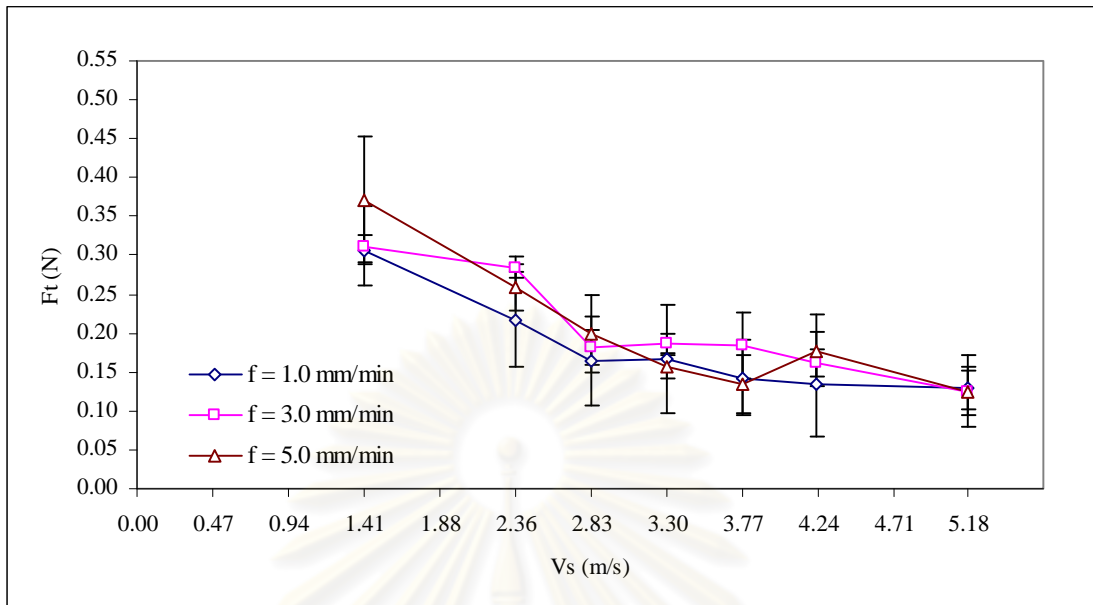
Figure 5.11   Relationship between tangential force (Ft) and grinding speed (Vs)
with various cross head speeds (f) for abrasive size (A) of 20 µm
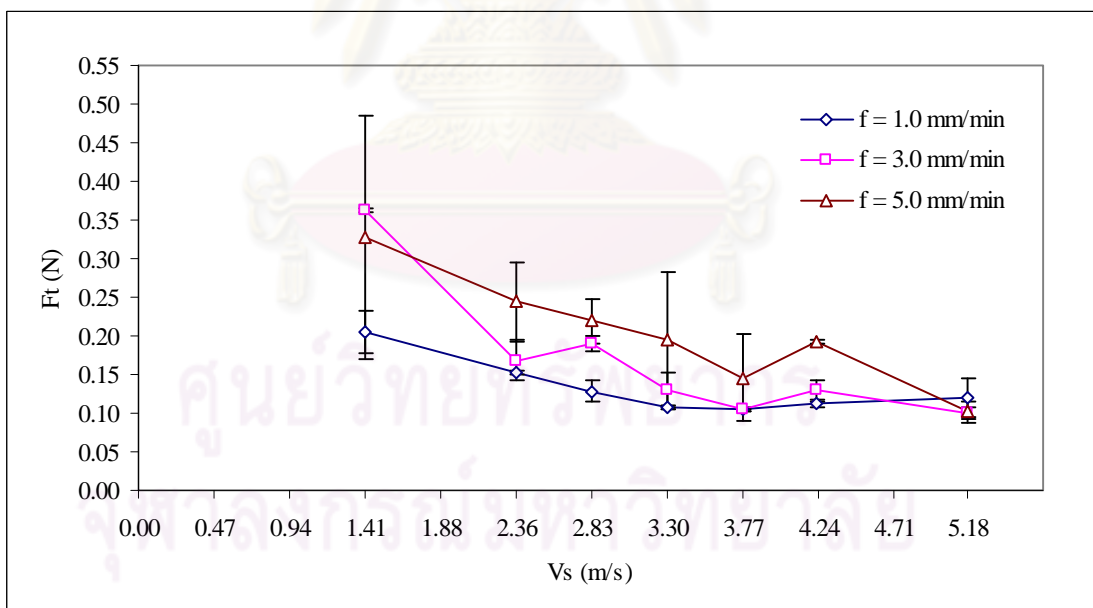
Figure 5.12   Relationship between tangential force (Ft) and grinding speed (Vs)
with various cross head speeds (f) for abrasive size (A) of 53 µm
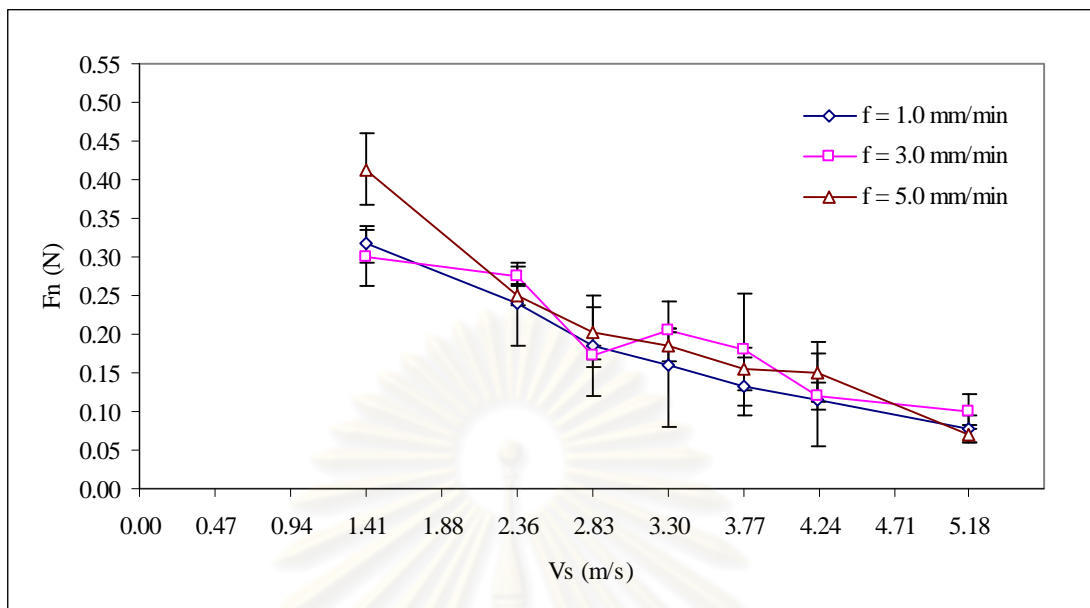
Figure 5.13   Relationship between normal force (Fn) and grinding speed (Vs)
with various cross head speeds (f) for abrasive size (A) of 20 µm
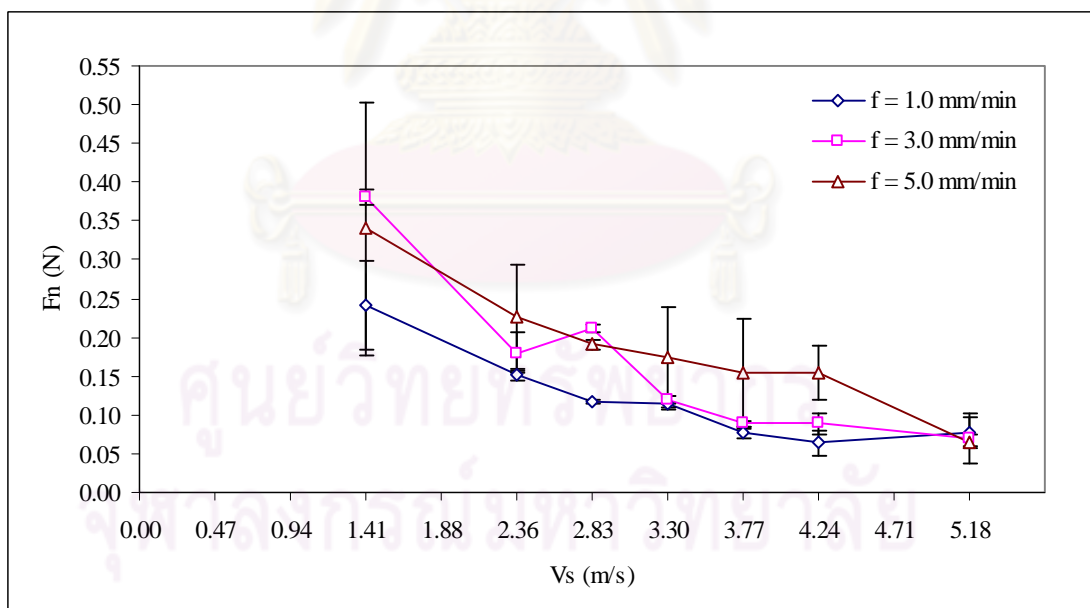
Figure 5.14   Relationship between normal force (Fn) and grinding speed (Vs)
with various cross head speeds (f) for abrasive size (A) of 53 µm
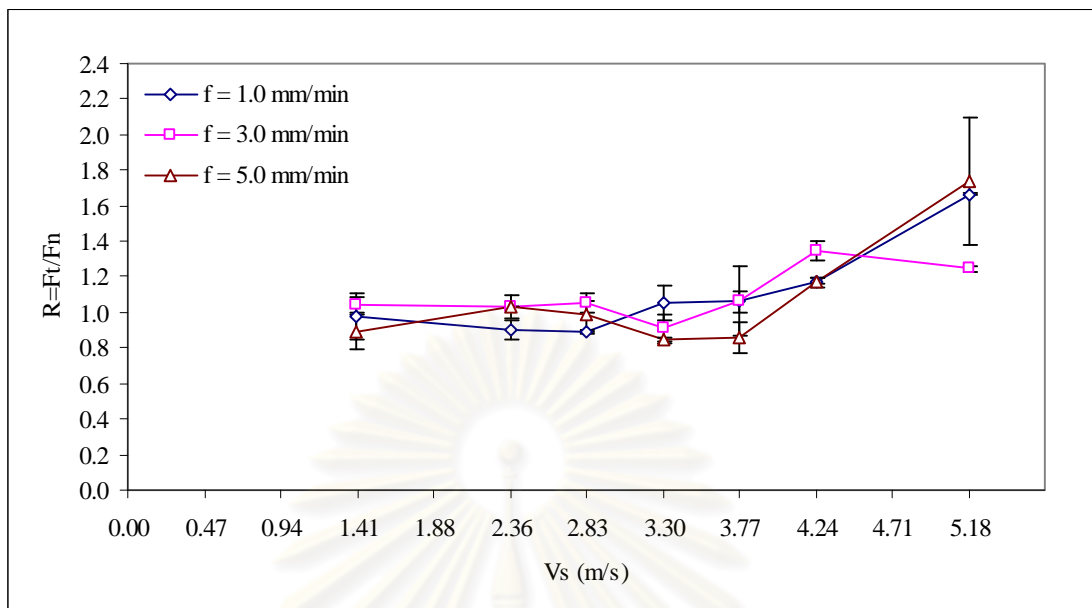
Figure 5.15   Relationship between grinding force ratio (Ft/Fn) and grinding speed
(Vs) with various cross head speeds (f) for abrasive size (A) of 20 µm
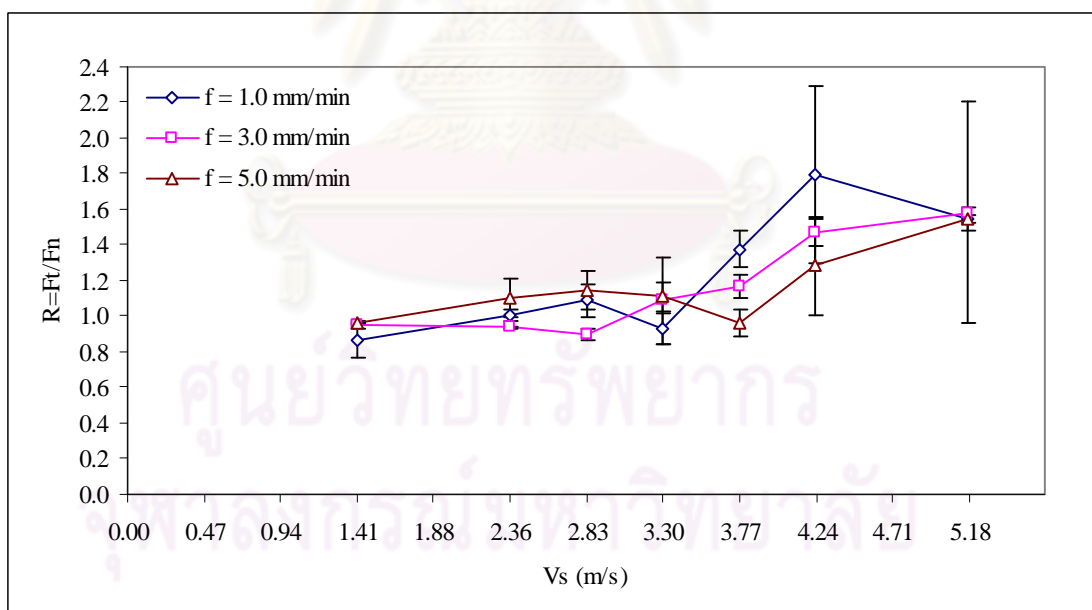
Figure 5.16   Relationship between grinding force ratio (Ft/Fn) and grinding speed
(Vs) with various cross head speeds (f) for abrasive size (A) of 53 µm

5.4 Material Removal Rate (MRR) Results

Averages and standard deviations of material removal rates from experimental data from Table 4.7 in Chapter IV were graphically drawn versus grinding speeds with various cross head speeds for abrasive grit sizes of 20 and 53 µm in Figure 5.17 and 5.18. It was obvious that the material removal rate directly depended on cross head speed and seemed to perform a small upward trend when increasing grinding speed. Moreover, there was a bit increased removal rate for a greater abrasive grit size. The ranges of removal rate for cross head speeds of 1.0, 3.0, and 5.0 mm/min were about 7, 25, 43, respectively.
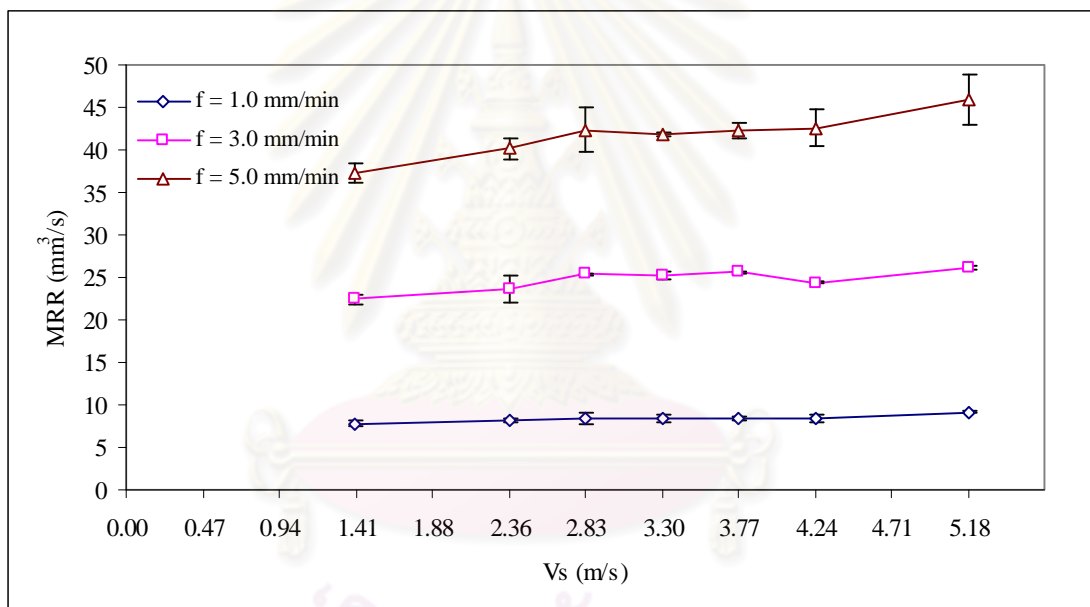
Figure 5.17   Relationship between material removal rate (MRR) and grinding speed (Vs) with various cross head speeds (f) for abrasive size (A) of 20 µm
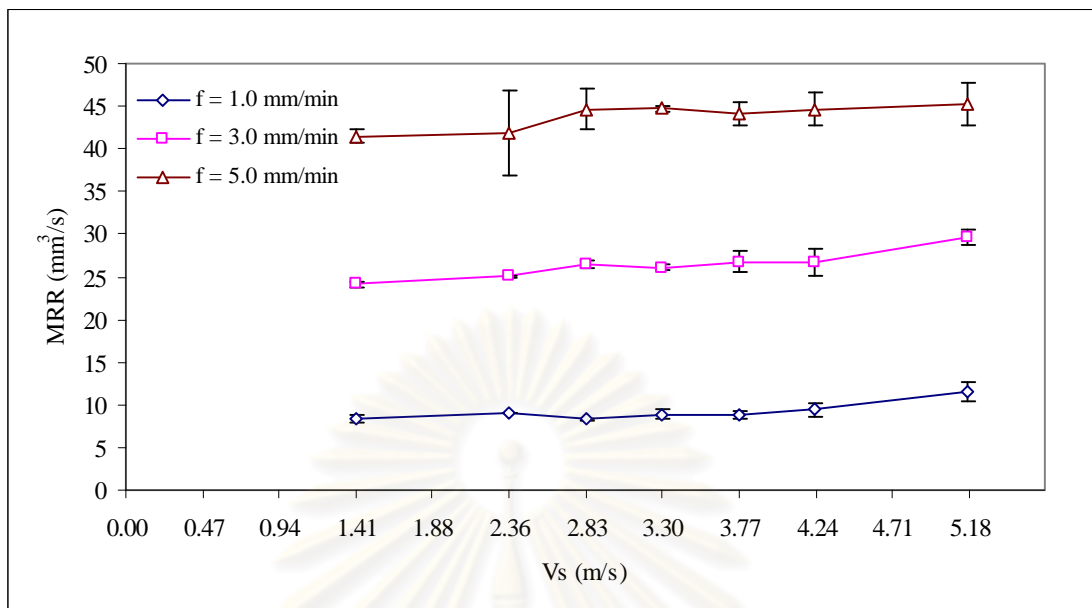
Figure 5.18   Relationship between material removal rate (MRR) and grinding speed
(Vs) with various cross head speeds (f) for abrasive size (A) of 53 µm

5.5 Specific Grinding Energy (u) Results

Specific grinding energy data from Table 4.8 in Chapter IV were graphically demonstrated for averages and standard deviations versus grinding speed with various cross head speeds for abrasive grit sizes of 20 and 53 µm in Figure 5.19 and 5.20. From the plots, the specific grinding energy markedly decreased from about 70 to 13 MJ/m^3 for abrasive grit size of 20 µm and about 60 to 13 MJ/m^3 for abrasive grit size of 53 µm when increasing cross head speed from 1.0 to 5.0 mm/min. Increasing grinding speed from 1.41 to 5.18 m/s for cross head speed of 1.0 mm/min from both abrasive grit sizes resulted in slightly upward trends but likely stable for faster cross head speeds of 3.0 and 5.0 mm/min.
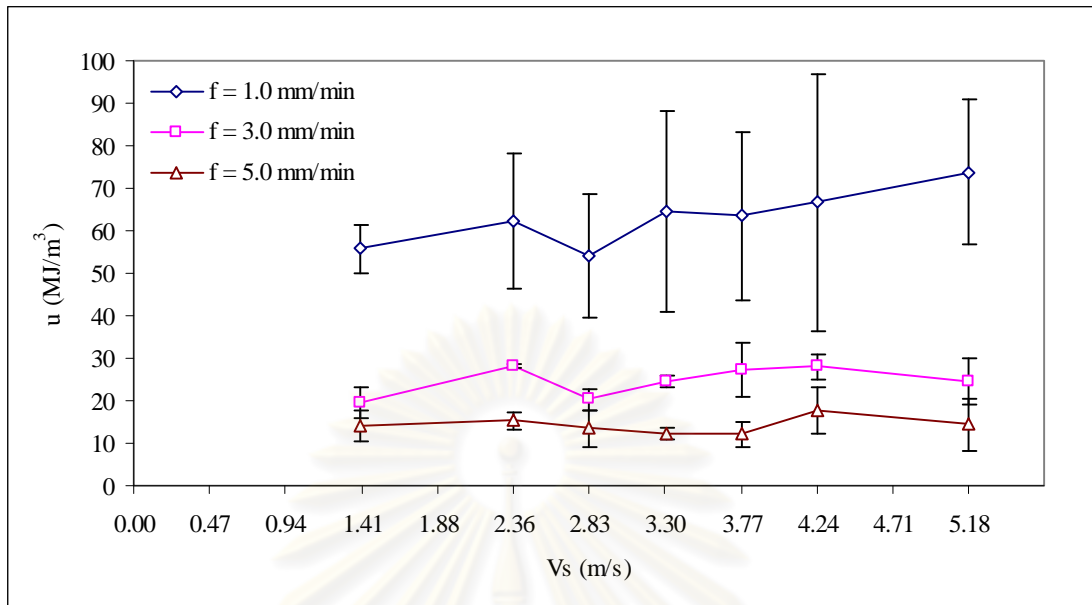
Figure 5.19   Relationship between specific grinding energy (u) and grinding speed
(Vs) with various cross head speeds (f) for abrasive size (A) of 20 µm
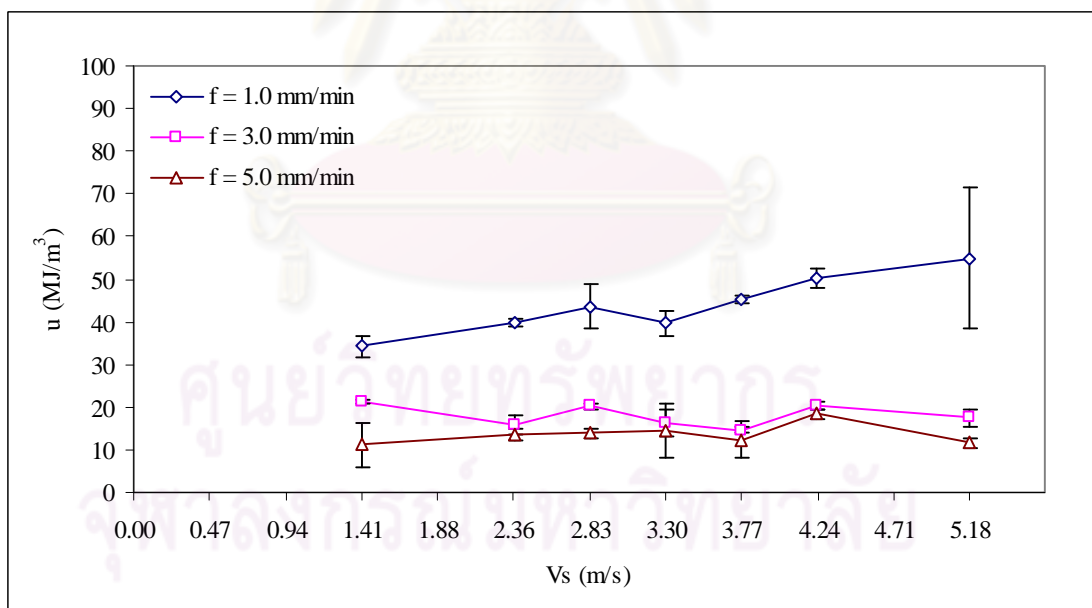
Figure 5.20   Relationship between specific grinding energy (u) and grinding speed
(Vs) with various cross head speeds (f) for abrasive size (A) of 53 µm

5.6 Statistical Analysis Results

5.6.1 Effects of Grinding Factors on Grinding Responses

In this section, analysis of variance (ANOVA) results were illustrated in order to examine influential spherical grinding factors on responses via general full factorial design as planned in Chapter III. Experimental data in Chapter IV were used in the analysis.

5.6.1.1 Effects of Grinding Factors on Circularity Error (CE)

From analysis of variance (ANOVA) in Table 5.6, grinding speed (Vs), cross head speed (f), their interaction (Vs*f), interaction between grinding speed and abrasive grit size (Vs*A), interaction between cross head speed and abrasive grit size (f*A), and interaction among the three factors (Vs*f*A) were significant with P-value less than 0.05. Grinding speed (Vs) was indicated to be the most significant factor affecting circularity error with 75.7% contribution followed by interaction between grinding speed and cross head speed (Vs*f) with 8.5% contribution. In addition, main effects and interaction plots were shown in Figure 5.21 and 5.22.

Table 5.6 ANOVA for circularity error (CE)

Source	DF	SS	MS	F Ratio	P-value	% Contribution	Remark
Vs	6	10.635	10.635	116.12	<.0001	75.7%	Significant
f	2	0.715	0.715	23.41	<.0001	5.1%	Significant
A	1	0.000	0.000	0.00	1.0000	0.0%	
Vs*f	12	1.192	1.192	6.51	<.0001	8.5%	Significant
Vs*A	6	0.336	0.336	3.67	0.0051	2.4%	Significant
f*A	2	0.137	0.137	4.48	0.0172	1.0%	Significant
Vs*f*A	12	1.027	1.027	5.61	<.0001	7.3%	Significant
Error	42	0.641	0.015			0.1%	
Total	83	14.682					
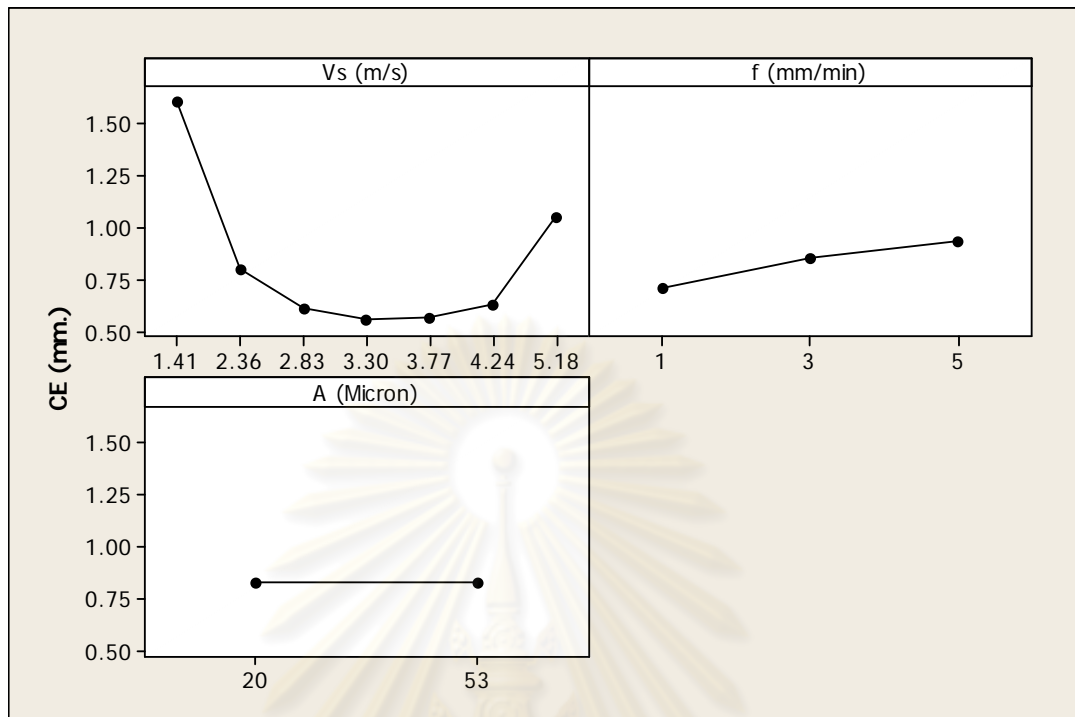
Figure 5.21   Main effect plots for circularity error (CE)
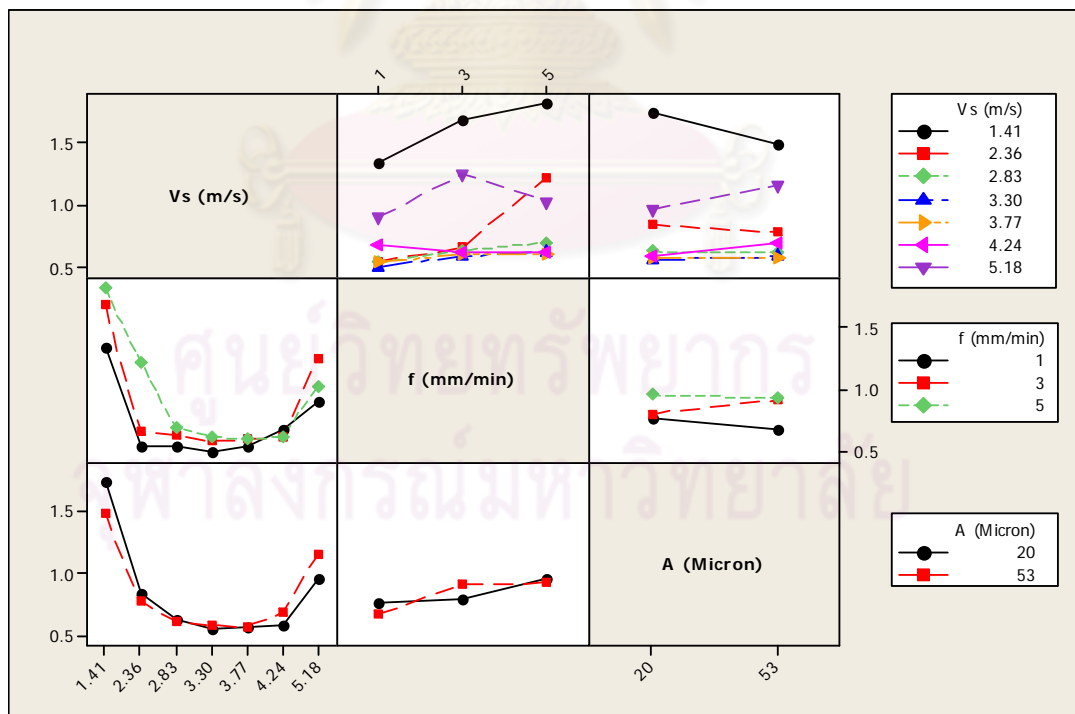
Figure 5.22   Interaction plots for circularity error (CE)

5.6.1.2 Effects of Grinding Factors on Finished Diameter (D)

Analysis of variance (ANOVA) in Table 5.7 indicated that grinding speed (Vs), cross head speed (f) and abrasive grit size (A) along with their interactions (Vs*f, Vs*A, f*A, and Vs*f*A) were significant factors affecting finished diameter for P-value less than 0.05. Moreover, grinding speed (Vs) was the most influential factor with 39.6% contribution followed by abrasive grit size (A) with 23.2% contribution. To graphically illustrate the effects of grinding factors on finished diameter, main effects and interaction plots were shown in Figure 5.23 and 5.24.

Table 5.7   ANOVA for finished diameter (D)

Source	DF	SS	MS	F Ratio	P-value	% Contribution	Remark
Vs	6	12.136	2.023	51.79	<.0001	39.6%	Significant
f	2	0.553	0.277	7.08	0.0022	5.4%	Significant
A	1	1.188	1.188	30.42	<.0001	23.2%	Significant
Vs*f	12	5.992	0.499	12.79	<.0001	9.8%	Significant
Vs*A	6	2.840	0.473	12.12	<.0001	9.3%	Significant
f*A	2	0.738	0.369	9.45	0.0004	7.2%	Significant
Vs*f*A	12	2.916	0.243	6.22	<.0001	4.8%	Significant
Error	42	1.640	0.039			0.8%	
Total	83	28.004					
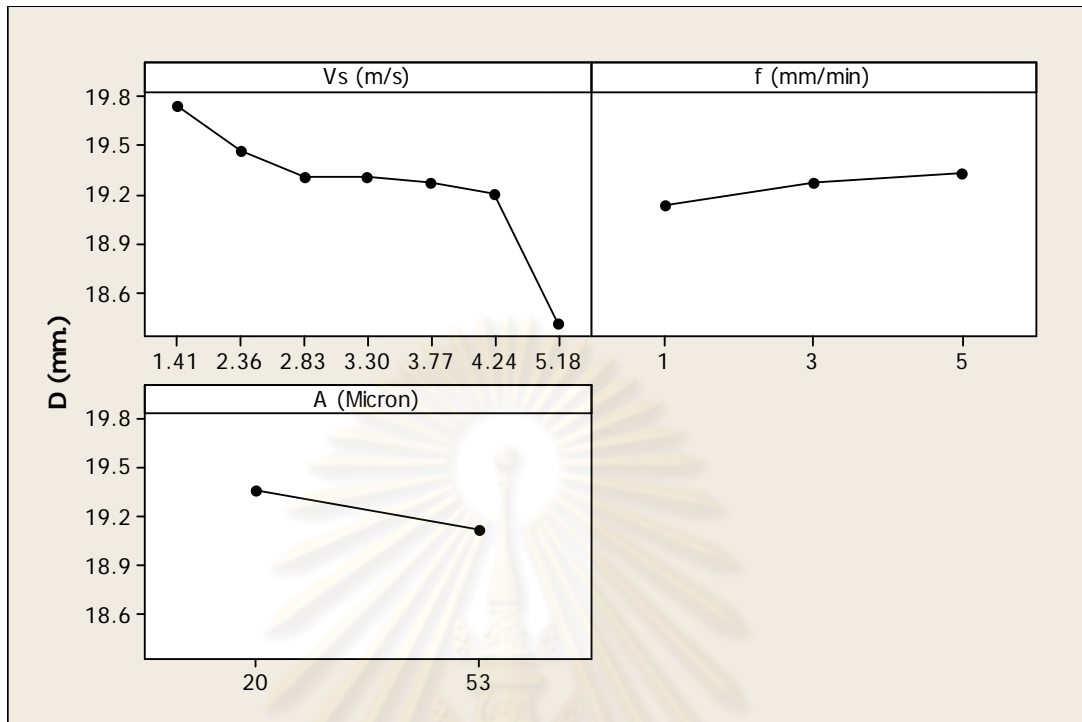
Figure 5.23   Main effect plots for finished diameter (D)
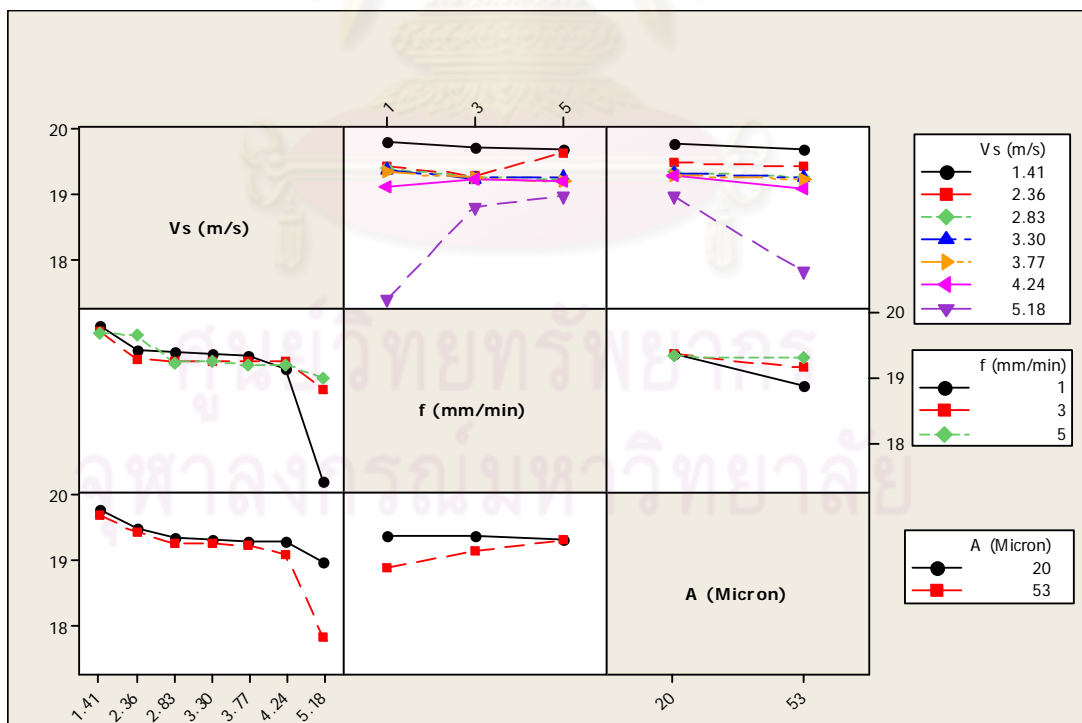
Figure 5.24   Interaction plots for finished diameter (D)

5.6.1.3 Effects of Grinding Factors on Tangential Force (Ft)

Analysis of variance (ANOVA) in Table 5.8 showed that main effects of grinding speed (Vs), cross head speed (f), and abrasive grit size (A) significantly influenced tangential force with P-value less than 0.05. On the other hand, their interactions did not perform significant effects at all. In addition, grinding speed (Vs) was the most significant factor with 55.3% contribution, followed by abrasive grit size (A) and cross head speed (f) with percent contributions of 16.7% and 16.6%, respectively. Main effects and interaction plots were shown in Figure 5.25 and 5.26.

Table 5.8   ANOVA for tangential force (Ft)

Source	DF	SS	MS	F Ratio	P-value	% Contribution	Remark
Vs	6	0.323	0.054	26.05	<.0001	55.3%	Significant
f	2	0.032	0.016	7.81	0.0013	16.6%	Significant
A	1	0.016	0.016	7.88	0.0075	16.7%	Significant
Vs*f	12	0.019	0.002	0.78	0.6687	1.7%	
Vs*A	6	0.007	0.001	0.59	0.7379	1.2%	
f*A	2	0.009	0.004	2.16	0.1283	4.6%	
Vs*f*A	12	0.021	0.002	0.83	0.6230	1.8%	
Error	42	0.087	0.002			2.1%	
Total	83	0.515					
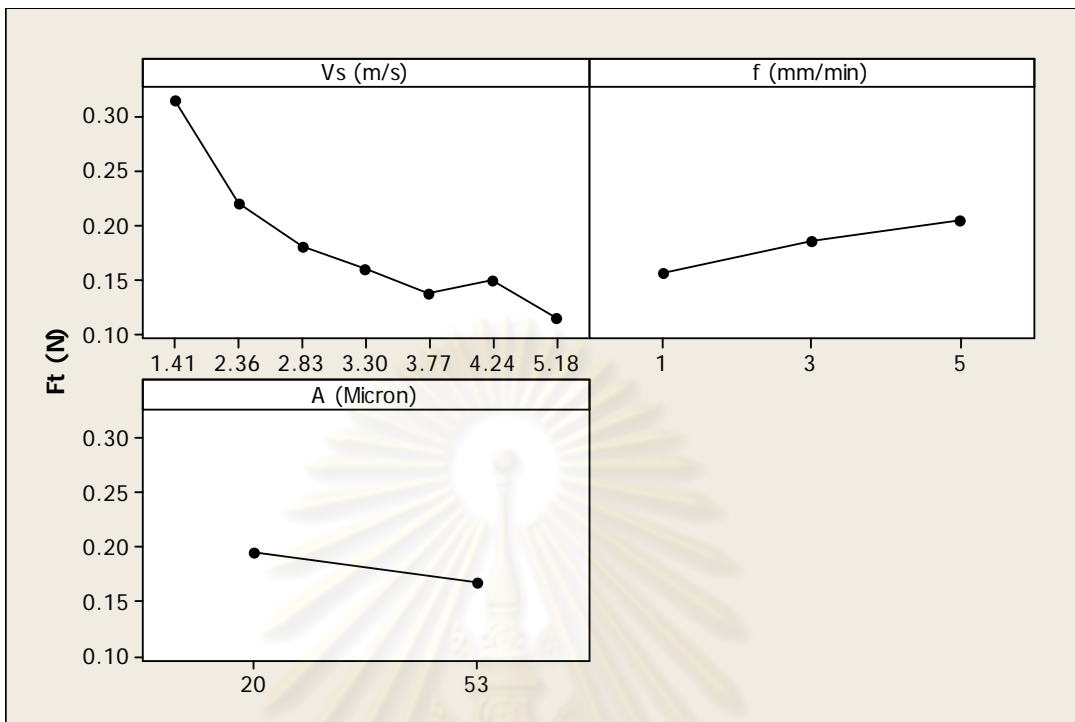
Figure 5.25　Main effect plots for tangential force (Ft)
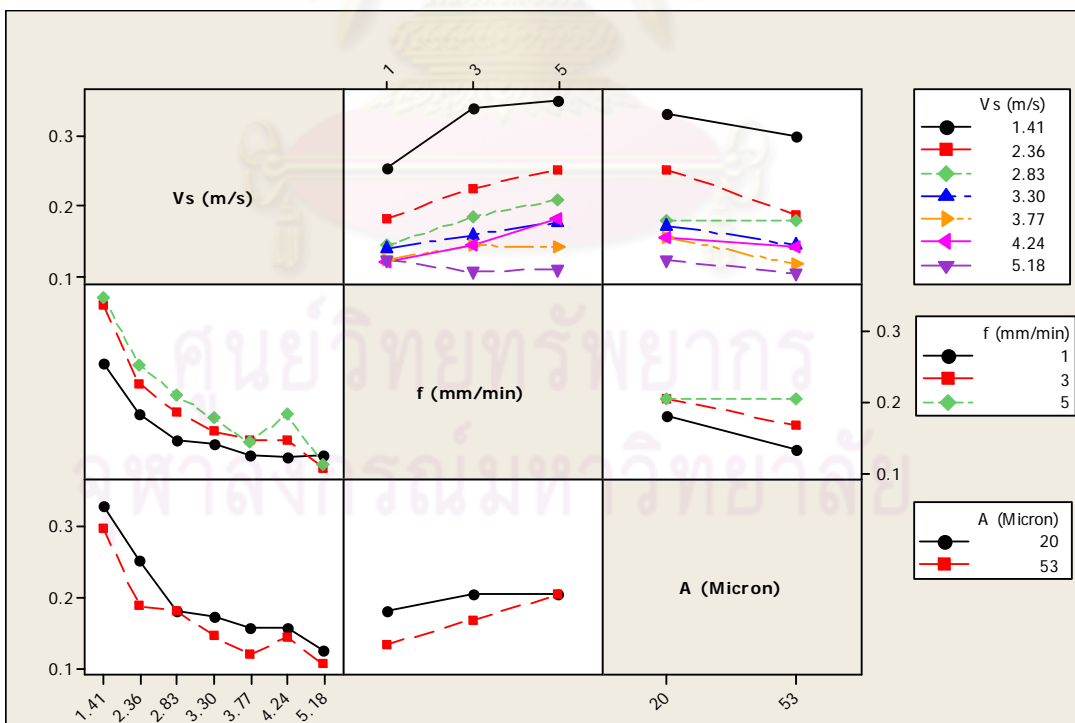
Figure 5.26　Interaction plots for tangential force (Ft)

5.6.1.4 Effects of Grinding Factors on Normal Force (Fn)

Table 5.9 illustrated analysis of variance (ANOVA) for normal force. It was shown that normal force was influenced by grinding speed (Vs), cross head speed (f), and abrasive grit size (A) with P-value less than 0.05. In contrary, interactions had no significant effects. Moreover, grinding speed (Vs) was the most influential factor with 62.6% contribution. While, percent contributions of abrasive grit size (A) and cross head speed (f) were 18.2% and 12.0%, respectively. Main effects and interaction plots in Figure 5.27 and 5.28 performed as the same pattern as tangential force.

Table 5.9   ANOVA for normal force (Fn)

Source	DF	SS	MS	F Ratio	P-value	% Contribution	Remark
Vs	6	0.502	0.084	41.72	<.0001	62.6%	Significant
f	2	0.032	0.016	8.00	0.0011	12.0%	Significant
A	1	0.024	0.024	12.14	0.0012	18.2%	Significant
Vs*f	12	0.014	0.001	0.60	0.8324	0.9%	
Vs*A	6	0.009	0.001	0.73	0.6252	1.1%	
f*A	2	0.005	0.002	1.24	0.3008	1.9%	
Vs*f*A	12	0.028	0.002	1.18	0.3285	1.8%	
Error	42	0.084	0.002			1.5%	
Total	83	0.699					
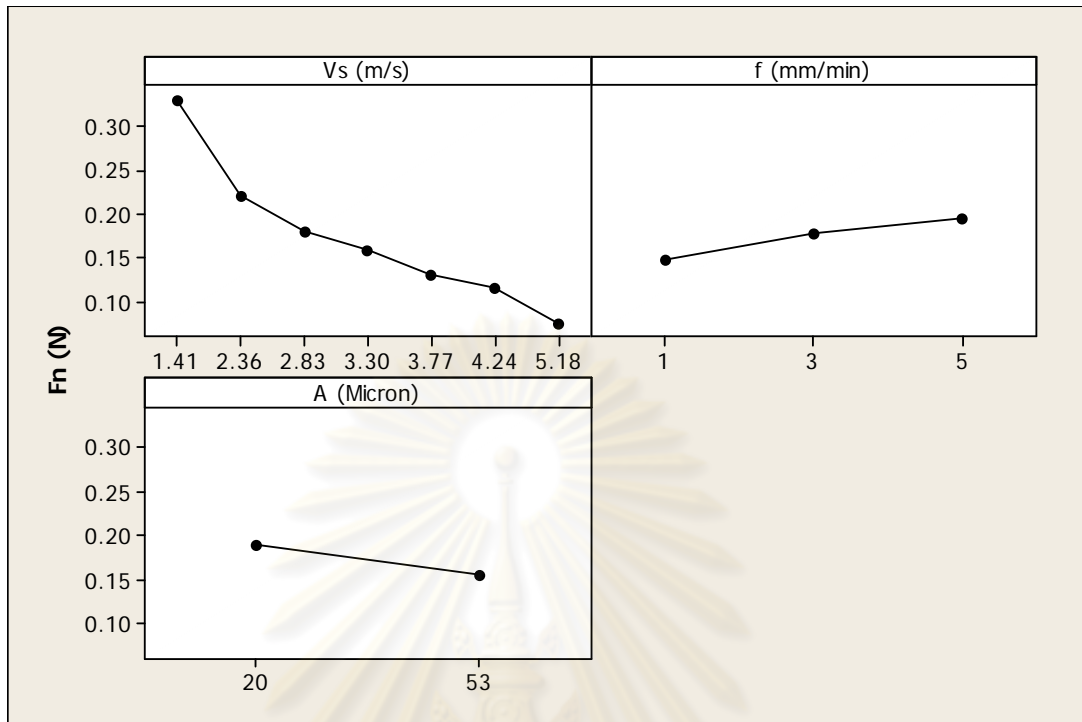
Figure 5.27   Main effect plots for normal force (Fn)
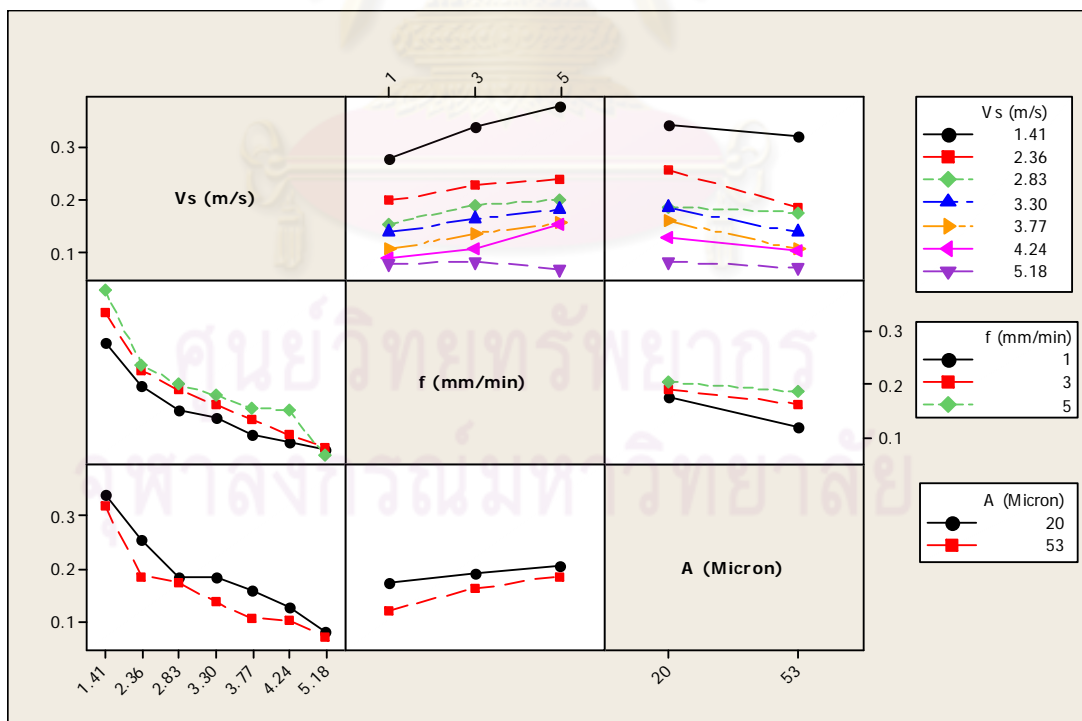
Figure 5.28   Interaction plots for normal force (Fn)

5.6.1.5 Effects of Grinding Factors on Grinding Force Ratio (R)

Analysis of variance (ANOVA) in Table 5.10 demonstrated that grinding speed (Vs) and abrasive grit size (A) were statistically significant according to P-value less than 0.05 with percent contributions of 65.4% and 16.9%, respectively. For the other factors, there was no evidence to indicate significant impacts on grinding force ratio. In addition, data mean plots of main effects and interactions were demonstrated in Figure 5.29 and 5.30.

Table 5.10   ANOVA for grinding force ratio (R)

Source	DF	SS	MS	F Ratio	P-value	% Contribution	Remark
Vs	6	3.890	0.648	24.87	<.0001	65.4%	Significant
f	2	0.035	0.017	0.67	0.5172	1.8%	
A	1	0.167	0.167	6.42	0.0151	16.9%	Significant
Vs*f	12	0.482	0.040	1.54	0.1482	4.0%	
Vs*A	6	0.222	0.037	1.42	0.2311	3.7%	
f*A	2	0.018	0.009	0.34	0.7143	0.9%	
Vs*f*A	12	0.558	0.046	1.78	0.0830	4.7%	
Error	42	1.095	0.026			2.6%	
Total	83	6.467					
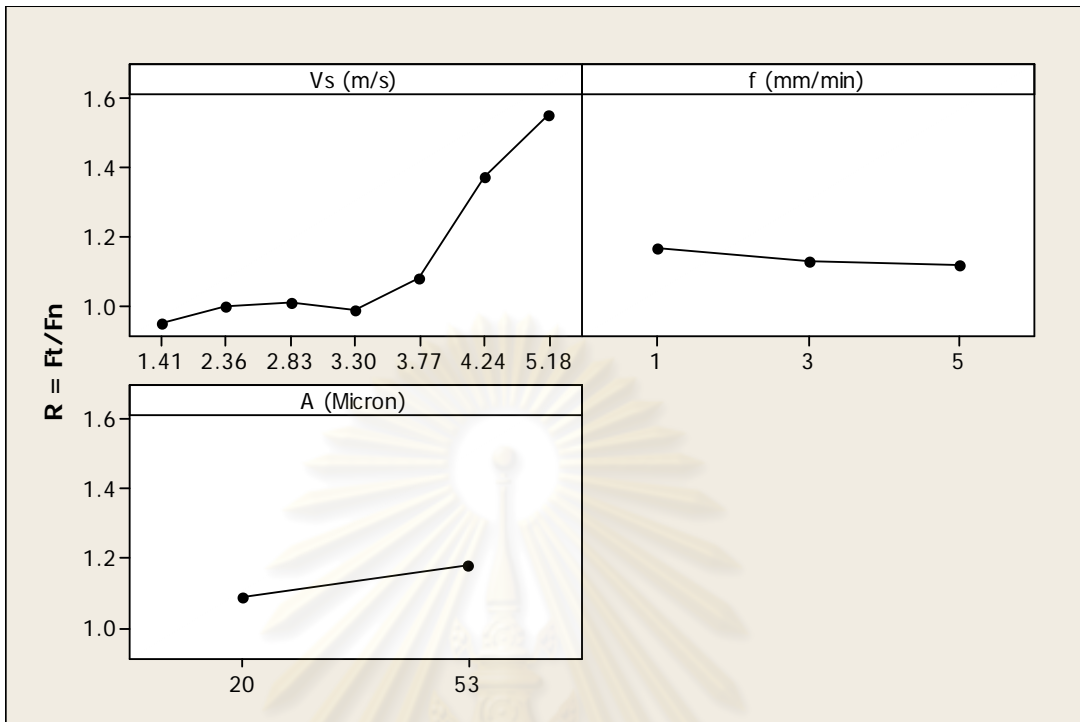
Figure 5.29   Main effect plots for grinding force ratio (R)
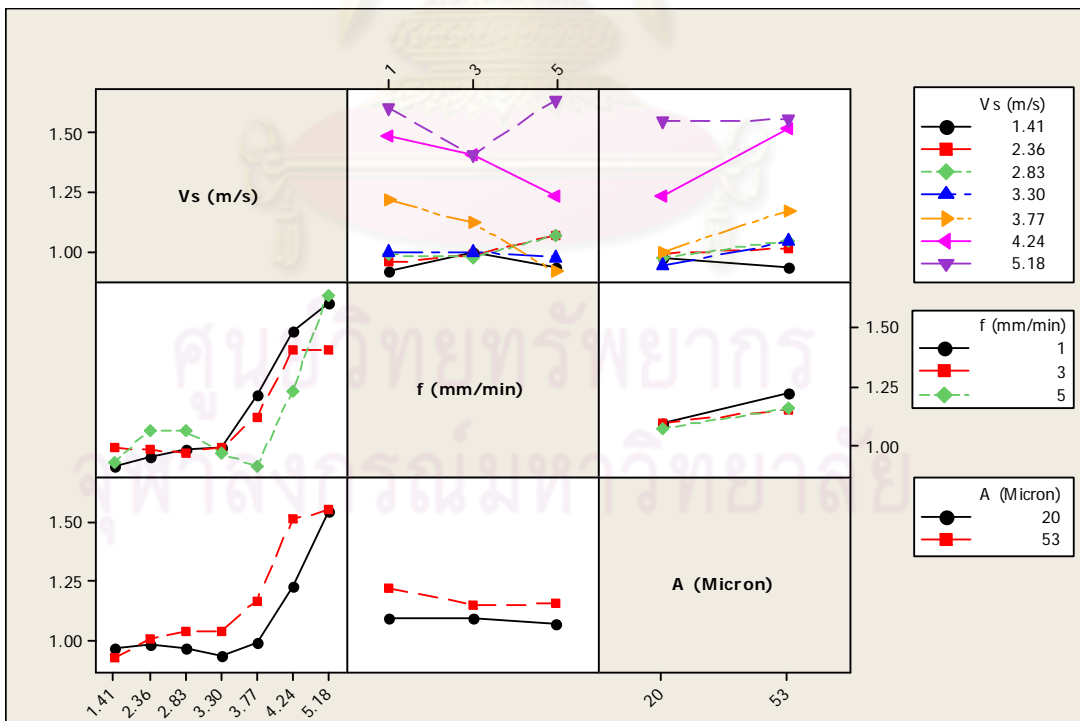
Figure 5.30   Interaction plots for grinding force ratio (R)

5.6.1.6 Effects of Grinding Factors on Material Removal Rate (MRR)

Analysis of variance (ANOVA) in Table 5.11 illustrated that grinding speed (Vs), cross head speed (f), and abrasive grit size (A) were the significant factors influencing material removal rate for significant level less than P-value of 0.05. From the table, material removal rate was directly dependent on cross head speed (f) with the highest percent contribution of 99.8%. While, grinding speed (Vs) and abrasive grit size (A) also being significant factors presented a little effect according to percent contribution less than 1%. Main effect and interaction plots were drawn in Figure 5.31 and 5.32.

Table 5.11   ANOVA for material removal rate (MRR)

Source	DF	SS	MS	F Ratio	P-value	% Contribution	Remark
Vs	6	129.318	21.553	11.80	<.0001	0.3%	Significant
f	2	16179.034	8089.517	4427.93	<.0001	99.0%	Significant
A	1	49.696	49.696	27.20	<.0001	0.6%	Significant
Vs*f	12	30.322	2.527	1.38	0.212	0.0%	
Vs*A	6	2.850	0.475	0.26	0.9523	0.0%	
f*A	2	6.037	3.019	1.65	0.2039	0.0%	
Vs*f*A	12	18.117	1.510	0.83	0.6232	0.0%	
Error	42	76.731	1.827			0.0%	
Total	83	16492.105					
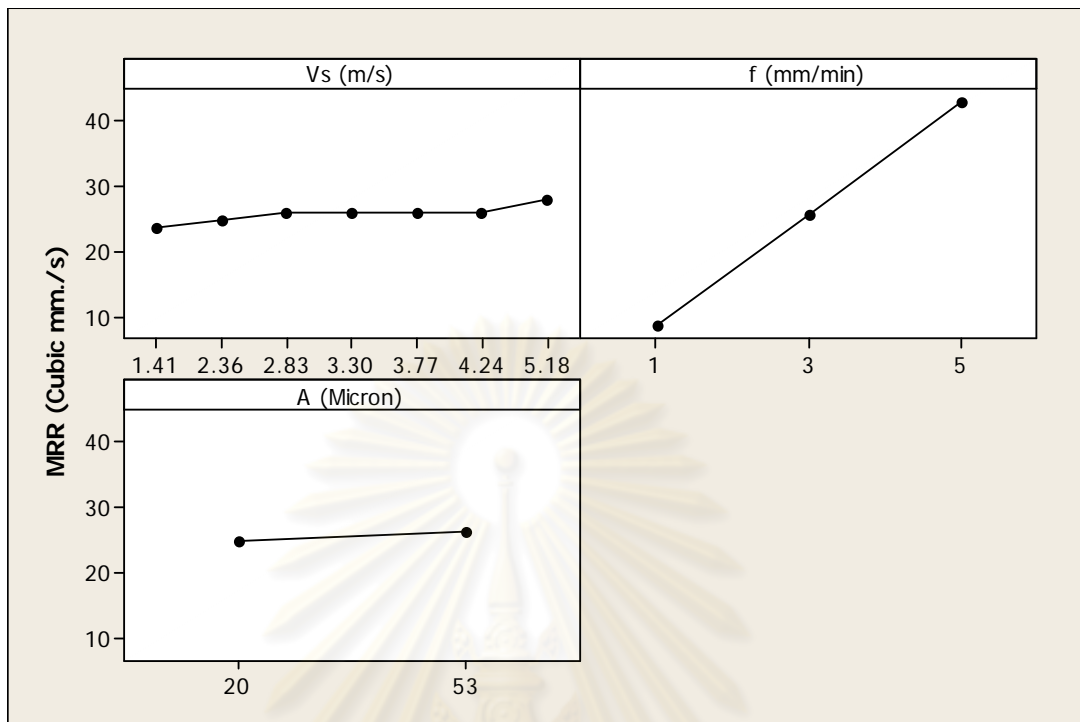
Figure 5.31   Main effect plots for material removal rate (MRR)
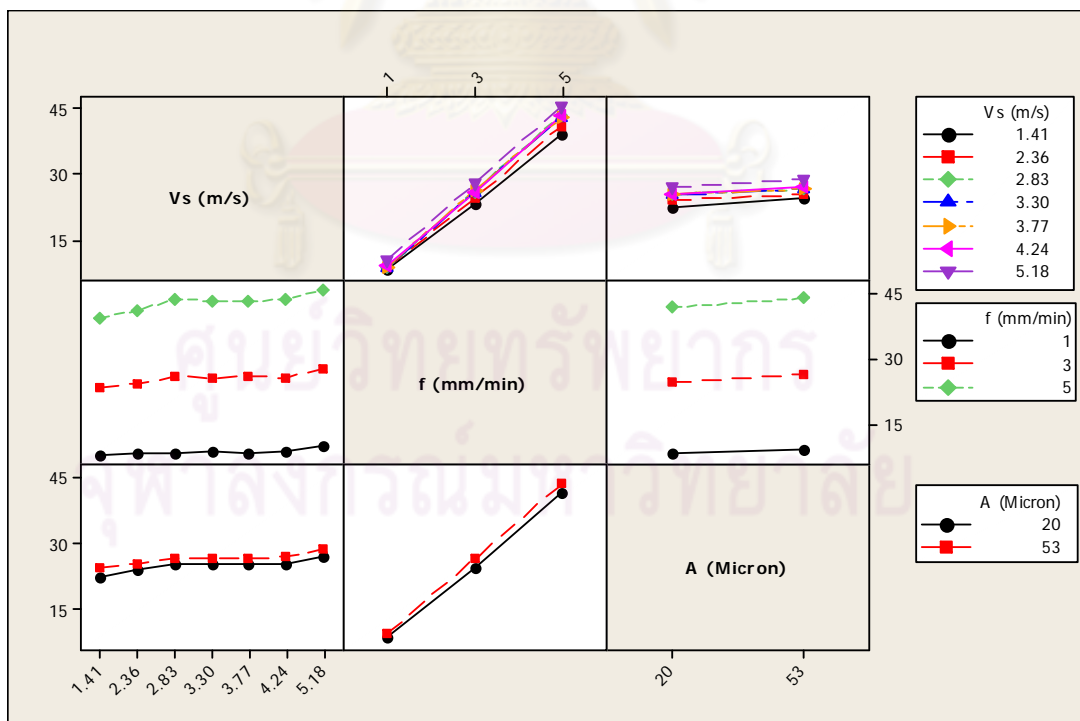
Figure 5.32   Interaction plots for material removal rate (MRR)

5.6.1.7 Effects of Grinding Factors on Specific Grinding Energy (u)

Results from analysis of variance (ANOVA) in Table 5.12 indicated that cross head speed (f), abrasive grit size (A) and their interaction (f*A) were significant factors. In addition, cross head speed (f) was the most dominating factors with 83.3% contribution while abrasive grit size (A) and interaction of cross head speed and abrasive grit size (f*A) had percent contributions of only 10.8% and 4.1%, respectively. Main effect and interaction plots of grinding factors on specific grinding energy were demonstrated in Figure 5.33 and 5.34.

Table 5.12   ANOVA for specific grinding energy (u)

Source	DF	SS	MS	F Ratio	P-value	% Contribution	Remark
Vs	6	531.715	88.619	1.13	0.3636	0.6%	
f	2	24715.776	12357.888	157.12	<.0001	83.3%	Significant
A	1	1604.314	1604.314	20.40	<.0001	10.8%	Significant
Vs*f	12	594.239	49.520	0.63	0.8049	0.3%	
Vs*A	6	147.120	24.520	0.31	0.9273	0.2%	
f*A	2	1227.775	613.888	7.81	0.0013	4.1%	Significant
Vs*f*A	12	191.334	15.945	0.20	0.9976	0.1%	
Error	42	3303.435	78.653			0.5%	
Total	83	32315.707					
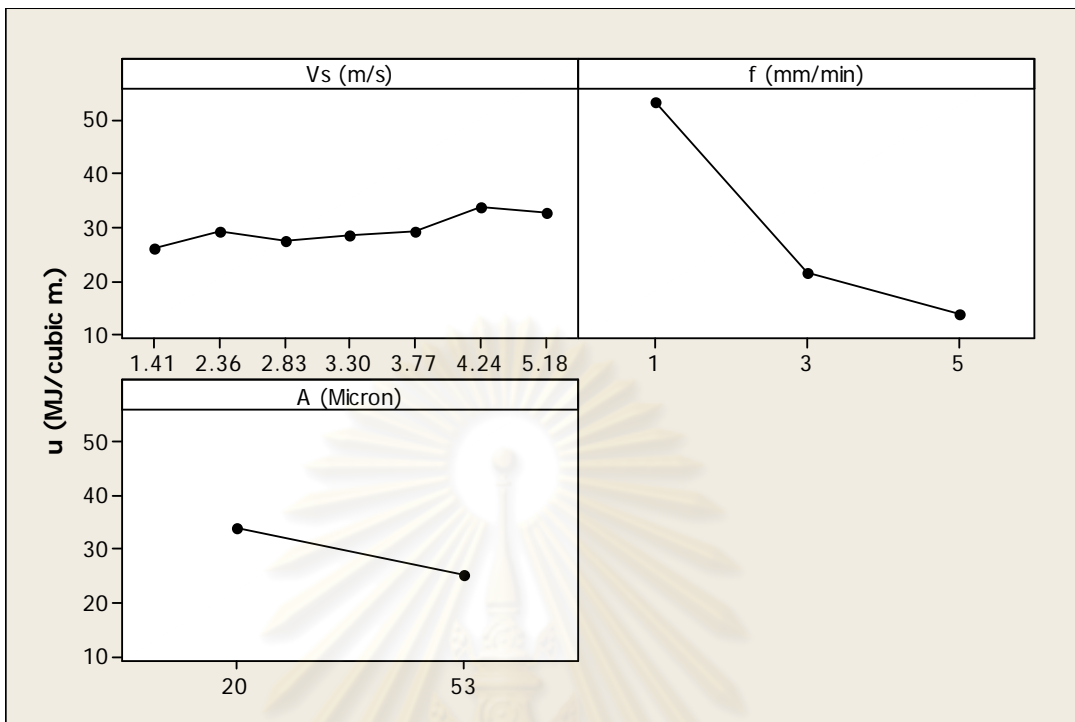
Figure 5.33   Main effect plots for specific grinding energy (u)
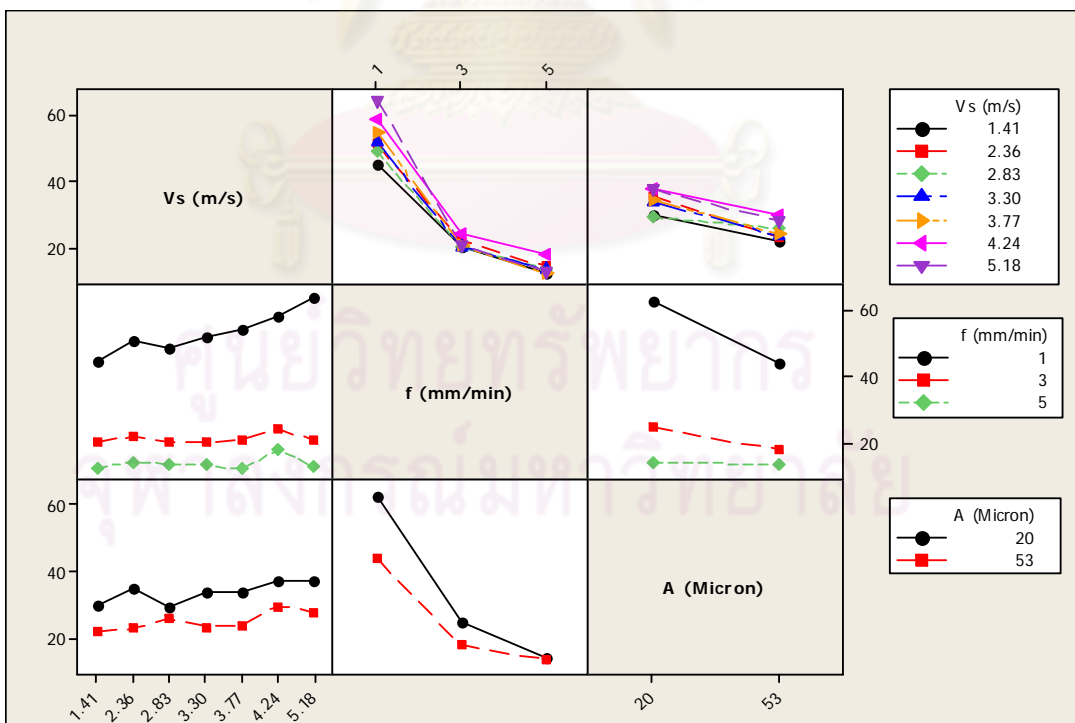
Figure 5.34   Interaction plots for specific grinding energy (u)

5.6.2 Regression Analysis

Experimental data were also used to construct regression equations for grinding response estimation in terms of grinding factors namely grinding speed (Vs), cross head speed (f), and abrasive grit size (A). Second order models were introduced, and step wise regression was carried out to eliminate non significant terms from the equations.

5.6.2.1 Circularity Error (CE) and Grinding Condition Relation

Full quadratic equation and analysis of variance (ANOVA) for the regression model for circularity error (*CE*) were illustrated in Equation 5.1 and Table 5.13, respectively. It was found that the model was significant regarding P-value less than 0.05 with R-Square and R-Square (adj.) of 0.8161 and 0.7964. Furthermore, by applying stepwise regression technique, some insignificant terms (f*f and f*A) were cut from the model, and the reduced model of circularity error (*CE Red.*) was developed as shown in Equation 5.2. Analysis of variance in Table 5.14 indicated that the reduced model were significant with R-Square and R-Square (adj.) of 0.8144 and 0.7999. However, lack of fit was still significant with P-value less than 0.05. The coefficients of both regression models in terms of grinding factors were concluded in Table 5.15.

$$CE = 3.23 - 1.60\,Vs + 0.21\,f - 0.012\,A + 0.22\,Vs*Vs - 0.007\,f*f - 0.038\,Vs*f$$
$$+ 0.003\,Vs*A + 0.0004\,f*A \qquad (5.1)$$

$$CE_{Red.} = 3.23 - 1.60\,Vs + 0.18\,f - 0.011\,A + 0.22\,Vs*Vs - 0.038\,Vs*f$$
$$+ 0.003\,Vs*A \qquad (5.2)$$

Table 5.13   ANOVA of regression model for circularity error (CE)

Source	DF	SS	MS	F-Ratio	P-value	Remark
Model	8	11.982	1.498	41.59	<.0001	Significant
Vs	1	1.921	1.921	53.35	<.0001	Significant
f	1	0.700	0.700	19.43	<.0001	Significant
A	1	0.000	0.000	0.00	1.000	
Vs*Vs	1	8.561	8.561	237.73	<.0001	Significant
f*f	1	0.015	0.015	0.41	0.5226	
Vs*f	1	0.420	0.420	11.66	0.001	Significant
Vs*A	1	0.308	0.308	8.56	0.0045	Significant
f*A	1	0.010	0.010	0.27	0.6038	
Residual	75	2.701	0.036			
Lack-of-Fit	33	2.060	0.062	4.09	<.0001	Significant
Pure error	42	0.641	0.015			
Total	83	14.682				
R-Square		0.8161				
R-Square (adj.)		0.7964				

Table 5.14   ANOVA of regression model for circularity error (CE) after removing insignificant terms

Source	DF	SS	MS	F-Ratio	P-value	Remark
Model	6	11.957	1.993	56.30	<.0001	Significant
Vs	1	1.921	1.921	54.28	<.0001	Significant
f	1	0.700	0.700	19.77	<.0001	Significant
A	1	0.000	0.000	0.00	1.000	
Vs*Vs	1	8.561	8.561	241.87	<.0001	Significant
Vs*f	1	0.420	0.420	11.86	0.0009	Significant
Vs*A	1	0.308	0.308	8.71	0.0042	Significant
Residual	77	2.725	0.035			
Lack-of-Fit	35	2.084	0.060	3.90	<.0001	Significant
Pure error	42	0.641	0.015			
Total	83	14.682				
R-Square		0.8144				
R-Square (adj.)		0.7999				

Table 5.15   The coefficients of grinding factors for circularity error estimation
in full and reduced regression model (*CE, CE $_{Red.}$*)

Term	Regression coefficients	
	CE	*CE $_{Red.}$*
Intercept	3.23	3.23
Vs	-1.60	-1.60
f	0.21	0.18
A	-0.012	-0.011
Vs*Vs	0.22	0.22
f*f	-0.007	
Vs*f	-0.038	-0.038
Vs*A	0.003	0.003
f*A	0.0004	

5.6.2.2 Finished Diameter (D) and Grinding Condition Relation

Experimental data from the grinding speed ranged between 2.83 and 3.77 m/s for all cross head speeds and abrasive grit sizes where all sphere shapes were formed with minimal circularity errors were used to develop regression model. Full quadratic equation of finished diameter (D) and its reduced equation ($D_{Red.}$) after removing insignificant terms were shown in Equation 5.3 and 5.4, respectively. Analysis of variance in Table 5.16 and Table 5.17 indicated both models significant and adequacy to estimate finished diameter regarding P-value of the models less than 0.05 and also insignificant lack of fit. In addition, R-Square and R-Square (adj.) were found to be 0.7285, 6480 for the full model and 0.7198, 0.6837 for the reduced model, respectively. Grinding speed (Vs), cross head speed (f), and abrasive grit size (A) in linear terms and square terms of cross head speed (f*f) were illustrated in the reduced model. The coefficients of the regression models in terms of grinding factors were indicated in Table 5.18.

$$D \quad = \quad 19.21 + 0.27\,Vs - 0.12\,f - 0.003\,A - 0.053\,Vs{*}Vs + 0.012\,f{*}f$$
$$+ 0.005\,Vs{*}\text{f} + 0.0005\,Vs{*}A - 0.0001\,f{*}A \qquad (5.3)$$

$$D_{Red.} \quad = \quad 19.67 - 0.041\,Vs - 0.103\,f - 0.002\,A + 0.011\,f{*}f \qquad (5.4)$$

Table 5.16   ANOVA of regression model for finished diameter (D)

Source	DF	SS	MS	F-Ratio	P-value	Remark
Model	8	0.175	0.022	9.06	<.0001	Significant
Vs	1	0.009	0.009	3.66	0.0665	
f	1	0.112	0.112	46.50	<.0001	Significant
A	1	0.035	0.035	14.46	0.0007	Significant
Vs*Vs	1	0.001	0.001	0.45	0.5072	
f*f	1	0.017	0.017	6.97	0.0136	Significant
Vs*f	1	0.000	0.000	0.13	0.7243	
Vs*A	1	0.000	0.000	0.17	0.6809	
f*A	1	0.000	0.000	0.11	0.7420	
Residual	27	0.065	0.002			
Lack-of-Fit	9	0.016	0.002	0.64	0.7494	
Pure error	18	0.049	0.003			
Total	35	0.240				
R-Square		0.7285				
R-Square (adj.)		0.6480				

Table 5.17   ANOVA of regression model for finished diameter (D) after removing insignificant terms

Source	DF	SS	MS	F-Ratio	P-value	Remark
Model	4	0.173	0.043	19.91	<.0001	Significant
Vs	1	0.009	0.009	4.07	0.0524	
f	1	0.112	0.112	51.73	<.0001	Significant
A	1	0.035	0.035	16.08	0.0004	Significant
f*f	1	0.017	0.017	7.76	0.0090	Significant
Residual	31	0.067	0.002			
Lack-of-Fit	13	0.018	0.001	0.50	0.8954	
Pure error	18	0.049	0.003			
Total	35	0.240				
R-Square		0.7198				
R-Square (adj.)		0.6837				

Table 5.18   The coefficients of grinding factors for finished diameter estimation
in full and reduced regression model (D, $D_{Red.}$)

Term	Regression coefficients	
	D	$D_{Red.}$
Intercept	19.21	19.67
Vs	0.27	-0.041
f	-0.12	-0.103
A	-0.003	-0.002
Vs*Vs	-0.053	
f*f	0.012	0.011
Vs*f	0.005	
Vs*A	0.0005	
f*A	-0.0001	

5.6.2.3 Tangential Force (Ft) and Grinding Condition Relation

The full regression model for tangential force (*Ft*) expressed in Equation 5.5 was indicated to be significant referred to P-value less than 0.05 with R-Square and R-Square (adj.) of 0.7478 and 0.7209 as shown in the analysis of variance in Table 5.19. In addition, the terms as following, linear terms of grinding speed (Vs), cross head speed (f), abrasive grit size (A), square terms of grinding speed (Vs*Vs), interactions of grinding speed and cross head speed (Vs*f), and interaction of cross head speed and abrasive grit size (f*A) were significant. After removing insignificant terms (f*f and Vs*A), the reduced model of tangential force (*Ft Red.*) was developed in Equation 5.6 and found to be significant regarding P-value less than 0.05 as shown in Table 5.20. R-Square and R-Square (adj.) were 0.7447 and 0.7249, respectively. Lack of fit of the reduced model regarding P-value of 0.9284 was not significant. This meant that the reduced model could be effectively used to estimate tangential force through grinding factors. The coefficients of the full and reduced regression model were shown in Table 5.21.

$$Ft = 0.475 - 0.138\,Vs + 0.029\,f - 0.0025\,A + 0.015\,Vs{*}Vs - 0.0016\,f{*}f$$
$$- 0.0063\,Vs{*}f + 0.0002\,Vs{*}A + 0.0004\,f{*}A \qquad (5.5)$$

$$Ft_{Red.} = 0.465 - 0.132\,Vs + 0.019\,f - 0.002\,A + 0.0154\,Vs{*}Vs - 0.0063\,Vs{*}f$$
$$+ 0.0004\,f{*}A \qquad (5.6)$$

Table 5.19   ANOVA of regression model for tangential force (Ft)

Source	DF	SS	MS	F-Ratio	P-value	Remark
Model	8	0.385	0.048	27.80	<.0001	Significant
Vs	1	0.273	0.273	157.83	<.0001	Significant
f	1	0.032	0.032	18.25	<.0001	Significant
A	1	0.016	0.016	9.42	0.0030	Significant
Vs*Vs	1	0.041	0.041	23.82	<.0001	Significant
f*f	1	0.001	0.001	0.42	0.5183	
Vs*f	1	0.012	0.012	6.81	0.0109	Significant
Vs*A	1	0.001	0.001	0.48	0.4892	
f*A	1	0.008	0.008	4.63	0.0346	Significant
Residual	75	0.130	0.002			
Lack-of-Fit	33	0.043	0.001	0.63	0.914	
Pure error	42	0.087	0.002			
Total	83	0.515				
R-Square		0.7478				
R-Square (adj.)		0.7209				

Table 5.20   ANOVA of regression model for tangential force (Ft) after removing insignificant terms

Source	DF	SS	MS	F-Ratio	P-value	Remark
Model	6	0.383	0.064	37.44	<.0001	Significant
Vs	1	0.273	0.273	160.11	<.0001	Significant
f	1	0.032	0.032	18.51	<.0001	Significant
A	1	0.016	0.016	9.55	0.0028	Significant
Vs*Vs	1	0.041	0.041	24.16	<.0001	Significant
Vs*f	1	0.012	0.012	6.91	0.0104	Significant
f*A	1	0.008	0.008	4.70	0.0333	Significant
Residual	77	0.131	0.002			
Lack-of-Fit	35	0.045	0.001	0.62	0.9284	
Pure error	42	0.087	0.002			
Total	83	0.515				
R-Square		0.7447				
R-Square (adj.)		0.7249				

Table 5.21   The coefficients of grinding factors for tangential force estimation
in full and reduced regression model (*Ft, Ft $_{Red.}$*)

Term	Regression coefficients	
	Ft	*Ft $_{Red.}$*
Intercept	0.475	0.465
Vs	-0.138	-0.132
f	0.029	0.019
A	-0.0025	-0.002
Vs*Vs	0.015	0.0154
f*f	-0.0016	
Vs*f	-0.0063	-0.0063
Vs*A	0.0002	
f*A	0.0004	0.0004

ศูนย์วิทยทรัพยากร
จุฬาลงกรณ์มหาวิทยาลัย

5.6.2.4 Normal Force (Fn) and Grinding Condition Relation

Analysis of variance in Table 5.22 indicated that the full regression model of normal force (Fn) in Equation 5.7 was significant according to P-value less than 0.05 with R-Square and R-Square (adj.) of 0.8115 and 0.7914. Linear terms of grinding speed (Vs), cross head speed (f), abrasive grit size (A), square terms of grinding speed (Vs*Vs), and interactions of grinding speed and cross head speed (Vs*f) were reported to be significant. The reduced model of normal force ($Fn_{Red.}$) in Equation 5.8 was provided by stepwise regression technique, having R-Square and R-Square (adj.) of 0.8034 and 0.7908 as shown in Table 5.23. Model adequacy checking in terms of lack of fit was found to be not significant (P-value = 0.824), implying the model able to explain experimental data. In addition, Table 5.24 concluded the coefficients of the full and reduced regression model for normal force estimation.

$$Fn = 0.504 - 0.142\,Vs + 0.026\,f - 0.0023\,A + 0.0132\,Vs^*Vs - 0.0013\,f^*f$$
$$- 0.005\,Vs^*f + 0.0001\,Vs^*A + 0.0003\,f^*A \tag{5.7}$$

$$Fn_{Red.} = 0.466 - 0.137\,Vs + 0.028f - 0.001A + 0.0132Vs^*Vs - 0.005Vs^*f \tag{5.8}$$

Table 5.22   ANOVA of regression model for normal force (Fn)

Source	DF	SS	MS	F-Ratio	P-value	Remark
Model	8	0.568	0.071	40.37	<.0001	Significant
Vs	1	0.467	0.467	265.54	<.0001	Significant
f	1	0.032	0.032	17.97	<.0001	Significant
A	1	0.024	0.024	13.85	0.0004	Significant
Vs*Vs	1	0.031	0.031	17.39	<.0001	Significant
f*f	1	0.001	0.001	0.28	0.5951	
Vs*f	1	0.007	0.007	4.18	0.0444	Significant
Vs*A	1	0.001	0.001	0.29	0.5914	
f*A	1	0.005	0.005	2.64	0.1082	
Residual	75	0.132	0.002			
Lack-of-Fit	33	0.048	0.001	0.72	0.8356	
Pure error	42	0.084	0.002			
Total	83	0.699				
R-Square		0.8115				
R-Square (adj.)		0.7914				

Table 5.23   ANOVA of regression model for normal force (Fn) after removing
insignificant terms

Source	DF	SS	MS	F-Ratio	P-value	Remark
Model	5	0.562	0.112	63.77	<.0001	Significant
Vs	1	0.467	0.467	264.8	<.0001	Significant
f	1	0.032	0.032	17.92	<.0001	Significant
A	1	0.024	0.024	13.81	0.0004	Significant
Vs*Vs	1	0.031	0.031	17.34	<.0001	Significant
Vs*f	1	0.007	0.007	4.17	0.0445	Significant
Residual	78	0.138	0.002			
Lack-of-Fit	36	0.053	0.002	0.74	0.8240	
Pure error	42	0.084	0.002			
Total	83	0.699				
R-Square		0.8034				
R-Square (adj.)		0.7908				

Table 5.24   The coefficients of grinding factors for normal force estimation
in full and reduced regression model (*Fn, Fn $_{Red.}$*)

Term	Regression coefficients	
	Fn	*Fn $_{Red.}$*
Intercept	0.504	0.466
Vs	-0.142	-0.137
f	0.026	0.028
A	-0.0023	-0.001
Vs*Vs	0.0132	0.0132
f*f	-0.0013	
Vs*f	-0.005	-0.005
Vs*A	0.0001	
f*A	0.0003	

5.6.2.5 Grinding Force Ratio (R) and Grinding Condition Relation

The full regression model for grinding force ratio (R) was expressed in Equation 5.9, and it was found in Table 5.25 that the model was significant according to P-value less than 0.05 with R-Square and R-Square (adj.) of 0.6042 and 0.5620. Linear and square term of grinding speed (Vs, Vs*Vs) and linear term of abrasive grit size (A) were effective in the model. Insignificant terms were removed, and the reduced regression model of grinding force ratio ($R_{Red.}$) was modified as expressed in Equation 5.10. R-Square and R-Square (adj.) were 0.5826 and 0.5669 as shown in Table 5.26. Moreover, P-value of lack of fit was found to be 0.1136, implying adequacy model for grinding force ratio estimation. Additionally, the coefficients of the full and reduced regression model for grinding force ratio estimation were illustrated in Table 5.27.

$$R \quad = \quad 1.112 - 0.236\,Vs + 0.022\,f - 0.0004\,A + 0.0595\,Vs*Vs + 0.0036\,f*f$$
$$- 0.0128\,Vs*f + 0.0013\,Vs*A - 0.0003\,f*A \tag{5.9}$$

$$R_{Red.} \quad = \quad 1.066 - 0.229\,Vs + 0.003\,A + 0.0595\,Vs*Vs \tag{5.10}$$

ศูนย์วิทยทรัพยากร
จุฬาลงกรณ์มหาวิทยาลัย

Table 5.25　ANOVA of regression model for grinding force ratio (R = Ft/Fn)

Source	DF	SS	MS	F-Ratio	P-value	Remark
Model	8	3.907	0.488	14.31	<.0001	Significant
Vs	1	2.999	2.999	87.89	<.0001	Significant
f	1	0.031	0.031	0.91	0.3427	
A	1	0.167	0.167	4.91	0.0298	Significant
Vs*Vs	1	0.616	0.616	18.05	<.0001	Significant
f*f	1	0.004	0.004	0.11	0.7392	
Vs*f	1	0.049	0.049	1.43	0.2358	
Vs*A	1	0.049	0.049	1.43	0.2358	
f*A	1	0.007	0.007	0.21	0.6447	
Residual	75	2.560	0.034			
Lack-of-Fit	33	1.465	0.044	1.70	0.0518	
Pure error	42	1.095	0.026			
Total	83	6.467				
R-Square		0.6042				
R-Square (adj.)		0.5620				

Table 5.26　ANOVA of regression model for grinding force ratio (R = Ft/Fn) after removing insignificant terms

Source	DF	SS	MS	F-Ratio	P-value	Remark
Model	3	3.767	1.256	37.22	<.0001*	Significant
Vs	1	2.999	2.999	88.89	<.0001*	Significant
A	1	0.167	0.167	4.96	0.0287*	Significant
Vs*Vs	1	0.616	0.616	18.26	<.0001*	Significant
Residual	80	2.699	0.034			
Lack-of-Fit	10	0.512	0.051	1.64	0.1136	
Pure error	70	2.187	0.031			
Total	83	6.467				
R-Square		0.5826				
R-Square (adj.)		0.5669				

Table 5.27   The coefficients of grinding factors for grinding force ratio estimation
in full and reduced regression model (R, $R_{Red.}$)

Term	Regression coefficients	
	R	$R_{Red.}$
Intercept	1.112	1.066
Vs	-0.236	-0.229
f	0.022	
A	-0.0004	0.003
Vs*Vs	0.0595	0.0595
f*f	0.0036	
Vs*f	-0.0128	
Vs*A	0.0013	
f*A	-0.0003	

5.6.2.6 Material Removal Rate (MRR) and Grinding Condition Relation

The full regression model of material removal rate (*MRR*) in terms of grinding variables was expressed in Equation 5.11 and indicated to be significant according to the analysis of variance in Table 5.28 with R-Square and R-Square (adj.) of 0.9926 and 0.9918, respectively. After removing insignificant terms, linear terms of grinding speed (Vs), cross head speed (f), and their interaction (Vs*f) along with abrasive grit size (A) were in the reduced model of material removal rate (*MRR* $_{Red.}$) illustrated in Equation 5.12. In addition, analysis of variance in Table 5.29 reported the reduced model relevant regarding P-value for lack of fit of 0.783 with R-Square and R-Square (adj.) of 0.9922 and 0.9918, respectively. In addition, the coefficients of the full and reduced regression model for material removal rate were shown in Table 5.30.

$$
\begin{aligned}
MRR \quad = \quad & -1.163 + 0.399Vs + 6.935f + 0.021A - 0.016Vs*Vs + 0.062f*f \\
& + 0.255Vs*f - 0.001Vs*A + 0.01f*A
\end{aligned} \tag{5.11}
$$

$$
MRR_{Red.} = \quad -2.318 + 0.252\,Vs + 7.656\,f + 0.047\,A + 0.255\,Vs*f \tag{5.12}
$$

Table 5.28   ANOVA of regression model for material removal rate (MRR)

Source	DF	SS	MS	F-Ratio	P-value	Remark
Model	8	16369.740	2046.220	1254.18	<.0001	Significant
Vs	1	115.902	115.902	71.04	<.0001	Significant
f	1	16177.881	16177.881	9915.84	<.0001	Significant
A	1	49.696	49.696	30.46	<.0001	Significant
Vs*Vs	1	0.047	0.047	0.03	0.8653	
f*f	1	1.153	1.153	0.71	0.4031	
Vs*f	1	19.441	19.441	11.92	0.0009	Significant
Vs*A	1	0.034	0.034	0.02	0.8860	
f*A	1	5.557	5.557	3.41	0.0689	
Residual	75	122.364	1.630			
Lack-of-Fit	33	45.633	1.383	0.76	0.7944	
Pure error	42	76.731	1.827			
Total	83	16492.104				
R-Square		0.9926				
R-Square (adj.)		0.9918				

Table 5.29   ANOVA of regression model for material removal rate (MRR) after removing insignificant terms

Source	DF	SS	MS	F-Ratio	P-value	Remark
Model	4	16362.950	4090.740	2502.18	<.0001	Significant
Vs	1	115.932	115.932	70.91	<.0001	Significant
f	1	16177.881	16177.881	9895.50	<.0001	Significant
A	1	49.696	49.696	30.40	<.0001	Significant
Vs*f	1	19.441	19.441	11.89	0.0009	Significant
Residual	79	129.155	1.635			
Lack-of-Fit	37	52.424	1.417	0.78	0.7830	
Pure error	42	76.731	1.827			
Total	83	16492.104				
R-Square		0.9922				
R-Square (adj.)		0.9918				

Table 5.30   The coefficients of grinding factors for material removal rate estimation
in full and reduced regression model (*MRR, MRR Red.*)

Term	Regression coefficients	
	MRR	*MRR Red.*
Intercept	-1.163	-2.318
Vs	0.399	0.252
f	6.935	7.656
A	0.021	0.047
Vs*Vs	-0.016	
f*f	0.062	
Vs*f	0.255	0.255
Vs*A	-0.001	
f*A	0.01	

ศูนย์วิทยทรัพยากร
จุฬาลงกรณ์มหาวิทยาลัย

5.6.2.7 Specific Grinding Energy (u) and Grinding Condition Relation

   Specific grinding energy in the spherical grinding process for porous polyurethane foam could be modeled in Equation 5.13 in terms of full regression equation (u). Table 5.31 illustrated that the full model was significant with P-value less than 0.05, and R-Square and R-Square (adj.) were 0.8756 and 0.8623, respectively. Insignificant terms as following, square term of grinding speed (Vs*Vs) and interaction term between grinding speed and abrasive grit size (Vs*A) were removed from the model. As a result, the reduced model of specific grinding energy ($u_{Red.}$) performed in Equation 5.14 comprising the effective terms of linear, square, interaction terms of cross head speed (f, f*f, Vs*f, f*A) and linear terms of grinding speed (Vs) and abrasive grit size (A). Analysis of variance in Table 5.32 indicated that the reduced model was adequacy with P-value for lack of fit of 0.9999, and R-Square and R-Square (adj.) were reported to be 0.8754 and 0.8657, respectively. The coefficients of the full and reduced regression model for specific grinding energy estimation were indicated in Table 5.33.

u = $86.17 + 4.89\,Vs - 29.70\,f - 0.65\,A + 0.11\,Vs{*}Vs + 3.09\,f{*}f$
       $-\,1.15\,Vs{*}f - 0.009\,Vs{*}A + 0.14\,f{*}A$ (5.13)

$u_{Red.}$ = $86.13 + 5.32\,Vs - 29.70\,f - 0.68\,A + 3.09\,f{*}f - 1.15\,Vs{*}f$
       $+\,0.14\,f{*}A$ (5.14)

Table 5.31   ANOVA of regression model for specific grinding energy (u)

Source	DF	SS	MS	F-Ratio	P-value	Remark
Model	8	28294.794	3536.850	65.97	<.0001	Significant
Vs	1	397.290	397.290	7.41	0.0081	Significant
f	1	21871.159	21871.159	407.95	<.0001	Significant
A	1	1604.314	1604.314	29.92	<.0001	Significant
Vs*Vs	1	2.242	2.242	0.04	0.8385	
f*f	1	2844.617	2844.617	53.06	<.0001	Significant
Vs*f	1	391.037	391.037	7.29	0.0085	Significant
Vs*A	1	2.263	2.263	0.04	0.8378	
f*A	1	1182.202	1182.202	22.05	<.0001	Significant
Residual	75	4020.913	53.612			
Lack-of-Fit	33	717.478	21.742	0.28	0.9999	
Pure error	42	3303.435	78.653			
Total	83	32315.707				
R-Square		0.8756				
R-Square (adj.)		0.8623				

Table 5.32   ANOVA of regression model for specific grinding energy (u) after removing insignificant terms

Source	DF	SS	MS	F-Ratio	P-value	Remark
Model	6	28290.289	4715.050	90.192	<.0001	Significant
Vs	1	396.961	396.961	7.59	0.0073	Significant
f	1	21871.159	21871.159	418.36	<.0001	Significant
A	1	1604.314	1604.314	30.69	<.0001	Significant
f*f	1	2844.617	2844.617	54.41	<.0001	Significant
Vs*f	1	391.037	391.037	7.48	0.0077	Significant
f*A	1	1182.202	1182.202	22.61	<.0001	Significant
Residual	77	4025.418	52.278			
Lack-of-Fit	35	721.983	20.628	0.26	0.9999	
Pure error	42	3303.435	78.653			
Total	83	32315.707				
R-Square		0.8754				
R-Square (adj.)		0.8657				

Table 5.33   The coefficients of grinding factors for specific grinding energy

estimation in full and reduced regression model (u, $u_{Red.}$)

Term	Regression coefficients	
	u	$u_{Red.}$
Intercept	86.17	86.13
Vs	4.89	5.32
f	-29.70	-29.70
A	-0.65	-0.68
Vs*Vs	0.11	
f*f	3.09	3.09
Vs*f	-1.15	-1.15
Vs*A	-0.009	
f*A	0.14	0.14

ศูนย์วิทยทรัพยากร

จุฬาลงกรณ์มหาวิทยาลัย

5.6.3 Summary of Statistical Results

From the analysis of variance of general full factorial design, significant factors and their interactions affecting various grinding responses were concluded in Table 5.34. Grinding speed (Vs) was the most influential factor affecting circularity error (CE), finished diameter (D), tangential force (Ft), normal force (Fn), and grinding force ratio (R=Ft/Fn) with 75.7%, 39.6%, 55.3%, 62.6%, and 65.4% contribution, respectively. While, cross head speed (f) was found to be the most significant factor for material removal rate (MRR) and specific grinding energy (u) with 99.8% and 87.2% contribution, respectively.

Furthermore, the regression models developed from stepwise regression technique used for grinding response estimation in terms of grinding factors were summarized in Table 5.35. All the models except finished diameter could be used to estimate grinding responses for grinding speeds between 1.41 and 5.18 m/s, cross head speeds between 1.0 and 5.0 mm/min, and abrasive grit sizes of 20 and 53 µm. For finished diameter, the model could be used for grinding speed between 2.83 and 3.77 m/s, cross head speed between 1.0 and 5.0 mm/min, and abrasive grit sizes of 20 and 53 µm.

Table 5.34 Conclusions of significant grinding factors and percent contribution on grinding responses

		Grinding responses						
		1.CE	2.D	3.Ft	4.Fn	5.R=Ft/Fn	6.MRR	7.u
Grinding factors	1.Vs	75.7%*	39.6%*	55.3%*	62.6%*	65.4%*	0.3%*	0.60%
	2.f	5.1%*	5.4%*	16.6%*	12.0%*	1.80%	99.0%*	83.3%*
	3.A	0.00%	23.2%*	16.7%*	18.2%*	16.9%*	0.6%*	10.8%*
	4.Vs*f	8.5%*	9.8%*	1.70%	0.90%	4.00%	0.00%	0.30%
	5.Vs*A	2.4%*	9.3%*	1.20%	1.10%	3.70%	0.00%	0.20%
	6.f*A	1.0%*	7.2%*	4.60%	1.90%	0.90%	0.00%	4.1%*
	7.Vs*f*A	7.3%*	4.8%*	1.80%	1.80%	4.70%	0.00%	0.10%
	Error	0.10%	0.80%	2.10%	1.50%	2.60%	0.00%	0.50%

Remark: * = Significant

Table 5.35   Regression equations for grinding response estimations

Response variables	Regression equations	R-Square	R-Square (adj.)
1. Circularity error	$(CE_{Red.})$ = 3.23 - 1.60 Vs + 0.18 f - 0.011 A + 0.22 $Vs*Vs$ - 0.038 $Vs*f$ + 0.003 $Vs*A$	0.8144	0.7999
2. Finished diameter	$(D_{Red.})$ = 19.67 - 0.041 Vs - 0.103 f - 0.002 A + 0.011 $f*f$	0.7198	0.6837
3. Tangential force	$(Ft_{Red.})$ = 0.465 - 0.132 Vs + 0.019 f - 0.002 A + 0.0154 $Vs*Vs$ - 0.0063$Vs*f$ + 0.0004$f*A$	0.7447	0.7249
4. Normal force	$(Fn_{Red.})$ = 0.466 - 0.137 Vs + 0.028 f - 0.001A + 0.0132$Vs*Vs$ - 0.005$Vs*f$	0.8034	0.7908
5. Grinding force ratio	$(R_{Red.})$ = 1.066 - 0.229 Vs + 0.003 A + 0.0595 $Vs*Vs$	0.5826	0.5669
6. Material removal rate	$(MRR_{Red.})$ = -2.318 + 0.252 Vs + 7.656 f + 0.047 A + 0.255 $Vs*f$	0.9922	0.9918
7. Specific grinding energy	$(u_{Red.})$ = 86.13 + 5.32 Vs - 29.70 f - 0.68 A + 3.09 $f*f$ - 1.15 $Vs*f$ + 0.14 $f*A$	0.8754	0.8657

Remark: CE $_{Red.}$, Ft $_{Red.}$, Fn $_{Red.}$, R $_{Red.}$, MRR $_{Red.}$, and u $_{Red.}$ Equation used for the range of Vs = 1.41 – 5.18 m/s, f = 1.0 – 5.0 mm/min, A = 20 and 53 µm.

D $_{Red.}$Equation used for the range of Vs = 2.83 – 3.77 m/s, f = 1.0 – 5.0 mm/min, A = 20 and 53 µm.

5.6.4 Confirmation results

Confirmation results of finished shapes run by the experimental plan in Chapter III were illustrated in Table 5.36. It was found that sphere shapes of the ground specimen were formed for all grinding conditions corresponded to the results as illustrated in Table 5.3.

In addition, actual results including circularity error, finished diameter, tangential force, normal force, grinding force ratio, material removal rate, and specific grinding energy from the confirmation experiment were found out and compared with the estimated results calculated from the reduced regression equations as previously developed in Table 5.37. From the table, there were no statistical indications to indicate significant differences between the values from experiment and the values from estimation for all responses except for finished diameter according to P-value less than 0.05.

Table 5.36   Summarized shape results of confirmation experiment

		Abrasive grit size (A)					
		20 µm			53 µm		
Cross head speed (f)		1.0 mm/min	3.0 mm/min	5.0 mm/min	1.0 mm/min	3.0 mm/min	5.0 mm/min
Grinding speed (Vs)	2.83 m/s	S	S	S	S	S	S
	3.30 m/s	S	S	S	S	S	S
	3.77 m/s	S	S	S	S	S	S

Remark :　　　S　　=　　Sphere shape

Table 5.37   Comparisons between actual and estimated values of grinding responses for various grinding parameters

No.	Exp. run number	Grinding speed; Vs (m/s)	Cross head speed; f (mm/min)	Abrasive grit size; A (μm)	Circularity error; CE (mm)		Finished diameter; D (mm)		Material removal rate; MRR (mm^3/s)		Tangential force; Ft (N)		Normal force; Fn (N)		Grinding force ratio; R = Ft/Fn		Specific grinding energy; u (MJ/m^3)	
					A	E	A	E	A	E	A	E	A	E	A	E	A	E
1	1	2.83	1	20	0.60	0.53	19.41	19.43	8.21	7.71	0.18	0.18	0.17	0.18	1.03	0.95	61.4	60.4
2	3	2.83	3	20	0.60	0.68	19.33	19.31	26.91	24.46	0.13	0.20	0.13	0.21	1.00	0.95	13.5	24.8
3	2	2.83	5	20	0.63	0.82	19.22	19.28	41.65	41.22	0.24	0.22	0.25	0.23	0.94	0.95	16.2	13.9
4	9	2.83	1	53	0.66	0.48	19.38	19.36	9.63	9.24	0.10	0.13	0.12	0.14	0.81	1.04	29.5	42.5
5	8	2.83	3	53	0.48	0.63	19.25	19.24	25.78	26.00	0.22	0.17	0.19	0.17	1.15	1.04	23.7	16.1
6	5	2.83	5	53	0.77	0.77	19.23	19.21	47.03	42.76	0.27	0.22	0.25	0.20	1.09	1.04	16.3	14.3
7	10	3.30	1	20	0.46	0.43	19.36	19.41	8.80	7.95	0.22	0.16	0.20	0.15	1.08	1.01	82.3	62.4
8	18	3.30	3	20	0.61	0.54	19.28	19.29	26.61	24.94	0.10	0.18	0.09	0.17	1.05	1.01	12.1	25.7
9	12	3.30	5	20	0.60	0.65	19.25	19.26	40.53	41.94	0.24	0.19	0.25	0.20	0.96	1.01	19.7	13.7
10	14	3.30	1	53	0.53	0.43	19.32	19.34	9.41	9.48	0.11	0.11	0.08	0.12	1.32	1.10	37.8	44.5
11	11	3.30	3	53	0.49	0.54	19.20	19.22	26.87	26.48	0.15	0.15	0.12	0.14	1.21	1.10	18.2	17.0
12	13	3.30	5	53	0.69	0.65	19.14	19.19	44.52	43.48	0.19	0.18	0.18	0.16	1.11	1.10	14.4	14.1
13	6	3.77	1	20	0.50	0.43	19.32	19.39	9.02	8.18	0.13	0.15	0.09	0.13	1.51	1.10	55.1	64.4
14	7	3.77	3	20	0.68	0.50	19.25	19.27	27.39	25.42	0.08	0.16	0.08	0.15	0.99	1.10	11.3	26.6
15	4	3.77	5	20	0.51	0.58	19.21	19.24	43.23	42.66	0.28	0.16	0.26	0.16	1.11	1.10	24.7	13.5
16	17	3.77	1	53	0.46	0.48	19.29	19.32	9.14	9.72	0.15	0.10	0.10	0.09	1.52	1.19	61.5	46.5
17	15	3.77	3	53	0.57	0.55	19.18	19.20	24.63	26.96	0.12	0.13	0.10	0.11	1.27	1.19	18.5	17.9
18	16	3.77	5	53	0.60	0.63	19.12	19.17	42.94	44.20	0.17	0.16	0.14	0.13	1.18	1.19	14.5	14.0
				Avg	0.58	0.57	19.26	19.29	26.24	25.71	0.17	0.16	0.16	0.16	1.13	1.07	29.5	29.6
				SD	0.09	0.11	0.08	0.08	14.47	14.31	0.06	0.03	0.06	0.04	0.19	0.08	21.2	18.6
				P-value	0.779		0.004 ***		0.157		0.567		0.85		0.08		0.97	

Remark: A = Actual value from confirmation experiment,   E = Estimated value from reduced model,   *** = Significant

Chapter VI

Discussion

In this chapter, the results from the spherical grinding system for porous polyurethane foam ground with the circular groove developed were discussed in terms of finished shape, circularity error, finished diameter, grinding forces, grinding force ratio, material removal rate, and specific grinding energy.

6.1 Finished Shape, Circularity Error (CE), and Finished Diameter (D)

From the experimental results and analysis of variance in the previous Chapter, grinding speed (Vs) played a vital role in sphere shape formation with percent contribution of 75.7% for circularity error and 39.6% for finished diameter, dominating any other variable such as cross head speed (f) and abrasive grit size (A). Circularity error of 0.61 mm according to upper confidence interval level could be indicated to be the critical value for sphere shape confirmation. Grinding with grinding speed between 2.83 and 3.77 m/s and cross head speed of 1.0 mm/min for both abrasive grit sizes of 20 and 53 µm contributed to sphere shapes with minimal circularity errors. Figure 6.1 summarized averaged circularity errors (CE) and finished diameters (D) by finished shapes. The averages of D and CE of the sphere shape were 19.30 and 0.59 mm, respectively. According to egg shape, D and CE were large being 19.73 and 1.51 mm. On the other hand, partial sphere and squircle size regarding finished diameters of 18.86 and 17.11 mm were smaller than those of sphere and egg shape, while circularity errors were quite high at 1.08 and 0.78 mm.

In spherical surface generation mechanism, it was observed from the experiment that the specimens ground with the low grinding speed of 1.41 m/s and 2.36 m/s for various cross head speeds and abrasive grit sizes did not rotate across their own axes but just orbited and plowed around the groove with low speeds. As a result, egg shapes with large finished diameter and high circularity error occurred. On the other hand, the specimens ground with the grinding speed between 2.83 and 3.77

m/s were induced to skid across their axes and to change their positions while rotating around the groove, promoting more ground surface area with random positions and consecutively resulting in sphere shape formation with minimal circularity errors. At the higher grinding speed above 4.24 m/s, the ground specimens were induced to rotate around the groove too fast to change their positions randomly in the contact between specimen, circular groove, and grinding wheel. This resulted in partial sphere and squircle shape formation with small finished sizes and high circularity errors. Reduction in finished diameters resulting from increasing grinding speed can be explained by Archard's wear equation that material removal rate is directly proportional to sliding speed of an abrasive process (Liu and Li, 2001). In addition, larger abrasive grit size used contributed to more penetrating depth of cut causing small finished diameters.

The greater the grinding area, the higher possibility of forming sphere shape corresponded to the previous work from Lee *et al.* (2006) and Stolarski (1999) who stated in lapping process that to receive the roundness ball, the motion of a ball should be random, and the orientation of the ball being ground should be different to its previous orientation. For most previous research in spherical grinding processes especially in magnetic fluid grinding and V-groove lapping that circularity errors lower than 1 µm were required, grinding speed in terms of rotational shaft speed was also indicated to be the influential variable to generate rounded balls.

Table 6.1 showed characteristics of various spherical grinding processes as developed in the previous research for magnetic fluid grinding and lapping process compared with the work done in this research. It was found that to grind different materials having different properties particularly pore structures and strengths, grinding techniques, grinding geometry, and grinding speed were varied. And, the results in terms of surface roughness and circularity error were markedly different between dense and porous materials.

Storlarski and Tobe (1997) and Child *et al.* (1995) who researched in magnetic fluid grinding and lapping for spherical grinding brittle ceramic balls stated that minimal circularity errors could be achieved for grinding with small abrasive grit sizes. This is because small grit depth of cut by using small grit size led to more surface grinding area and contributed to effective spherical surface generation and

surface damage reduction. Brittle and porous materials in general are inevitably prone to surface deterioration by machining; therefore, care should be taken in process parameter design. In the spherical grinding system developed, there was no significant effect of abrasive grit size on circularity error from the statistical analysis. However, to reduce the risk of crack damages, the smaller abrasive grit size maybe recommended.
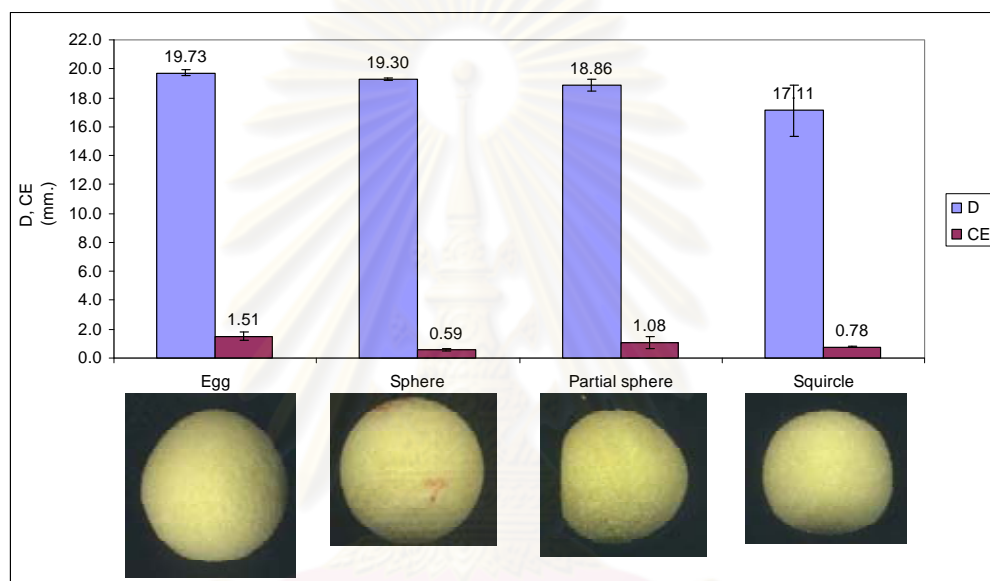
Figure 6.1   Summarry of averaged circularity error (CE) and finished diameter (D) for various finished shapes

Table 6.1   Comparisons of characteristics of various spherical grinding processes

Process	Magnetic fluid grinding	V-groove lapping	Circular groove grinding
Material	Silicon nitride	Silicon nitride	Polyurethane
Bulk density (Mg/m^3)	3.16	3.16	0.125
Porosity (%)	Dense	Dense	~90%
Fracture toughness	5.3 – 6.6	5.3 – 6.6	-
Hardness (GPa)	~16	~16	-
Grinding conditions			
Rotational speed (rpm)	1,000 – 10,000	50	600 - 800
Grinding results			
Load (N)	1	10	<1
Finished diameter (mm)	~13	~13	~19
Surface roughness (nm)	4	4	-
Circularity error (µm)	0.15 – 0.25	1 – 32	460 – 760

6.2 Grinding Forces (Ft and Fn)

6.2.1 Relationship between Grinding Factors and Grinding Forces

Grinding forces in terms of tangential (Ft) and normal (Fn) force were mainly affected by grinding speed (Vs) according to the percent contributions of 55.3% and 62.6% in the analysis of variance results in Chapter V. Both tangential and normal force were slightly decreased as increasing grinding speed corresponded to much previous research for conventional surface grinding of ceramics developed by Malkin and Hwang (1996); Yui and Lee (1996); Ramesh *et al.* (2001); Shen *et al.* (2002); Tang *et al.* (2009); Yallese *et al.* (2009). This can be explained in the power dissipation equation for grinding process (Marinescu *et al*., 2004) that grinding speed is inverted to tangential force as shown in Equation 6.1.

$$P \quad = \quad Ft*Vs \qquad\qquad (6.1)$$

Where

P = Power, Watt or N*m/s

Ft = Tangential force, N

Vs = Grinding speed, m/s

In addition, the cross head speed (f), another significant parameter in the spherical grinding system, could be equivalent to work table speed or feed rate in the conventional grinding conveying specimens to encounter grinding wheel. Increasing cross head speed resulted in higher grinding forces, conformed to the results from the work developed by Liu *et al.* (2001) for surface grinding dense ceramic materials and Pei and Starsbaugh (2002) for vertical grinding silicon wafers.

Grinding with the smaller abrasive grit size (A) contributed to greater grinding forces, which was different from the results from the research presented by Liu *et al.* (2001); Qi *et al.* (1997); Plaskos *et al.* (2003) for dense materials. In general, larger abrasive grit size leads to larger depth of cut and contact stress between the grit and the work piece, resulting in greater grinding force per grit (Liu *et al.,* 2002). The contradict result for porous material grinding in this research could be explained that

inhomogeneous microstructures and mechanical properties may give high variation in grinding forces. The more porosity, the less strength properties and consequently the less grinding force as stated by Kalpakjian and Schmid (2001) that not only grinding conditions such as cutting speed, feed rate, and depth of cut but also strength of materials being ground can affect grinding force for material removal processes.

6.2.2 Relationship between Grinding Force Signal Characteristics and Spherical Forming

From the grinding force profiles illustrated in Chapter IV for grinding force signal analysis in time domain, the slope of linear estimations was investigated for various finished shapes in the spherical forming. Table 6.2 and 6.3 summarized the slopes and root mean squares of tangential (Ft) and normal (Fn) force, finished diameter (D), circularity error (CE), and finished shape resulting from the selected grinding condition for Replication 1 and 2, respectively. The relation among the slopes of tangential and normal force signals, finished shape, and circularity error was graphically illustrated via matrix plots in Figure 6.2 to 6.4. It was found that the slopes of finished sphere shapes generated from the grinding speed range of 2.83 to 3.77 m/s were obviously distinguished and between those of partial sphere, squircle and egg shapes. The lower slopes contributed to partial sphere and squircle shape formation. On the other hand, the higher slopes gave finished egg shapes for all grinding conditions.

In addition, summarized statistics in Table 6.4 and average values of the slope graphically shown in Figure 6.5 could give an obvious distinction of grinding force signal characteristics for various finished shapes. The slopes of tangential and normal force signal for finished sphere shape from all conditions were reported in average of 0.64×10^{-4} N/s and 8.2×10^{-4} N/s, respectively. While, the 95% confidence intervals were 0.19×10^{-4} N/s and 1.1×10^{-4} N/s for tangential force and 6.3×10^{-4} N/s and 9.9×10^{-4} N/s for normal force. It could be observed from the tangential force (Ft) profiles that stable forces applied on the specimen according to the slope nearly zero contributed to the finished sphere shape formation. Storlarski and Tobe (1997) stated that lapping loads applied remarkably affected roundness errors of the silicon nitride ball, but they did not illustrate any indications of grinding force patterns. In this

research, the attempt of studying grinding force profiles in spherical forming was in depth investigated.

Aside from time domain for grinding force signal analysis, frequency domain was also investigated in terms of spectral density meaning to the grinding force intensity at various frequencies. Table 6.5 and 6.6 illustrated the peak frequencies and root mean squares of tangential (Ft) and normal (Fn), finished diameter (D), circularity error (CE), and finished shape from the selected grinding condition for Replication 1 and 2, respectively. It was observed that the peak frequencies of tangential force (Ft) were about 5.3, 6.2, and 7.1 Hz at the grinding speed of 2.83, 3.30, and 3.77 m/s respectively where the finished sphere shapes were formed.

For normal force (Fn), the peak frequencies were located at about 5.3 and 9.4 Hz for the grinding speed of 2.83 m/s, 6.2 and 7.5 Hz for the grinding speed of 3.30 m/s, and 5.8 and 7.1 Hz for the grinding speed of 3.77 m/s. At the lowest grinding speed of 1.41 m/s where egg shapes were formed, the low peak frequency approximately 2.6 and 2.4 Hz for tangential force (Ft) and normal force (Fn) were represented. For the partial sphere and squircle shape ground with the highest grinding speed of 5.18 m/s, peak frequencies did not obviously appear for all grinding conditions.

Summary of grinding force signal characteristics in terms of the average slope, the peak frequency, and the average root mean square of grinding forces for various finished shapes under the selected grinding conditions for grinding force signal analysis was illustrated in Table 6.7. The finished sphere shape having average diameter (D) of around 19.27 to 19.31 mm and circularity error (CE) of about 0.57 to 0.62 mm were formed at the average slopes from 0.28×10^{-4} to 0.89×10^{-4} N/s for tangential force (Ft) and 7.41×10^{-4} to 9.08×10^{-4} N/s for normal force (Fn) whereas the average root mean squares were between 0.14 and 0.18 N for Ft and 0.13 and 0.18 N for Fn. In addition, the obvious peak frequencies in the spectral densities of the finished sphere shape for tangential force (Ft) were between 5.3 and 7.1 Hz at the grinding speed between 2.83 and 3.77 m/s. For normal force (Fn), the peak frequencies performed at 5.3 and 9.4 Hz, 6.2 and 7.5 Hz, and 5.8 and 7.1 Hz for the grinding speeds of 2.83, 3.30, and 3.77 m/s for all cross head speeds and abrasive grit sizes, respectively.

From the frequency domain results of the tangential force (Ft), the shift of the peak frequencies from 2.6 to 7.1 Hz was performed as increasing grinding speeds (Vs) from 1.41 to 3.77 m/s corresponded to the work of Girardin *et al.* (2010) for tool wear detection in milling operation and the work developed by Fang *et al.* (2009) in the study of cutting force vibration for turning an aluminum alloy. In the past research, grinding or cutting force signals in time and frequency domain was applied for cutting tool failure monitoring under various working conditions particularly in metal cutting as presented by Kalvoda and Hwang (2010); Sarhan *et al.* (2001) and etc. Besides, An *et al.* (1997) demonstrated the patterns of the cutting force signals in the frequency domain affecting surface roughness of the finished specimen for diverse cutting tool materials and geometries in turning glass fiber reinforced plastics. In contrary, this research work presented grinding force monitoring for the attempt of investigating spherical surface forming for porous materials in the presence of polyurethane foam.

Table 6.2   Slope and root mean square of tangential (Ft) and normal (Fn) force, finished diameter (D), circularity error (CE), and finished shape from selected grinding conditions for Replication 1

Grinding conditions			Slope (x 10^{-4}N/s)		Root Mean Square (N)		D (mm)	CE (mm)	Shape
Vs (m/s)	f (mm/min)	A (µm)	Ft	Fn	Ft	Fn			
1.41	1	20	4.11	5.09	0.32	0.30	19.93	1.69	E
		53	1.30	3.93	0.19	0.20	19.85	1.20	E
	3	20	3.03	8.83	0.28	0.27	20.03	1.77	E
		53	5.67	15.04	0.36	0.39	19.57	1.49	E
	5	20	9.85	22.40	0.31	0.38	19.34	1.87	E
		53	6.18	28.15	0.44	0.46	19.84	1.93	E
2.83	1	20	0.57	2.97	0.12	0.14	19.48	0.53	S
		53	0.30	2.30	0.12	0.12	19.35	0.55	S
	3	20	-0.43	8.28	0.16	0.16	19.37	0.62	S
		53	-0.81	10.28	0.18	0.21	19.20	0.63	S
	5	20	2.34	13.73	0.16	0.18	19.36	0.67	S
		53	2.46	15.58	0.24	0.20	19.24	0.76	S
3.30	1	20	0.54	0.21	0.12	0.10	19.37	0.55	S
		53	-0.19	1.89	0.11	0.12	19.36	0.47	S
	3	20	0.84	10.70	0.18	0.21	19.31	0.48	S
		53	-0.14	6.28	0.11	0.12	19.18	0.61	S
	5	20	1.18	14.69	0.15	0.17	19.34	0.54	S
		53	-0.65	18.45	0.26	0.22	19.21	0.73	S
3.77	1	20	0.40	2.13	0.11	0.11	19.38	0.47	S
		53	-0.13	0.55	0.10	0.07	19.33	0.49	S
	3	20	3.21	13.28	0.22	0.23	19.38	0.59	S
		53	-0.44	4.65	0.10	0.09	19.18	0.56	S
	5	20	0.63	11.68	0.11	0.14	19.26	0.54	S
		53	2.86	18.03	0.19	0.20	19.24	0.60	S
5.18	1	20	-1.29	-0.66	0.11	0.07	18.21	1.35	PS
		53	-2.04	-0.74	0.10	0.06	15.74	0.77	SQ
	3	20	-2.98	0.21	0.10	0.08	19.09	0.77	SQ
		53	-3.48	-1.15	0.09	0.05	18.17	1.81	PS
	5	20	-3.71	0.05	0.09	0.06	18.94	1.21	PS
		53	-6.78	-1.35	0.11	0.07	19.02	0.83	PS

Remark: E = Egg, S = Sphere, PS = Partial sphere, SQ = Squircle

Table 6.3 Slope and root mean square of tangential (Ft) and normal (Fn) force, finished diameter (D), circularity error (CE), and finished shape from selected grinding conditions for Replication 2

Grinding conditions			Slope (x 10^{-4}N/s)		Root Mean Square (N)		D (mm)	CE (mm)	Shape
Vs (m/s)	f (mm/min)	A (μm)	Ft	Fn	Ft	Fn			
1.41	1	20	2.80	5.37	0.29	0.33	19.86	1.36	E
		53	2.15	5.46	0.22	0.28	19.64	1.11	E
	3	20	5.58	7.86	0.35	0.32	19.61	1.98	E
		53	6.24	11.73	0.36	0.37	19.67	1.49	E
	5	20	11.73	24.19	0.43	0.45	19.94	1.75	E
		53	3.85	11.89	0.22	0.22	19.71	1.71	E
2.83	1	20	0.42	4.21	0.20	0.23	19.42	0.51	S
		53	-0.15	2.18	0.14	0.12	19.38	0.53	S
	3	20	2.77	7.53	0.20	0.18	19.27	0.64	S
		53	-0.68	12.40	0.20	0.21	19.26	0.62	S
	5	20	3.11	15.72	0.24	0.23	19.18	0.75	S
		53	0.82	13.74	0.20	0.19	19.22	0.58	S
3.30	1	20	1.19	4.36	0.22	0.22	19.40	0.50	S
		53	0.38	1.87	0.11	0.11	19.40	0.46	S
	3	20	2.92	7.81	0.20	0.20	19.28	0.61	S
		53	-1.30	5.67	0.15	0.12	19.26	0.62	S
	5	20	-1.30	14.01	0.17	0.20	19.30	0.62	S
		53	-0.10	9.58	0.13	0.13	19.23	0.57	S
3.77	1	20	0.97	3.06	0.18	0.16	19.35	0.64	S
		53	0.16	1.60	0.11	0.08	19.33	0.52	S
	3	20	2.77	6.99	0.16	0.13	19.25	0.59	S
		53	-0.41	5.28	0.10	0.09	19.24	0.63	S
	5	20	-0.22	13.84	0.16	0.18	19.18	0.60	S
		53	-0.82	7.82	0.11	0.10	19.15	0.62	S
5.18	1	20	-0.77	0.28	0.15	0.09	19.19	0.68	PS
		53	-2.13	-1.13	0.14	0.09	16.49	0.78	SQ
	3	20	-0.13	4.32	0.14	0.11	19.36	0.70	PS
		53	-1.80	1.29	0.10	0.09	18.68	1.70	PS
	5	20	-0.50	2.54	0.16	0.08	19.06	1.05	PS
		53	-2.74	1.36	0.09	0.06	18.97	1.01	PS

Remark: E = Egg, S = Sphere, PS = Partial sphere, SQ = Squircle
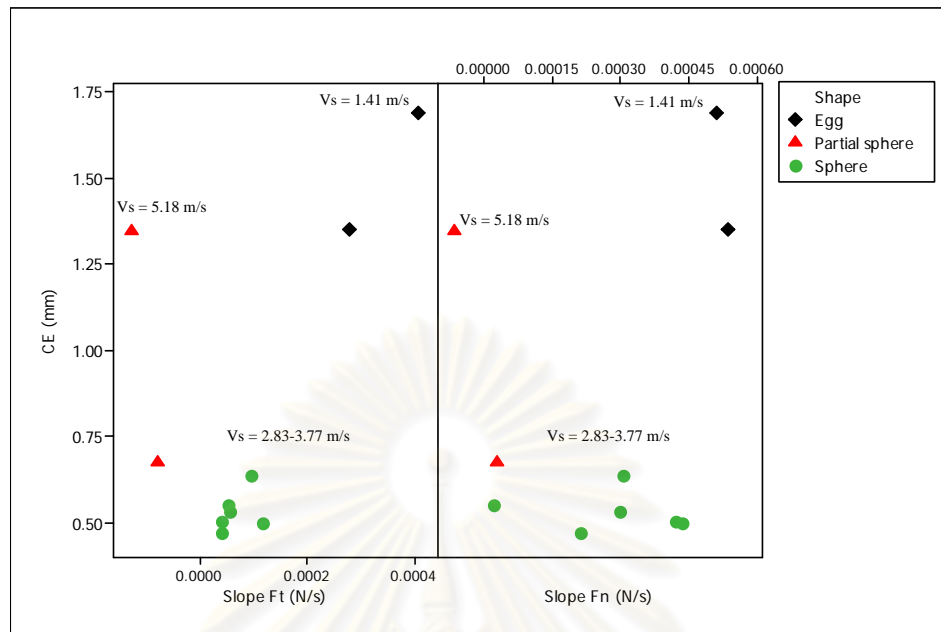
a) Abrasive grit size (A) = 20 µm
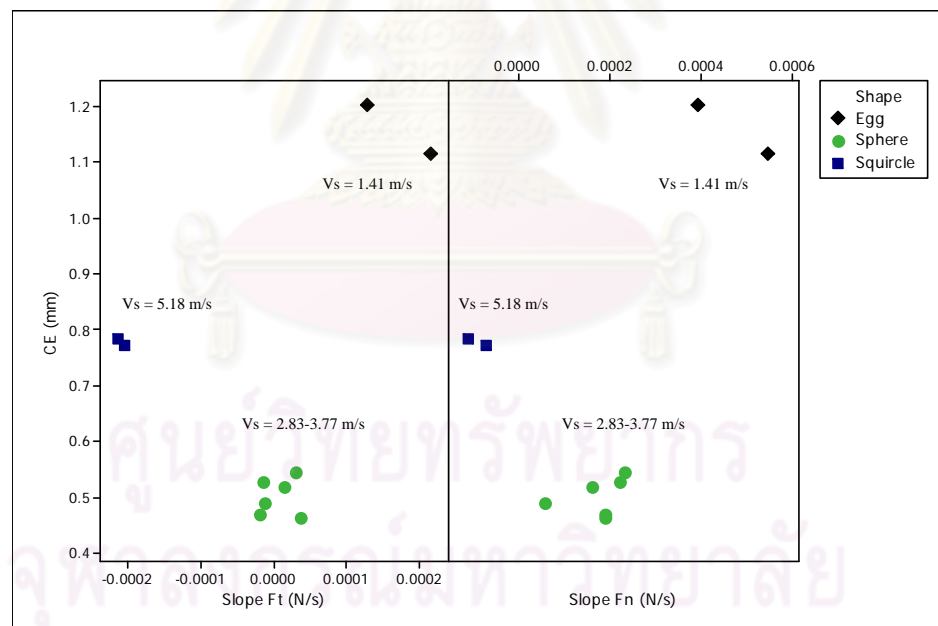
b) Abrasive grit size (A) = 53 µm

Figure 6.2   Relationships among slope of tangential (Ft) and normal (Fn) force
signal, circularity errors (CE), and finished shapes for cross head speed
(f) of 1.0 mm/min with various grinding speeds (Vs): a) Abrasive grit
size (A) = 20 µm and b) Abrasive grit size (A) = 53 µm
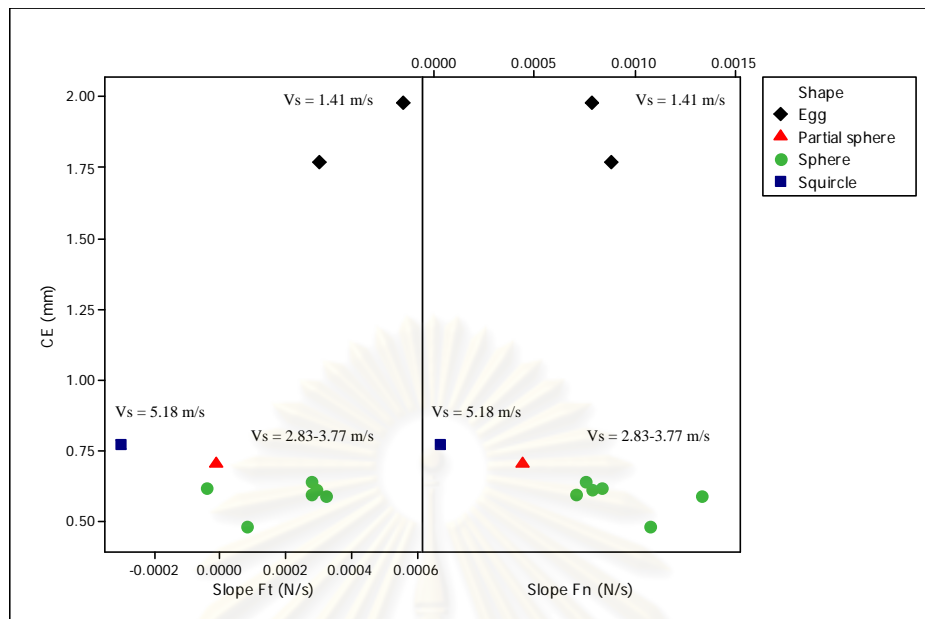
a) Abrasive grit size (A) = 20 µm for various grinding speeds (Vs)
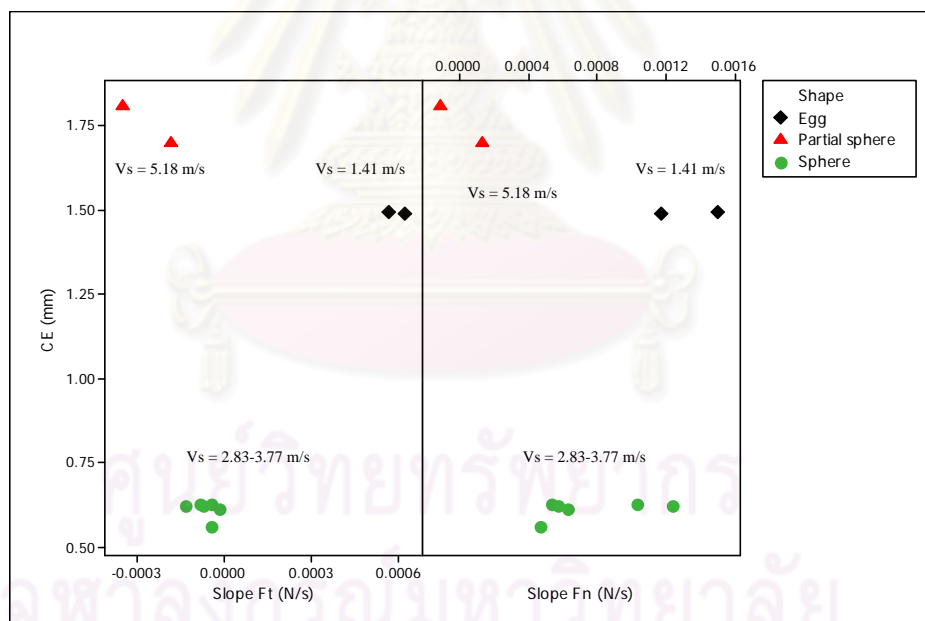
b) Abrasive grit size (A) = 53 µm for various grinding speeds (Vs)

Figure 6.3   Relationships among slope of tangential (Ft) and normal (Fn) force signal, circularity errors (CE), and finished shapes for cross head speed (f) of 3.0 mm/min with various grinding speeds (Vs): a) Abrasive grit size (A) = 20 µm and b) Abrasive grit size (A) = 53 µm
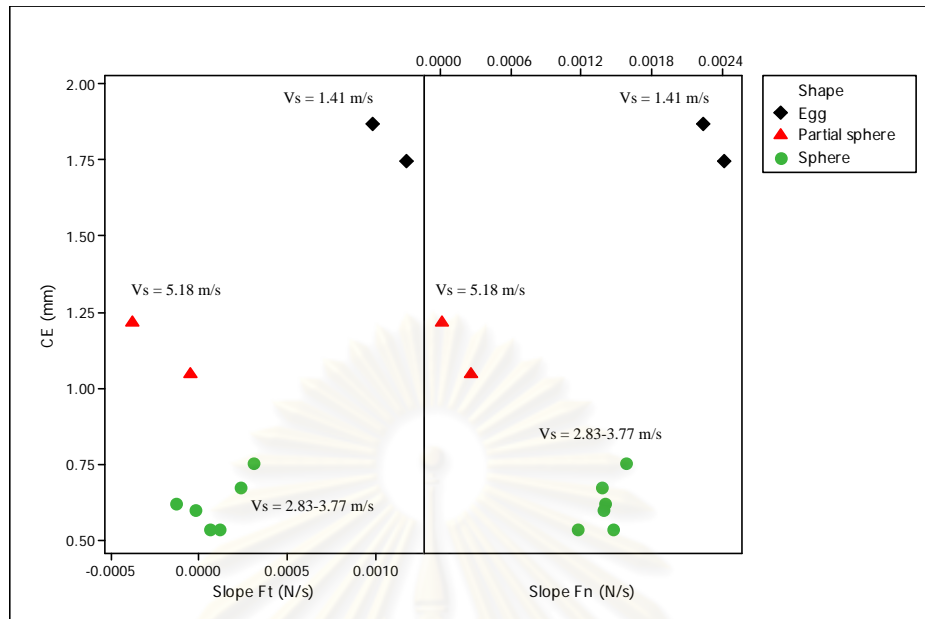
a) Abrasive grit size (A) = 20 µm for various grinding speeds (Vs)
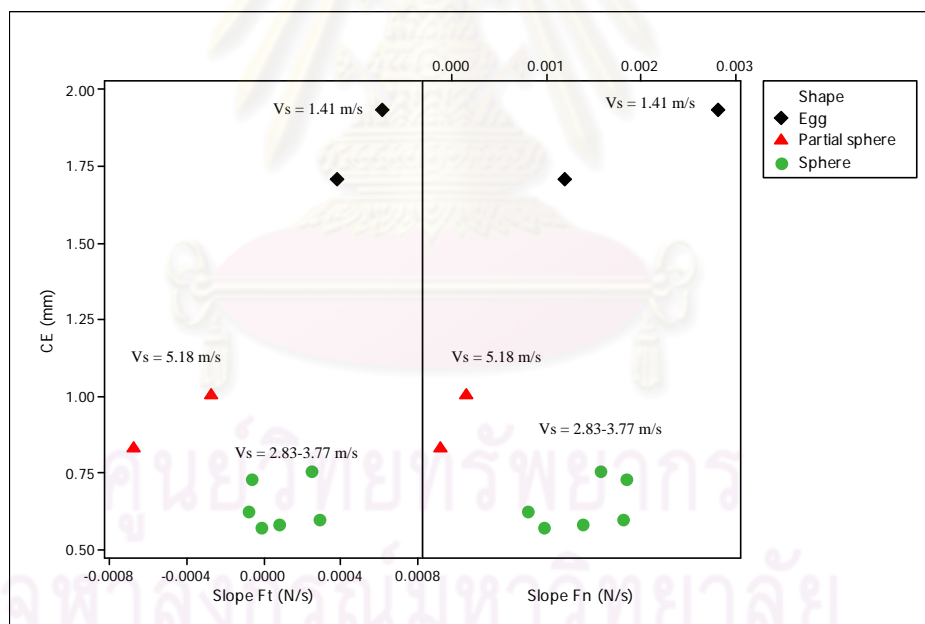
b) Abrasive grit size (A) = 53 µm for various grinding speeds (Vs)

Figure 6.4   Relationships among slope of tangential (Ft) and normal (Fn) force
signal, circularity errors (CE), and finished shapes for cross head speed
(f) of 5.0 mm/min with various grinding speeds (Vs): a) Abrasive grit
size (A) = 20 µm and b) Abrasive grit size (A) = 53 µm

Table 6.4   Summarized statistics for slope of Ft and Fn by finished shapes

Shape	Slope of Ft (x 10^{-4} N/s)			Slope of Fn (x 10^{-4} N/s)			N
	95% C.I.	Avg	SD	95% C.I.	Avg	SD	
Egg	[3.3, 7.2]	5.2	3.1	[7.2, 17.7]	12.5	8.3	12
Sphere	[0.19, 1.1]	0.64	1.3	[6.3, 9.9]	8.2	5.4	36
Partial sphere	[-4.0, -0.75]	-2.4	2.1	[-0.68, 2.2]	0.74	1.9	9
Squircle	[-3.7, -1.1]	-2.4	0.5	[-2.3, 1.2]	-0.55	0.69	3

Remark: C.I. = Confidence interval, Avg = Average, SD = Standard deviation,

   N = Number of specimen
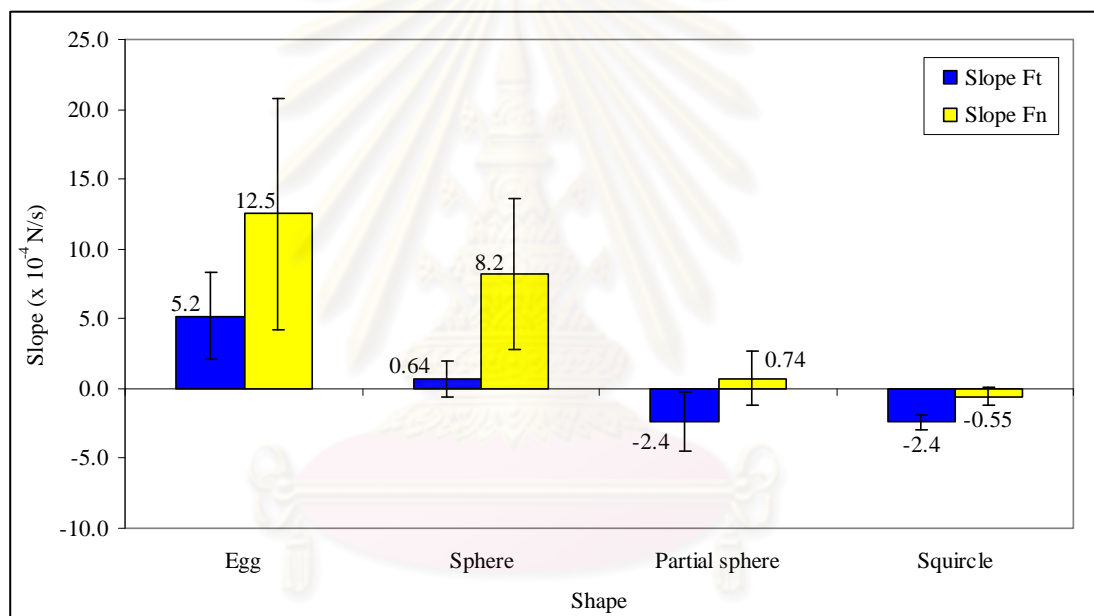
Figure 6.5   Averaged slope values of Ft and Fn for various finished shapes

Table 6.5   Peak frequency and root mean square of tangential (Ft) and normal (Fn)
force, finished diameter (D), circularity error (CE), and finished shape
from selected grinding conditions for Replication 1

Grinding conditions			Peak Freq. (Hz)		Root Mean Square (N)		D (mm)	CE (mm)	Shape
Vs (m/s)	f (mm/min)	A (μm)	Ft	Fn	Ft	Fn			
1.41	1	20	2.5	2.5	0.32	0.30	19.93	1.69	E
		53	2.6	2.6	0.19	0.20	19.85	1.20	E
	3	20	2.6	2.3	0.28	0.27	20.03	1.77	E
		53	2.5	2.3	0.36	0.39	19.57	1.49	E
	5	20	2.6	-	0.31	0.38	19.34	1.87	E
		53	2.6	-	0.44	0.46	19.84	1.93	E
2.83	1	20	5.3	5.3, 9.5	0.12	0.14	19.48	0.53	S
		53	5.4	5.4, 9.3	0.12	0.12	19.35	0.55	S
	3	20	5.3	5.3	0.16	0.16	19.37	0.62	S
		53	5.3	-	0.18	0.21	19.20	0.63	S
	5	20	-	5.2	0.16	0.18	19.36	0.67	S
		53	5.4	5.4, 9.3	0.24	0.20	19.24	0.76	S
3.30	1	20	6.3	6.3, 7.6	0.12	0.10	19.37	0.55	S
		53	6.2	6.2, 7.5	0.11	0.12	19.36	0.47	S
	3	20	6.2	6.2	0.18	0.21	19.31	0.48	S
		53	6.2	6.2, 7.5	0.11	0.12	19.18	0.61	S
	5	20	-	-	0.15	0.17	19.34	0.54	S
		53	-	-	0.26	0.22	19.21	0.73	S
3.77	1	20	7.1	5.8, 7.1	0.11	0.11	19.38	0.47	S
		53	7.1	5.9	0.10	0.07	19.33	0.49	S
	3	20	7.1	5.8, 7.1	0.22	0.23	19.38	0.59	S
		53	7.0	5.9	0.10	0.09	19.18	0.56	S
	5	20	7.1	5.8	0.11	0.14	19.26	0.54	S
		53	7.1	5.9	0.19	0.20	19.24	0.60	S
5.18	1	20	-	-	0.11	0.07	18.21	1.35	PS
		53	-	-	0.10	0.06	15.74	0.77	SQ
	3	20	-	-	0.10	0.08	19.09	0.77	SQ
		53	-	-	0.09	0.05	18.17	1.81	PS
	5	20	-	-	0.09	0.06	18.94	1.21	PS
		53	-	-	0.11	0.07	19.02	0.83	PS

Remark: E = Egg, S = Sphere, PS = Partial sphere, SQ = Squircle

Table 6.6   Peak frequency and root mean square of tangential (Ft) and normal (Fn) force, finished diameter (D), circularity error (CE), and finished shape from selected grinding conditions for Replication 2

Grinding conditions			Peak Freq. (Hz)		Root Mean Square (N)		D (mm)	CE (mm)	Shape
Vs (m/s)	f (mm/min)	A (µm)	Ft	Fn	Ft	Fn			
1.41	1	20	2.6	2.5	0.29	0.33	19.86	1.36	E
		53	2.6	2.6	0.22	0.28	19.64	1.11	E
	3	20	2.5	2.3	0.35	0.32	19.61	1.98	E
		53	2.5	2.5	0.36	0.37	19.67	1.49	E
	5	20	2.6	2.2	0.43	0.45	19.94	1.75	E
		53	-	-	0.22	0.22	19.71	1.71	E
2.83	1	20	5.2	5.2, 9.5	0.20	0.23	19.42	0.51	S
		53	5.4	5.3, 9.3	0.14	0.12	19.38	0.53	S
	3	20	5.4	5.4, 9.3	0.20	0.18	19.27	0.64	S
		53	5.3	9.5	0.20	0.21	19.26	0.62	S
	5	20	-	5.1	0.24	0.23	19.18	0.75	S
		53	-	-	0.20	0.19	19.22	0.58	S
3.30	1	20	6.2	6.2, 7.5	0.22	0.22	19.40	0.50	S
		53	6.2	6.3, 7.5	0.11	0.11	19.40	0.46	S
	3	20	6.2	6.2, 7.5	0.20	0.20	19.28	0.61	S
		53	6.2	6.3, 7.5	0.15	0.12	19.26	0.62	S
	5	20	6.2	5.9, 7.6	0.17	0.20	19.30	0.62	S
		53	-	-	0.13	0.13	19.23	0.57	S
3.77	1	20	7.1	5.8, 7.1	0.18	0.16	19.35	0.64	S
		53	7.1	5.8, 7.1	0.11	0.08	19.33	0.52	S
	3	20	7.1	5.8	0.16	0.13	19.25	0.59	S
		53	7.1	5.8, 7.1	0.10	0.09	19.24	0.63	S
	5	20	7.0	6.9	0.16	0.18	19.18	0.60	S
		53	7.1	5.8	0.11	0.10	19.15	0.62	S
5.18	1	20	-	-	0.15	0.09	19.19	0.68	PS
		53	-	-	0.14	0.09	16.49	0.78	SQ
	3	20	-	-	0.14	0.11	19.36	0.70	PS
		53	-	-	0.10	0.09	18.68	1.70	PS
	5	20	-	-	0.16	0.08	19.06	1.05	PS
		53	-	-	0.09	0.06	18.97	1.01	PS

Remark: E = Egg, S = Sphere, PS = Partial sphere, SQ = Squircle

Table 6.7   Summarized grinding force characteristics of various finished shapes from selected grinding conditions

Grinding conditions			Avg. Slope (x 10^{-4}N/s)		Avg. Peak freq. (Hz)		Avg. Root mean square (N)		D (mm) Avg ± SD	CE (mm) Avg ± SD	Finished shape
Vs (m/s)	f (mm/min)	A (µm)	Ft	Fn	Ft	Fn	Ft	Fn			
1.41	1.0, 3.0, 5.0	20, 53	5.2	12.5	2.6	2.4	0.31	0.33	19.75 ± 0.19	1.61 ± 0.28	Egg
2.83	1.0, 3.0, 5.0	20, 53	0.89	9.08	5.3	5.3, 9.4	0.18	0.18	19.31 ± 0.10	0.62 ± 0.08	Sphere
3.30	1.0, 3.0, 5.0	20, 53	0.28	7.96	6.2	6.2, 7.5	0.16	0.16	19.30 ± 0.07	0.56 ± 0.08	Sphere
3.77	1.0, 3.0, 5.0	20, 53	0.75	7.41	7.1	5.8, 7.1	0.14	0.13	19.27 ± 0.08	0.57 ± 0.06	Sphere
5.18	1.0, 3.0, 5.0	20, 53	-2.4	0.74	-	-	0.12	0.08	18.85 ± 0.41	1.15 ± 0.41	Partial sphere
5.18	1.0, 3.0	20, 53	-2.4	-0.55	-	-	0.11	0.08	17.11 ± 1.76	0.77 ± 0.01	Squircle

6.3 Grinding Force Ratio (R)

Grinding force ratio (R = Ft $_{RMS}$ / Fn $_{RMS}$), the proportion between tangential and normal force, may be used to describe the machining difficulty of materials during grinding, meaning to the cutting ability of grinding wheels (Chen *et al*, 2009). From the experimental results, grinding force ratio was between 0.80 and 2.15 according to Table 4.6 and slightly increased as increasing grinding speed (Vs) being the most significant parameter with 65.4 % contribution. The grinding force ratio from the spherical grinding system for porous polyurethane foam performed as the same pattern as those from the work presented by Yin *et al*. (2005); Agarwal and Rao (2008); Chen *et al.* (2009) for zirconia and silicon nitride in conventional surface grinding. At a high speed grinding, the ratio of tangential and normal force was higher than those of a conventional speed grinding. However, the grinding force ratio range from this research was revealed to be markedly higher than those from the previous work as mentioned.

Compared with the high speed surface grinding of dense ceramics developed by Huang *et al.* (2001) in Figure 6.6, the slope (0.8218) of the linear line from all experimental results of the spherical grinding system in Figure 6.7 was obviously higher than the slope (0.29145) of the previous work, implying high machining ability. This could be explained that porous materials have very low strength due to their pore structure matrixes resulting in susceptible material removal and a high grinding ability.

From the results in Figure 5.15 and 5.16, it was observed during experiment run that when increasing grinding speed above 3.77 m/s, the ground specimen was induced to float and orbit above the bottom of the circular groove pad to encounter the grinding wheel. Therefore, the interface areas between the specimen and the grinding wheel were larger than those between the specimen and the circular groove, leading to low normal forces acting on the dynamometer and consequently a high grinding force ratio.

Aside from indicating machining ability, the grinding force ratio in the spherical grinding could imply the spherical formation as well. In Figure 6.8, the root mean squares of tangential (Ft) and normal (Fn) force for various finished shapes from the selected grinding conditions for signal analysis were plotted versus each

other. Linear estimation with no interception and R-Square were illustrated for each finished shape. From the plot, it was found that the estimated grinding force ratio (the slope of linear equation) around 1.42 to 1.51 could give squircle and partial sphere formation with the R-Square of 0.491 and 0.1972, respectively. The estimated ratio of 0.99 with the R-Square of 0.792 contributed to finished sphere shapes formed, and at the ratio of 0.95 with R-square of 0.8847 egg shape came out. However, to quantify the grinding force ratio for various finished shapes summarized statistics in terms of 95% confidence interval, average, and standard deviation were demonstrated in Table 6.8. The finished sphere shape was ground with the average grinding force ratio of 1.03 ± 0.15 with 95% confidence interval between 0.98 and 1.08. The average grinding force ratios of the other shapes were 0.95 ± 0.08 for egg shape, 1.44 ± 0.18 for squircle, and 1.59 ± 0.29 for partial sphere. Variation in grinding force ratio for each shape could be affected by the variation of pore structures of the material being ground that normally influence the mechanical strengths and grinding forces.
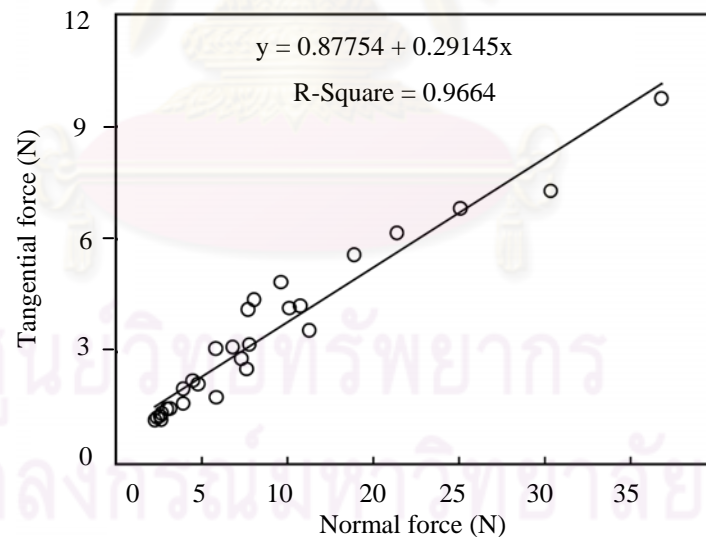
Figure 6.6   Relationship between specific tangential and normal force for high speed surface grinding of dense ceramic (Huang *et al.,* 2001)
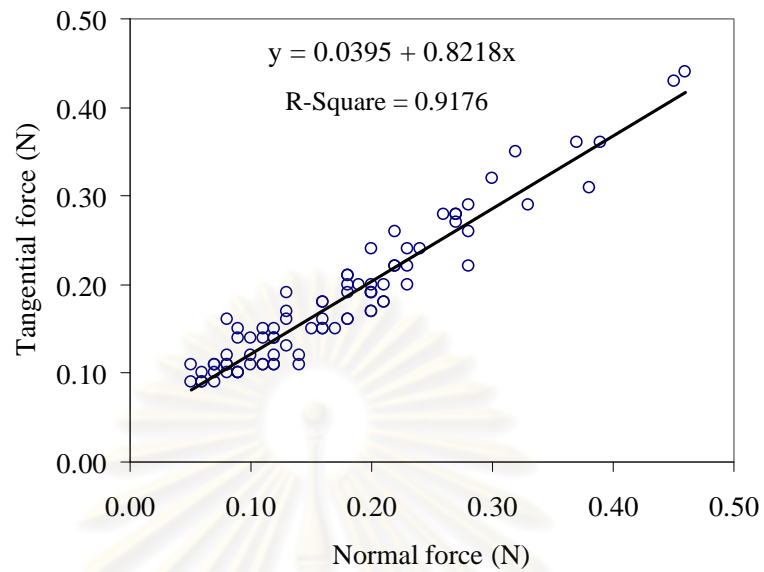
Figure 6.7   Relationship between tangential and normal force for spherical grinding
of porous polyurethane foam
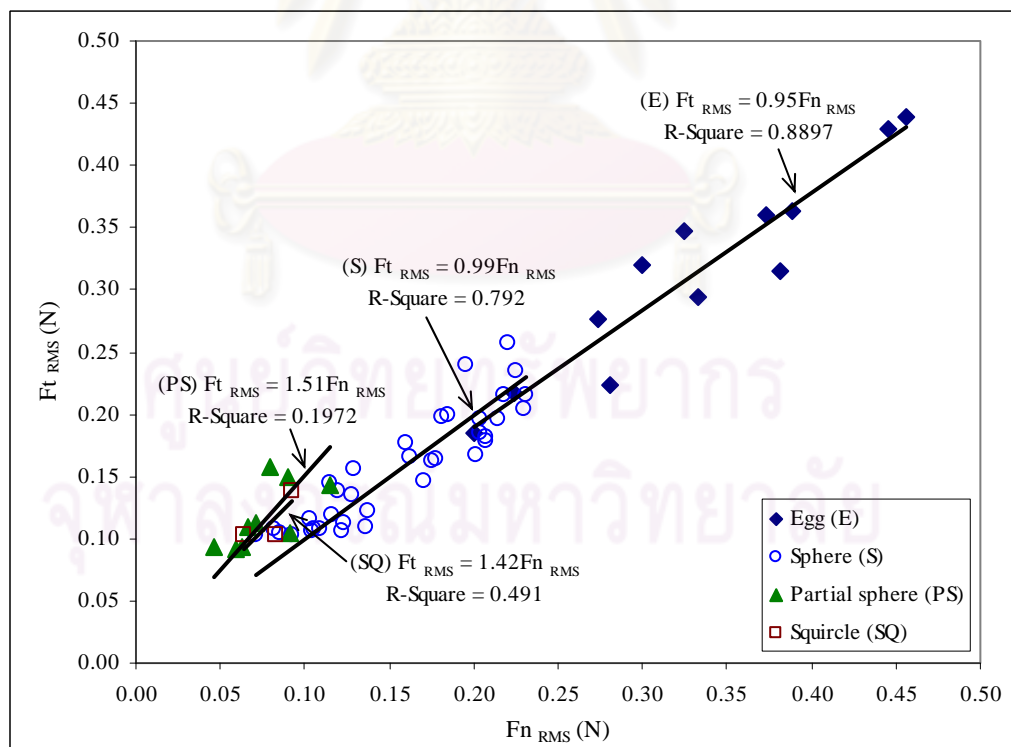
Figure 6.8   Relationship between tangential (Ft) and normal (Fn) force for selected
various finished shapes

Table 6.8   Summarized statistics for grinding force ratio by finished shapes

Shape	Grinding force ratio (R = Ft $_{RMS}$ / Fn $_{RMS}$)			
	95% C.I.	Avg	SD	N
Egg	[0.90, 1.00]	0.95	0.08	12
Sphere	[0.98, 1.08]	1.03	0.15	36
Partial sphere	[1.40, 1.78]	1.59	0.29	9
Squircle	[1.23, 1.65]	1.44	0.18	3

Remark: C.I. = Confidence interval, Avg = Average, SD = Standard deviation,

N = Number of specimen

6.4 Material Removal Rate (MRR)

As can be seen from the results in Chapter V, material removal rate was remarkably affected by cross head speed (f) of circular groove pad that was dependent on different time consumption for each head speed used. Total distance of circular groove pad from initial (31.30 mm.) to final (19.50 mm.) head distance was fixed to be 11.8 mm for all grinding conditions. As a result, the faster cross head speed, the lesser time consumed and the higher removal rate. Interval time spent for each cross head speed to reach the same distance of 11.8 mm. was shown in Table 6.9.

In addition, grinding speed (Vs) and abrasive grit size (A) were also declared to be statistically significant according to P – value less than 0.05 in spite of low contribution of 0.3% and 0.6% in Table 5.11. This could be discussed that increasing grinding speed resulted in finished diameter reduction as explained by Archard's wear equation and consecutively affected material removal rate. Also, because of more penetrating depth of cut, larger abrasive grit size used led to small finished diameters and high removal rates.

Table 6.9   Time consumption for various cross head speeds

Cross head speed; f (mm/min)	Time; T (min)
1.0	11.80
3.0	3.93
5.0	2.36

6.5 Specific Grinding Energy (u)

Specific grinding energy is one of the most important characteristics in material removal processes, which is defined as the energy expended per unit volume of material removal (Malkin and Hwang, 1996). Specific grinding energy in the spherical grinding porous polyurethane foam was ranged from 7.5 to 88 MJ/m^3.

From the statistical results, cross head speed (f) was the most influential parameter with 83.3% contribution. The main effect plot in Figure 5.33 showed that the specific grinding energy substantially decreased when increasing cross head speeds. This is well agreed with much previous work both in conventional surface grinding for dense materials and in orthogonal cutting for porous materials that specific grinding energy decreased as increasing material removal rate, which is directly related to increasing cross head speed and depth of cut. Malkin and Hwang (1996) stated that specific grinding energy was inverted to material removal rate. Tso (1995) presented a downward trend of specific grinding energy in surface grinding for Inconel 718 with increasing feed rate of the work piece material. Plaskos *et al.* (2003) concluded that specific cutting energy for bone cutting decreased for the increase of depth of cut. And, Song *et al.* (2009) presented the inverse relationship among specific grinding energy, depth of cut and feed rate of dental cutting for leucite-reinforced glass ceramic. Although having no explicit impact, increasing grinding speed seemingly contributed to a higher specific grinding energy as illustrated from experimental results in Figure 5.19 and 5.20 corresponding to the work of Yin *et al.* (2005) for surface grinding of alumina.

From much previous research, specific grinding energy was strongly dependent on the material to be ground as well as grinding conditions such as grinding wheel speed, work piece speed, and depth of cut. The higher strength of materials the higher energy required for chip formation. In ductile regime grinding used to reduce crack damages and to improve surface integrity for brittle materials, high specific grinding energy occurred when increasing grinding wheel speed and reducing work piece speed and depth of cut.

In this research, the magnitude of specific grinding energy reported from 7.5 to 88 MJ/m^3 was very low when compared with that from approximately 8,000 to 98,000 MJ/m^3 for surface grinding of alumina investigated by Huang and Liu (2003). This is because alumina has distinguished strength properties than polyurethane foam comprising pore structures resulting in low mechanical strength. Besides the material structures, atomic bond is one of the possible reasons influencing material strength and consequently the variations in specific grinding energy as stated by Ramesh *et al.* (2001).

Chapter VII

Conclusions

This chapter summarized the outcomes from this research work for spherical grinding porous polyurethane foam. In addition, future research work, and suggestions were also proposed to further enhance the spherical grinding technique more relevant and precise.

7.1 Conclusions

1) Porous polyurethane foam used as a specimen in this research had Pore size between 200 and 400 µm, Bulk density of 0.125 Mg/m^3, Porosity of 89.6%, Flexural strength of 2.14 MPa and Compressive strength of 1.05 MPa with Weibull modulus of 4.52 and 7.88, respectively.

2) Grinding speed (Vs), cross head speed (f), interaction between grinding speed and cross head speed (Vs*f), interaction between grinding speed and abrasive grit size (Vs*A), interaction between cross head speed and abrasive grit size (f*A), and interaction of the three parameters (Vs*f*A) significantly affected circularity error (CE) of the ground specimen.

3) All grinding parameters, including grinding speed (Vs), cross head speed (f), abrasive grit size (A), and their interactions (Vs*f, Vs*A, f*A, Vs*f*A) significantly influenced on the finished diameter (D). In addition, the gradual decrease in finished diameter occurred at the grinding speed between 2.83 to 4.24 m/s.

4) Finished shapes after grinding found were 4-types which were egg, sphere, partial sphere, and squircle.

5) The finished sphere specimen could be formed with the range of 95% confidence interval for the circularity error (CE) between 0.57 and 0.61 mm and the finished diameter (D) between 19.28 and 19.32 mm.

6) Grinding speed (Vs) between 2.83 and 3.77 m/s could form the spherical work pieces whereas the grinding speed of 3.30 m/s, cross head speed (f) of 1.0 mm/min, and abrasive grit size (A) of 53 μm provided the minimum circularity error of 0.47 mm.

7) Tangential force (Ft) and normal force (Fn) were influenced by grinding speed (Vs), cross head speed (f), and abrasive grit size (A), and also were markedly decreased with increasing grinding speeds. Grinding force ratio (R) was significantly affected by grinding speed (Vs) and abrasive grit size (A) and was increased with increasing grinding speeds.

8) Material removal rate (MRR) was statistically affected by grinding speed (Vs), cross head speed (f), and abrasive grit size (A) and obviously increased with increasing cross head speeds from 1.0 to 5.0 mm/min.

9) Cross head speed (f), abrasive grit size (A), and their interaction (f*A) significantly influenced on the specific grinding energy (u) which was reduced by increasing the cross head speeds.

10) Grinding speed (Vs) was the most influential factor in spherical forming porous polyurethane foam. The circularity error (CE), finished diameter (D), tangential force (Ft), normal force (Fn), and grinding force ratio (R) were contributed by 75.7%, 39.6%, 55.3%, 62.6%, and 65.4%, respectively.

11) Cross head speed (f) mainly affected on the material removal rate (MRR) and specific grinding energy (u) with the contributions of 99.9% and 83.3%, respectively.

12) From the time domain analysis of the selected grinding conditions, the slopes of tangential and normal force signals in linear estimation were in average of 0.64×10^{-4} N/s and 8.2×10^{-4} N/s, respectively at the grinding speeds (Vs) between 2.83 and 3.77 m/s for all cross head speeds and abrasive grit sizes where the spherical formation was performed.

13) From the frequency domain analysis of the selected grinding conditions, the peak frequencies of the finished sphere specimens formed were ranged between 5.3 and 7.1 Hz at the grinding speed between 2.83 and 3.77 m/s for tangential force signal, and were 5.3 and 9.4 Hz, 6.2 and 7.5 Hz, and 5.8 and 7.1 Hz at the grinding speeds of 2.83, 3.30, and 3.77 m/s respectively for normal force signal for all cross head speeds and abrasive grit sizes.

14) Grinding force ratio ($R = Ft_{RMS} / Fn_{RMS}$) in average of 1.03 ± 0.15 with 95% confidence interval between 0.98 and 1.08 could indicate spherical formation in the spherical grinding system developed at the grinding speeds between 2.83 and 3.77 m/s for all cross head speeds and abrasive grit sizes.

7.2 Future Research Work

After this research work conducted for the spherical grinding system of porous polyurethane foam, there were some interesting research topics which could be further studied in the field of machining porous materials as following,

1) The effect of material properties such as bulk density and mechanical strengths on grinding forces and spherical forming should be investigated.

2) Other abrasive grit sizes and types could be carried out to improve surface integrity and circularity error of the ground specimen. Also, efficiency and machining cost should be studied.

3) Further study of precise spherical measurement such as Coordinate Measuring Machine (CMM) may be used to measure finished diameter and circularity error. However, measuring methods should be carefully selected because pores of the material can lead to error in measurement.

4) Proper grinding conditions in terms of grinding speed, cross head speed, and abrasives for other porous material parts such as commercial hydroxyapatite implants for eye ball surgery should be further investigated via the spherical grinding system as developed in order to improve dimensional accuracy, reduce shape variations, and reduce risk of crack damages resulting from conventional hand grinding. This could minimize time consumption and product prices.

7.3 Research Suggestions

Suggestions in terms of grinding techniques to form wide ranges of finished sizes and a sphere shape of other materials using the spherical grinding system in this research work were proposed as follows,

1) To form a bigger finished size of sphere than 19.30 mm in average as illustrated in this research, a bigger as received cube specimen and also the new circular groove could be required.

2) The smaller finished size of sphere could be obtained from the spherical grinding system proposed with the circular groove size of 11.30 mm in radius and as received cube specimen of 21 mm by adjusting the final head distance (H_i) below 19.50 mm.

3) As received specimen nearly sphere shape produced from various porous material fabrication techniques could contribute to shorter processing time than that from as received cube specimen as proposed in this research for spherical forming.

4) A stand alone machine of the spherical grinding with the circular groove system could be equipped with the adjustable grinding speed and cross head speed control unit, grinding force measurement, and in process monitoring system.

5) To form other porous materials in sphere shape, the ranges of grinding speed and cross head speed should be adjustable in order to receive grinding force ratio of 1.0.

References

Agarwal, S.; and Rao, P. V. Experimental investigation of surface/subsurface damage formation and material removal mechanisms in SiC grinding. <u>International Journal of Machine Tools & Manufacture</u> 48 (2008): 698-710.

An, S. O.; Lee, E. S.; and Noh, S. L. A study on the cutting characteristics of glass fiber reinforced plastics with respect to tool materials and geometries. <u>Journal of Materials Processing Technology</u> 68 (1997): 60-67.

ASTM D790-03. 2003. Standard Test Methods for Flexural Properties of Unreinforced and Reinforced Plastics and Electrical Insulating Materials, <u>American Society for Testing and Materials</u>, West Conshohocken, Pennsylvania, U.S.A.

ASTM D1621-04a. 2004. Standard Test Method for Compressive Properties of Rigid Cellular Plastics, <u>American Society for Testing and Materials</u>, West Conshohocken, Pennsylvania, U.S.A.

ASTM D1622-03. 2003. Standard Test Method for Apparent Density of Rigid Cellular Plastics, <u>American Society for Testing and Materials</u>, West Conshohocken, Pennsylvania, U.S.A.

Atzeni, E.; and Iuliano, L. Experimental study on grinding of a sintered friction material. <u>Journal of Materials Processing Technology</u> 196 (2008): 184-189.

Bagci, E.; and Aykut, S. A study of Taguchi optimization method for identifying optimum surface roughness in CNC face milling of cobalt-based alloy (stellite 6) <u>International Journal of Advanced Manufacturing Technology</u> 29 (2006): 940-947.

Bajpai, P. K.; and Benghuzzi, A., J. <u>Biomed. Mater. Res</u> 22 (1988): 1245-1266.

Barge, M.; Rech, J.; Hamdi H.; and Bergheau J. Experimental study of abrasive Process. Wear 264 (2008): 382-388.

Bross, I. D. J.," Critical Levels, Statistical Language and Scientific Inference," in Godambe VP and Sprott, eds Foundations of Statistical Inference. Holt, Rinehart & Winston of Canada. 1971.

Chalasani, R.; Warren, L. P.; Conway, R. M.; and Nissan, B. B. Porous Orbital Implants in Enucleation: A Systematic Review. SURVEY OF OPHTHALMOLOGY 52 (2007): 145-155.

Chaopanich, I.; Goyadoolya, K.; and Puajindanetr, S. Spherical Surface Forming Mechanism of Porous Materials via Groove Grinding System. The IE Network Conference (2007): 551-559.

Chelule, K. L.; Coole, T. J.; and Cheshire, D. G. An investigation into the machinability of hydroxyapatite for bone restoration implants. Journal of Materials Processing Technology 135 (2003): 242–246.

Chen, J.; Huang, H.; and Xu, X. An experimental study on the grinding of alumina with a monolayer brazed diamond wheel. International Journal of Advanced Manufacturing Technology 41 (2009): 16-23.

Chen, X.; and Rowe, W. B. ANALYSIS AND SIMULATION OF THE GRINDING PROCESS: PART II: MECHANICS OF GRINDING. Int. J. Mach. Tools Manufact 36 (1996): 883-896.

Childs, T. H. C.; Jones, D. A.; Mahmood, S.; Zhang, B.; Kato, K.; and Umehara, N. Magnetic fluid grinding mechanics. Wear 175 (1994) 189-198.

Childs, T. H. C.; Mahmood, S.; and Yoon, H. J. Magnetic fluid grinding of ceramic balls. Tribology International 28 (1995): 341-348.

Childs, T. H. C.; Mahmood, S.; and Yoon, H. J. The material removal mechanism in magnetic fluid grinding of ceramic ball bearings. Proceedings of the Institution of Mechanical Engineers Part B, 208 (B1) (1994): 47-60.

Cho, D. W.; Lee, S. J.; and Chu, C. N. The state of machining process monitoring research in Korea. International Journal of Machine Tools & Manufacture 39 (1999): 1697-1715.

Choi, Y. J.; Park, M. S.; and Chub, C. N. Prediction of drill failure using features extraction in time and frequency domains of feed motor current. International Journal of Machine Tools & Manufacture 48 (2008): 29-39.

Dallas, D. Tool and Manufacturing Engineering 3rd Edition, 1976.

Dhanish, B. P.; and Mathew, J. Effect of CMM point coordinate uncertainty on uncertainties in determination of circular features. Measurement 39 (2006): 522-531.

Eckert, K. L.; Roesler, U.; Mathey, M.; Mayer, J.; Wintermantel, F.; and Hofman, J. Open Porous Ceramics for Cell Transplantation Devices: a New Biomaterial, First Results. Bioceramics Vol.6 (1993): 251-255.

Evant, A. G.; and Marshall, D. B. Fundamentals of Friction and Wear of Materials. American Society of Mechanical Engineering (1981): 439-452.

Fang, M.; Pai, P. S.; and Mosquea, S. The effect of built-up edge on the cutting vibrations in machining 2024-T351 aluminum alloy. International Journal of Advanced Manufacturing Technology (2009).

Gadelmawla, E.S. Simple and efficient algorithms for roundness evaluation from the coordinate measurement data. Measurement 43 (2010): 223–235.

Gibson, L. J.; and Ashby, M. F. Cellular solids: Structure & Properties. Exeter, UK: PERGAMON PRESS, A. Wheaton & Co. Ltd., 1988.

Gilbert, D. G.; Ashby, M. F.; and Beaumont, P. W. R. J. Mat. Sci. 21, 3194 (1986).

Girardin, F.; Remond, D.; and Rigal, J. F. An original approach with a non-dedicated sensor. Mechanical Systems and Signal Processing 24 (2010): 1907-1920.

Griffith, A. A., et al. The phenomenon of rupture and flow in solids. Phil. Trans. R. Soc. London, Ser.A 221 (4) (1920): 163.

Hearn, G. E., and Metcalfe, A. V. Spectral Analysis in Engineering: Concepts and Cases. London: Arnold, 1995.

Hecker, R.; Liang, S.; Wu, X.; Xia, P.; and Wei, D. Grinding force and power modeling based on chip thickness analysis. International Journal of Advanced Manufacturing Technology (2004).

Hench, L. L. J. Am. Ceram. Soc. 81 (1998): 1705-1728.

Hing, K. A.; Best, S. M.; and Bonfield, W. Characterization of porous hydroxyapatite. Journal of Materials Science: Materials in medicine 10 (1999): 135-145.

Huec, J. C. L.; Schaeverbeke, T.; Clement, D.; Faber, J.; and Rebeller, A. L. Influence of porosity on the mechanical resistance of hydroxyapatite ceramics under compressive stress. Journal of Biomaterials 16 (1995): 113-118.

Huang, H.; and Liu, Y. Experimental investigations of machining characteristics and removal mechanisms of advanced ceramics in high speed deep grinding. International Journal of Machine Tools & Manufacture 43 (2003): 811-823.

Huang, H.; Liu, Y.; Teo, P. L.; and Hwee, L. K. High Speed Deep Grinding of Tetragonal Zirconia. SIMTech Technical Report (2001).

Huang, H.; Yin, L.; and Zhou, L. High speed grinding of silicon nitride with resin bond diamond wheels. Journal of Materials Processing Technology 141 (2003): 329-336.

Hwang, T.; Evans, C.; and Malkin, S. Size effect for specific energy in grinding of silicon nitride. Wear 229 (1999): 862-867.

ISO 1101. 1983. Technical Drawings – Geometrical Tolerancing, International Organization for Standardization, Geneva, Switzerland.

Japanese Society for Precision Engineering, Grinding Engineering, Omsha Publishing House, Tokyo, 1987.

Jiang, M.; and Komanduri, R. On the finishing of Si_3N_4 balls for bearing applications. Wear 215 (1998): 267-278.

Jordan, D. R., M.D. A new variety of Hydroxyapatite: The Chinese Implant, Ophthalmic Plastic and Reconstructive Surgery 15 (1999): 420-424.

Jordan, D. R., M.D. Fibrovascularization of Porous Polyethylene (Medpor) Orbital Implant in a Rabbit Model, Ophthalmic Plastic and Reconstructive Surgery 20 (2004): 136-143.

Kalpakjian, S. Manufacturing Processes for Engineering Materials 2nd Edition, 1992.

Kalpakjian, S., and Schmid, S. Manufacturing Engineering and Technology, 4th Edition, 2001.

Kamboj, R.; Dhara, S.; and Bhargava, P. Machining behavior of green gelcast ceramics. Journal of the European Ceramic Society 23 (2003): 1005–1011.

Kanada, T. Estimation of sphericity by means of statistical processing for roundness of spherical parts. Journal of Precision Engineering 20 (1997): 117 - 122.

Kang, J.; and Hadfield, M. Examination of the material removal mechanisms during the lapping process of advanced ceramic rolling elements. Wear 258 (2005): 2–12.

Kalvoda, T.; and Hwang, Y. R. A cuttertoolmonitoringinmachiningprocessusing Hilbert-Huang transform. International Journal of Machine Tools & Manufacture 50 (2010): 495-501.

Kang, J.; and Hadfield, M. Parameter optimization by Taguchi methods for finishing advanced ceramic balls using a novel eccentric lapping machine. Proc. Instn. Mech. Engrs. Part B J. Eng. 215 (2001): 69–78.

Kim, K. Effects of the Grinding Conditions on the Machining Elasticity Parameter. International Journal of the Korean Society of Precision Engineering 4 (2003): 62-67.

Knowles, J. Journal of Physics D: Applied physics 3 (1970): 1346-1351.

Komanduri, R.; Hou, Z. B.; Umehara, N.; Raghunandan, M; Jiang, M.; and Bhagavatula, S. R. A "gentle" method for finishing Si_3N_4 balls for hybrid bearing applications. Tribology Letters 7 (1999): 39-49.

Kwak, J. S.; Song, J. B. Trouble Diagnosis of the Grinding Process by Using AE Signals. International Journal of Machine Tools and Manufacture 41 (2001): 899-913.

Lacefield, W. R. An Introduction to Bioceramics, Hench L.L., and Wilson J. (Eds), Hydroxyapatite Coating. World Scientific, London, (1993): 223-238.

Lee, E. J.; Koh, Y.; Yoon, B.; Kim, H.; and Kim, H. W. Highly porous hydroxyapatite bioceramics with interconnected pore channels using camphene-based freeze casting. Materials Letters 61 (2007): 2270-2273.

Lee, R. T.; Hwang, Y. C.; and Chiou, Y. C. Lapping of ultra-precision ball surfaces part I: Concentric V-groove lapping system. International Journal of Machine Tools and Manufacture 46 (2006): 1146-1156.

Li, Y.; Gracewski, S. M.; Funkenbusch, P.; and Ruckman, J. Tool wear and profile development in contour grinding of optical materials, International Journal of Machine Tools and Manufacture 44 (2004): 427-438.

Liu, D. M. Influence of Porosity and Pore Size on the Compressive Strength of Porous Hydroxyapatite Ceramic. Ceramics International 23 (1997): 135-139.

Liu, R. and Li, D. Y. Modification of Archard's equation by taking account of elastic/pseudoelastic properties of materials. Wear. 251 (2001): 956-964.

Liu, T.; Latella, B.; and Zhang, L. Grinding of Ceramics: Strength, Surface Features and Grinding Conditions. Key Engineering Materials 196 (2001): 53-60.

Liu, X.; Zhang, B.; and Deng, Z. Grinding of nanostructured ceramic coatings: surface observations and material removal mechanisms. International Journal of Machine Tools & Manufacture 42 (2002): 1665-1676.

Malak, S. F.; and Anderson, I. A. Orthogonal cutting of polyurethane foam. International Journal of Mechanical Sciences 47 (2005): 867–883.

Malkin, S. Grinding technology, theory and applications of machining with abrasives. Society of Manufacturing Engineers (SME), Michigan, 1989.

Malkin, S.; and Hwang, T. W. Grinding Mechanisms for Ceramics, Annals of the ClRP, Vol.45/2, 1996.

Malkin, S.; and Kannappan, S. Effects of grain size and operating parameters on the Mechanics of grinding. J. Eng. Ind. Trans, ASME Ser. B 94 (1972): 833-842.

Malkin, S.; and Ritter, J. R. J. Eng. Ind., (1989) 165 – 174.

Marinescu, I. D.; Rowe, W. B.; Dimitrov, B.; and Inasaki, I. Tribology of Abrasive Machining Process, William Andrew Publishing, New York, U.S.A., 2004.

Marinescu, I. D.; Tonshoff, H. K.; and Inasaki, I. HANDBOOK OF CERAMIC GRINDING AND POLISHING, NOYES PUBLICATIONS, Park Ridge, New Jersey, U.S.A., WILLIAM ANDREW PUBLISHING, LLC, Norwich, New York, U.S.A., 2000.

Montanaro, L.; Jorand, Y.; Fantozzi, G.; and Negro, A. Ceramic Foams by Powder Processing. Journal of the European Ceramic Society 18 (1998): 1339-1350.

Moshfeghi, D. M.; Moshfeghi, A. A.; and Finger, P. T. Enucleation: Major review. SURVEY OF OPHTHALMOLOGY 44 (2000): 277-301.

Munoz, E. R.; Diaz, J. R.; Rodriguez, J. R.; Brostow, W.; and Castano, V. M. Hydroxyapatite spheres with controlled porosity for eye ball prosthesis: processing and characterization, Journal of Material Science: Materials in Medicine 12 (2001): 305-311.

Pabst, W.; Gregorova, E.; and Ticha, G. Elasticity of porous ceramics-A critical study of modulus-porosity relations. Journal of the European Ceramic Society 26 (2006): 1085-1097.

Pei, Z. J.; and Strasbaugh, A. Fine grinding of silicon wafers: designed experiments. International Journal of Machine Tools & Manufacture 42 (2002): 395-404.

Plaskos, C.; Hodgson, A. J.; and Cinquin, P. Modelling and Optimization of Bone-Cutting Forces in Orthopaedic Surgery, R.E. Ellis and T.M. Peters (Eds.): MICCAI LNCS 2878 (2003): 254–261.

Polonchuk, L.; Elbel, J.; Eckert, L.; Blum, J.; Wintermantel E.; and Eppenberger H.M., Biomaterials 21 (2000): 539-550.

Ponin, S. Study of Strength Properties of Cattle Bone Material Using Indentation Method, Master's Thesis, Department of Graduate School, Chulalongkorn University, 1987.

Preston, F. W. The theory and design of plate glass polishing machines. J Soc Glass Technol 11 (1927): 214–56.

Qi, H. S.; Rowe, W., B.; and Mills, B. Experimental investigation of contact behaviour in grinding. Tribology intemational 30 (1997): 283-294.

Raghunandan, M.; Umehara, N.; and Komanduri, R. On the possibility of chemo-mechanical action in magnetic float polishing of silicon nitride. ASME, J. of Tribology Vol.118 No.4 (1996): 721-727.

Raghunandan, M.; Umehara, N.; Noori-Khajavi, A.; and Komanduri, R. Trans. ASME J.Manufacturing Science & Engineering 119 (1997) 520.

Ramesh, K.; Yeo, S. H.; Gowri, S.; and Zhou, L. Experimental Evaluation of Super High-Speed Grinding of Advanced Ceramics. <u>International Journal of Advanced Manufacturing Technology</u> 17 (2001): 87-92.

Ravaglioli, A.; and Krajewski, A. <u>Mater. Sci. Forum</u> 250 (1997): 221-230.

Ravaglioli, A.; Krajewski, A.; Pantieri, I.; and Scarpa, G. <u>Ceram. Acta</u> 10 (1998): 19-30.

Rice, R. W.; and Speronello, B. K. Effect of Microstructure on Rate of Machining of Ceramics. <u>Journal of The American Ceramic Society</u> 59 (1976): 330-333.

Rodil, T. Edge effect on abrasive wear mechanisms and wear resistance in WC-6wt.%Co hardmetals, <u>Report in exchange program</u> (2006).

Rogers-foy, J. M.; Powers, D. L.; Brosnan, D. A.; Barefoot, S. F.; Friedman, R. J.; and LaBerge, M. <u>J. Invest. Surg</u>. 12 (1999): 263-275.

Salgado, D.; and Alonso, F. Tool Wear Detection in Turning Operations Using Singular Spectrum Analysis. <u>Journal of Materials Processing Technology</u> 171 (2006): 451-458.

Sarhan, A.; Sayed, R.; Nassr, A. A.; and El-Zahry, R. M. Interrelationships between cutting force variation and tool wear in end-milling. <u>Journal of Materials Processing Technology</u> 109 (2001): 229-235.

Samuel, G. L.; and Shunmugam, M. S. Evaluation of circularity and sphericity form coordinate measurement data. <u>Journal of Materials Processing Technology</u> 139 (2003): 90-95.

Shannon, C. E. "Communication in the presence of noise". Proc. Institute of Radio Engineers 37 (1949): 10-21.

Shen, J.; Luo, C.; Zeng, W.; Xu, X.; and Gao, Y. Ceramic grinding under constant pressure. Journal of Materials Processing Technology 129 (2002): 176-181.

Shaw, M. C. Principles of Abrasive Processes. Oxford University Press, Oxford, UK, 1996.

Song, L.; and Wang, D. Sphericity error evaluation based on 3D optical measurement. Proceedings of the Romanian Academy 8 (2007).

Song, X. F.; Yin, L.; and Han, Y. G. In-process assessment of dental cutting of a leucite-reinforced glass–ceramic. Medical Engineering & Physics 31 (2009): 214-220.

Sopyan; Mel, M.; Ramesh, S.; and Khalid, K. A. Porous hydroxyapatite for artificial bone applications. Science and Technology of Advanced Materials 8 (2007): 116–123.

Stolarski, T. A. Mechano-chemical wear of ceramics. JOURNAL OF MATERIALS SCIENCE 34 (1999): 3609 – 3622.

Stolarski, T. A.; and Tobe, S. The effect of accelerated material removal on roundness and residual stresses in ceramic balls. wear 205 (1997): 206-213.

Sun, J.; and Hong, G. S.; Rahman, M.; and Wong,Y.S. Identification of Feature Set for Effective Tool Condition Monitoring by AE Sensing. International Journal of Production Research 42 (2004): 901-918.

Sze, Y. K.; Lee, W. B.; Cheung, C. F.; and To, S. A power spectrum analysis of effect of rolling texture on cutting forces in single-point diamond turning. Journal of Materials Processing Technology 180 (2006): 305–309.

Tang, J.; Du, J.; and Chen, Y. Modeling and experimental study of grinding forces in surface grinding. Journal of Materials Processing Technology 209 (2009): 2847-2854.

Thompson, J. A Proposal for the Calculation of Wear. Mechanical Engineering Dept, MIT, 2006.

Tian, J. T.; and Tian, J. Preparation of porous hydroxyapatite. JOURNAL OF MATERIALS SCIENCE 36 (2001): 3061 – 3066.

Tong, S.; Gracewski, S.; and Funkenbusch, P. Measurement of the Preston coefficient of resin and bronze bond tools for deterministic micro grinding of glass. Precision Engineering 30 (2006): 115–122.

Tso, P. L. Study on the grinding of Inconel 718. Journal of Materials Processing Technology 55 (1995): 421-426.

Umehara, N.; and Kato, K. A study on magnetic fluid grinding (1st report: The effect of the floating pad on removal rate of Si3N4 balls). Transactions of the Japan Society of Mechanical Engineers 54 (503) (1988): 1599-1604.

Umehara, N.; and Kato, K. Magnetic fluid grinding of advanced ceramic balls. Wear 200 (1996): 148-153.

Umehara, N.; and Kato, K. Principles of magnetic fluid grinding of ceramic balls. Journal of Applied Electromagnetics in Materials 1 (1990): 37-43.

Wang, J. C. Young's modulus of porous materials: Part 1 Theoretical derivation of modulus-porosity correlation. JOURNAL OF MATERIALS SCIENCE 19 (1984): 801-808.

Wintermantel, E.; and Ha, S. W. Biokompatible Werkstoffe und Bauweisen. Springer, Berlin (1996): 423.

Xu, Y.; Wang, D.; Yang, L.; and Honggao Tang. Hydrothermal conversion of coral into hydroxyapatite. Materials Characterization 47 (2001): 83-87.

Yallese, M. A.; Chaoui, K.; Zeghib, N.; Boulanouar, L.; and Rigal, J. F. Hard machining of hardened bearing steel using cubic boron nitride tool. Journal of Materials Processing Technology 209 (2009): 1092-1104.

Yin, L.; Huang, H.; Ramesh, K.; and Huang, T. High speed versus conventional grinding in high removal rate machining of alumina and alumina–titania. International Journal of Machine Tools & Manufacture 45 (2005): 897-907.

Yui, A.; and Lee, H. Surface grinding with ultra high speed CBN wheel. Journal of Materials Processing Technology 62 (1996): 393-396.

Zhang, H.; Chen, W.; and Chen, Z. Grindability of high-temperature alloy with ceramic alumina wheels. Front. Mech. Eng. China 3(2) (2008): 139-145.

Zhang, Y.; Xu, H. H. K.; and Takagi, S. In-situ hardening hydroxyapatite-based scaffold for bone repair. J Mater Sci: Mater Med 7 (2006): 437-445.

IOI. Bio-Eye Hydroxyapatite Orbital Implants [Online]. Available from: http://www.ioi.com [2007]

National Institute of Standards and Technology. <u>Exploratory Data Analysis</u> [Online]. Available from: http://www.itl.nist.gov/div898/handbook/eda/eda.htm [2010]

Porous Materials Inc. <u>The Automotive Industry</u> [Online]. Available from: http://www.pmiapp.com/industries/automotive.html [2008]

APPENDICES

Appendix A

Table A-1   Bulk density and porosity of porous polyurethane foam

No.	Width (mm)	Thickness (mm)	Length (mm)	Mass (g)	Volume (x 10^{-6} m^3)	Bulk density (Mg/m^3)	Porosity (%)
1	21.24	21.32	20.39	1.169	9.231	0.127	89.4%
2	21.05	21.06	20.20	1.119	8.951	0.125	89.6%
3	21.04	21.33	20.33	1.127	9.124	0.124	89.7%
4	21.02	20.33	21.05	1.096	8.989	0.122	89.8%
5	21.12	21.26	20.39	1.147	9.153	0.125	89.6%
6	21.31	21.29	20.19	1.130	9.156	0.123	89.7%
7	20.19	21.30	21.31	1.135	9.158	0.124	89.7%
8	21.31	20.89	21.13	1.466	9.404	0.156	87.0%
9	21.49	21.27	21.08	1.535	9.629	0.159	86.7%
10	21.50	21.33	21.26	1.534	9.747	0.157	86.9%
11	20.86	21.39	21.41	1.488	9.549	0.156	87.0%
12	21.06	21.08	21.44	1.534	9.518	0.161	86.6%
13	20.95	21.33	21.15	1.480	9.449	0.157	86.9%
14	21.21	21.23	20.99	1.536	9.449	0.163	86.5%
15	20.95	20.89	21.05	1.195	9.208	0.130	89.2%
16	21.13	21.19	20.26	1.178	9.069	0.130	89.2%
17	21.15	20.83	20.98	1.173	9.238	0.127	89.4%
18	21.04	21.03	20.89	1.254	9.237	0.136	88.7%
19	20.86	21.06	21.18	1.359	9.300	0.146	87.8%
20	19.94	21.23	21.17	1.205	8.958	0.135	88.8%
21	20.87	20.97	20.80	1.244	9.101	0.137	88.6%
22	20.65	21.04	21.43	1.150	9.306	0.124	89.7%
23	21.34	21.19	20.31	1.152	9.180	0.125	89.5%
24	20.74	21.12	21.10	1.070	9.236	0.116	90.3%
25	21.31	21.10	21.07	1.222	9.472	0.129	89.2%
26	20.59	21.44	20.91	1.166	9.226	0.126	89.5%
27	20.82	21.45	21.79	1.139	9.729	0.117	90.2%
28	21.30	20.93	21.22	1.115	9.458	0.118	90.2%
29	20.88	21.38	21.08	1.013	9.406	0.108	91.0%
30	21.20	21.44	20.84	1.036	9.468	0.109	90.9%
31	21.33	21.61	20.85	1.021	9.611	0.106	91.1%
32	20.87	21.09	21.62	1.016	9.514	0.107	91.1%

Table A-1   Bulk density and porosity of porous polyurethane foam (Cont.)

No.	Width (mm)	Thickness (mm)	Length (mm)	Mass (g)	Volume (x 10^{-6} m^3)	Bulk density (Mg/m^3)	Porosity (%)
33	21.13	20.81	20.99	1.001	9.227	0.108	91.0%
34	21.75	21.33	20.85	1.043	9.671	0.108	91.0%
35	21.47	21.40	20.85	1.020	9.575	0.107	91.1%
36	20.70	21.19	21.05	1.251	9.233	0.135	88.7%
37	21.04	20.72	21.22	1.197	9.249	0.129	89.2%
38	21.04	21.12	21.06	1.212	9.356	0.130	89.2%
39	21.04	21.04	20.96	1.204	9.274	0.130	89.2%
40	21.21	21.08	21.11	1.221	9.434	0.129	89.2%
41	21.21	21.07	21.11	1.278	9.432	0.136	88.7%
42	20.93	21.15	21.18	1.275	9.369	0.136	88.7%
43	21.20	20.89	20.46	1.092	9.057	0.121	90.0%
44	21.47	21.12	20.34	1.121	9.223	0.122	89.9%
45	20.71	20.99	21.22	1.146	9.218	0.124	89.6%
46	21.37	20.96	20.32	1.124	9.097	0.124	89.7%
47	21.23	21.46	20.54	1.143	9.356	0.122	89.8%
48	21.10	20.15	21.06	1.112	8.948	0.124	89.6%
49	21.06	20.60	20.67	1.109	8.963	0.124	89.7%
50	19.86	21.65	22.07	1.163	9.487	0.123	89.8%
51	22.18	19.71	22.09	1.196	9.650	0.124	89.7%
52	20.18	21.63	21.57	1.163	9.411	0.124	89.7%
53	20.25	20.91	21.82	1.107	9.239	0.120	90.0%
54	21.51	20.07	21.77	1.162	9.394	0.124	89.7%
55	19.93	21.91	21.59	1.201	9.425	0.127	89.4%
56	20.02	21.63	21.96	1.160	9.503	0.122	89.8%
57	21.17	20.76	21.24	1.228	9.333	0.132	89.0%
58	21.01	21.03	20.66	1.131	9.122	0.124	89.7%
59	21.36	20.38	20.58	1.154	8.955	0.129	89.3%
60	20.81	21.20	21.08	1.170	9.295	0.126	89.5%
61	21.09	20.81	20.87	1.145	9.155	0.125	89.6%
62	21.03	19.85	21.13	1.181	8.818	0.134	88.8%
63	21.17	21.22	20.79	1.174	9.335	0.126	89.5%
64	21.02	21.11	21.03	1.288	9.329	0.138	88.5%
65	21.05	21.01	20.86	1.187	9.221	0.129	89.3%

Table A-1   Bulk density and porosity of porous polyurethane foam (Cont.)

No.	Width (mm)	Thickness (mm)	Length (mm)	Mass (g)	Volume (x 10^{-6} m^3)	Bulk density (Mg/m^3)	Porosity (%)
66	20.90	20.95	20.93	1.248	9.160	0.136	88.6%
67	21.18	20.94	20.93	1.172	9.280	0.126	89.5%
68	20.90	20.90	21.25	1.176	9.278	0.127	89.4%
69	21.22	20.98	20.94	1.205	9.322	0.129	89.2%
70	21.22	20.87	21.25	1.256	9.406	0.134	88.9%
71	21.38	21.24	20.98	1.136	9.527	0.119	90.1%
72	21.37	20.93	21.18	1.080	9.469	0.114	90.5%
73	21.21	21.00	21.18	1.052	9.429	0.112	90.7%
74	21.19	21.26	21.12	1.143	9.512	0.120	90.0%
75	20.63	21.61	21.31	1.112	9.496	0.117	90.2%
76	20.90	21.57	21.18	1.150	9.544	0.120	90.0%
77	21.31	21.21	21.19	1.053	9.573	0.110	90.8%
78	20.92	21.00	20.47	0.898	8.986	0.100	91.7%
79	21.12	21.03	20.60	0.976	9.150	0.107	91.1%
80	21.17	21.22	20.52	0.960	9.216	0.104	91.3%
81	21.08	20.51	21.00	0.970	9.073	0.107	91.1%
82	20.49	21.36	21.03	0.923	9.200	0.100	91.6%
83	20.74	21.36	21.16	0.990	9.367	0.106	91.2%
84	21.12	20.55	21.04	0.965	9.127	0.106	91.2%

Appendix B

Table B-1   Flexural strength of porous polyurethane foam

No.	Width (mm)	Thickness (mm)	Support span (mm)	Cross head speed (mm/min)	Max.Load (N)	Flexural strength (MPa)
1	9.56	8.04	40	0.3317	14.63	1.42
2	9.94	7.96	40	0.3352	18.13	1.73
3	9.90	7.26	40	0.3676	16.50	1.90
4	9.76	6.02	40	0.4430	8.63	1.46
5	9.95	5.98	40	0.4459	12.38	2.09
6	12.88	4.94	40	0.5398	9.88	1.89
7	11.43	6.28	40	0.4246	12.00	1.60
8	9.36	7.32	40	0.3643	16.63	1.99
9	9.74	5.98	40	0.4459	16.38	2.82
10	9.32	7.43	40	0.3591	17.25	2.01
11	9.52	7.26	40	0.3671	24.38	2.91
12	9.07	6.74	40	0.3958	19.88	2.90
13	7.90	5.64	40	0.4725	13.25	3.16
14	9.25	7.41	40	0.3599	19.00	2.25
15	8.53	6.82	40	0.3908	18.63	2.82
16	9.37	7.47	40	0.3568	20.25	2.32
17	9.04	7.76	40	0.3435	24.25	2.67
18	8.27	6.96	40	0.3831	16.00	2.40
19	9.00	7.25	40	0.3680	10.25	1.30
20	9.23	7.35	40	0.3630	10.50	1.26
21	9.50	7.43	40	0.3587	11.88	1.36
22	8.75	7.14	40	0.3733	11.63	1.56
23	8.76	7.29	40	0.3660	15.38	1.98
24	9.02	7.08	40	0.3768	12.88	1.71
25	8.92	6.71	40	0.3976	10.13	1.51
26	8.77	6.67	40	0.4000	10.88	1.68
27	8.18	5.07	40	0.5263	7.00	2.00
28	8.75	6.40	40	0.4169	12.38	2.07
29	8.82	7.54	40	3.5383	13.25	1.59
30	9.58	4.84	40	5.5058	5.38	1.44
31	9.42	7.71	40	3.4602	16.13	1.73
32	9.30	7.20	40	3.7037	10.00	1.24
33	9.30	7.59	40	3.5149	14.88	1.67
34	10.02	6.05	40	0.4408	12.75	2.09
35	10.03	5.90	40	0.4522	12.88	2.22
36	9.99	5.92	40	0.4502	9.13	1.56
37	9.84	5.95	40	0.4484	11.13	1.92

Appendix C

Table C-1   Compressive strength of porous polyurethane foam

No.	Initial cross-sectional area (mm^2)	Load at yield point (N)	Compressive strength (MPa)
1	369.27	335.89	0.91
2	376.09	338.28	0.90
3	372.20	293.40	0.79
4	371.84	348.40	0.94
5	384.55	325.25	0.85
6	416.56	465.80	1.12
7	413.04	519.56	1.26
8	415.88	511.44	1.23
9	424.07	345.90	0.82
10	413.35	487.20	1.18

Appendix D

Table D-1   Finished diameter and circularity error results from VMM

Experiment run No.	D (mm)					CE (mm)				
	Plane 1	Plane 2	Plane 3	Plane 4	Avg.	Plane 1	Plane 2	Plane 3	Plane 4	Avg.
58	19.35	20.43	20.52	19.41	19.93	1.61	1.91	2.11	1.13	1.69
78	19.53	19.50	19.43	19.49	19.49	0.53	0.73	0.72	0.44	0.60
64	19.47	19.50	19.47	19.46	19.48	0.40	0.58	0.53	0.62	0.53
46	19.37	19.39	19.35	19.38	19.37	0.51	0.62	0.47	0.63	0.55
82	19.36	19.35	19.41	19.39	19.38	0.42	0.50	0.40	0.58	0.47
75	19.34	19.39	19.37	19.40	19.37	0.74	0.76	0.52	0.39	0.60
56	18.25	18.10	18.04	18.43	18.21	0.62	1.95	1.82	1.00	1.35
39	19.22	20.35	20.25	19.62	19.86	0.55	1.90	2.03	0.94	1.36
28	19.46	19.50	19.46	19.42	19.46	0.39	0.59	0.46	0.59	0.51
6	19.45	19.40	19.41	19.42	19.42	0.49	0.54	0.53	0.46	0.51
34	19.40	19.41	19.40	19.40	19.40	0.44	0.47	0.64	0.46	0.50
25	19.35	19.37	19.34	19.34	19.35	0.65	0.54	0.81	0.56	0.64
18	19.35	19.34	19.36	19.36	19.35	0.69	0.61	0.42	0.65	0.59
8	19.20	19.13	19.16	19.28	19.19	0.49	0.62	1.03	0.58	0.68
63	19.27	20.94	20.14	19.79	20.03	0.88	2.63	2.29	1.27	1.77
65	19.42	19.35	19.35	19.40	19.38	0.76	0.62	0.61	0.67	0.67
53	19.39	19.39	19.33	19.36	19.37	0.52	0.71	0.55	0.71	0.62
52	19.29	19.34	19.32	19.29	19.31	0.50	0.48	0.42	0.52	0.48
70	19.37	19.36	19.42	18.38	19.38	0.60	0.58	0.56	0.63	0.59
48	19.32	19.28	19.33	19.24	19.29	0.71	0.62	0.66	0.59	0.64
45	19.06	19.05	19.10	19.16	19.09	1.12	0.74	0.61	0.63	0.77
27	18.46	20.17	20.28	19.54	19.61	0.79	2.74	2.59	1.79	1.98
1	19.29	19.34	19.30	19.32	19.31	0.72	0.64	0.59	0.64	0.65
13	19.29	19.25	19.25	19.30	19.27	0.65	0.72	0.58	0.61	0.64
29	19.32	19.26	19.29	19.25	19.28	0.57	0.62	0.67	0.57	0.61
17	19.25	19.28	19.22	19.25	19.25	0.64	0.52	0.70	0.52	0.59
15	19.33	19.30	19.31	19.29	19.31	0.56	0.53	0.45	0.41	0.49
24	19.35	19.37	19.37	19.34	19.36	0.78	0.81	0.42	0.81	0.70
79	18.80	19.61	19.78	19.17	19.34	0.90	1.91	2.31	2.36	1.87
71	19.03	20.16	20.20	19.49	19.72	0.59	1.81	1.81	1.00	1.30
54	19.34	19.37	19.37	19.35	19.36	0.65	0.43	0.83	0.78	0.67
77	19.35	19.34	19.36	19.31	19.34	0.46	0.48	0.58	0.62	0.54
60	19.26	19.29	19.22	19.27	19.26	0.43	0.62	0.55	0.54	0.54
59	19.22	19.22	19.22	19.24	19.23	0.50	0.52	0.55	0.72	0.57
47	19.10	18.87	18.71	19.08	18.94	0.56	1.92	1.72	0.65	1.21
23	19.10	20.49	20.36	19.81	19.94	0.86	2.36	2.35	1.42	1.75
7	19.08	20.12	20.13	19.25	19.64	0.72	1.67	1.88	0.78	1.26
22	19.21	19.20	19.16	19.15	19.18	0.61	0.75	0.91	0.73	0.75
41	19.31	19.27	19.30	19.31	19.30	0.48	0.91	0.66	0.43	0.62
30	19.15	19.17	19.23	19.18	19.18	0.52	0.72	0.59	0.58	0.60
35	19.30	19.25	19.31	19.30	19.29	0.68	0.67	0.66	0.45	0.61
16	19.27	18.94	18.76	19.27	19.06	0.50	1.59	1.57	0.52	1.05
57	19.29	20.24	20.30	19.57	19.85	0.47	1.68	1.68	0.97	1.20
73	19.47	19.47	19.43	19.40	19.44	0.38	0.45	0.60	0.46	0.47
43	19.41	19.31	19.35	19.34	19.35	0.51	0.42	0.49	0.78	0.55

Table D-1   Finished diameter and circularity error results from VMM (Cont.)

Experiment run No.	D (mm)					CE (mm)				
	Plane 1	Plane 2	Plane 3	Plane 4	Avg.	Plane 1	Plane 2	Plane 3	Plane 4	Avg.
84	19.35	19.33	19.37	19.39	19.36	0.43	0.45	0.55	0.46	0.47
66	19.34	19.35	19.31	19.31	19.33	0.44	0.42	0.44	0.68	0.49
83	19.32	19.23	19.30	19.33	19.30	0.57	0.53	0.89	0.56	0.64
67	15.74	15.67	15.72	15.85	15.74	0.78	0.66	0.61	1.04	0.77
21	19.31	19.73	19.88	19.63	19.64	0.83	1.36	1.26	1.00	1.11
2	19.32	19.44	19.42	19.41	19.40	0.41	0.37	0.88	0.62	0.57
20	19.41	19.33	19.38	19.39	19.38	0.73	0.47	0.47	0.45	0.53
4	19.40	19.38	19.39	19.43	19.40	0.37	0.60	0.45	0.43	0.46
38	19.31	19.37	19.29	19.34	19.33	0.45	0.50	0.43	0.69	0.52
10	18.59	18.50	18.53	18.45	18.52	0.59	1.11	1.13	0.72	0.88
5	17.33	16.99	15.34	16.32	16.49	0.99	0.76	0.56	0.79	0.78
81	18.98	20.03	19.62	19.65	19.57	1.21	1.70	2.09	0.98	1.49
80	19.25	19.24	19.22	19.23	19.23	0.74	0.67	0.45	0.87	0.68
51	19.22	19.18	19.22	19.20	19.20	0.67	0.62	0.60	0.63	0.63
68	19.17	19.21	19.17	19.16	19.18	0.67	0.57	0.53	0.68	0.61
55	19.20	19.19	19.15	19.19	19.18	0.67	0.47	0.55	0.54	0.56
62	19.24	19.19	19.22	19.20	19.21	0.65	0.71	0.52	0.59	0.62
61	18.74	17.77	17.44	18.72	18.17	0.71	2.70	3.05	0.77	1.81
3	19.07	20.04	20.00	19.56	19.67	0.77	1.73	2.14	1.31	1.49
33	19.32	19.16	19.33	19.28	19.27	0.60	0.67	0.57	0.55	0.60
31	19.24	19.25	19.30	19.26	19.26	0.67	0.58	0.62	0.60	0.62
40	19.28	19.29	19.24	19.22	19.26	0.51	0.69	0.75	0.54	0.62
26	19.24	19.24	19.21	19.26	19.24	0.64	0.51	0.85	0.50	0.63
11	19.22	19.20	19.22	19.15	19.20	0.85	0.66	0.45	0.77	0.68
42	19.21	18.09	18.21	19.23	18.68	0.63	2.68	2.98	0.50	1.70
69	18.95	20.32	20.50	19.60	19.84	0.89	2.11	2.46	2.27	1.93
50	19.24	19.67	19.77	19.36	19.51	0.62	1.36	1.03	0.56	0.89
49	19.29	19.21	19.22	19.25	19.24	0.86	0.71	0.81	0.64	0.76
76	19.24	19.18	19.25	19.18	19.21	0.72	0.82	0.57	0.80	0.73
44	19.24	19.24	19.24	19.23	19.24	0.60	0.91	0.39	0.50	0.60
74	19.22	19.19	19.23	19.21	19.21	0.56	0.73	0.60	0.65	0.63
72	19.06	18.95	19.00	19.06	19.02	0.69	1.11	0.67	0.87	0.83
36	18.98	20.03	20.19	19.63	19.71	0.72	2.07	2.44	1.59	1.71
19	19.11	20.33	20.25	19.36	19.76	0.89	1.75	1.96	1.13	1.43
37	19.27	19.25	19.19	19.16	19.22	0.59	0.47	0.62	0.65	0.58
9	19.20	19.22	19.24	19.25	19.23	0.54	0.44	0.67	0.65	0.57
12	19.14	19.13	19.14	19.20	19.15	0.89	0.50	0.58	0.53	0.62
14	19.17	19.13	19.10	19.12	19.13	0.76	0.58	0.65	0.62	0.65
32	19.04	18.84	18.84	19.17	18.97	0.68	1.26	1.46	0.63	1.01

Appendix E

a) Vs =1.41 m/s for Ft

b) Vs = 1.41 m/s for Fn

c) Vs = 2.83 m/s for Ft

d) Vs = 2.83 m/s for Fn

e) Vs = 3.30 m/s for Ft

f) Vs = 3.30 m/s for Fn

g) Vs = 3.77 m/s for Ft

h) Vs = 3.77 m/s for Fn

i) Vs = 5.18 m/s for Ft

j) Vs = 5.18 m/s for Fn

Figure E-1   Grinding forces (Ft, Fn) versus grinding time (t) with linear estimation

for f = 1.0 mm/min and A = 20 µm with various Vs (Replication 1)

a) Vs =1.41 m/s for Ft

b) Vs = 1.41 m/s for Fn

c) Vs = 2.83 m/s for Ft

d) Vs = 2.83 m/s for Fn

e) Vs = 3.30 m/s for Ft

f) Vs = 3.30 m/s for Fn

g) Vs = 3.77 m/s for Ft

h) Vs = 3.77 m/s for Fn

i) Vs = 5.18 m/s for Ft

j) Vs = 5.18 m/s for Fn

Figure E-2   Grinding forces (Ft, Fn) versus grinding time (t) with linear estimation

for f = 1.0 mm/min and A = 20 μm with various Vs (Replication 2)

a) Vs =1.41 m/s for Ft

b) Vs = 1.41 m/s for Fn

c) Vs = 2.83 m/s for Ft

d) Vs = 2.83 m/s for Ft

e) Vs = 3.30 m/s for Ft

f) Vs = 3.30 m/s for Fn

g) Vs = 3.77 m/s for Ft

h) Vs = 3.77 m/s for Fn

i) Vs = 5.18 m/s for Ft

j) Vs = 5.18 m/s for Fn

Figure E-3   Grinding forces (Ft, Fn) versus grinding time (t) with linear estimation

for f = 1.0 mm/min and A = 53 µm with various Vs (Replication 1)

a) Vs = 1.41 m/s for Ft

b) Vs = 1.41 m/s for Fn

c) Vs = 2.83 m/s for Ft

d) Vs = 2.83 m/s for Fn

e) Vs = 3.30 m/s for Ft

f) Vs = 3.30 m/s for Fn

g) Vs = 3.77 m/s for Ft
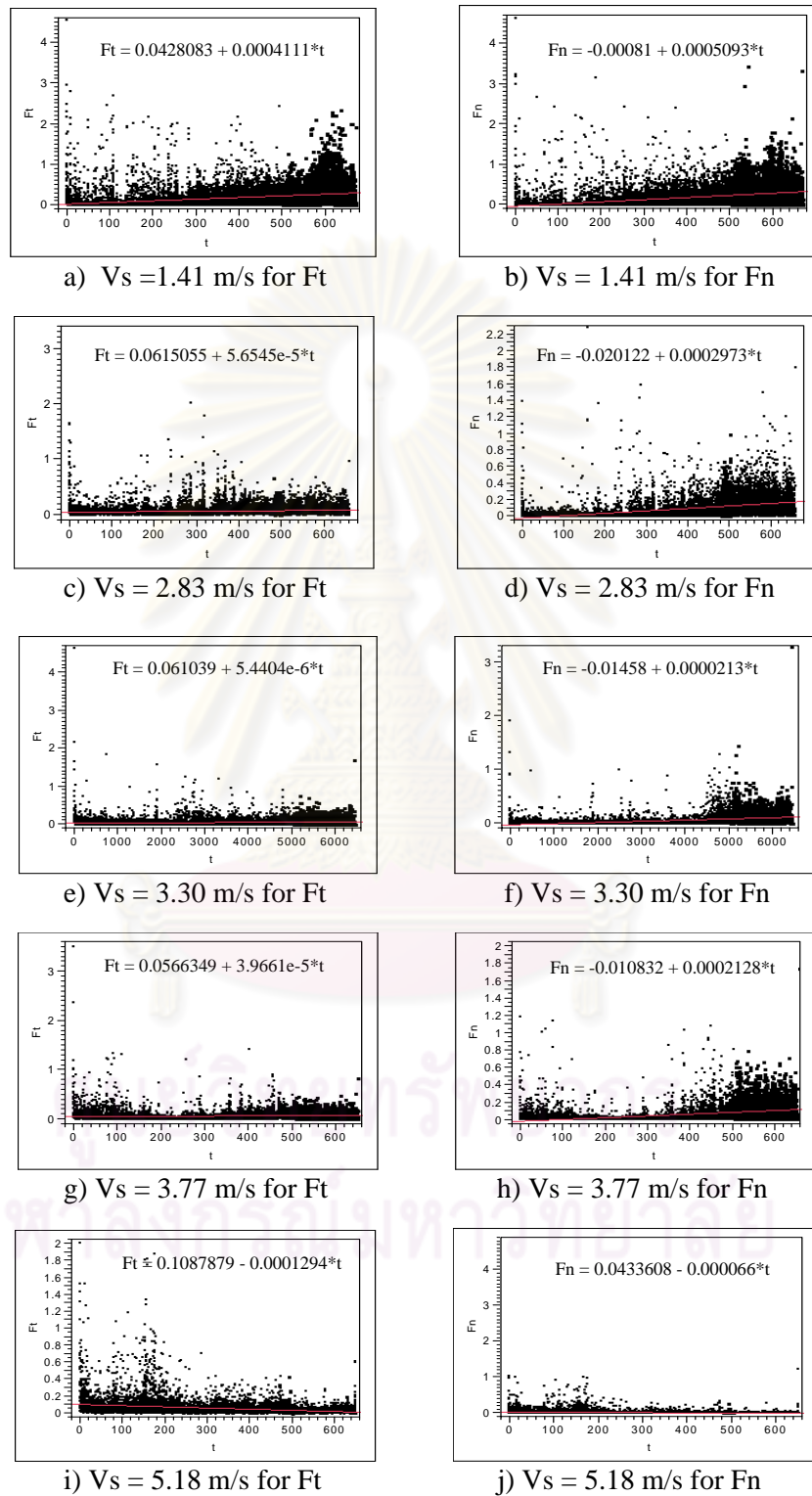
h) Vs = 3.77 m/s for Fn

i) Vs = 5.18 m/s for Ft

j) Vs = 5.18 m/s for Fn

Figure E-4   Grinding forces (Ft, Fn) versus grinding time (t) with linear estimation

for f = 1.0 mm/min and A = 53 µm with various Vs (Replication 2)

a) Vs =1.41 m/s for Ft

b) Vs = 1.41 m/s for Fn

c) Vs = 2.83 m/s for Ft

d) Vs = 2.83 m/s for Fn

e) Vs = 3.30 m/s for Ft

f) Vs = 3.30 m/s for Fn

g) Vs = 3.77 m/s for Ft
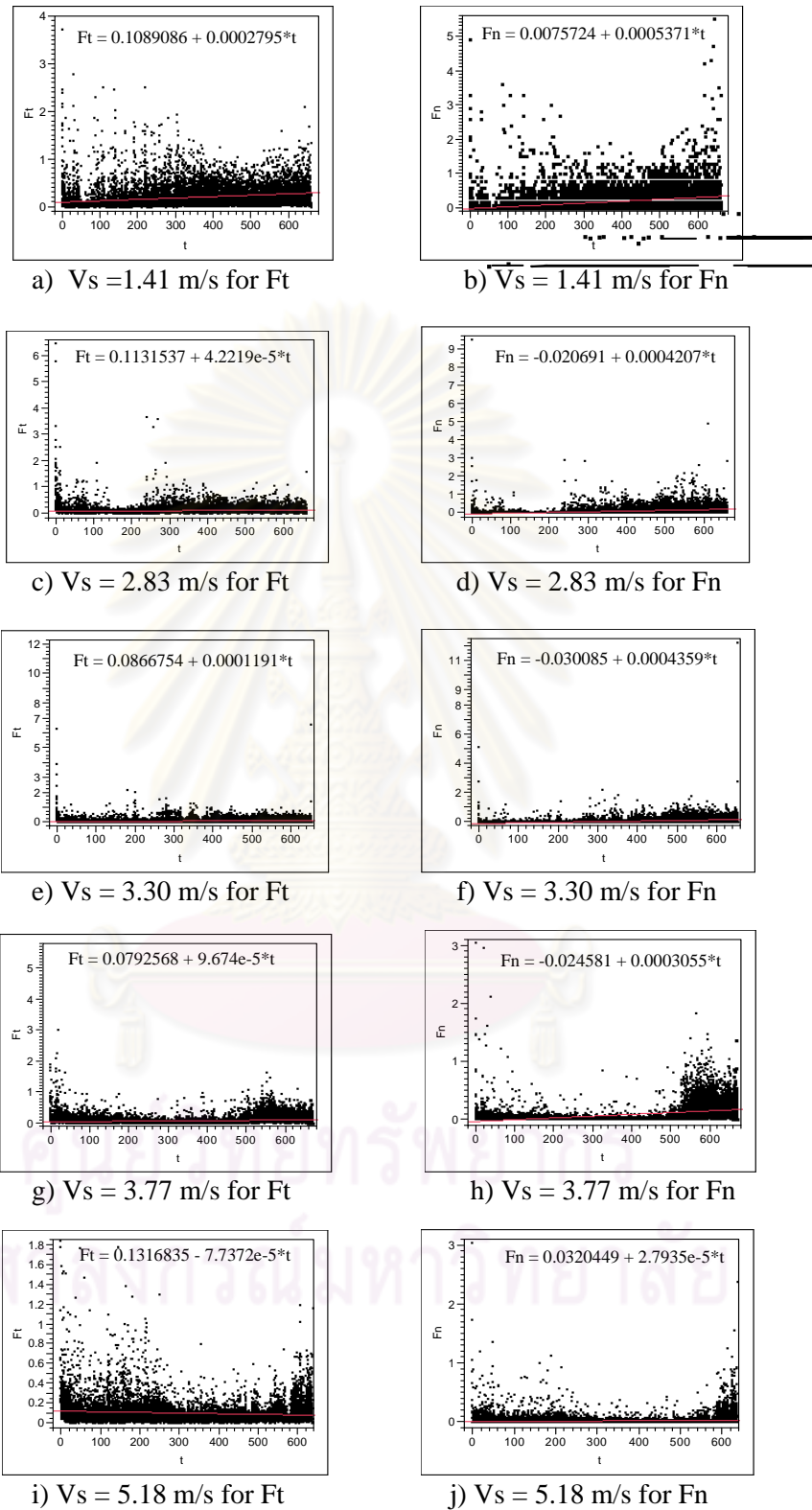
h) Vs = 3.77 m/s for Fn

i) Vs = 5.18 m/s for Ft

j) Vs = 5.18 m/s for Fn

Figure E-5   Grinding forces (Ft, Fn) versus grinding time (t) with linear estimation

for f = 3.0 mm/min and A = 20 µm with various Vs (Replication 1)

a) Vs =1.41 m/s for Ft

b) Vs = 1.41 m/s for Fn

c) Vs = 2.83 m/s for Ft

d) Vs = 2.83 m/s for Fn

e) Vs = 3.30 m/s for Ft

f) Vs = 3.30 m/s for Fn

g) Vs = 3.77 m/s for Ft

h) Vs = 3.77 m/s for Fn

i) Vs = 5.18 m/s for Ft

j) Vs = 5.18 m/s for Fn

Figure E-6   Grinding forces (Ft, Fn) versus grinding time (t) with linear estimation

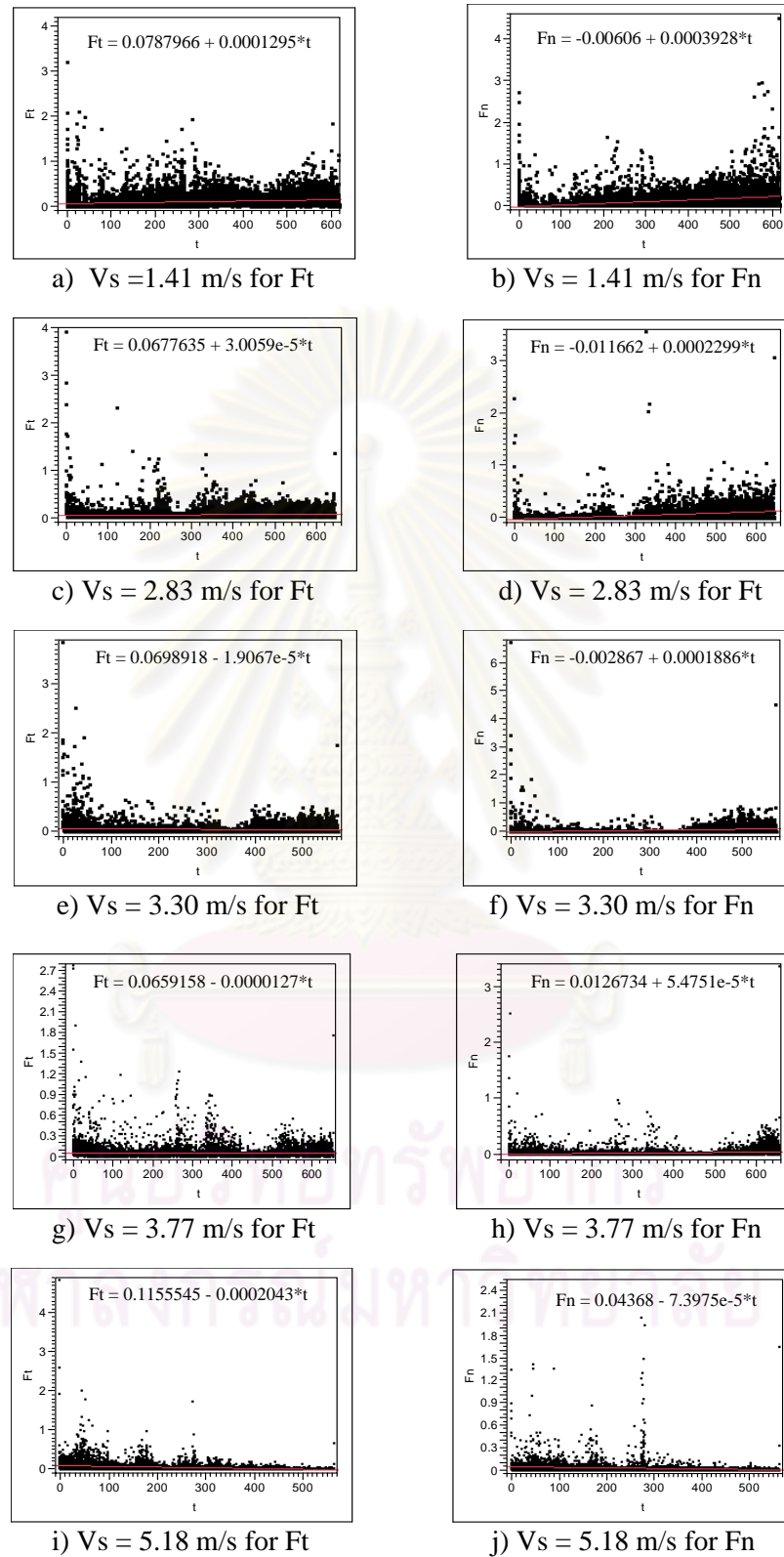for f = 3.0 mm/min and A = 20 µm with various Vs (Replication 2)

a) Vs =1.41 m/s for Ft

b) Vs = 1.41 m/s for Fn

c) Vs = 2.83 m/s for Ft

d) Vs = 2.83 m/s for Fn

e) Vs = 3.30 m/s for Ft

f) Vs = 3.30 m/s for Fn

g) Vs = 3.77 m/s for Ft
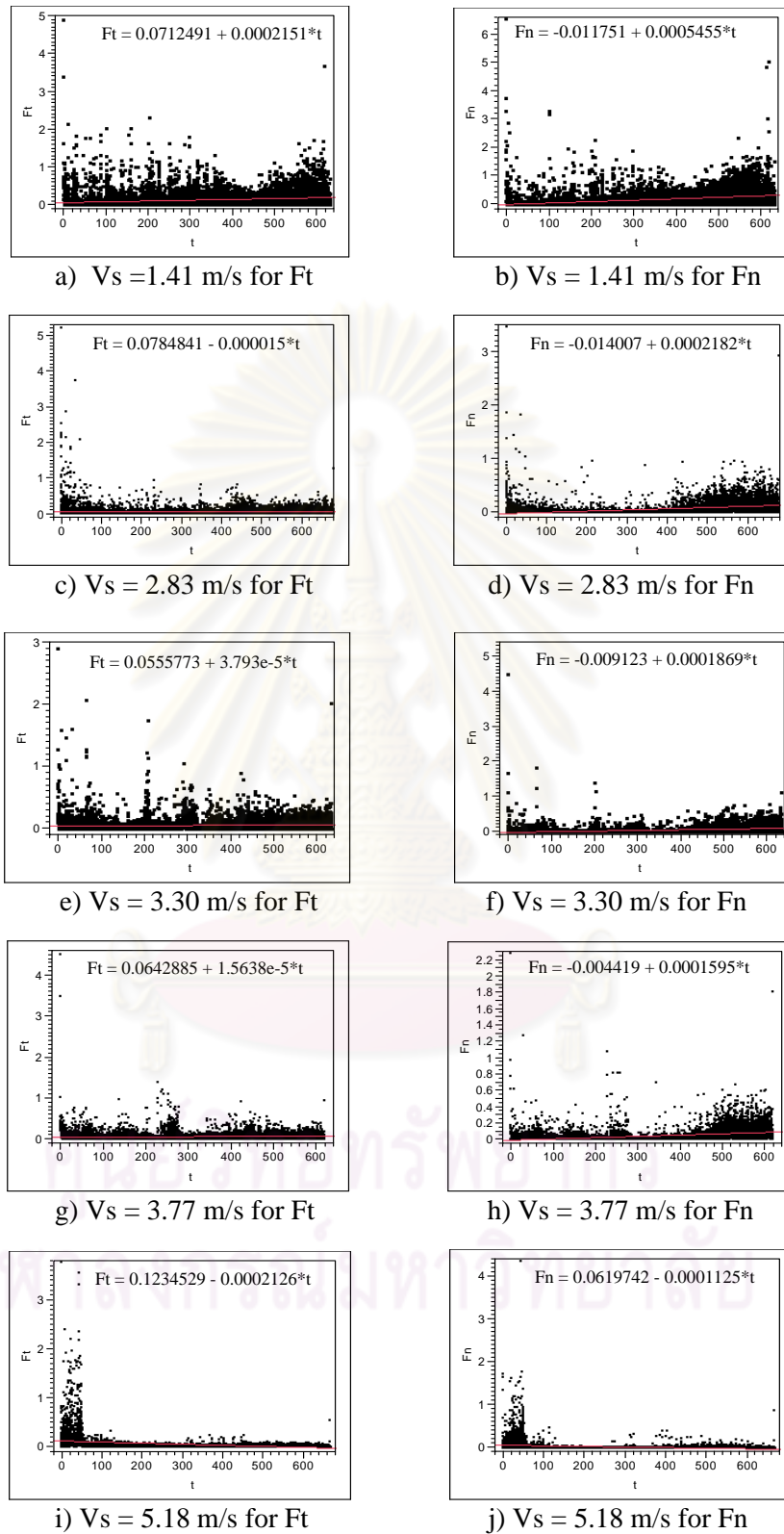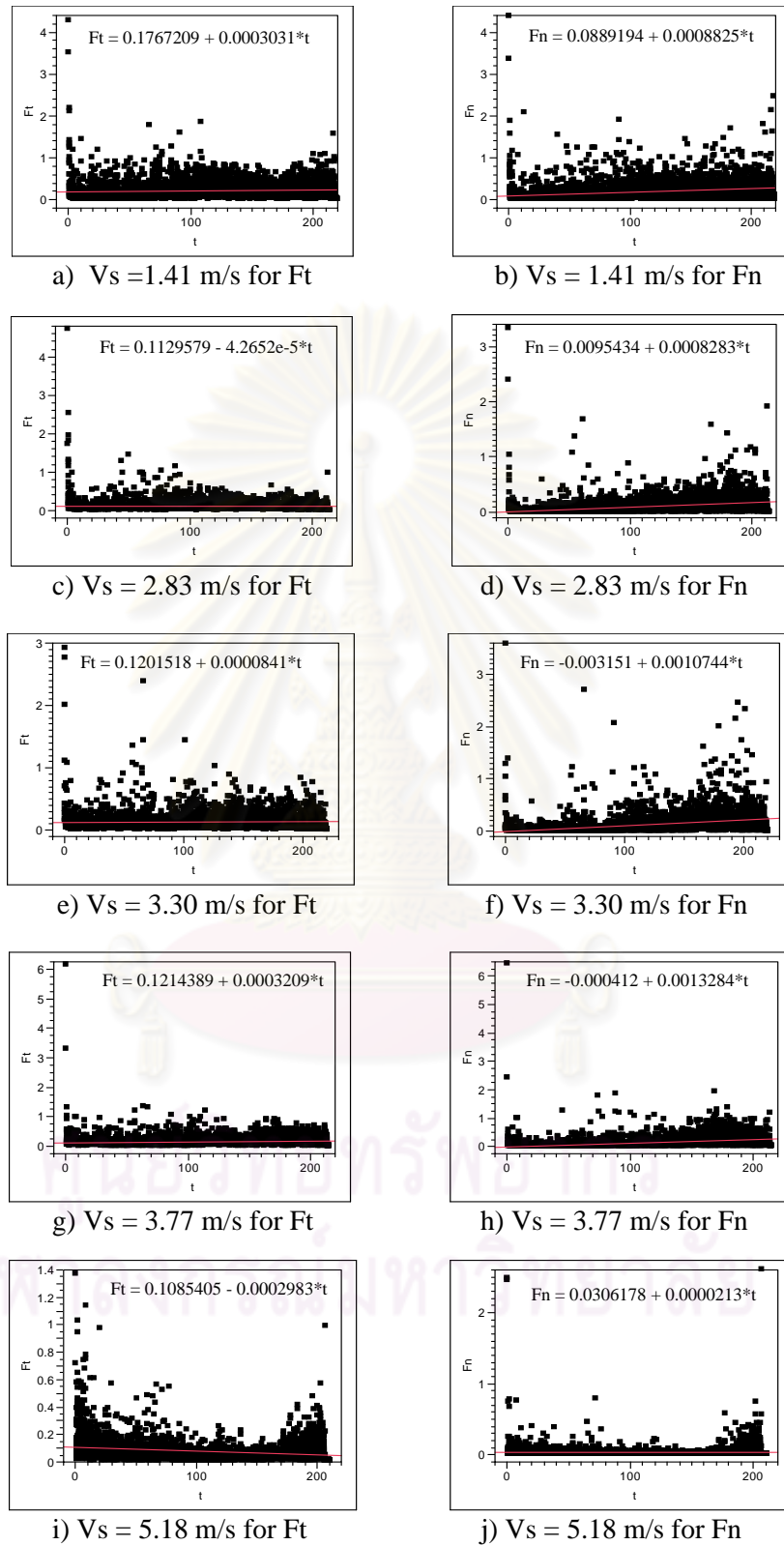
h) Vs = 3.77 m/s for Fn

i) Vs = 5.18 m/s for Ft

j) Vs = 5.18 m/s for Fn

Figure E-7   Grinding forces (Ft, Fn) versus grinding time (t) with linear estimation

for f = 3.0 mm/min and A = 53 µm with various Vs (Replication 1)

a) Vs =1.41 m/s for Ft

b) Vs = 1.41 m/s for Fn

c) Vs = 2.83 m/s for Ft

d) Vs = 2.83 m/s for Fn

e) Vs = 3.30 m/s for Ft

f) Vs = 3.30 m/s for Fn

g) Vs = 3.77 m/s for Ft

h) Vs = 3.77 m/s for Fn

i) Vs = 5.18 m/s for Ft

j) Vs = 5.18 m/s for Fn

Figure E-8   Grinding forces (N) versus grinding time (sec.) with linear estimation

for f = 3.0 mm/min and A = 53 µm with various Vs (Replication 2)

a) Vs = 1.41 m/s for Ft

b) Vs = 1.41 m/s for Fn

c) Vs = 2.83 m/s for Ft

d) Vs = 2.83 m/s for Fn

e) Vs = 3.30 m/s for Ft

f) Vs = 3.30 m/s for Fn

g) Vs = 3.77 m/s for Ft

h) Vs = 3.77 m/s for Fn

i) Vs = 5.18 m/s for Ft

j) Vs = 5.18 m/s for Fn

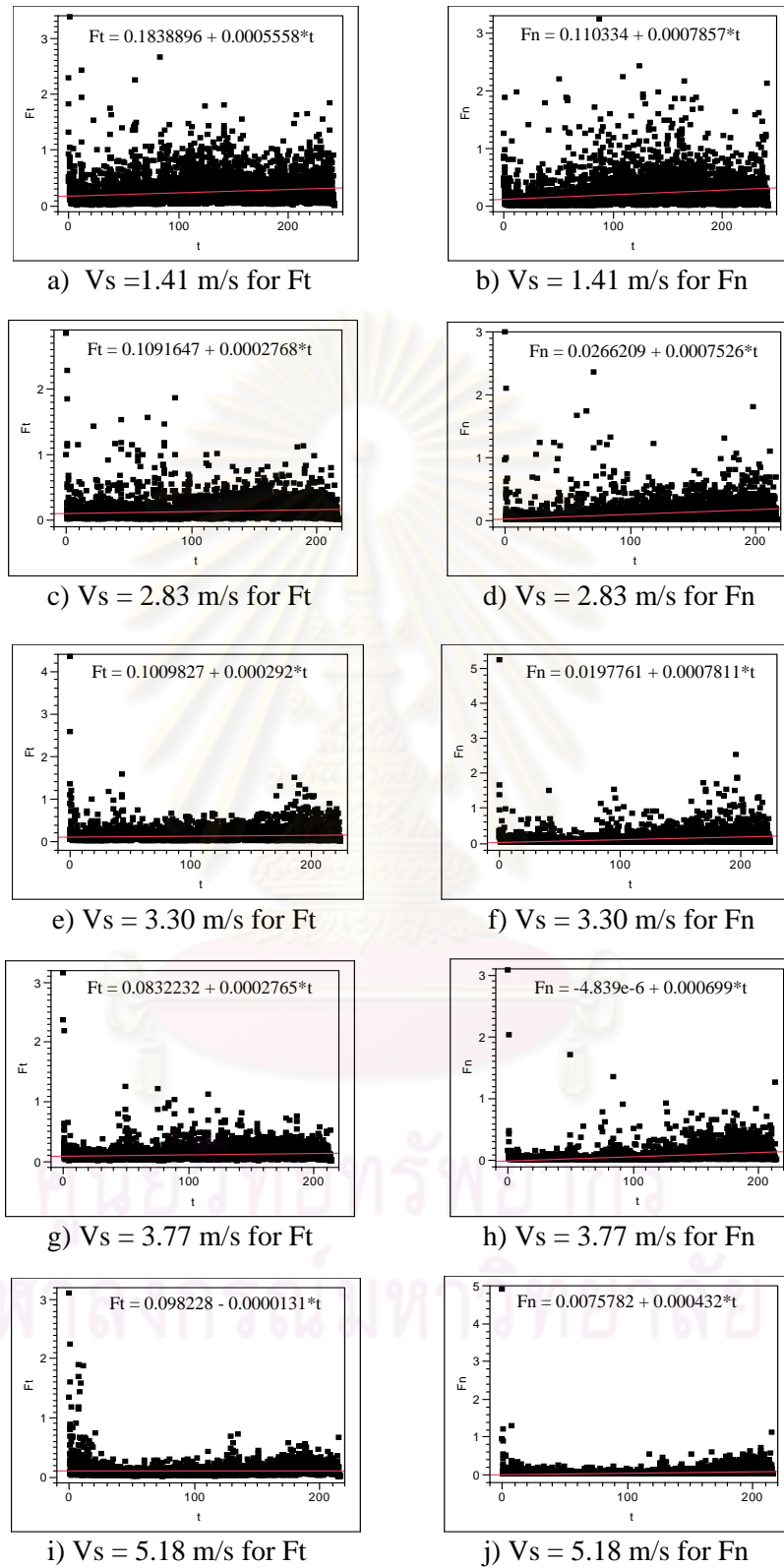Figure E-9   Grinding forces (Ft, Fn) versus grinding time (t) with linear estimation

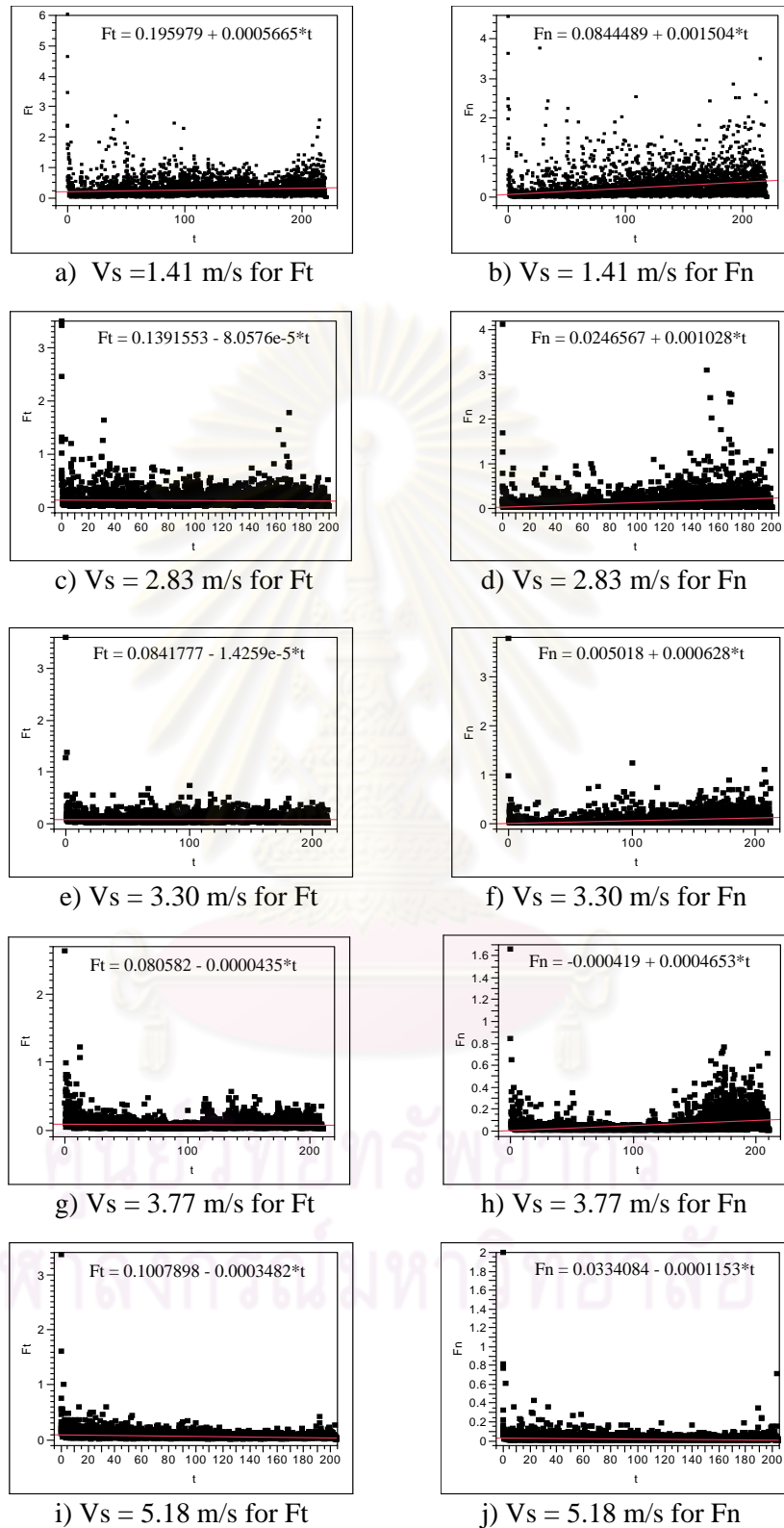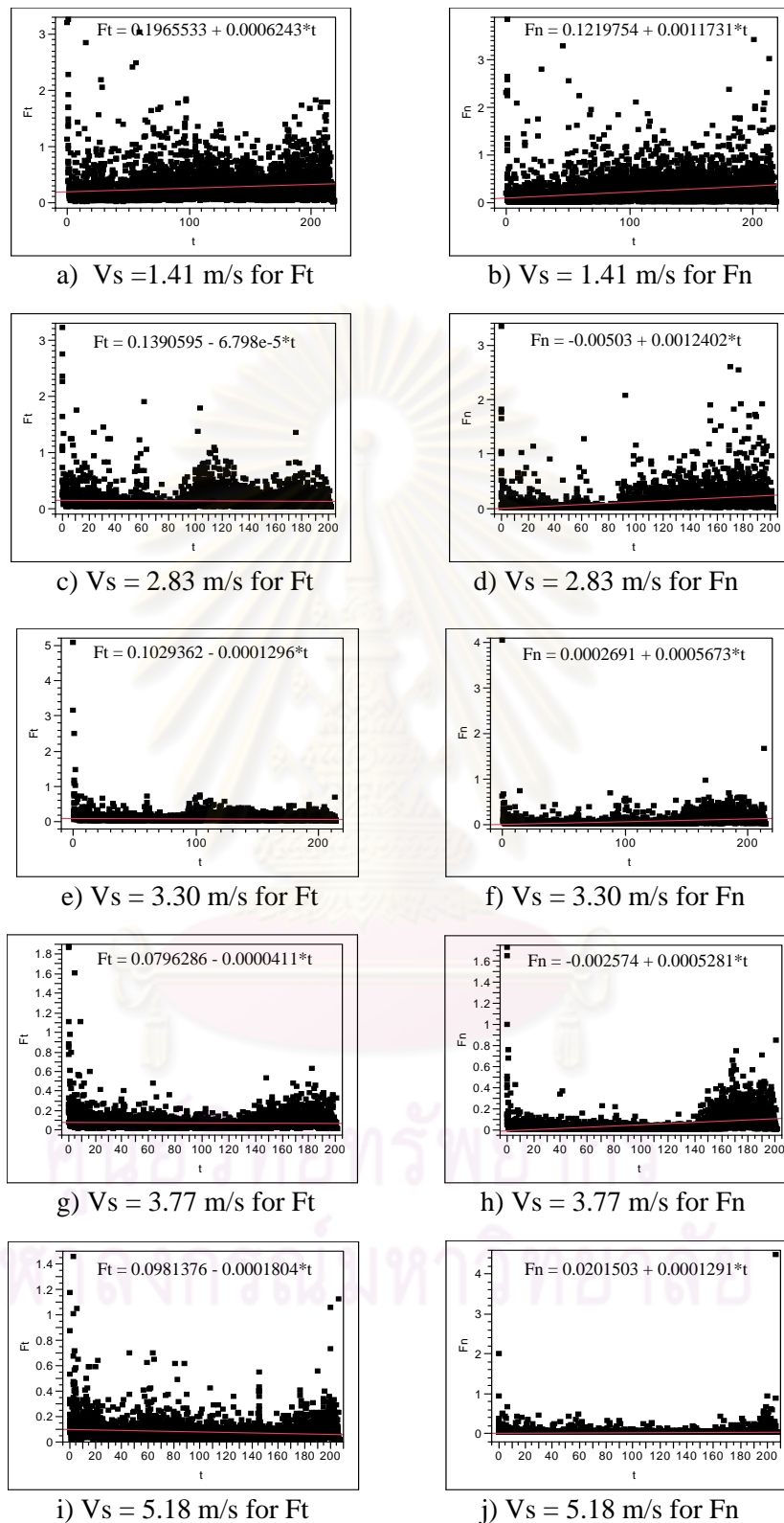for f = 5.0 mm/min and A = 20 µm with various Vs (Replication 1)

a) Vs =1.41 m/s for Ft

b) Vs = 1.41 m/s for Fn

c) Vs = 2.83 m/s for Ft

d) Vs = 2.83 m/s for Fn

e) Vs = 3.30 m/s for Ft

f) Vs = 3.30 m/s for Fn

g) Vs = 3.77 m/s for Ft

h) Vs = 3.77 m/s for Fn

i) Vs = 5.18 m/s for Ft

j) Vs = 5.18 m/s for Fn

Figure E-10   Grinding forces (Ft, Fn) versus grinding time (t) with linear estimation
for f = 5.0 mm/min and A = 20 µm with various Vs (Replication 2)

a) Vs =1.41 m/s for Ft

b) Vs = 1.41 m/s for Fn

c) Vs = 2.83 m/s for Ft

d) Vs = 2.83 m/s for Fn

e) Vs = 3.30 m/s for Ft

f) Vs = 3.30 m/s for Fn

g) Vs = 3.77 m/s for Ft

h) Vs = 3.77 m/s for Fn

i) Vs = 5.18 m/s for Ft

j) Vs = 5.18 m/s for Fn

Figure E-11   Grinding forces (Ft, Fn) versus grinding time (t) with linear estimation

for f = 5.0 mm/min and A = 53 µm with various Vs (Replication 1)

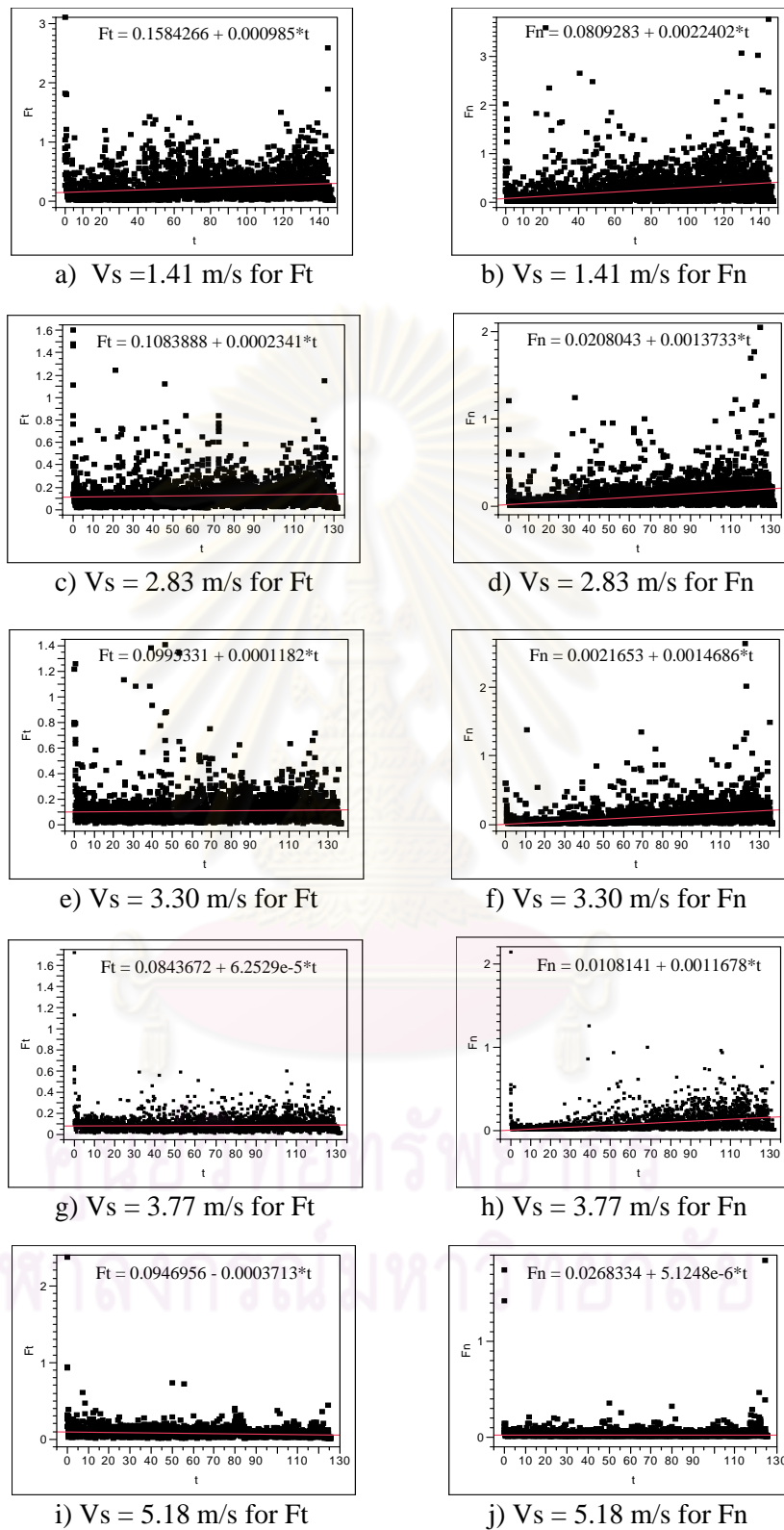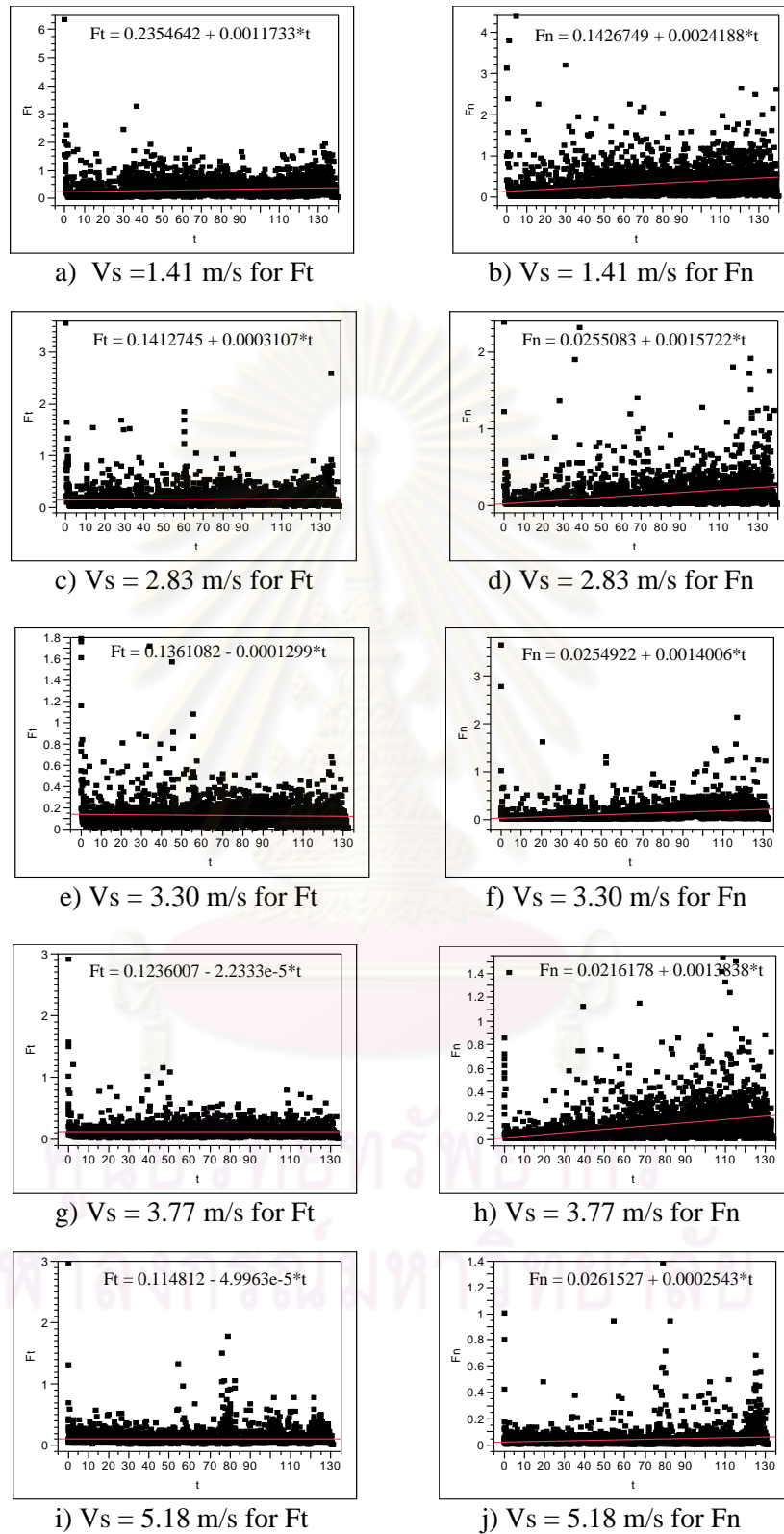a) Vs =1.41 m/s for Ft

b) Vs = 1.41 m/s for Fn

c) Vs = 2.83 m/s for Ft

d) Vs = 2.83 m/s for Fn

e) Vs = 3.30 m/s for Ft

f) Vs = 3.30 m/s for Fn

g) Vs = 3.77 m/s for Ft
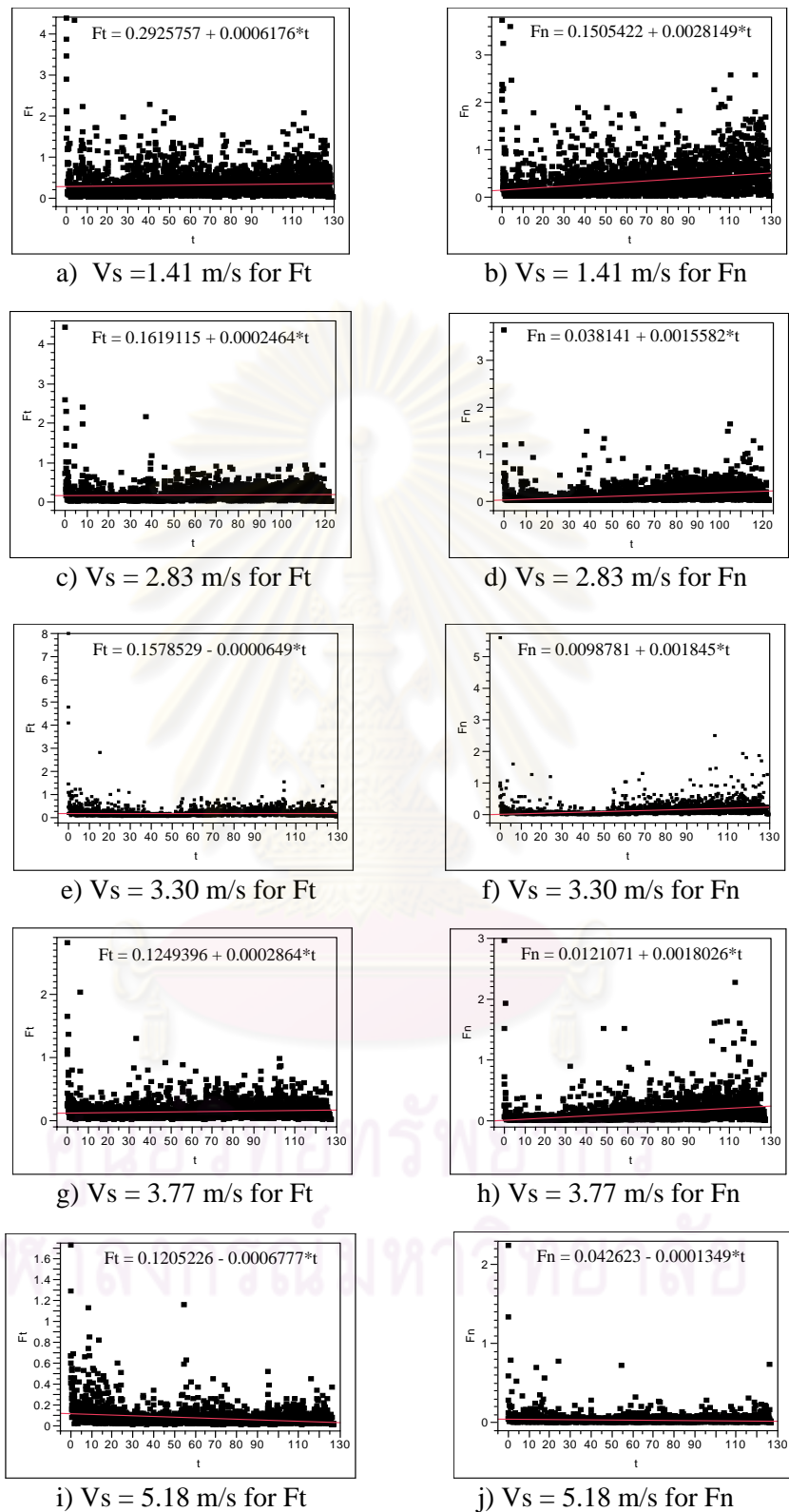
h) Vs = 3.77 m/s for Fn

i) Vs = 5.18 m/s for Ft

j) Vs = 5.18 m/s for Fn
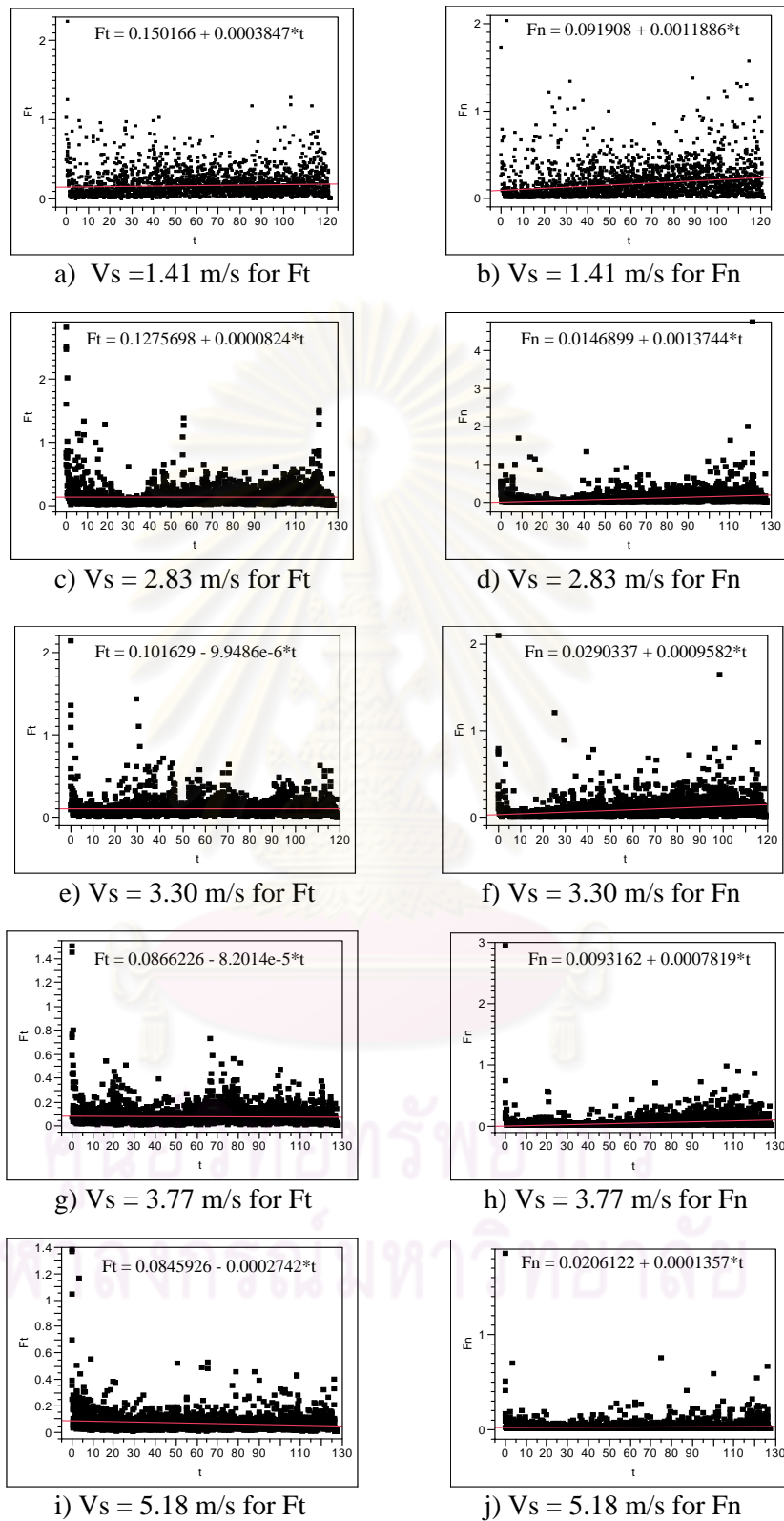
Figure E-12   Grinding forces (Ft, Fn) versus grinding time (t) with linear estimation

for f = 5.0 mm/min and A = 53 µm with various Vs (Replication 2)

a) Vs =1.41 m/s for Ft

b) Vs = 1.41 m/s for Fn

c) Vs = 2.83 m/s for Ft

d) Vs = 2.83 m/s for Fn

e) Vs = 3.30 m/s for Ft

f) Vs = 3.30 m/s for Fn

e) Vs = 3.77 m/s for Ft

f) Vs = 3.77 m/s for Fn

g) Vs = 5.18 m/s for Ft

h) Vs = 5.18 m/s for Fn

Figure E-13   Spectral density of grinding forces for f = 1.0 mm/min and A = 20 μm
with various Vs (Replication 1)

a) Vs =1.41 m/s for Ft

b) Vs = 1.41 m/s for Fn

c) Vs = 2.83 m/s for Ft

d) Vs = 2.83 m/s for Fn

e) Vs = 3.30 m/s for Ft

f) Vs = 3.30 m/s for Fn

g) Vs = 3.77 m/s for Ft

h) Vs = 3.77 m/s for Fn
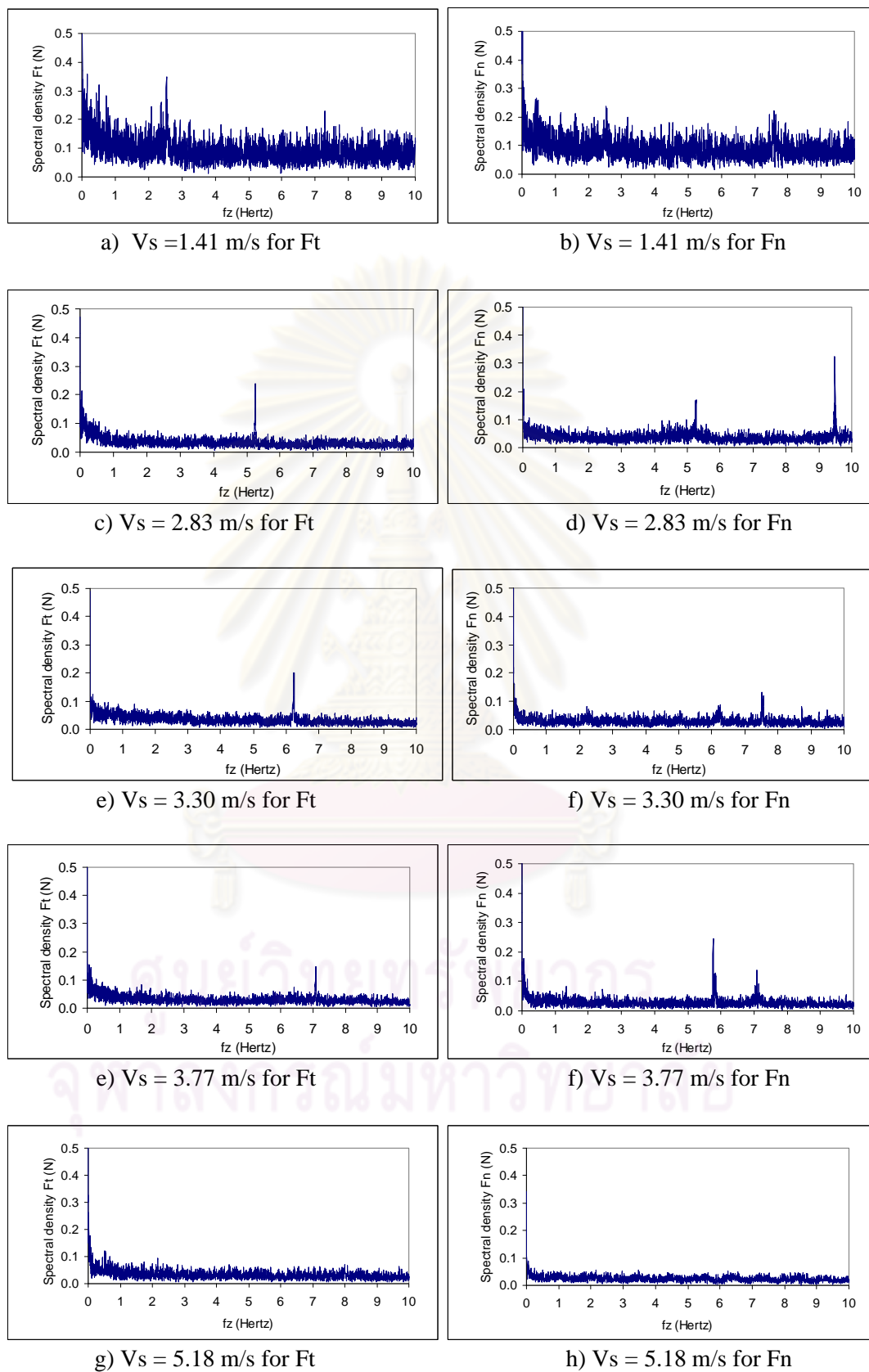
i) Vs = 5.18 m/s for Ft

j) Vs = 5.18 m/s for Fn
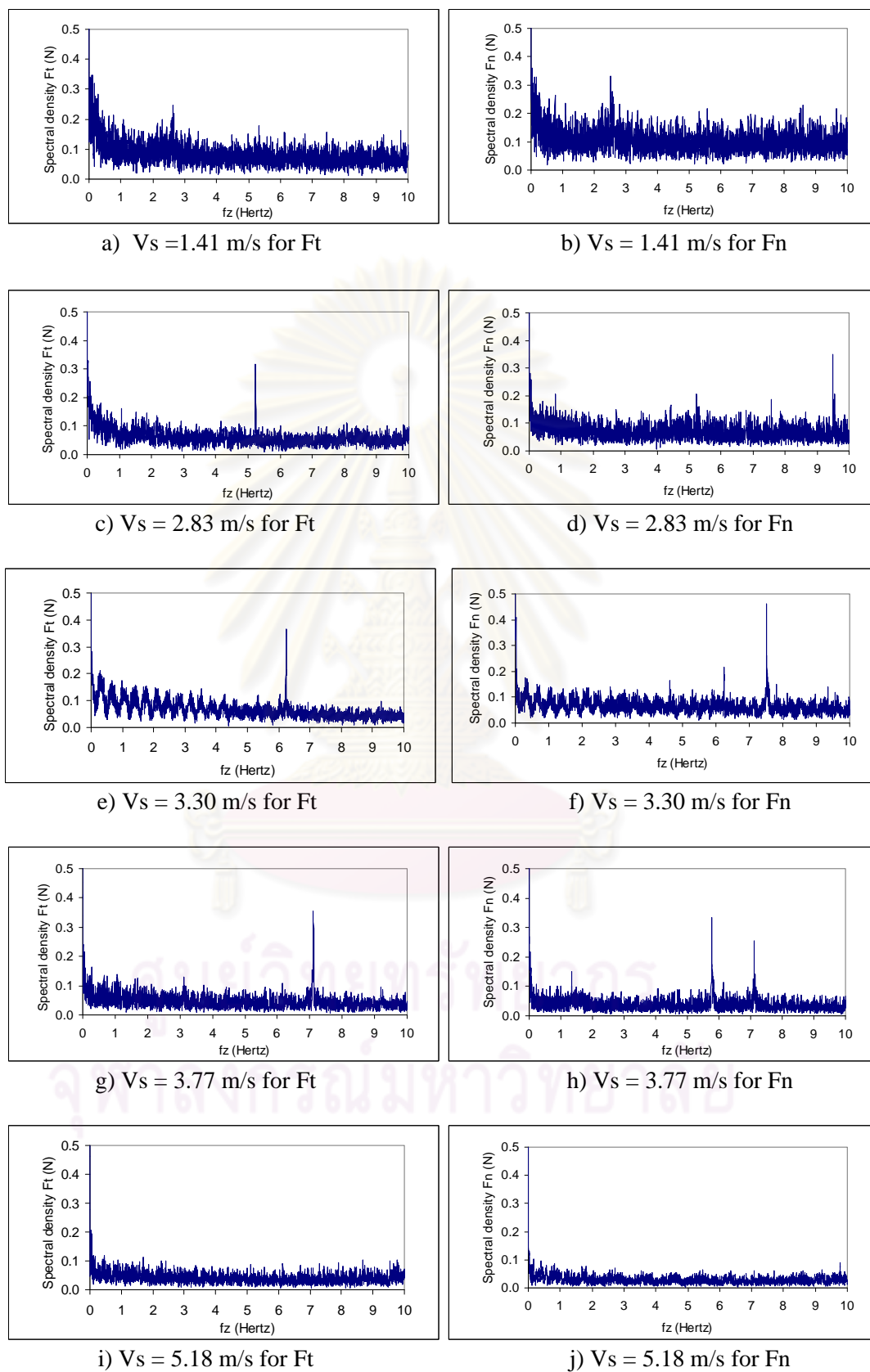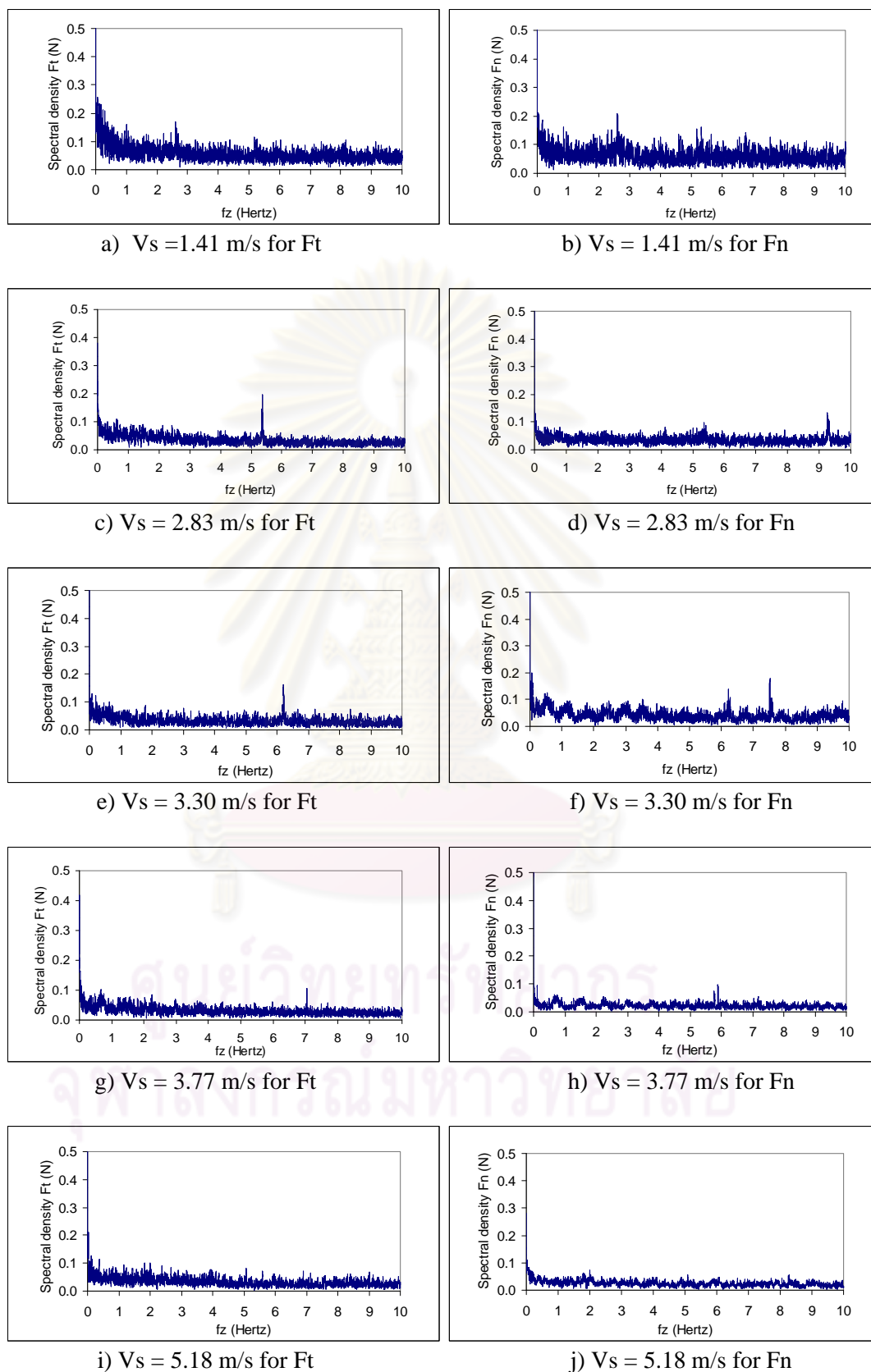
Figure E-14   Spectral density of grinding forces for f = 1.0 mm/min and A = 20 μm
with various Vs (Replication 2)

Figure E-15   Spectral density of grinding forces for f = 1.0 mm/min and A = 53 µm
with various Vs (Replication 1)

a) Vs =1.41 m/s for Ft

b) Vs = 1.41 m/s for Fn

c) Vs = 2.83 m/s for Ft

d) Vs = 2.83 m/s for Fn

e) Vs = 3.30 m/s for Ft

f) Vs = 3.30 m/s for Fn

g) Vs = 3.77 m/s for Ft

h) Vs = 3.77 m/s for Fn

i) Vs = 5.18 m/s for Ft

j) Vs = 5.18 m/s for Fn

Figure E-16   Spectral density of grinding forces for f = 1.0 mm/min and A = 53 µm
with various Vs (Replication 2)

a) Vs =1.41 m/s for Ft

b) Vs = 1.41 m/s for Fn

c) Vs = 2.83 m/s for Ft

d) Vs = 2.83 m/s for Fn

e) Vs = 3.30 m/s for Ft

f) Vs = 3.30 m/s for Fn

g) Vs = 3.77 m/s for Ft

h) Vs = 3.77 m/s for Fn

i) Vs = 5.18 m/s for Ft

j) Vs = 5.18 m/s for Fn
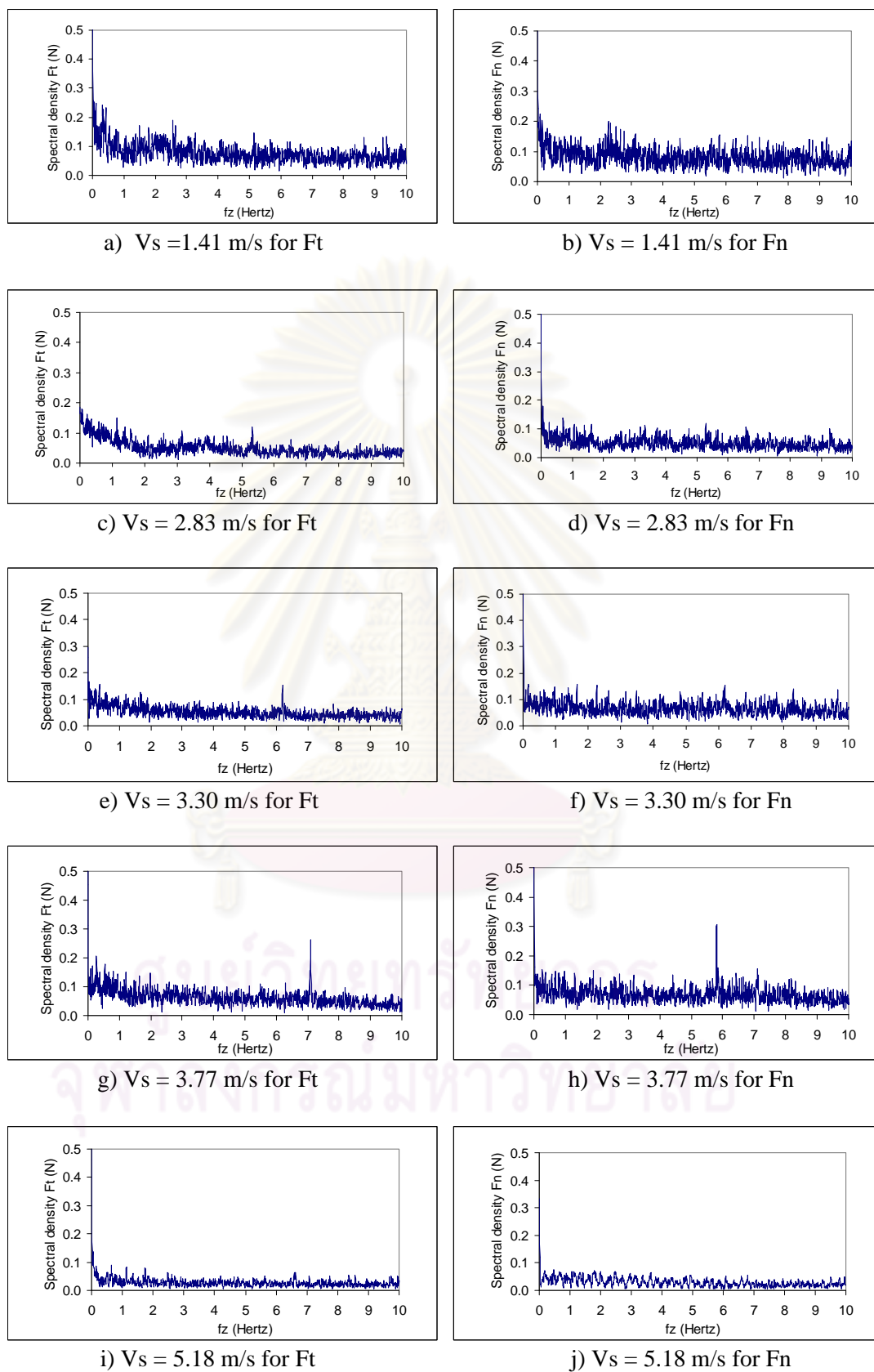
Figure E-17   Spectral density of grinding forces for f = 3.0 mm/min and A = 20 μm
with various Vs (Replication 1)

a) Vs =1.41 m/s for Ft
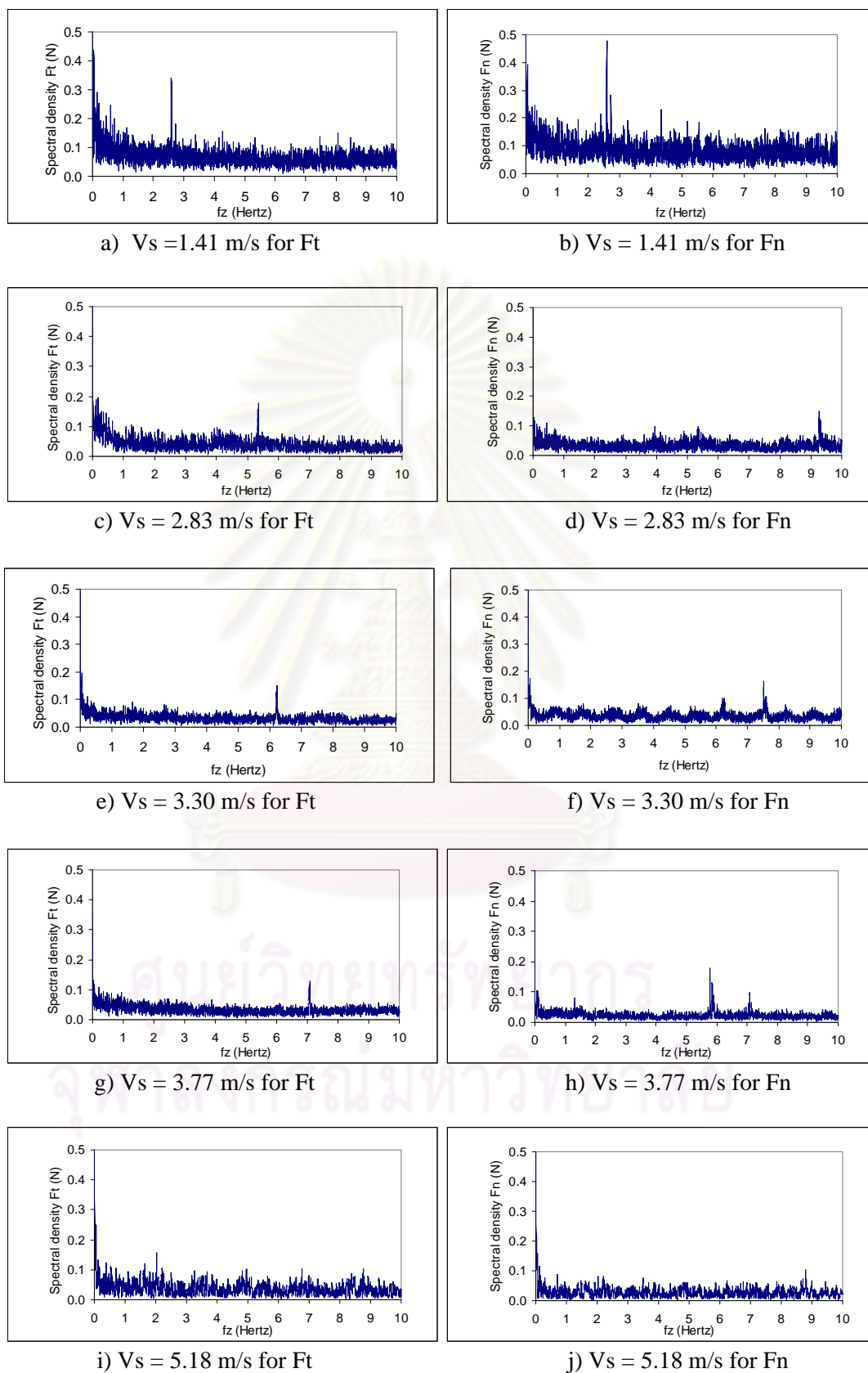
b) Vs = 1.41 m/s for Fn

c) Vs = 2.83 m/s for Ft

d) Vs = 2.83 m/s for Fn

e) Vs = 3.30 m/s for Ft

f) Vs = 3.30 m/s for Fn

g) Vs = 3.77 m/s for Ft

h) Vs = 3.77 m/s for Fn

i) Vs = 5.18 m/s for Ft

j) Vs = 5.18 m/s for Fn

Figure E-18   Spectral density of grinding forces for f = 3.0 mm/min and A = 20 µm
with various Vs (Replication 2)

a) Vs =1.41 m/s for Ft

b) Vs = 1.41 m/s for Fn

c) Vs = 2.83 m/s for Ft

d) Vs = 2.83 m/s for Fn

e) Vs = 3.30 m/s for Ft

f) Vs = 3.30 m/s for Fn

g) Vs = 3.77 m/s for Ft

h) Vs = 3.77 m/s for Fn
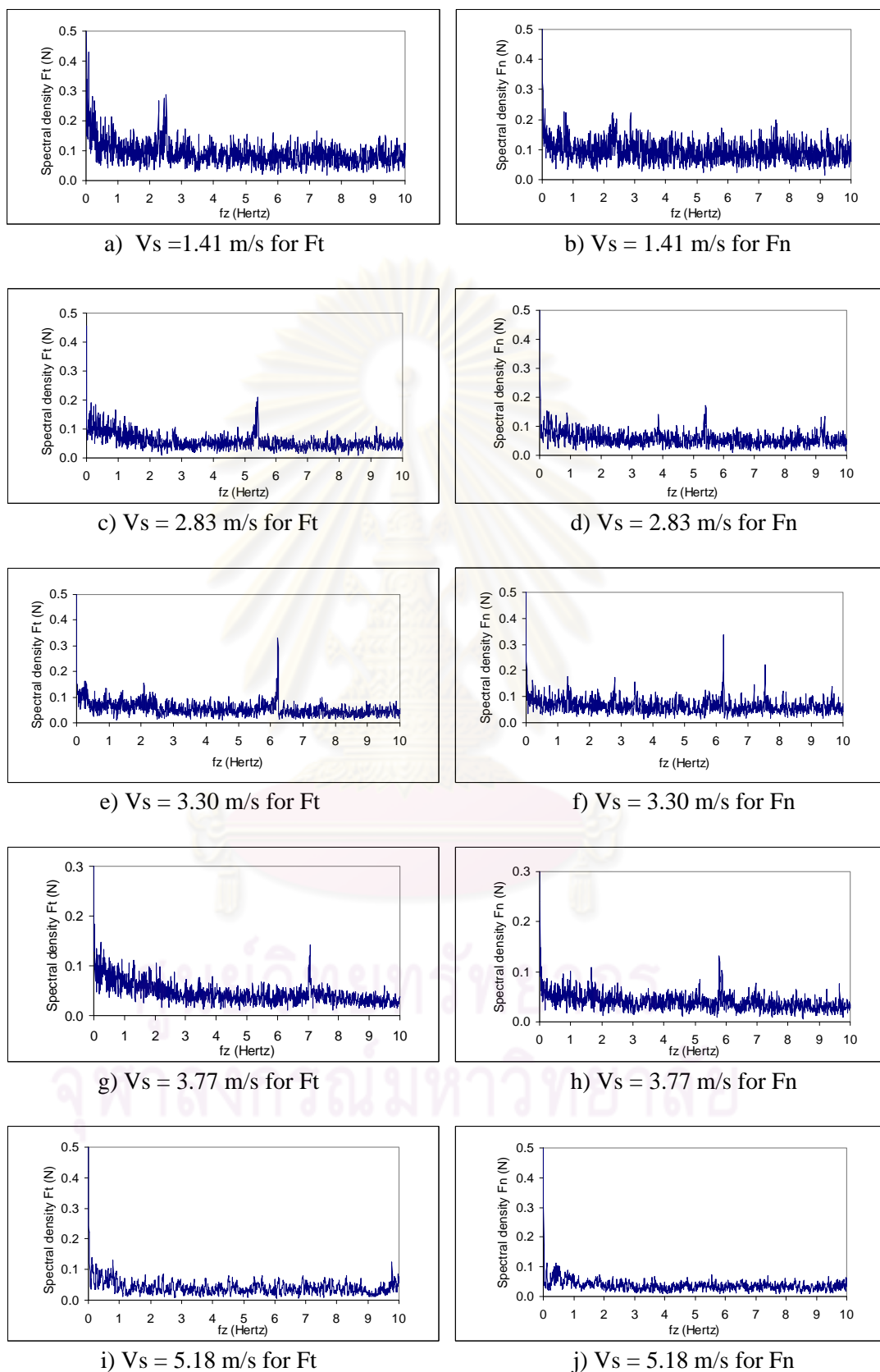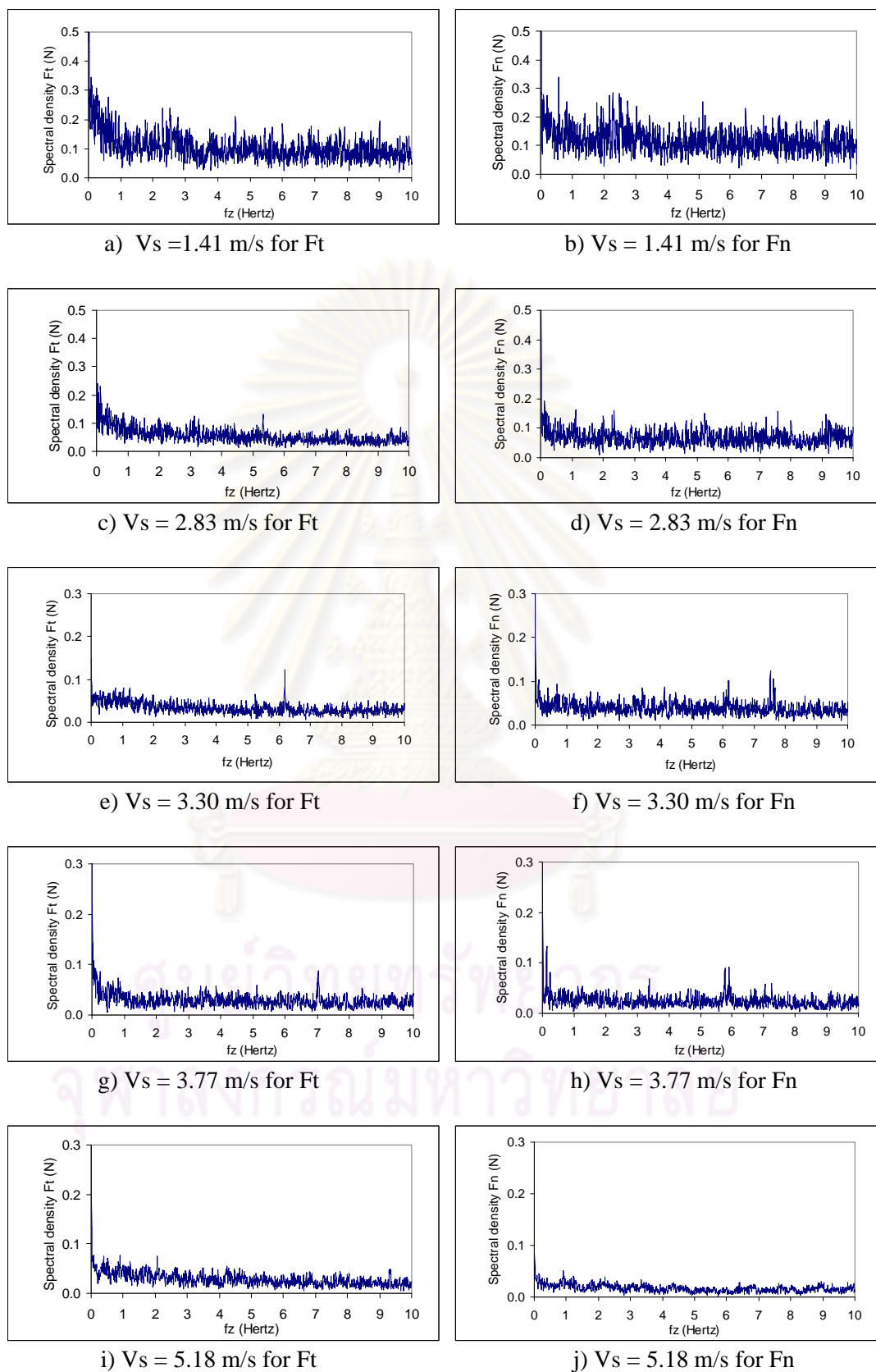
i) Vs = 5.18 m/s for Ft

j) Vs = 5.18 m/s for Fn

Figure E-19   Spectral density of grinding forces for f = 3.0 mm/min and A = 53 μm
                      with various Vs (Replication 1)

a) Vs =1.41 m/s for Ft

b) Vs = 1.41 m/s for Fn

c) Vs = 2.83 m/s for Ft

d) Vs = 2.83 m/s for Fn

e) Vs = 3.30 m/s for Ft

f) Vs = 3.30 m/s for Fn

g) Vs = 3.77 m/s for Ft
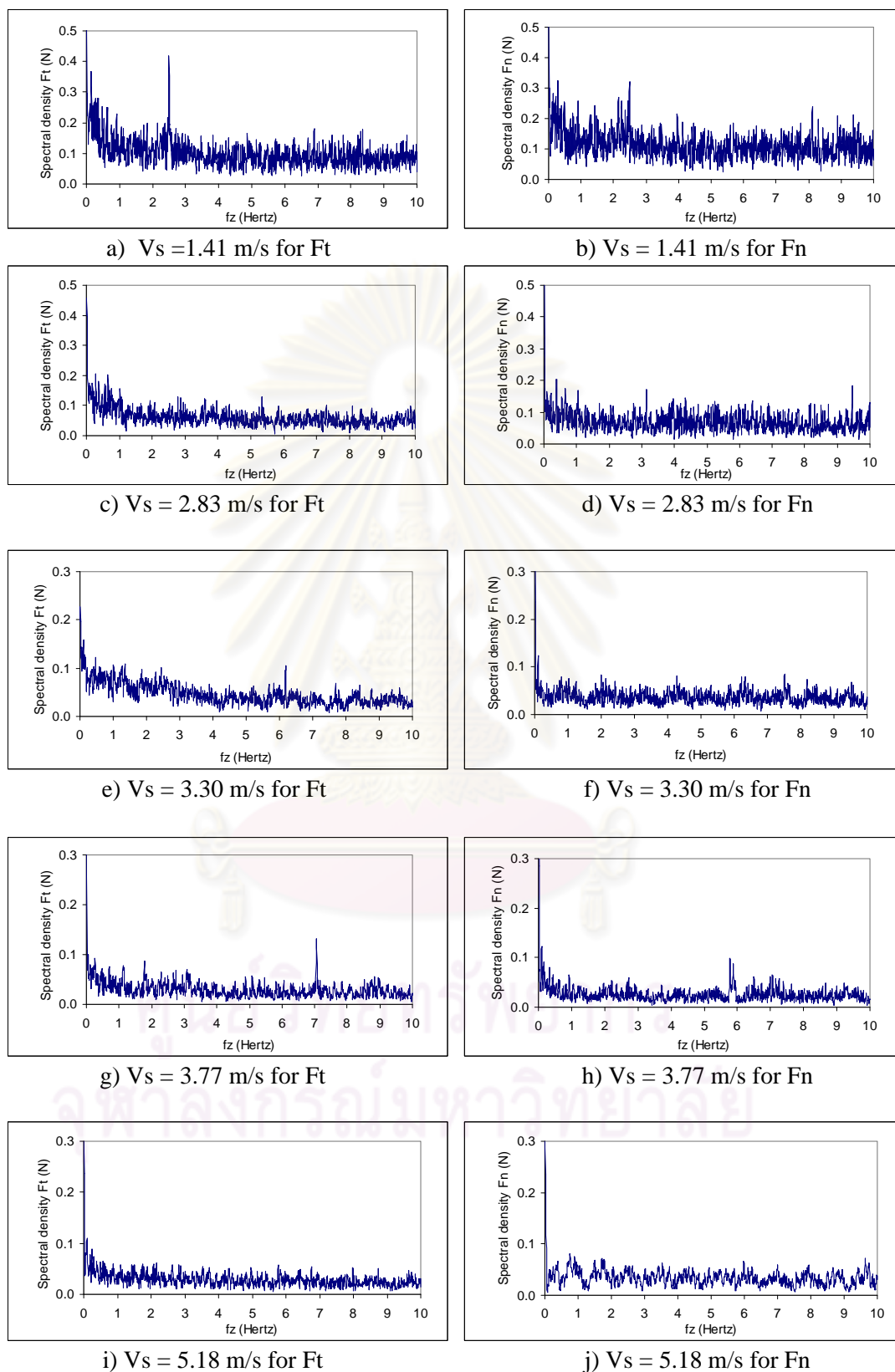
h) Vs = 3.77 m/s for Fn

i) Vs = 5.18 m/s for Ft

j) Vs = 5.18 m/s for Fn

Figure E-20   Spectral density of grinding forces for f = 3.0 mm/min and A = 53 μm
with various Vs (Replication 2)

a) Vs =1.41 m/s for Ft

b) Vs = 1.41 m/s for Fn

c) Vs = 2.83 m/s for Ft

d) Vs = 2.83 m/s for Fn

e) Vs = 3.30 m/s for Ft

f) Vs = 3.30 m/s for Fn

g) Vs = 3.77 m/s for Ft

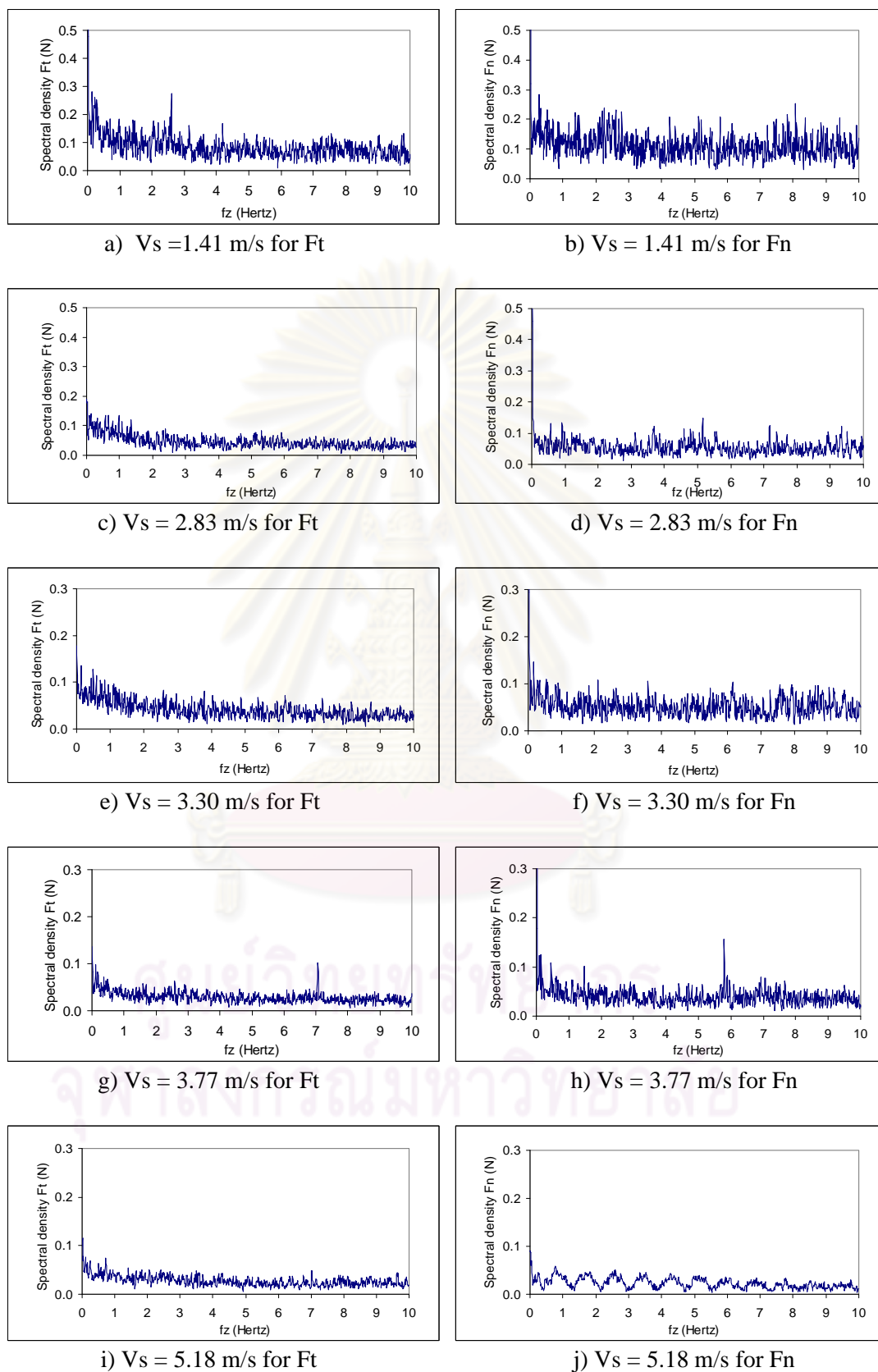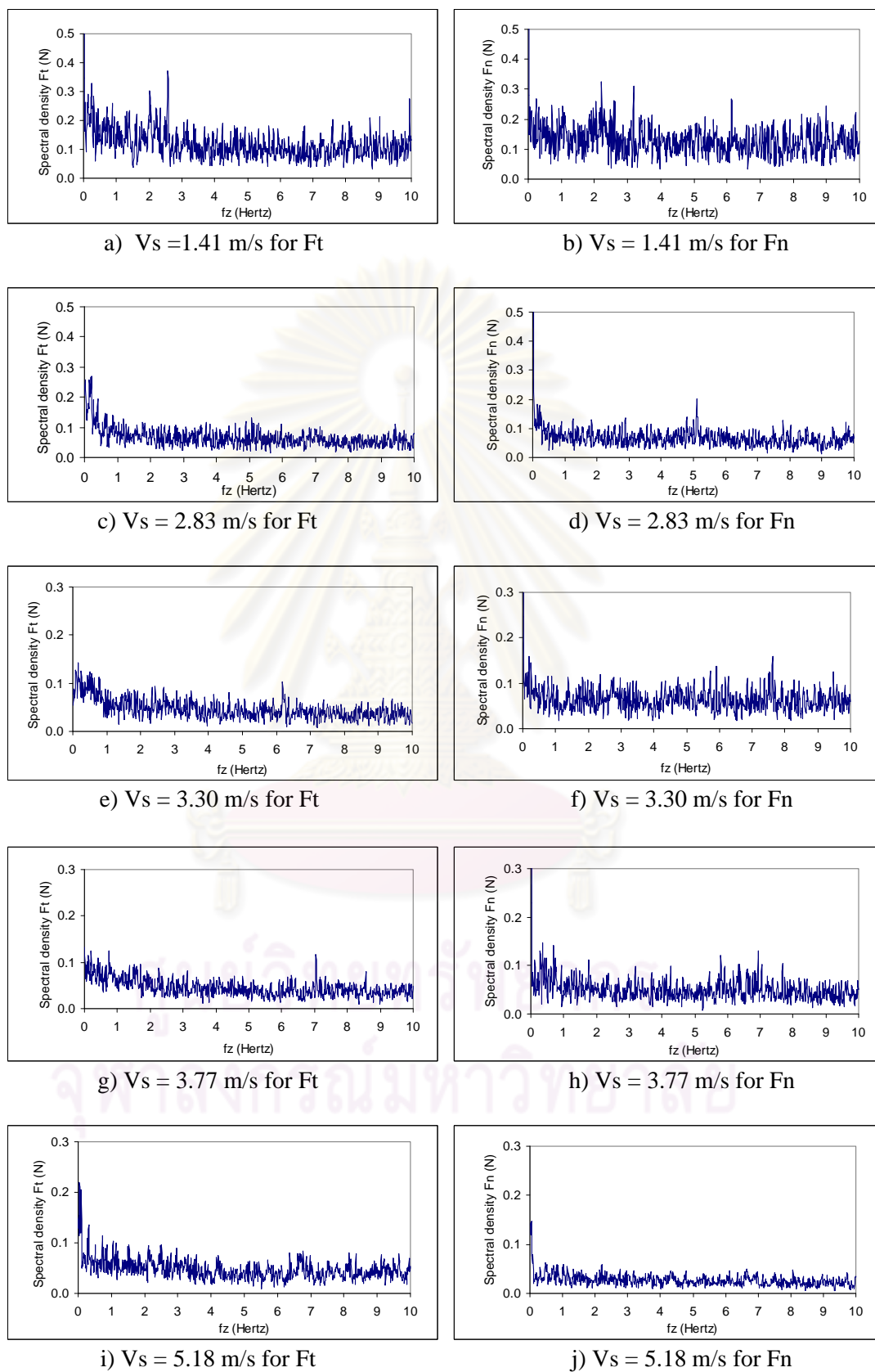h) Vs = 3.77 m/s for Fn

i) Vs = 5.18 m/s for Ft

j) Vs = 5.18 m/s for Fn

Figure E-21   Spectral density of grinding forces for f = 5.0 mm/min and A = 20 μm
with various Vs (Replication 1)

Figure E-22   Spectral density of grinding forces for f = 5.0 mm/min and A = 20 µm
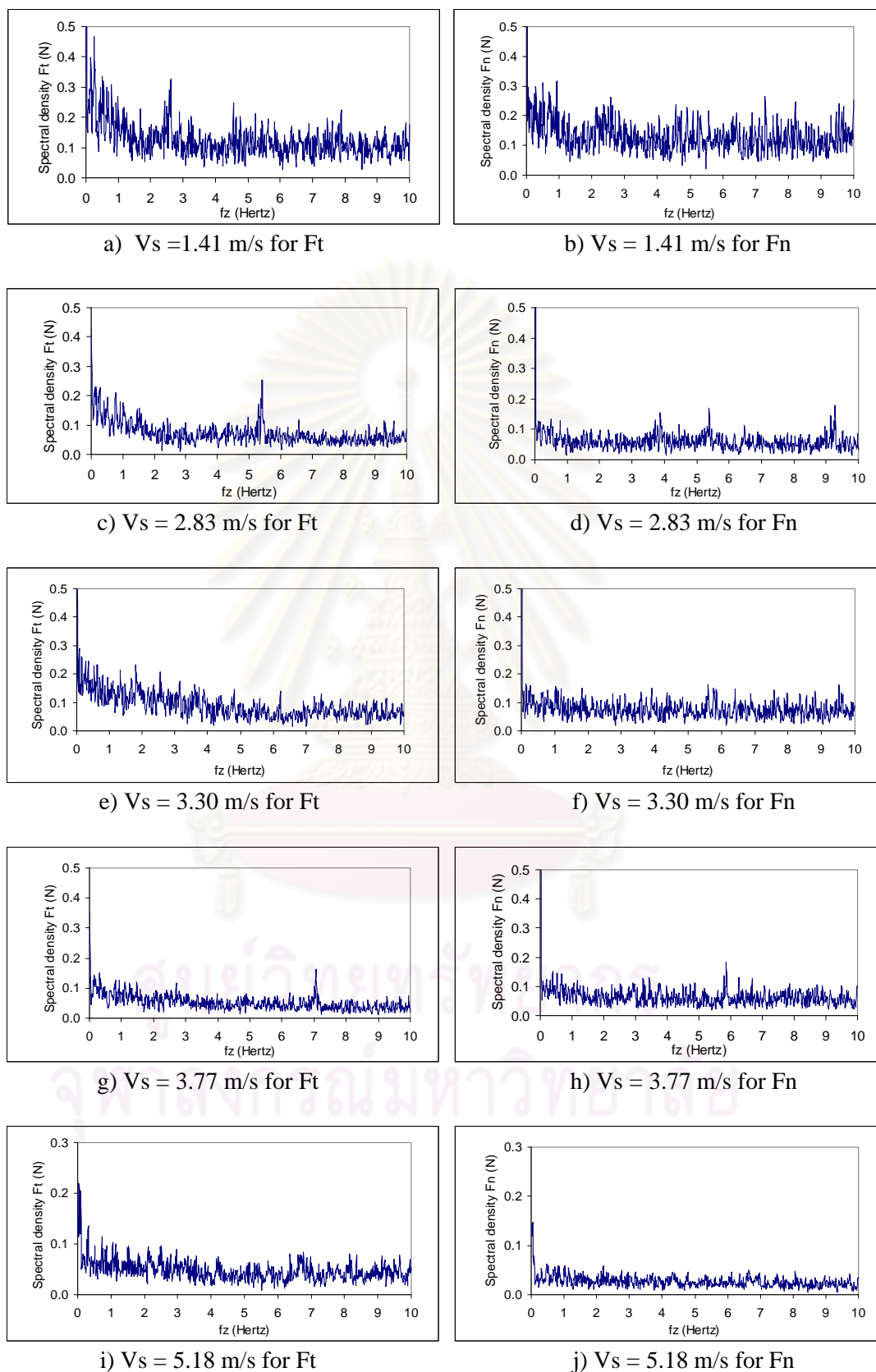with various Vs (Replication 2)

a) Vs =1.41 m/s for Ft

b) Vs = 1.41 m/s for Fn

c) Vs = 2.83 m/s for Ft

d) Vs = 2.83 m/s for Fn

e) Vs = 3.30 m/s for Ft

f) Vs = 3.30 m/s for Fn

g) Vs = 3.77 m/s for Ft

h) Vs = 3.77 m/s for Fn

i) Vs = 5.18 m/s for Ft

j) Vs = 5.18 m/s for Fn

Figure E-23   Spectral density of grinding forces for f = 5.0 mm/min and A = 53 μm with various Vs (Replication 1)

a) Vs =1.41 m/s for Ft

b) Vs = 1.41 m/s for Fn

c) Vs = 2.83 m/s for Ft

d) Vs = 2.83 m/s for Fn

e) Vs = 3.30 m/s for Ft

f) Vs = 3.30 m/s for Fn

g) Vs = 3.77 m/s for Ft

h) Vs = 3.77 m/s for Fn

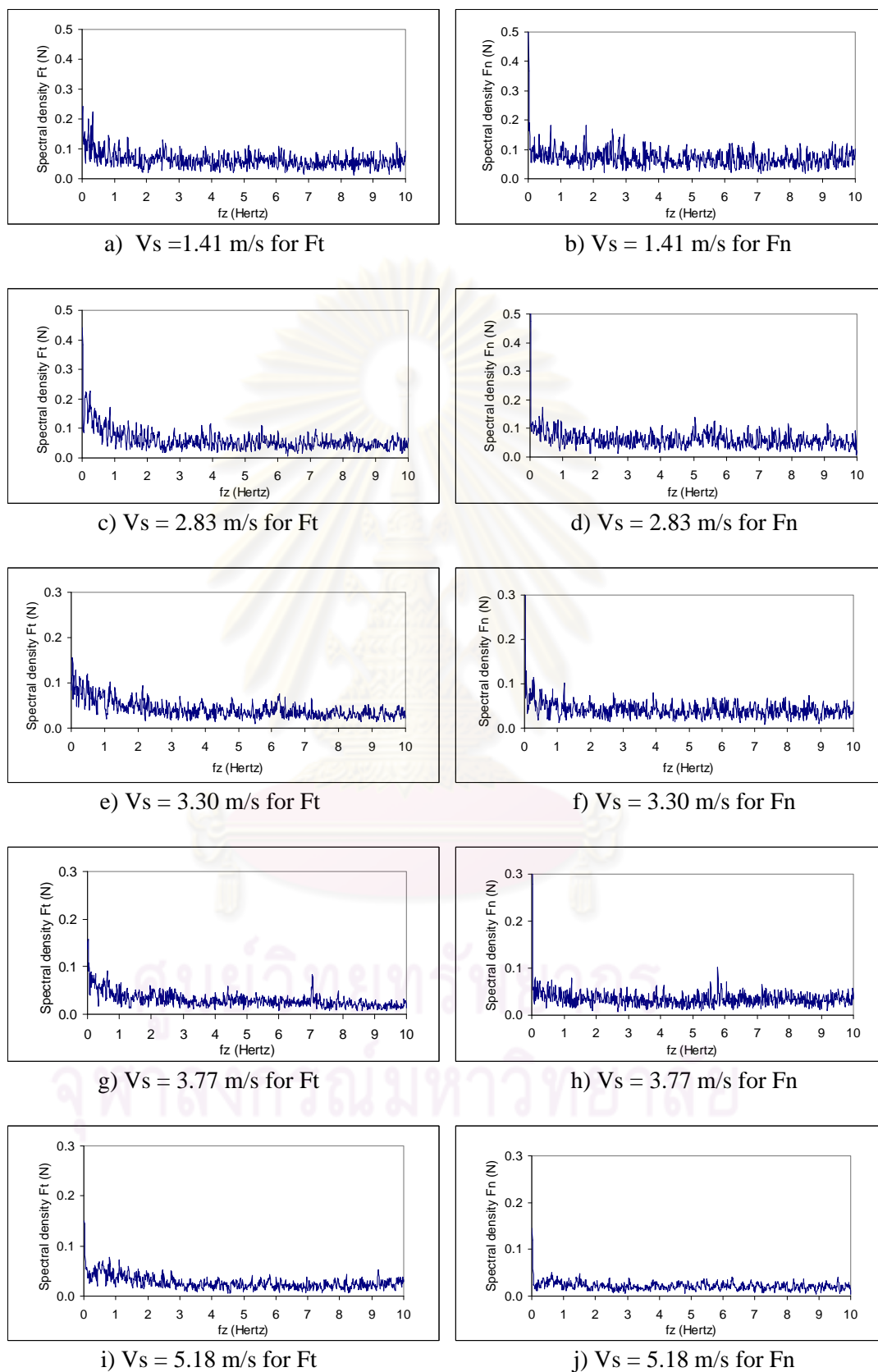i) Vs = 5.18 m/s for Ft

j) Vs = 5.18 m/s for Fn

Figure E-24   Spectral density of grinding forces for f = 5.0 mm/min and A = 53 μm
             with various Vs (Replication 2)

Biography

Mr.Isarawit Chaopanich was born in Kalasin, Thailand, on July 24, 1975. He graduated with a Bachelor's degree and Master's degree of Engineering in Industrial Engineering from Chulalongkorn University in 1997 and 2000, respectively. He had worked for six years before has been studied for a Doctoral degree of Engineering in Industrial Engineering, Chulalongkorn University in 2006.